OPTIMUM PROBES
FOR
NEAR-FIELD ANTENNA MEASUREMENTS ON A PLANE

A THESIS
Presented to
The Faculty of the Division of Graduate Studies
By
Gene K. Huddleston

In Partial Fulfillment
of the Requirements for the Degree
Doctor of Philosophy
in the School of Electrical Engineering

Georgia Institute of Technology
August 1978

OPTIMUM PROBES
FOR
NEAR-FIELD ANTENNA MEASUREMENTS ON A PLANE

Approved:

Demetrius T. Paris, Chairman

Edward B. Joy

Date Approved by Chairman August 24, 1978

ACKNOWLEDGMENTS

I gratefully acknowledge the advice and support of Demetrius T. Paris, Professor and Director of the School of Electrical Engineering, throughout the course of this research. Clearly, without his constant cajoling and unending encouragement, this work could not have been possible.

Grateful acknowledgment is also extended to members of the faculty and staff of the School of Electrical Engineering and Engineering Experiment Station as follows: to Edward B. Joy for his keen interest in the problem and for his excellent advice on near-field measurements; to William J. Dittman, Harold W. Huey, Gene R. Dixon, and Raleigh M. Ford for their help and consideration in the mechanical design and fabrication of the probes and probe positioner; to Hugh W. Denny for the loan of the azimuth positioner; to J. Lee Edwards, C. Patrick Burns, Larry E. Corey, C. E. Ryan, E. E. Weaver, and Steve F. Gildner for their advice and help in using the automated near-field range; to T. P. Barnwell, R. M. Price, D. G. Bodnar, Glenn N. Caplin, and Frank T. Riherd for special help in transferring data; especially to James J. Gallagher for the loan of his excellent microwave synchronizer equipment for the duration of the experiment; and to R. M. Goodman, Director, Systems and Techniques Laboratory, for the use of the measurement facilities at the Engineering Experiment Station.

Special gratitude is extended to Jake Scherer, Rome Air Development Center, Griffis Air Force Base, New York, for the support provided

through the Post-Doctoral Program at a time crucial to the successful completion of this work.

I express my appreciation to Kathy Ketchum Massett for the marvelous typing of the manuscript and for the dependable and timely manner in which she did it. I also thank Catherine Liabastre for her help in preparing the illustrations.

Finally, I express my gratitude to my darling wife, Victoria, and to our children for their patience, understanding, and support, without which I would not have succeeded.

TABLE OF CONTENTS

LIST OF TABLES

LIST OF ILLUSTRATIONS

SUMMARY

The accurate prediction of far-field radiation patterns from near-field antenna measurements on a finite planar surface is an area of considerable interest and practical importance. This research is concerned with the specification of the probe antenna which produces the *most* accurate prediction for a specified antenna under test. An optimum probe criterion is defined by using the properties of the prolate spheroidal wave functions as they relate to the uncertainty principle and Fourier transform theory. It is shown that an optimum rectangular horn probe exists for the near-field measurement on a linearly polarized test antenna, and that its use produces the most accurate far-field predictions. A computer-aided procedure for the design of the optimum probe is described.

The properties of the prolate spheroidal wave functions are used to establish the general criterion that the optimum probe is one that maximizes the proportion of the power of its response within the measurement area. A digital computer simulation of the near-field measurement process is used in conjunction with the general criterion to determine the optimum design parameters for rectangular horn probe antennas, including dielectric-loaded, open-end waveguide probes. It is found that a rectangular probe aperture approximately one wavelength on each side is optimum.

The optimality criterion and probe design procedure are verified experimentally by calculating the far-field patterns of a $4.5\lambda \times 5.1\lambda$

phased array antenna from near-field data obtained using three different rectangular probe antennas. True patterns are calculated from the near-field data over a very large measurement area. The optimality of a E-plane horn probe is demonstrated by comparing the errors in the predicted far fields when the measured near-field area and power received are truncated to various levels. It is found that all three probe antennas produce remarkably accurate results in spite of the truncation of the measurement area. It is also found that the probe having the most directive far-field pattern produces the most concentrated near-field response, the most accurate measured spectra, and the most accurate far-field pattern predictions.

CHAPTER I

INTRODUCTION

1.1 Definition of the Problem

The objective of this research is to establish criteria for the selection of optimum probes for near-field antenna measurements on a finite planar surface. An optimum probe is defined here as one which minimizes those errors in the predicted far fields which may be caused by the finiteness of the measurement area and by spatial data sampling over this area.

The properties of prolate spheroidal wave functions are used to establish the general criterion that the optimum prove is one that maximizes the proportion of the power of its near-field response within the measurement area, subject to the constraint that the far fields of the probe contain no zeroes within the angular region where probe compensation is desired. Mathematical modeling and digital computer simulation of the near-field measurement technique are used in conjunction with the above criterion to determine the optimum design parameters for the class of practical probe configurations consisting of rectangular horn antennas, including dielectric-loaded, open-end waveguide probes. The method is verified experimentally by comparing the errors produced in the predicted far fields when the measured near field area and power received are truncated to various levels for the cases of three probes of varying aperture dimensions and concentrations of responses.

This research has been carried out to gain a better understanding

of the planar near-field technique by clarifying the relationships between the properties of the measurement probe, the size of the measurement area, the directivity of the antenna being measured, and the resulting uncertainties in the calculated plane wave spectra and predicted far fields. In addition, the development of a probe design procedure is sought to enhance the accuracy of the near-field technique, particularly in measurement situations where a significant portion of energy is radiated outside the measurement area by the test antenna.

1.2 Background

Kerns [1] developed the theory of probe-compensated near-field measurements on a planar surface by using a generalization of a part of the theory of waveguide junctions and scattering matrices [2] and the plane wave spectrum expansion described by Clemmow [3]. Joy [4] pointed out the wavenumber-limited character of the measured near-field data and established sampling criteria for measurements on a planar surface based on Shannon's sampling theorem [5]. Measurements performed by Joy using three different probe antennas demonstrated the arbitrariness of the measuring antenna for the case of the highly directive parabolic dish test antenna and large measurement area used.

Leach [6] reformulated the theory of near-field measurements using the reciprocity theorem [7]. He specialized it to the case of a cylindrical surface enclosing the test antenna using the vector expansion representation of electromagnetic fields described by Stratton [8]. Angular sampling criteria were established for measurements around the cylinder while those established by Joy were invoked for the axial

direction. A method was developed for converting measured far-field probe data from a spherical surface to coefficients in the required cylindrical wave expansion. No particular emphasis was placed on the choice of measurement probe other than ensuring that no nulls were present in its pattern over a hemisphere. The test antenna was a slotted waveguide array which produced a broad azimuthal pattern and a narrow beam in the elevation plane. Slight discrepancies in agreement between theory and experiment were attributed to stray reflections in the measurement environment.

Other investigators have also contributed to the development of near-field measurement techniques. Hamid [9] developed a technique which used two identical probes to obtain the autocorrelation function of the near field on a plane from which the Fraunhoefer patterns were obtained. No probe compensation was used. Brown and Jull [10] have described a two-dimensional technique for cylindrical surfaces which assumes no z-dependence of the fields and which includes probe compensation. Jensen [11] has described a method applicable to spherical surfaces which requires certain idealizing assumptions about the probe to make the method practical. Wacker [12] compared the near-field techniques for planar, cylindrical, and spherical surfaces and developed the details of a spherical near-field technique which necessarily omits probe compensation.

The planar measurement surface is advantageous because of the simplicity of computations and the straightforward manner in which data is collected; however, actual measurements must be restricted to a finite portion of the plane and uncertainties are introduced due to

omission of the infinite plane.

Rodrigue et al. [13] demonstrated that the far-field antenna patterns determined on a planar near-field range were as accurate as those determined on a far-field range for the case of a 22λ-diameter parabolic dish antenna which produced sum and difference beams on the axis of symmetry of the dish. A small pyramidal horn antenna was used to scan the 43λ x 43λ measurement area with sample spacings in x and y of λ/3. Small differences in the levels of first sidelobes were attributed to limitations of the far-field ranges while greater differences in the other sidelobes at wider angles were attributed to lack of resolution in the near-field data processing techniques. At the edge of the measurement area, the measured probe response was less than -40dB with respect to the maximum response obtained near the center of the measurement area.

In a later investigation to demonstrate near-field accuracies for a phased array antenna [14], larger differences between near-field and far-field results were observed for the case where the beams (sum and difference) were steered 72° off broadside in the azimuth plane. The small horn antenna used earlier [13] was used again to collect near-field data on a 21λ x 21λ measurement plane situated 2λ in front of the 14.6λ-diameter phased array. Measured probe response was only -25dB at the edge of the measurement area. Significant differences between near-field and far-field results for the sidelobe structure in the central portion of the patterns were attributed to the effects of temperature variations. Reasonably good agreement was observed for the main beam and grating lobes at ±72°; however, for polar angles greater than

76°, serious differences in agreement were observed in the patterns contrary to the expectation that good agreement should have been obtained out to the optical limit of 84 to 86 degrees.

Huddleston et al. [15] repeated the measurements on the phased array [14] using a $.84\lambda \times .95\lambda$ pyramidal horn and a $\lambda/2$ electric dipole as probes. The dipole data showed increased fine structure in the central portion of the patterns. These additional errors were attributed to extraneous range reflections; however, aliasing errors as discussed below were also a likely source. The small aperture horn produced more accurate results since it was better able to discriminate against range reflections and/or aliasing errors. Neither probe produced accurate results in the patterns beyond approximately 76°.

Yaghjian [16] concluded from an approximate mathematical analysis that the planar near-field technique does not yield accurate information about the fields outside the solid angle formed by the edge of the aperture of the test antenna and the boundary of the scan area. Newell and Crawford [17] reached the same conclusion from experimental data taken on scan planes at different distances in front of the same test antenna.

It is appropriate at this point to formulate the aliasing problem in the familiar domains of time and frequency since much of the background information to follow is cast in these terms. The extension to two dimensions as required for near-field measurements is straightforward [18].

Let $s(t)$ be a band-limited function so that its Fourier transform $S(f)$ is non-zero only over the finite interval $|f| \leq W$; i.e.,

$$S(f) = \begin{cases} \int_{-\infty}^{\infty} s(t)e^{-j2\pi ft}dt \quad , & |f| \le W \\ 0 \quad , & \text{otherwise} \end{cases} \tag{1-1}$$

Then by the inversion integral [19],

$$s(t) = \int_{-W}^{W} S(f)e^{j2\pi ft}df \quad . \tag{1-2}$$

When a linear probe is used to measure s(t), the resulting time signal g(t) is given by

$$g(t) = \int_{-\infty}^{\infty} s(\tau)h(t-\tau)d\tau = s(t) \circledast h(t) \tag{1-3}$$

where h(t) is characteristic of the probe and where $\circledast$ denotes convolution. By the convolution theorem [19], the *spectrum G(f) of g(t)* is given by

$$G(f) = S(f)H(f)$$

where $h(t) \leftrightarrow H(f)$ is a Fourier transform pair. In the absence of noise and where $H(f) \neq 0$, S(f) can recovered from G(f) by inverse filtering (probe compensation) as

$$S(f) = G(f)/H(f) \quad . \tag{1-4}$$

In practice, g(t) is measured over only a finite interval

(-T/2, T/2), the effect of which is to multiply g(t) by a window function p(t) to yield the time-limited function

$$\hat{g}(t) = g(t)p(t) \tag{1-5}$$

with corresponding transform [19]

$$\hat{G}(f) = \int_{-\infty}^{\infty} G(\eta - f)P(\eta)d\eta = G(f) \circledast P(f) \tag{1-6}$$

where $p(t) \leftrightarrow P(f)$ is a Fourier transform pair. As is often the case, p(t) may be the rectangular window with transform

$$P(f) = T \frac{\sin \pi fT}{\pi fT} \tag{1-7}$$

which extends over the entire frequency axis.

The function $\hat{g}(t)$ is not band-limited, and the sampling theorem [5] does not strictly apply. However, if $\hat{g}(t)$ is sampled at an interval Δt corresponding to a folding frequency $W_M = (2\Delta t)^{-1}$, then the Fourier spectrum of the sampled $\hat{g}(t)$ is an "aliased" version of the spectrum of $\hat{g}(t)$ as given by

$$\hat{G}_a(f) = \sum_{m=-\infty}^{\infty} \hat{G}(f + 2mW_M) \quad . \tag{1-8}$$

The aliased spectrum $\hat{G}_a(f)$ is periodic with period $2W_M$. For any f such that $|f| \leq W_M$, $\hat{G}_a(f)$ is a summation of values of $\hat{G}(f + 2mW_M)$; i.e., the high frequency components of $\hat{G}$ are aliased or folded back into $\hat{G}_a$ for

$|f| \leq W_M$. Only when $\hat{g}(t)$ is bandlimited and $W_M \geq W$ is $\hat{G}_a$ an exact replica of $\hat{G}$ in the band $|f| \leq W$.

Some band-limited functions are known to undergo time-limiting and exhibit less error in their transforms than others. Obviously, the probe and the window used to precondition the data can influence the character of the function $\hat{G}(f)$ being processed; hence, it would seem that the judicious choice of either or both of these functions could greatly influence the accuracy of the final estimate of $\hat{G}_a(f)$.

Gabor [20] obtained an uncertainty relation for time signals which stated that the product of the rms time duration of a signal and its rms frequency width is greater than or equal to one-half; i.e., a signal cannot simultaneously be limited in time and frequency. He further established that the signal which occupies the minimum area $\Delta t \Delta f = 1/2$ is the product of a harmonic oscillation with a pulse of the form of a Gaussian probability function. An arbitrary time signal could then be expanded in an infinite series of such elementary "sine-type" and "cosine-type" signals with the implication that the information contained in a finite number of terms would be maximized; however, the elementary signals were not orthogonal and, therefore, rather inconvenient to use. No analysis of errors introduced by using only a finite number of terms of the series was done.

Chalk [21] considered the problems of determining an optimum pulse shape for use in pulse communications. It was well known that with the rectangular pulse, the spectra were widely spread, and that by rounding the corners of the pulse, the spread and interchannel interference could be reduced. An optimum pulse was defined as one which maximized the

ratio of energy inside the allocated frequency band to the total energy of the pulse. Solution of the resulting homogeneous Fredholm integral equation yielded a zeroeth order prolate spheroidal wave function as the optimum pulse shape although Chalk did not explicitly identify his series expansion as being that of these functions. The optimum pulse and its spectrum possessed the same shape. Their sharpnesses were reciprocal and described by the product of time duration T and frequency bandwidth 2W. The results implied that the use of such optimum pulses would minimize adjacent channel interference since the percentage of energy outside the allocated bandwidth is minimum.

Slepian and Pollak [22] derived certain properties of the prolate spheroidal wave functions which make them ideally suited for the study of certain questions regarding the relationship between functions and their Fourier transforms. Of particular interest is the fact that these functions are orthogonal over a given finite interval as well as over the infinite interval. The prolate spheroidal wave functions are particularly suited to the study of band-limited signals and the uncertainty relations.

Landau and Pollak [23] re-examined the uncertainty relations using the prolate spheroidal wave functions. Whereas Gabor [20] used second moments in his definitions of time duration and frequency bandwidth, Landau and Pollak presented a more useful form of the uncertainty principle which related the proportion of energy β^2 in the given frequency band $\Omega = 2\pi W$ to the proportion of energy α^2 in the given time duration T. In the special case of band-limited functions such that $\beta^2 = 1$, it was shown that $\alpha \leq \sqrt{\lambda_o}$, where λ_o is the largest eigenvalue of the integral

equation considered earlier by Chalk [21]. In this case, equality $\Omega T = 2c$ is achieved for the zeroeth order prolate spheroidal wave function ψ_o, where c is a parameter of the eigenvalue λ_o. It was further shown that for small $\lambda_o = \alpha^2$, the usual $si(t) = (\sin \Omega t)/t$ sampling function is essentially as good as the optimal function $\psi_o(c,t)$; however, for $\alpha^2 = .92$, $\Omega T = 4.5$ suffices for ψ_o while use of Si(t) requires $\Omega T = 8.5$. For a proportion of $\alpha^2 = .99$, the minimum ΩT is 6.25 for ψ_o while Si(t) would require a value of $T = 30$. For a fixed *bandwidth* Ω, *larger values* of ΩT imply larger durations T.

As an extension of the above results, Landau and Pollack [24] established the mathematical truth in the engineering intuition that there are approximately 2WT independent signals ϕ_i of bandwidth W concentrated in an interval of length T. Roughly speaking, the result is true when the ϕ_i are chosen to be the prolate spheroidal wave functions, but is not true for sampling functions of the form sint/t. Specifically, it was established that the mean square error incurred in estimating the band-limited function f(t) using $N = 2WT + 1$ terms in a series expansion involving prolate spheroidal wave functions is bounded above by a quantity which is proportional to the percentage of energy of f(t) outside of the interval of length T. Such was shown not to be the case for the sampling functions in general; however, the error was still related to this concentration of energy.

Other investigators have contributed to a better understanding of the prolate spheroidal wave functions. Stratton, et al., [25] provided numerical tables of the prolate and oblate spheroidal wave functions to facilitate solutions of the wave equation in such coordinate systems.

Flammer [26] presents a similar treatment and sets of tables. Slepian [27] extended the earlier works of Landau and Pollak [23,24] to many dimensions and provided some useful asympotic expansions for the single dimension case [28]. Slepian and Sonneblick [29] have computed and published tables of eigenvalues for the zeroeth order functions.

Prolate spheroidal wave functions have been applied to antenna problems to some extent. Fong [30] made use of spheroidal functions to determine the finite length line source which realizes a specified radiation pattern subject to the constraint that the source have a superdirective ratio less than or equal to a fixed value. A mean square error criterion was used. Rhodes [31] formulated the maximum directivity problem for a continuous line source in terms of the prolate spheroidal functions and solved it exactly in terms of these functions by making use of their double orthogonality properties. He also applied these functions to the problem of determining the aperture-limited function which produces the best approximation to a radiation pattern specified over only the visible region, and, in so doing, extended the Fredholm integral equation to include a weight factor $(1-\eta)^{\alpha}$ as required to account for the edge behavior of aperture-limited fields. It is noteworthy that Rhodes considered only aperture fields of limited spatial extent and, hence, unlimited extent in the wavenumber domain; on the other hand, near-field techniques consider wave number-limited functions and measured fields of unlimited spatial extent.

It has been long recognized that the accuracy of data sampling techniques can be greatly enhanced by preconditioning the data to remove frequency components above the folding frequency as established by the

sampling interval; i.e., by passing the raw data through a lowpass filter [32]. The measurement probe or transducer itself can be selected to provide some of the desired filtering although, in most cases of time signals, one is more concerned with distortions of the original data rather than with any beneficial effects of the measurement probe.

The effects of the probe on two-dimensional digital data has also been recognized. Hunt and Breedlove [33] analyzed the effects of finite spot size (probe) on the accuracy of the reconstituted image in digital image processing. Their generally tutorial treatment of this often overlooked facet of image processing shows that the finite spot size which samples the actual image can be used to advantage to control the effects of aliasing in the displayed image. Aliasing in the displayed image is usually not of great concern if 90 to 95 percent of the image energy lies in a region of frequencies below the folding frequency [34]; however, the judgement of the quality of pictorial information is a subjective matter.

Legault [34] examined in detail the aliasing problem in two-dimensional sampled imagery and the influence of the detector (probe) on the reconstructed image. After Peterson and Middleton [35], the Fourier transform of the reconstructed image is given by

$$O(\underline{r}) = [B(\underline{r})/A] \sum_{n=-\infty}^{\infty} A^*(\underline{r}+\underline{b}_n) S(\underline{r}+\underline{b}_n) M^*(\underline{r}+\underline{b}_n) \qquad (1\text{-}9)$$

where $\underline{r}$ designates a vector representing a multi-dimensional spatial frequency domain; $B(\underline{r})$, $A(\underline{r})$, $S(\underline{r})$, and $M(\underline{r})$ are the Fourier transforms of the distribution of luminence over the area of each display light

source, response over the area of the detector, distribution of intensity over the scene being imaged and sampled, and the point spread function of the optical system, respectively. $O(\underline{r})$ is periodic with period $\underline{b}_n$. $B(\underline{r})$ denotes the reconstruction function and A*M* acts as a prefilter (* denotes complex conjugate). As the above equation shows, aliasing occurs before the display, and no display response $B(\underline{r})$ can eliminate aliasing. Legault concluded, however, that a scanning sampling detector whose response is uniform over its area will be "matched" to the system when its area is twice as large as the spacing between sampling centers; i.e., the optimum detector does not attempt to measure the image at a point but rather carries part of the prefiltering burden so that the effects of aliasing can be minimized.

The use of window functions in image processing is well known [36]. The general approach has been to multiply the original data by a purely mathematical window function which gently tapers the data at the extremes of the measurement interval to preclude the introduction of high frequency components due to abrupt changes in the data. That window functions such as the Hanning filter and elliptical arc fulfill their aim of smoothing out high frequency details is indisputable; however, the drawback to this approach is that it cannot discriminate between significant and superficial frequency components, and so it blindly smooths out both. The price paid is an overall blurring of the entire signal which may be acceptable in some cases but not, perhaps, in others.

Dyson [37] reviewed the types of probes that he considered most suited for the measurement of the fields close to an antenna. Ideally, it was desired to measure the unperturbed normal electric and tangential

magnetic fields on arbitrarily shaped surfaces; hence, the infinitesimal electric dipole and magnetic dipole would constitute ideal probes for such point measurements. Use of such probes for near-field measurements on a planar surface would require no probe compensation provided that a large enough measurement area were used to preclude aliasing errors in the data processing.

Richmond and Tice [38] investigated the applicability of small open-end waveguide probes to the measurement of near-fields. An undersized rectangular waveguide filled with dielectric material was used to realize a probe which gave excellent results as compared to a scattering technique [39]. No probe compensation technique was considered.

CHAPTER II

THEORY

2.1 Introduction

In this chapter the mathematical background for determining criteria for optimum probes for near-field measurements is developed. The development begins with a presentation of the theory of plane wave spectrum representation of electromagnetic fields with emphasis on its application to the near-field measurement technique. Next, the salient features and mathematical relationships of the theory and application of planar near-field, probe-compensated measurements are presented. Within the framework established by the foregoing, the expansion of the probe response in terms of prolate spheroidal wave functions is developed, and its properties are exploited to derive a maximum power criterion for the optimum probe response.

2.2 Plane Wave Expansions

Let $\hat{x}$, $\hat{y}$, and $\hat{z}$ be unit vectors along the x, y, and z axes of a Cartesian coordinate system. Then each of the rectangular components of $\underline{E}$ and $\underline{H}$ in the assumed lossless, linear, homogeneous, isotropic medium must satisfy the scalar wave equation

$$\nabla^2\psi + k^2\psi = 0 \quad . \tag{2-1}$$

where

$$k^2\mu\epsilon = (2\pi/\lambda)^2 \tag{2-2}$$

and where ω is the radian frequency, μ is the permeability of the medium, ϵ is the permittivity, and λ is the wavelength. Time variations of the form $e^{j\omega t}$ are understood and suppressed. Solving Equation (2-1) by separation of variables yields elementary solutions of the form [31]

$$\psi(x,y,z) = A(k_x,k_y)e^{-j(k_x x + k_y y + k_z z)} \tag{2-3}$$

where k_x and k_y must be purely real to satisfy the radiation condition [31] and where

$$k_z = + \sqrt{k^2 - k_x^2 - k_y^2} \tag{2-4}$$

for the region $z > 0$.

The most general solution of Equation (2-1) in the region $z > 0$ will be a linear combination of all physically admissible elementary solutions; viz.,

$$E_\ell(x,y,z) = \int_{-\infty}^{+\infty}\int_{-\infty}^{+\infty} A_\ell(k_x,k_y)e^{-j(k_x x+k_y y+k_z z)}\,dk_x dk_y \tag{2-5}$$

where ℓ denotes x, y, or z and where the unknown complex amplitude functions $A_\ell(k_x,k_y)$ are to be determined from specified boundary conditions. For example, if the two rectangular components of electric field are known on the $z = 0$ plane, then

$$E_x(x,y,0) = \int_{-\infty}^{+\infty}\int_{-\infty}^{+\infty} A_x(k_x,k_y)e^{-j(k_x x+k_y y)}\,dk_x dk_y \qquad (2\text{-}6)$$

$$E_y(x,y,0) = \int_{-\infty}^{+\infty}\int_{-\infty}^{+\infty} A_y(k_x,k_y)e^{-j(k_x x+k_y y)}\,dk_x dk_y \qquad (2\text{-}7)$$

Recognizing Equations (2-6) and (2-7) as (two-dimensional) Fourier transforms and applying the inversion integral [19] yields

$$A_x(k_x,k_y) = \frac{1}{(2\pi)^2}\int_{-\infty}^{+\infty}\int_{-\infty}^{+\infty} E_x(x,y,0)e^{+j(k_x x+k_y y)}\,dk_x dk_y \qquad (2\text{-}8)$$

$$A_y(k_x,k_y) = \frac{1}{(2\pi)^2}\int_{-\infty}^{+\infty}\int_{-\infty}^{+\infty} E_y(x,y,0)e^{+j(k_x x+k_y y)}\,dk_x dk_y \qquad (2\text{-}9)$$

It follows from the above that the electric field components, anywhere in the region $z > 0$, are given by

$$E_x(x,y,z) = \int_{-\infty}^{+\infty}\int_{-\infty}^{+\infty} A_x(k_x,k_y)e^{-j\underline{k}\cdot\underline{r}}dk_x dk_y \qquad (2\text{-}10)$$

$$E_y(x,y,z) = \int_{-\infty}^{+\infty}\int_{-\infty}^{+\infty} A_y(k_x,k_y)e^{-j\underline{k}\cdot\underline{r}}dk_x dk_y \qquad (2\text{-}11)$$

$$E_z(x,y,z) = \int_{-\infty}^{+\infty}\int_{-\infty}^{+\infty} A_z(k_x,k_y)e^{-j\underline{k}\cdot\underline{r}}dk_x dk_y \qquad (2\text{-}12)$$

where

$$A_z(k_x,k_y) = \frac{-k_x A_x(k_x,k_y) - k_y A_y(k_x,k_y)}{k_z} \qquad (2\text{-}13)$$

$$\underline{k} = \hat{x}k_x + \hat{y}k_y + \hat{x}k_z \tag{2-14}$$

$$\underline{r} = \hat{x}x + \hat{y}y + \hat{z}z \quad . \tag{2-15}$$

Equation (2-13) is obtained from Maxwell's equation for Gauss' Law ($\nabla \cdot \underline{D}=0$) when the differentiation is applied to the integral representations in Equation (2-5) with the differentiation being carried out under the integral sign. In a similar manner, the rectangular components of the magnetic field follow from differentiation of the integral representations in Equations (2-10) through (2-12) according to Maxwell's equation for Faraday's Law ($\nabla \times \underline{E} = -j\omega\mu H$); viz.,

$$H_x(x,y,z) = -\frac{1}{k\eta}\int_{-\infty}^{+\infty}\int_{-\infty}^{+\infty}\frac{k_x k_y A_x + (k^2-k_x^2)A_y}{k_z}\, e^{-j\underline{k}\cdot\underline{r}}dk_x dk_y \tag{2-16}$$

$$H_y(x,y,z) = \frac{1}{k\eta}\int_{-\infty}^{-\infty}\int_{-\infty}^{-\infty}\frac{(k^2-k_y^2)A_x + k_x k_y A_y}{k_z}\, e^{-j\underline{k}\cdot\underline{r}}dk_x dk_y \tag{2-17}$$

$$H_z(x,y,z) = -\frac{1}{k\eta}\int_{-\infty}^{+\infty}\int_{-\infty}^{+\infty}(k_y A_x - k_x A_y)e^{-j\underline{k}\cdot\underline{r}}dk_x dk_y \tag{2-18}$$

where η denotes the characteristic impedance $(\mu/\epsilon)^{\frac{1}{2}}$ of the lossless medium.

Each of the six complex components of the electromagnetic field $\underline{E}$, $\underline{H}$ in the half-space $z > 0$ are expressed above in terms of just two independent scalar functions A_x and A_y which are determined, in turn, by the tangential component (E_x and E_y) of the electric field on the infinite plane $z = 0$. Since the infinite plane is a surface closed at

infinity, these results are in keeping with the uniqueness theorem [8].

At large distances $r = \sqrt{x^2 + y^2 + z^2}$ from the origin of the coordinate system, each rectangular component of the electric field given by Equations (2-10) through (2-12) approaches asymptotically the value

$$E_\ell(x,y,z) \sim j2\pi k \frac{e^{-jkr}}{r} \cos\theta \; A_\ell(k\sin\theta\cos\phi, k\sin\theta\sin\phi) \tag{2-19}$$

in the spherical coordinate direction (θ,ϕ), where ℓ denotes x, y, or z [31]. The corresponding spherical vector components are given in terms of A_x and A_y by

$$E_\theta \sim j2\pi k \frac{e^{-jkr}}{r} [A_x\cos\phi + A_y\sin\phi] \tag{2-20}$$

$$E_\phi \sim j2\pi k \frac{e^{-jkr}}{r} \cos\theta [A_x\sin\phi - A_y\cos\phi] \tag{2-21}$$

where A_x and A_y are evaluated at

$$k_x = k\sin\theta\cos\phi \tag{2-22}$$

$$k_y = k\sin\theta\sin\phi \tag{2-23}$$

corresponding to the direction (θ,ϕ). Equations (2-19) through (2-23) are useful in evaluating the far-zone (radiation) fields of an antenna located near the origin from knowledge of the tangential near-zone electric field produced on the $z = 0$ plane by the antenna radiating into the half-space $z > 0$. The determination of the near-zone tangential electric

field requires measurement using a non-ideal probe whose characteristics necessarily bias the measurement; consequently, compensation must be made for the probe in the determination of the far-zone fields as described in the next section.

2.3 Probe-Compensated Near-Field Measurements

In the planar near-field technique, the transmitting test antenna is moved over a planar measurement surface located a distance z from the test antenna. The response of the probe is measured and sampled as the probe traverses the measurement plane. A second independent measurement is performed by rotating the probe by 90° (or by using a second, independent probe) and repeating the sampling scan of the measurement plane. From these sampled data measurements of probe response over the measurement plane, and from knowledge of the far fields of the probe antenna, the far fields of the test antenna can be determined as described in detail by Paris et al. [40] and as summarized below.

When the Lorentz reciprocity theorem is applied to surfaces S_1, S_2, and S_2' in Figure 2-1, the complex voltage response V_1 of the probe antenna located at the point $O'(x_o,y_o,z_o)$ is given for orientation #1 as shown by

$$V_1(x_o,y_o,z_o) =$$

$$\frac{2(2\pi)^2}{k\eta} \int_{-\infty}^{+\infty}\int_{-\infty}^{+\infty} \left[A_x \frac{-(k^2-k_y^2)B'_{x'}+k_x k_y B'_{y'}}{k_z} + A_y \frac{-k_x k_y B'_{x'}+(k^2-k_x^2)B'_{y'}}{k_z}\right]$$

$$\cdot\, e^{-j(k_x x_o + k_y y_o + k_z z_o)}\, dk_x dk_y \qquad (2\text{-}24)$$

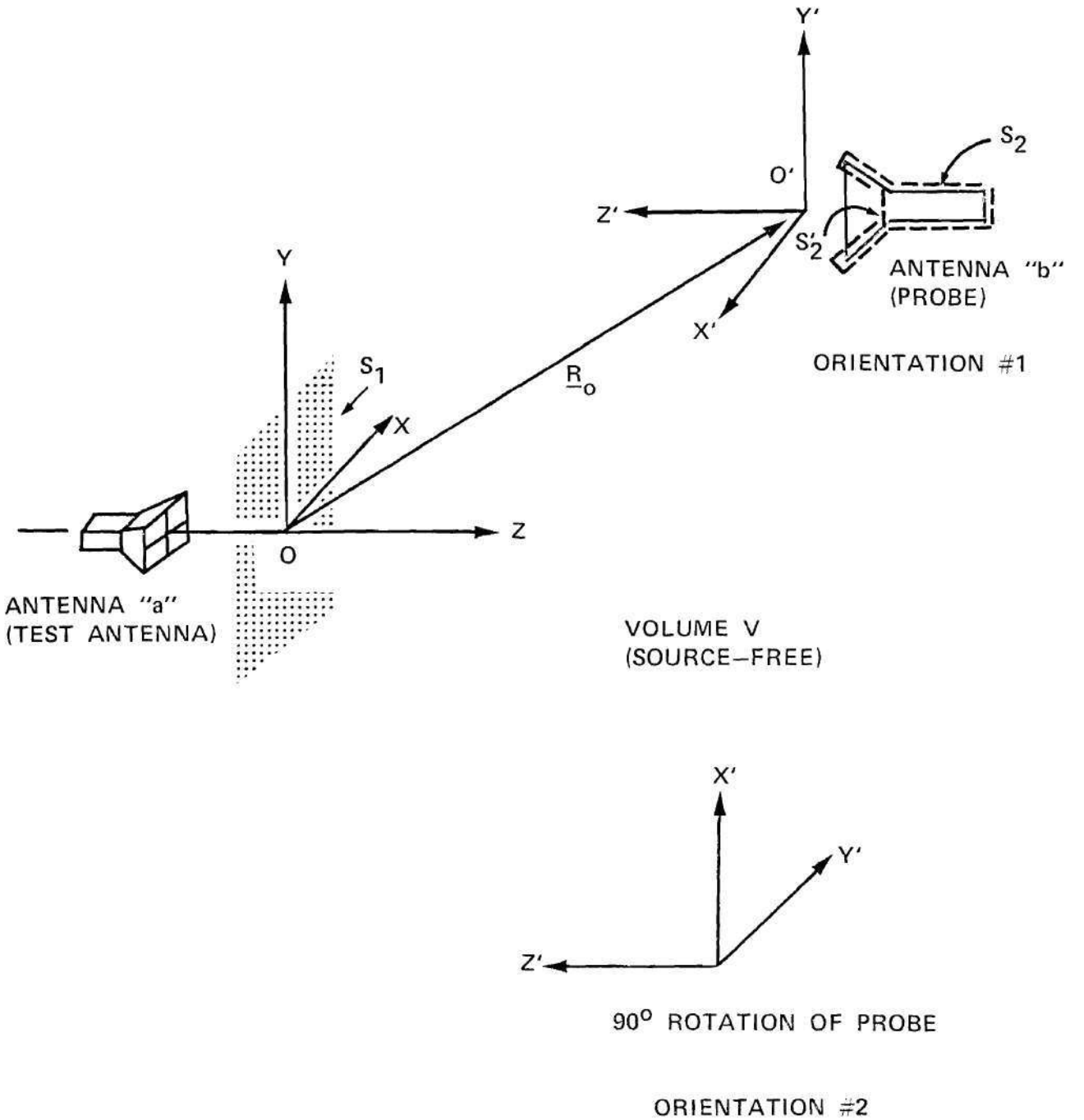

Figure 2-1. Geometry Pertaining to Near-Field Antenna Measurements on a Plane.

where the plane wave spectra A_x, A_y of the test antenna are functions of wavenumbers k_x, k_y; i.e.,

$$A_x = A_x(k_x,k_y) \tag{2-25}$$

$$A_y = A_y(k_x,k_y) \tag{2-26}$$

The vector components of the plane wave spectra of the probe along the x' and y' axes of the probe coordinate system are represented in Equation (2-24) by $B'_{x'}$, $B'_{y'}$, where the upper prime (on the B) is used to denote the evaluation of these quantities at the point $(k_x,-k_y)$; i.e.,

$$B'_{x'} = B_{x'}(k_x,-k_y) \tag{2-27}$$

$$B'_{y'} = B_{y'}(k_x,-k_y) \tag{2-28}$$

Equation (2-24) is an integral equation relating the voltage received by the probe to the plane wave spectra of the two antennas. The solution of this integral equation is straightforward since the integral is identical to a two-dimensional Fourier transform, and, by the inversion integral [19],

$$\left[A_x \frac{-(k^2-k_y^2)B'_{x'}+k_x k_y B'_{y'}}{k_z} + A_y \frac{-k_x k_y B'_{x'}+(k^2-k_x^2)B'_{y'}}{k_z} \right]$$

$$= \frac{1}{(2\pi)^2} \int_{-\infty}^{+\infty} \int_{-\infty}^{+\infty} V_1(x_o,y_o,z_o) e^{+j(k_x x_o + k_y y_o + k_z z_o)} dx_o dy_o$$

$$\triangleq A_1(k_x,k_y) \tag{2-29}$$

where the constants have been absorbed into V_1 and where A_1 is defined as the measured spectrum for orientation #1 of the probe antenna.

When the probe is rotated by 90° as shown in Figure 2-1, Fourier inversion of the resulting integral equation for this second orientation yields

$$A_x \frac{(k^2-k_y^2)B''_{y'}+k_x k_y B''_{x'}}{k_z} + A_y \frac{(k^2-k_x^2)B''_{x'}+k_x k_y B''_{y'}}{k_z}$$

$$= \frac{1}{(2\pi)^2} \int_{-\infty}^{+\infty} \int_{-\infty}^{+\infty} V_2(x_o,y_o,z_o) e^{+j(k_x x_o + k_y y_o + k_z z_o)} dx_o dy_o$$

$$\triangleq A_2(k_x,k_y) \tag{2-30}$$

where A_x and A_y are functions of k_x, k_y as in Equations (2-25) and (2-26) and where

$$B''_{x'} = B_{x'}(-k_y,-k_x) \tag{2-31}$$

$$B''_{y'} = B_{y'}(-k_y,-k_x) \tag{2-32}$$

Equations (2-29) and (2-30) comprise a linear system of two equations with two unknowns at each point (k_x,k_y). These equations may be rewritten as

$$k_z A_1 = A_x[-(k^2-k_y^2)B'_{x'}+k_x k_y B'_{y'}] + A_y[-k_x k_y B'_{x'} + (k^2-k_x^2)B'_{y'}] \tag{2-33}$$

$$k_z A_2 = A_x[(k^2-k_y^2)B''_{y'}+k_x k_y B''_{x'}] + A_y[(k^2-k_x^2)B''_{x'}+k_x k_y B''_{y'}] \tag{2-34}$$

Solutions to these equations may be found by applying Cramer's rule to obtain

$$A_x(k_x,k_y) = \frac{A_1 k_z a_{22} - A_2 k_z a_{12}}{a_{11}a_{22} - a_{21}a_{12}} \tag{2-35}$$

$$A_y(k_x,k_y) = \frac{A_1(-k_z a_{21}) + A_2 k_z a_{11}}{a_{11}a_{22} - a_{21}a_{12}} \tag{2-36}$$

where

$$k_z a_{11} = -(k^2-k_y^2)k_z B'_x + k_x k_y k_z B'_y \tag{2-37}$$

$$k_z a_{12} = -k_x k_y k_z B'_x + (k^2-k_x^2)k_z B'_y \tag{2-38}$$

$$k_z a_{21} = k_x k_y k_z B''_x + (k^2-k_y^2)k_z B''_y \tag{2-39}$$

$$k_z a_{22} = (k^2-k_x^2)k_z B''_x + k_x k_y k_z B''_y \tag{2-40}$$

$$a_{11}a_{22} - a_{21}a_{12} = -k_z B'_x k_z B''_x - k_z B'_y k_z B''_y \tag{2-41}$$

and where $B_{x'}$ and $B_{y'}$ are now referenced for convenience to the unprimed coordinate system simply by dropping the prime on the subscript.

Examination of Equation (2-19) shows that for values of k_z which correspond to real directions (θ,ϕ), multiplication of a plane wave spectrum by k_z gives a result which is proportional to the corresponding field quantity at a great distance; i.e., to the far field. Comparison of Equations (2-37) through (2-41) to Equation (2-19) shows that the

former may be rewritten in terms of the far fields of the probe antenna; viz.,

$$k_z a_{11} = -(k^2-k_y^2)B'_{xff} + k_x k_y B'_{yff} \tag{2-42}$$

$$k_z a_{12} = -k_x k_y B'_{xff} + (k^2-k_x^2)B'_{yff} \tag{2-43}$$

$$k_z a_{21} = k_x k_y B''_{xff} + (k^2-k_y^2)B''_{yff} \tag{2-44}$$

$$k_z a_{22} = (k^2-k_x^2)B''_{xff} + k_x k_y B''_{yff} \tag{2-45}$$

$$a_{11}a_{22} - a_{12}a_{21} = -B'_{xff}B''_{xff} - B'_{yff}B''_{yff} \tag{2-46}$$

These equations are valid for those values of $k_z > 0$ corresponding to real directions (θ,ϕ) as defined in Equations (2-22) and (2-23); i.e., for

$$k_x^2 + k_y^2 < k^2 \quad . \tag{2-47}$$

Equations (2-35) through (2-46) are the desired results and are basically those derived originally by Kerns [1]. They show that the plane wave spectra A_x, A_y of an antenna can be obtained from measurements made on a plane close to the antenna provided that the far fields B_{xff}, B_{yff} of the probe antenna are known. The results obtained in this manner are valid for only those values of k_x and k_y specified in Equation (2-47). The corresponding far fields of the test antenna follow from Equations (2-19) through (2-21). Also, the quantities B_x and B_y follow from

Equations (2-19) through (2-21) and measurements made in the far field of the probe antenna.

Joy [4] observed that the voltage received by the probe, as in Equation (2-24), can be written succinctly as

$$V_1(x_o,y_o,z_o) = \int_{-\infty}^{+\infty}\int_{-\infty}^{+\infty} (k_z \underline{A}\cdot\underline{B}' e^{-jk_z z_o}) e^{-j(k_x x_o + k_y y_o)} dk_x dk_y \qquad (2\text{-}48)$$

where

$$\underline{A} = \hat{x}A_x + \hat{y}A_y + \hat{z}A_z \qquad (2\text{-}49)$$

$$\underline{B}' = -\hat{x}B_x' + \hat{y}B_y' + \hat{z}B_z' \quad . \qquad (2\text{-}50)$$

Joy further observed that the exponential factor

$$e^{-jk_z z_o} = \begin{cases} e^{-jz_o\sqrt{k^2-(k_x^2+k_y^2)}}, & k_x^2+k_y^2 < k^2 \qquad (2\text{-}51) \\ e^{-z_o\sqrt{(k_x^2+k_y^2)-k^2}}, & k_x^2+k_y^2 > k^2 \qquad (2\text{-}52) \end{cases}$$

acts to limit the wavenumber extent of the quantity in parentheses in the integrand of Equation (2-48); i.e., the voltage received by the probe as it traverses the $z = 0$ plane in Figure 2-1 is essentially wavenumber-limited to a region R_k defined by $|k_x| \leq k_{xmax}$, $|k_y| \leq k_{ymax}$. Hence, by Shannon's sampling theorem [5], the received voltage can be represented by its samples spaced equidistantly in x and y at spacings

$$\Delta x = \pi / k_{xmax} \tag{2-53}$$

$$\Delta y = \pi / k_{ymax} \tag{2-54}$$

Indeed, since A_1 vanishes outside the region R_k, it can be expanded as a Fourier series $A_{1p}(k_x, k_y)$

$$A_{1p}(k_x, k_y) = \sum_{m=-\infty}^{+\infty} \sum_{n=-\infty}^{+\infty} \alpha_{mn} e^{j(m\Delta x k_x + n\Delta y k_y)} \tag{2-55}$$

where

$$\alpha_{mn} = \frac{1}{2k_{xmax} \cdot 2k_{ymax}} \iint_{Rk} A_1(k_x, k_y) e^{-j(k_x m\Delta x + k_y n\Delta y)} dk_x dk_y$$

$$= \frac{1}{4k_{xmax} k_{ymax}} V_1(m\Delta x, n\Delta y) \tag{2-56}$$

Since A_{1p} is the periodic repetition of A_1, the latter can be obtained from the former by multiplication of Equation (2-55) by the rectangular pulse function

$$P_{R_k}(k_x, k_y) = \begin{cases} 1 \ , & k_x, k_y \in R_k \\ 0 \ , & \text{otherwise} \end{cases} \tag{2-57}$$

i.e.,

$$A_1(k_x, k_y) = P_{R_k}(k_x, k_y) \sum_{m=-\infty}^{+\infty} \sum_{n=-\infty}^{+\infty} \alpha_{mn} e^{j(m\Delta x k_x + n\Delta y k_y)} \tag{2-58}$$

A representation of the measured voltage $V_1(x_o,y_o,z_o)$ in terms of its samples is obtained by taking the Fourier transform of Equation (2-55) and convolving the result with the Fourier transform of P_{R_k}. In the first instance, there results

$$F\{A_{lp}\} = \frac{\pi^2}{k_{xmax} \cdot k_{ymax}} \sum_{m=-\infty}^{+\infty} \sum_{n=-\infty}^{+\infty} V_1(m\Delta x, n\Delta y)\,\delta(x_o - m\Delta x, y_o - n\Delta y) \qquad (2\text{-}59)$$

where δ represents the Dirac delta function. The Fourier transform of P_{R_k} is [19]

$$F\{P_{R_k}\} = \frac{2\sin(x_o k_{xmax})}{x_o} \cdot \frac{2\sin(y_o k_{ymax})}{y_o} \quad . \qquad (2\text{-}60)$$

Carrying out the convolution yields

$$V_1(x_o,y_o,z_o) = (2\pi)^2 \sum_{m=-\infty}^{+\infty} \sum_{n=-\infty}^{+\infty} [V_1(m\Delta x, n\Delta y) \cdot \frac{\sin(k_{xmax}x_o - m\pi)}{(k_{xmax}x_o - m\pi)} \cdot \frac{\sin(k_{ymax}y_o - n\pi)}{(k_{ymax}y_o - n\pi)} \qquad (2\text{-}61)$$

which is the desired result.

Equations (2-55) and (2-61) show that the measured response of the probe need not be recorded for every (x_o,y_o,z_o) but only at discrete points which are integer multiples of Δx and Δy. Strictly speaking, however, an infinite number of samples is required to determine A_ℓ exactly at each point (k_x,k_y) as indicated by the infinite summations in these equations. The use of only a finite number of terms is tantamount to truncating the probe response $V_\ell(x,y)$ at the boundaries of the region R_{xy}

to produce a spatially-limited function $\tilde{V}_\ell(x,y)$ that cannot be also wavenumber-limited. Consequently, when the samples of $\tilde{V}_\ell(x,y)$ are used in Equation (2-55), there results a Fourier transform $\hat{A}_\ell(k_x,k_y)$ which is an "aliased" version of the true spectrum $\tilde{A}_\ell(k_x,k_y)$ of $\tilde{V}_\ell(x,y)$ [34]; viz.,

$$\hat{A}_\ell(k_x,k_y) = \frac{P(k_x,k_y)}{\Delta x \Delta y} \sum_{p=-\infty}^{\infty} \sum_{q=-\infty}^{\infty} \tilde{A}_\ell(k_x + 2pk_{xmax}, k_y + 2qk_{ymax}) \qquad (2\text{-}62)$$

where the function $P(k_x,k_y)$ is equal to unity for (k_x,k_y) inside R_k and is equal to zero elsewhere. The resulting spectrum $\hat{A}_\ell$ is corrupted by components of $\tilde{A}(k_x,k_y)$ which are non-zero for $|k_x| > k_{xmax}$, $|k_y| > k_{ymax}$. For example, at the point $k_x = k_{xmax}/2$, $k_y = k_{ymax}/2$, the spectrum is given by

$$\begin{aligned}\hat{A}_\ell(k_{xmax}/2, k_{ymax}/2) = {} & \tilde{A}_\ell(k_{xmax}/2, k_{ymax}/2) \\ & + \tilde{A}_\ell\left(\frac{5k_{xmax}}{2}, k_{ymax}/2\right) + \tilde{A}_\ell\left(\frac{-3k_{xmax}}{2}, \frac{k_{ymax}}{2}\right) \\ & + \tilde{A}_\ell\left(\frac{k_{xmax}}{2}, \frac{5k_{ymax}}{2}\right) + \tilde{A}_\ell\left(\frac{k_{xmax}}{2}, \frac{-3k_{ymax}}{2}\right) \\ & + \ldots \end{aligned} \qquad (2\text{-}63)$$

where the corruption of the true spectrum A_ℓ at the desired point by components at the "aliased" *wavenumbers* is obvious. It should also be noted that the desired spectrum $A_\ell(k_x,k_y)$ can in no way be recovered exactly since it is lost when the wavenumber-limited function $V_\ell(x,y)$ is truncated

to the finite region R_{xy}.

The uncertainties introduced in the measured spectrum by the finite measurement area and by the aliasing effects resulting from sampling a nonwavenumber-limited function are manifestations of the uncertainty principle [23]; viz., a function and its Fourier transform cannot be limited in extent simultaneously in the two domains. A method of analysis which makes possible a better understanding of the uncertainty relations and which more clearly identifies the sources of errors is required in order to establish criteria for the selection of probe antennas which minimize these errors.

2.4 Optimum Probes

An optimum probe is defined here as one which minimizes the error in the measured spectra $A_1(k_x,k_y)$ and $A_2(k_x,k_y)$ as given by Equations (2-29) and (2-30). The measure of error to be used is the mean square error (MSE) given by

$$MSE_\ell(A_\ell(k_x,k_y)) = \int_{-\infty}^{\infty}\int_{-\infty}^{\infty} |A_\ell(k_x,k_y) - \hat{A}_\ell(k_x,k_y)|^2 dk_x dk_y \qquad (2\text{-}64)$$

where $\ell = 1,2$ and where $\hat{}$ denotes estimate. In what follows is developed the theoretical basis for the determination of the estimate $\hat{A}_\ell$ which minimizes Equation (2-64). From these results, the characteristics of the optimum probe will then be deduced for arbitrary measurement situations involving different types of measurement antennas.

The measured spectrum A_ℓ is essentially zero outside the region R_k of the wavenumber plane due to the wavenumber-limiting action of the exponential factor in Equation (2-52). Therefore, this two-dimensional spectrum

can be expanded on R_k in a series of products of two complete sets of one-dimensional functions [31]; viz.,

$$A_\ell(k_x,k_y) = \sum_{m=0}^{\infty} \sum_{n=0}^{\infty} a_{mn}\psi_m(k_x)\psi_n(k_y) \quad . \tag{2-65}$$

The basis functions ψ_m, ψ_n need not be orthogonal on the region R_k, but computations are facilitated if they are. The region R_k is defined by $|k_x| \le k_{xmax}$, $|k_y| \le k_{ymax}$.

The most common one-dimensional functions to use in Equation (2-65) are the complex exponential functions shown in Equation (2-55), whereupon Equation (2-65) reduces to a Fourier series with coefficients given by Equation (2-56).

Another choice of basis functions ψ_m, ψ_n is a scaled version of the prolate spheroidal wave functions S_{on} described in Appendix A [22-27]. These scaled versions are defined by

$$\psi_m(c_x,k_x) = \frac{S_{on}(c_x,k_x/k_{xmax})}{\sqrt{k_{xmax}}} \tag{2-66}$$

$$\psi_n(c_y,k_y) = \frac{S_{on}(c_y,k_y/k_{ymax})}{\sqrt{k_{ymax}}} \tag{2-67}$$

Corresponding to these functions are their scaled counterparts in the xy domain; viz.,

$$\psi_m(c_x,x) = \frac{S_{on}(c_x,x/x_{max})}{\sqrt{x_{max}}} \tag{2-68}$$

$$\psi_n(c_y,y) = \frac{S_{on}(c_y,y/y_{max})}{\sqrt{y_{max}}} \tag{2-69}$$

where the finite region R_{xy} is defined by $|x| \leq x_{max}$ and $|y| \leq y_{max}$. The parameters c_x and c_y are arbitrary constants which are set equal to the quantities given below in order to effect a Fourier transform relationship between the functions defined in Equations (2-66) through (2-69); i.e.,

$$c_x = x_{max} k_{xmax} \tag{2-70}$$

$$c_y = y_{max} k_{ymax} \tag{2-71}$$

The function $\psi_m(c_x,k_x)$ satisfies the integral equation

$$\sqrt{c_x}\, \nu_{xn} \psi_n(c_x,k_x) = \int_{-x_{max}}^{x_{max}} \psi_n(c_x,x) e^{jk_x x} dx \tag{2-72}$$

while $\psi_n(c_x,x)$ satisfies the similar equation

$$\sqrt{c_x}\, \nu_{xn}^* \psi_n(c_x,x) = \int_{-k_{xmax}}^{k_{xmax}} \psi_n(c_x,k_x) e^{-jk_x x} dk_x \tag{2-73}$$

where ν_{xn}, $n = 0,1,\ldots$, are eigenvalues of the integral equation and where * denotes complex conjugate. The functions also satisfy the following integral equations on the $(-\infty,\infty)$ interval:

$$\sqrt{c_x}\, \nu_{xn} \gamma_{xn} \psi_n(c_x,k_x) p_{kmax}(k_x) = \int_{-\infty}^{\infty} \psi_n(c_x,x) e^{jk_x x} dx \tag{2-74}$$

$$\sqrt{c_x}\, \nu_{xn}^* \gamma_{xn} \psi_n(c_x,x) p_{xmax}(x) = \int_{-\infty}^{\infty} \psi_n(c_x,k_x) e^{-jk_x x} dk_x \tag{2-75}$$

In the above equations, $p_{kmax}(k_x)$ represents the rectangular window function whose value is unity for $|k_x| \leq k_{xmax}$ and is zero elsewhere.

The functions $\psi_n(c_x,k_x)$ are doubly orthogonal on the intervals $(-k_{xmax},k_{xmax})$ and $(-\infty,\infty)$, and the functions $\psi_n(c_x,x)$ are doubly orthogonal on $(-x_{max},x_{max})$ and $(-\infty,\infty)$. The orthogonality relations are as follows:

$$\int_{-k_{xmax}}^{k_{xmax}} \psi_m(c_x,k_x)\psi_n(c_x,k_x)dk_x = \lambda_{xn}\delta_{mn} \tag{2-76}$$

$$\int_{-\infty}^{\infty} \psi_m(c_x,k_x)\psi_n(c_x,k_x)dk_x = \lambda_{xn}\gamma_{xn}\delta_{mn} = \delta_{mn} \tag{2-77}$$

where δ_{mn} is the Kronecker delta. In accordance with established convention [26], the functions ψ_i are normalized to unity on $(-\infty,\infty)$ so that

$$\gamma_{xn} = 1/\lambda_{xn} \tag{2-78}$$

The positive real constants λ_{xn} *are eigenvalues* of an iterate [22] of the integral equation (2-72) and are related to the eigenvalues ν_{xn} by

$$\lambda_{xn}(c_x) = \frac{2c_x}{\pi}\left|\nu_{xn}\right|^2 \tag{2-79}$$

The eigenvalues ν_{xn} are either real or imaginary according to whether n is even or odd; i.e.,

$$\nu_{xn} = j^n|\nu_{xn}| \tag{2-80}$$

Two other useful relations are

$$\sqrt{c_x}\ \nu_{xn} = j^n\sqrt{2\pi\lambda_{xn}} \tag{2-81}$$

$$\sqrt{c_x}\ \nu^*_{xn} = (-j)^n\sqrt{2\pi\lambda_{xn}} \tag{2-82}$$

It follows from the above that

$$(-j)^n\sqrt{2\pi\lambda_{xn}}\ \psi_n(c_x,x) \leftrightarrow \psi_n(c_x,k_x)p_{kxmax}(k_x) \tag{2-83}$$

comprise a Fourier transform pair. Similar relations hold for the functions of y and k_y.

The coefficients a_{mn} in Equation (2-65) can now be determined using the orthogonality of the basis functions. Multiply both sides of Equation (2-65) by $\psi_p(k_x)\psi_q(k_y)$ and integrate both sides to obtain (c_x,c_y suppressed)

$$\int_{-k_{xmax}}^{k_{xmax}} \int_{-k_{ymax}}^{k_{ymax}} A_\ell(k_x,k_y)\psi_p(k_x)\psi_q(k_y)dk_y dk_x$$

$$= \sum_{m=0}^{\infty}\sum_{n=0}^{\infty} a_{mn} \int_{-k_{xmax}}^{k_{xmax}} \psi_p(k_x)\psi_m(k_x)dk_x \int_{-k_{ymax}}^{k_{ymax}} \psi_q(k_y)\psi_n(k_y)dk_y \tag{2-84}$$

where the order of integration and summation on the right hand side has been interchanged. From Equation (2-76),

$$a_{mn} = \frac{1}{\lambda_{xm}\lambda_{yn}} \int_{-k_{xmax}}^{k_{xmax}} \int_{-k_{ymax}}^{k_{ymax}} A_{\ell}(k_x,k_y)\psi_m(k_x)\psi_n(k_y)dk_y dk_x \qquad (2\text{-}85)$$

The Fourier transform of A_{ℓ} (i.e., the measured probe response V_{ℓ}) may also be expressed in terms of the same coefficients a_{mn}. Apply the two-dimensional Fourier integral to both sides of Equation (2-65) to yield

$$V_{\ell}(x,y) = \int_{-k_{xmax}}^{k_{xmax}} \int_{-k_{ymax}}^{k_{ymax}} A_{\ell}(k_x,k_y)e^{-j(k_x x+k_y y)} dk_y dk_x$$

$$= \sum_{m=0}^{\infty} \sum_{n=0}^{\infty} a_{mn} \int_{-k_{xmax}}^{k_{xmax}} \psi_m(k_x)e^{-jk_x x} dk_x \int_{-k_{ymax}}^{k_{ymax}} \psi_n(k_y)e^{-jk_y y} dk_y$$

(2-86)

where the order of integration and summation has been interchanged. Using Equation (2-73) in the right hand side of Equation (2-86) yields

$$V_{\ell}(x,y) = \sum_{m=0}^{\infty} \sum_{n=0}^{\infty} a_{mn}(-j)^{m+n} 2\pi\sqrt{\lambda_{xm}\lambda_{yn}}\, \psi_m(x)\psi_n(y) \qquad (2\text{-}87)$$

Hence, the probe response V_{ℓ} and the corresponding spectrum A_{ℓ} can both be expressed in terms of the same coefficients a_{mn}.

The coefficients a_{mn} can also be obtained from knowledge of V_{ℓ} over the infinite xy plane as shown below. Since the basis functions $\psi_m(x)$, $\psi_n(y)$ are each orthogonal on $(-\infty,\infty)$, V_{ℓ} can be expressed as

$$V_{\ell}(x,y) = \sum_{m=0}^{\infty} \sum_{n=0}^{\infty} b_{mn} \psi_m(x) \psi_n(y) \tag{2-88}$$

where the coefficients b_{mn} follow from the orthogonality relation in Equation (2-77) as

$$b_{mn} = \int_{-\infty}^{\infty} \int_{-\infty}^{\infty} V_{\ell}(x,y) \psi_m(x) \psi_n(y) dxdy \tag{2-89}$$

Also, since the basis functions are orthogonal on $(-x_{max}, x_{max})$ and $(-y_{max}, y_{max})$, the coefficients b_{mn} can be determined by

$$b_{mn} = \frac{1}{\lambda_{xm} \lambda_{yn}} \int_{-x_{max}}^{x_{max}} \int_{-y_{max}}^{y_{max}} V_{\ell}(x,y) \psi_m(x) \psi_n(y) dydx \tag{2-90}$$

Comparison of Equations (2-89) and (2-90) shows that a_{mn} and b_{mn} are related by

$$b_{mn} = a_{mn} (-j)^{m+n} 2\pi \sqrt{\lambda_{xm} \lambda_{yn}} \tag{2-91}$$

Equations (2-89) and (2-90) show that the coefficients b_{mn} (and, hence, a_{mn}) can be determined from knowledge of $V_{\ell}(x,y)$ only over the region R_{xy} defined by $|x| \leq x_{max}$, $|y| \leq y_{max}$; i.e., the function $V_{\ell}(x,y)$ can be determined everywhere on the xy-plane from knowledge of its values over only the finite region R_{xy}. This truth is a consequence of the fact that the (inverse) Fourier transform of V_{ℓ} is zero outside R_k; hence, V_{ℓ} is an entire function [18] of the (complex) variables x, y whose values in one region of the complex x and y planes can, in principle, be determined by analytic continuation from a known region [31]. The spheroidal

functions ψ_m, ψ_n provide a practical means of implementing such continuation; however, as a general observation, such continuation requires a greater degree of precision in the raw data than is normally available [31].

The expansion in Equation (2-88) suggests that $V_\ell(x,y)$ can be approximated by a finite number of (M+1)(N+1) terms; i.e.,

$$\hat{V}_\ell(x,y) = \sum_{m=0}^{M} \sum_{n=0}^{N} b_{mn}\psi_m(x)\psi_n(y) \tag{2-92}$$

where M and N are finite integers. The mean square error of this estimate is

$$\Delta_{MN}^2 = \int_{-\infty}^{\infty} \int_{-\infty}^{\infty} |V_\ell(x,y) - \hat{V}_\ell(x,y)|^2 dxdy \tag{2-93}$$

Substituting Equations (2-88) and (2-89) into Equation (2-93), combining the summations, and interchanging the order of integration and summation yields

$$\Delta_{MN}^2 = \sum_{m=M'}^{\infty} \sum_{n=N'}^{\infty} \sum_{p=M'}^{\infty} \sum_{q=N'}^{\infty} b_{mn} b_{pq}^* \int_{-\infty}^{\infty} \psi_m(x)\psi_p(x)dx \int_{-\infty}^{\infty} \psi_n(y)\psi_q(y)dy \tag{2-94}$$

where M' denotes (M+1) and N' denotes (N+1), and where the relation

$$\left|\sum_m \alpha_m\psi_m\right|^2 = \left(\sum_m \alpha_m\psi_m\right)\left(\sum_p \alpha_p\psi_p\right)^* = \sum_m \sum_p \alpha_m\alpha_p^*\psi_m\psi_p^* \tag{2-95}$$

has been used. The integrals in Equation (2-94) are given by Equation (2-77); hence, the quadruple summation reduces to a double summation and the mean square error is given by

$$\Delta^2_{MN} = \sum_{m=M'}^{\infty} \sum_{n=N'}^{\infty} |b_{mn}|^2 \tag{2-96}$$

The voltage response $V_\ell(x,y)$ of the probe at each point (x,y) on the $z = z_o$ plane is related to the real power received by the probe according to

$$P_\ell(x,y) = \frac{|V_\ell(x,y)|^2}{Re\{Z_b\}} \tag{2-97}$$

where Z_b is the load impedance of the probe when receiving. Although this quality is not the power density in the fields emanating from the test antenna, it may be interpreted as a measured power density so that the total measured power is given by the surface integral of Equation (2-97) over the entire xy-plane. For simplicity, the denominator of Equation (2-97) will be set equal to one ohm so that the power density and $|V_\ell|^2$ will be synonomous in what follows. This artifice is used to justify such synonomity and to simplify the semantics.

To obtain an upper bound on the mean square error given by Equation (2-96), first compute the power P_∞ of $V_\ell(x,y)$ as

$$P_\infty = \int_{-\infty}^{\infty} \int_{-\infty}^{\infty} |V_\ell(x,y)|^2 dxdy = \sum_{m=0}^{\infty} \sum_{n=0}^{\infty} |b_{mn}|^2 \tag{2-98}$$

by following the procedure leading up to Equation (2-96). Next define

a measure ϵ_{xy}^2 of the concentration of $|V_\ell|^2$ as

$$\frac{\int_{R_{xy}} \int |V_\ell(x,y)|^2 dxdy}{P_\infty} \triangleq 1 - \epsilon_{xy}^2 \qquad (2\text{-}99)$$

It is easily shown by following the procedure leading up to Equation (2-96) that

$$\int_{R_{xy}} \int |V_\ell(x,y)|^2 dxdy = \sum_{m=0}^{\infty} \sum_{n=0}^{\infty} |b_{mn}|^2 \lambda_{xm} \lambda_{yn} \qquad (2\text{-}100)$$

Combining Equations (2-98) through (2-100) yields

$$P_\infty \epsilon_{xy}^2 = \sum_{m=0}^{\infty} \sum_{n=0}^{\infty} |b_{mn}|^2 (1 - \lambda_{xm} \lambda_{yn}) \qquad (2\text{-}101)$$

It is clear that $P_\infty \epsilon_{xy}^2$ is the portion of the power of $V_\ell(x,y)$ that is not contained in the region R_{xy}; i.e., the "unconcentrated" part of the power of V_ℓ. To show that this unconcentrated part of the power is proportional to an upper bound on the mean square error Δ_{MN}^2, consider the inequality

$$(1 - \lambda_{xM} \lambda_{yN}) \sum_{m=M'}^{\infty} \sum_{n=N'}^{\infty} |b_{mn}|^2 \leq \sum_{m=0}^{\infty} \sum_{n=0}^{\infty} |b_{mn}|^2 (1 - \lambda_{xm} \lambda_{yn}) \quad . \qquad (2\text{-}102)$$

This inequality can be established by making a term-wise comparison and by using the ordering of the eigenvalues [22]

$$\lambda_{x0} > \lambda_{x1} > \lambda_{x2} > \cdots \qquad (2\text{-}103)$$

$$\lambda_{y0} > \lambda_{y1} > \lambda_{y2} > \cdots \tag{2-104}$$

It then follows from Equations (2-96) and (2-102) that

$$\Delta_{MN}^2 = \sum_{m=M'}^{\infty} \sum_{n=N'}^{\infty} |b_{mn}|^2 \leq \frac{P_\infty \epsilon_{xy}^2}{1 - \lambda_{xM}\lambda_{yN}} \tag{2-105}$$

where M and N are finite integers to be determined below.

Landau and Pollack [24] have established a bound on the eigenvalues appearing in Equation (2-105) while establishing the intuition that a time signal g(t) known for $|t| < T/2$ and bandlimited to $W = \Omega/2\pi$ Hz (Ω rad/sec) can be represented by $2WT = \Omega T/\pi$ samples. They established the bound that for any $T > 0$,

$$\lambda_{[2WT]+1}(c) \leq .915 \tag{2-106}$$

where [2WT] means the greatest integer less than 2WT. They show that the mean square error δ^2 is bounded by

$$\delta_{[2WT]+1}^2 = \int_{+\infty}^{+\infty} \left| g(t) - \sum_{n=0}^{[2WT]+1} a_n \psi_n(c,t) \right|^2 dt \leq c_1 \epsilon_T^2 \tag{2-107}$$

where c_1 may be taken as 12; i.e.,

$$\frac{\epsilon_T^2}{1 - \lambda_{[2WT]+1}} \leq \frac{\epsilon_T^2}{1 - .915} \leq 12\, \epsilon_T^2 \quad . \tag{2-108}$$

In the development, g(t) was normalized so that $P_\infty = 1$, and the value of c was established as

$$c = \Omega \frac{T}{2} = \frac{2\pi WT}{2} = \pi WT \quad . \tag{2-109}$$

For the case at hand, similar bounds may be established for $\lambda_{xM'}$ λ_{yN} as

$$\lambda_{xM}(x_{max} \cdot k_{xmax}) \leq .915 \tag{2-110}$$

$$\lambda_{yN}(y_{max} \cdot k_{ymax}) \leq .915 \tag{2-111}$$

It then follows that for

$$M = [\frac{2}{\pi} x_{max} k_{xmax}] + 1 \tag{2-112}$$

$$N = [\frac{2}{\pi} y_{max} k_{ymax}] + 1 \tag{2-113}$$

the mean square error Δ^2_{MN} is bounded by a quantity which is proportional to the unconcentrated part of the power of V_ℓ; i.e.,

$$\Delta^2_{MN} \leq \frac{\epsilon^2_{xy} P_\infty}{1 - \lambda_{xM}\lambda_{yN}} < 6.15\, \epsilon^2_{xy} P_\infty \quad . \tag{2-114}$$

This is one desired result.

Parseval's theorem is next invoked to show that the mean square error in the measured spectrum defined in Equation (2-64) is also proportional to ϵ^2_{xy}. Apply Parseval's theorem to Equation (2-90) to obtain

$$\frac{1}{(2\pi)^2} \int_{-\infty}^{+\infty} \int_{-\infty}^{+\infty} |V_\ell - \hat{V}_\ell|^2 dxdy = \int_{-\infty}^{+\infty} \int_{-\infty}^{+\infty} |A_\ell - \hat{A}_\ell|^2 dk_x dk_y \tag{2-115}$$

where $\hat{A}_\ell$ is the inverse Fourier transform of $\hat{V}_\ell$ and is given by a truncated version of Equation (2-65) as

$$\hat{A}_\ell(k_x,k_y) = \sum_{m=0}^{M} \sum_{n=0}^{N} a_{mn}\psi_m(c_x,k_x)\psi_n(c_y,k_y) \tag{2-116}$$

Combining Equations (2-115) and (2-116) yields

$$\int_{-k_{xmax}}^{+k_{xmax}} \int_{-k_{ymax}}^{+k_{ymax}} |A_\ell - \hat{A}_\ell|^2 dk_x dk_y \leq \frac{6.15P_\infty \epsilon_{xy}^2}{(2\pi)^2} \tag{2-117}$$

where the infinite limits on the integrals have been replaced with the finite limits since $(A_\ell - \hat{A}_\ell)$ vanishes outside R_k. *This is another desired result.*

It is concluded from Equation (2-117) that the probe which minimizes the mean square error in the measured spectrum is the probe whose response $V_\ell(x_o,y_o)$ is most concentrated in the finite measurement area R_{xy}; hence, the probe which minimizes ϵ_{xy}^2 is the optimum probe for a particular measurement situation.*

The above conclusion is strictly true in the case of expansions using the prolate spheroidal wave functions but has not been established in the case of expansions using the usual sampling functions in the two-dimensional case. It has been established in the one-dimensional case that $[\frac{2}{\pi} x_{max} k_{xmax}] + 1$ sampling functions will approximate a band-limited function in a mean square sense to within a constant times the square root of the unconcentrated part ϵ_x^2 of the function; i.e.,

*The probe enters Equation (2-117) as clarified below in Equation (2-120).

$$\int_{-\infty}^{\infty} \left| g(x) - \sum_{|m| \le [\frac{2}{\pi} x_{max} k_{xmax}]+1} g(m\Delta x) \frac{\sin(2k_{xmax} x_{max} - m\pi)}{(2k_{xmax} x_{max} - m\pi)} \right|^2 dx \le \pi\epsilon_x + \epsilon_x^2 \tag{2-118}$$

And by Parseval's theorem, the corresponding error bound on the transform is also proportional to this same quantity; viz.,

$$\frac{1}{2\pi} \int_{-k_{xmax}}^{k_{xmax}} |G(k_x) - \hat{G}(k_x)|^2 dk_x \le \pi\epsilon_x + \epsilon_x^2 \tag{2-119}$$

While a similar result has not been established in the two dimensional case, it will be seen from the experimental results presented below that the maximum power criterion does indeed lead to a probe which minimizes the errors in the two dimensional Fourier transform of the measured near field data and in the resulting probe-compensated far fields.

A procedure for identifying an optimum probe within a specified class of probes is as follows. Let the vector $\underline{u}$ represent the physical design parameters of the probe such that the probe spectrum $\underline{B}$ is a function of $\underline{u}$. Consequently, the probe response is also a function of $\underline{u}$; i.e.,

$$V_1(x,y,\underline{u}) = \iint_{R_k} [(-k_z \underline{A}(k_x,k_y) \cdot \underline{B}(k_x,-k_y,\underline{u})] e^{-j(k_x x + k_y y)} dk_x dk_y \tag{2-120}$$

It is desired to find the set of parameters $\underline{u}$ which minimizes ϵ_{xy}^2 in Equation (2-99) for a specified measurement area R_{xy} and test antenna as described by its plane wave spectrum $\underline{A}(k_x,k_y)$. Such a probe would then be the optimum probe sought.

The procedure is repeated for the other orientation (90° rotation) of the probe antenna. A second set of design parameters $\underline{u}'$ is then

obtained to identify the optimum probe for this measurement. If the parameters $\underline{u}$ and $\underline{u}'$ are not equal, two probes within the specified class of probes are indicated. On the other hand, if it is desired to use only one probe, a compromise on the values of $\underline{u}$ and $\underline{u}'$ may be made so that the probe used in each orientation almost minimizes ϵ_{xy}^2 in each case.

The above procedure can be implemented by computer-simulation of the near-field measurement technique. By utilizing over-sampling and an extended measurement area in the xy-plane, conventional Fast Fourier Transform techniques can be used with negligible errors to facilitate calculations in the computer model. Alternatively, direct computation of the reaction integral for the probe response may be used. The latter approach was taken in this research and is described in the next chapter.

2.5 Ideal Probes

The concept of an optimum probe goes hand and hand with the existence of an ideal near-field probe; i.e., a probe whose response is such as to produce measured plane wave spectra A_1, A_2 which require no compensation [51].

In Equation (2-29), set the coefficient of A_x equal to zero and set the coefficient of A_y equal to a complex constant c_1. The measured spectrum A_1 for the first orientation then becomes proportional to A_y of the test antenna; i.e.,

$$A_1(k_x,k_y) = c_1 A_y(k_x,k_y) \tag{2-121}$$

and

$$-(k^2-k_y^2)B_{x'}(k_x,-k_y) + k_x k_y B_{y'}(k_x,-k_y) = 0 \tag{2-122}$$

$$-k_x k_y B_{x'}(k_x,-k_y) + (k^2-k_x^2)B_{y'}(k_x,-k_y) = c_1 k_z \tag{2-123}$$

Rewriting the last two equations at the point (k_x,k_y) rather than at $(k_x,-k_y)$, and solving the resulting system of linear equations yields

$$B_{x'}(k_x,k_y) = -\frac{k_x k_y}{k^2-k_y^2} B_{y'}(k_x,k_y) \tag{2-124}$$

and

$$B_{y'}(k_x,k_y) = c_1 \frac{1-k_{yn}^2}{k_{zn}} \tag{2-125}$$

where normalized wavenumbers k_{xn}, k_{yn} are used for convenience.

To identify the last two equations as the relations for a short electric dipole aligned with the y'-axis of the probe coordinate system, define a spherical coordinate system with the y'-axis as the pole. Let ξ represent the polar (elevation) angle measured from the +y' axis, and let $\hat{\xi}$ represent the unit vector oriented in the direction of increasing ξ. Also, let α represent the azimuthal angle (measured from +z' toward +x'), and let $\hat{\alpha}$ be the corresponding unit vector. Using rectangular to spherical coordinate transformations, and interpreting k_{xn}, k_{yn}, k_{zn} as direction cosines, it can be shown that the elevation and azimuth components of the far electric field ($E_{rff} \equiv 0$) may be written in terms of the plane wave spectra $B_{x'}$, $B_{y'}$ as

$$E_{\xi ff}(k_{xn},k_{yn}) = \frac{-k_{zn}}{\sqrt{1-k_{yn}^2}} B_{y'} \tag{2-126}$$

$$E_{\alpha ff}(k_{xn},k_{yn}) = \sqrt{1-k_{yn}^2}\, B_{x'} + \frac{k_{xn}k_{yn}}{\sqrt{1-k_{tn}^2}} B_{y'} \tag{2-127}$$

For the electric dipole oriented along the y'-axis, $E_{\alpha ff}$ is identically zero, and Equation (2-127) reduces identically to Equation (2-124). Substituting Equation (2-125) into Equation (2-126) results in

$$E_{\xi ff}(k_{xn},k_{yn}) = c_1\sqrt{1-k_{yn}^2} = c_1 \sin\xi \tag{2-128}$$

which is just the far-field radiation pattern of a short electric dipole oriented along the y-axis, as was to be shown.

Following through with these relations in the measurement equations, Equations (2-29) and (2-30), there results

$$A_1(k_x,k_y) = c_1 A_y(k_x,k_y) \tag{2-129}$$

$$A_2(k_x,k_y) = c_2 A_x(k_x,k_y) \tag{2-130}$$

where c_1, c_2 are complex constants. In obtaining Equation (2-130), the coefficient of A_y in Equation (2-30) was set equal to zero, and the coefficient of A_x was set equal to c_2. The resulting equations are those for a short electric dipole aligned with the y'-axis of the probe coordinate system when rotated by ninety degrees, corresponding to orientation

2 of Figure 2-1. The desired plane wave spectra A_x, A_y of the test antenna then follow directly from Equations (2-129) and (2-130), at least for the case of $k_x^2 + k_y^2 < k^2$, which corresponds to radiating plane waves and the visible region of space.

The concept of duality suggests that a small magnetic loop antenna should work equally well as an ideal probe to determine the magnetic field plane wave spectra G_x, G_y of the test antenna. To see that this is indeed the case, use Equations (2-16) and (2-17) to write the measurement equations in terms of magnetic field plane wave spectra as

$$G_1(k_x,k_y) = \eta^2 \left\{ G_x(k_x,k_y) \left[\frac{(k^2-k_y^2)G_{x'p}(k_x,-k_y) - k_x k_y G_{y'p}(k_x,-k_y)}{k_z} \right] \right.$$
$$\left. + G_y(k_x,k_y) \left[k_x k_y G_{x'p}(k_x,-k_y) - (k^2-k_x^2)G_{y'p}(k_x,-k_y) \right] \right\} \tag{2-131}$$

$$G_2(k_x,k_y) = \eta^2 \left\{ G_x(k_x,k_y) \left[-k_x k_y G_{x'p}(-k_y,-k_x) - (k^2-k_y^2)G_{y'p}(-k_y,-k_x) \right] \right.$$
$$\left. + G_y(k_x,k_y) \left[-(k^2-k_x^2)G_{x'p}(-k_y,-k_x) - k_x k_y G_{y'p}(-k_y,-k_x) \right] \right\} \tag{2-132}$$

where $G_{x'p}$, $G_{y'p}$ denote the (magnetic) plane wave spectra of the probe. By following the same procedure as that used above for the electric dipole, and recognizing that a magnetic dipole (loop) oriented with its moment aligned with the y'-axis in the probe coordinate system produces

a magnetic far field having only an elevation component, there results for the measurement equations,

$$G_1(k_x,k_y) = d_1 G_y(k_x,k_y) \tag{2-133}$$

$$G_2(k_x,k_y) = d_2 G_x(k_x,k_y) \tag{2-134}$$

where d_1 and d_2 are complex constants. The desired plane wave spectra G_x, G_y of the test antenna follow directly from the above equations, for the case of $k_x^2 + k_y^2 < k^2$. The far magnetic field components $H_{\ell ff}(k_x,k_y)$ follow from the use of G_x, G_y in Equation (2-19) in lieu of A_x, A_y.

It is interesting to observe that the measurement equations can also be written using electric field *quantities* for the test antenna and magnetic field quantities for the probe; viz.,

$$A_1(k_x,k_y) = -k\eta[A_x(k_x,k_y)G_{y,p}(k_x,-k_y) + A_y(k_x,k_y)G_{x,p}(k_x,-k_y)] \tag{2-135}$$

$$A_2(k_x,k_y) = -k\eta[A_x(k_x,k_y)G_{x,p}(-k_y,-k_x) - A_y(k_x,k_y)G_{y,p}(-k_y,-k_x)] \tag{2-136}$$

Another combination is also possible.

It is concluded from the above results, and is intuitively obvious, that either an infinitesimally small electric-dipole or magnetic-dipole antenna constitutes an ideal near-field probe. This conclusion is based on the assumption that the measured spectra A_1, A_2 or G_1, G_2 are obtained without error by inverse Fourier transformation of the

measured probe response over the measurement area. Due to the finite size of the measurement area and spatial sampling of the field over this area, errors will be introduced into the values obtained for these spectra. *The results of the last section strongly indicate that the near-field probe whose response is most concentrated in the given measurement area will produce a spectrum having the least (mean square) error.* Since ideal dipoles respond to the field at a point, it is felt that their responses would be less concentrated than those of more directive probes and, hence, less desirable in some practical instances.

It is recognized that for large measurement areas and/or for test antennas which radiate insignificant amounts of power at angles far from the normal to the measurement plane, the probe used is indeed arbitrary. Whereas one probe may produce a more concentrated response, the difference may be so slight as to produce unnoticeable effects in either the measured spectra or predicted far fields. *It is in those cases where the measurement area is restricted in size, and/or the test antenna radiates significant power at wide angles, that an optimally designed probe may produce significantly better end results.* The extent to which this is true in a particular measurement situation is examined in succeeding chapters.

CHAPTER III

COMPUTER SIMULATION

3.1 Introduction

This chapter presents a mathematical analysis of the near-field measurement technique and the results of the computer simulations done to demonstrate the existence of an optimum probe and to identify the optimum design parameters of rectangular horn probes used to measure a phased array antenna. The basic analysis uses the Lorentz reciprocity theorem to determine mathematical expressions for the response of the probe antenna when in the near field of the test antenna. Direct integration of the reaction fields on the probe aperture is used. A model for a phased array antenna consisting of a triangular lattice of circular waveguide elements is presented. Mathematical models for the fields radiated by the probes, based on Schelkunoff's equivalence theorem, are also presented. Computer calculations of the various probe responses are presented in support of the determination of optimum probe design parameters.

3.2 Analysis of Near-Field Probe Response

The voltage received by the probe antenna in the near field of the test antenna can be developed from the Lorentz reciprocity theorem [43].

Consider the two antennas shown in Figure 2-1 of the preceding chapter. It is desired to determine the response of Antenna "b" (the probe) when Antenna "a" (the test antenna) is energized. This response

will be a function of the position of Antenna "b" in the unprimed (reference) coordinate system as expressed by the position vector

$$\underline{r}_o = \hat{x}x_o + \hat{y}y_o + \hat{z}z_o \quad . \tag{3-1}$$

The primed coordinate system is fixed with respect to Antenna "b" and is oriented such that the z-axis and the z'-axis are always parallel and anti-directed. Surface S_1 is changed for this analysis from the infinite $z = 0$ plane shown to a surface that coincides with the probe aperture and the surface of the probe antenna. Surface S_2 encloses Antenna "b," and that portion of S_2 which extends over the cross-section of the transmission line connecting Antenna "b" to its source is denoted by S_2'. Hence, surfaces S_1 and S_2 enclose the source-free volume V comprised of the volume occupied by the flared part of the horn probe antenna. Note that with respect to the volume V, the unit outward normal to S_1 (probe aperture) is $-\hat{z} = +\hat{z}'$.

Application of the reciprocity theorem to the source-free volume V yields

$$\oint_{S_1+S_2} (\underline{E}_a \times \underline{H}_b - \underline{E}_b \times \underline{H}_a) \cdot \hat{n} da = 0 \tag{3-2}$$

where

$\underline{E}_a, \underline{H}_a$ are the fields produced on the surface $S = S_1+S_2$ when Antenna "a" is energized (and Antenna "b" is passive)

$\underline{E}_b, \underline{H}_b$ are the fields produced on the surface $S = S_1 + S_2$ when Antenna "b" is energized (and Antenna "a" is passive)

$\hat{n}$ is the unit outward normal to surface S

It is tacitly assumed that surface S_2' coincides with the cross-section of a uniform transmission line connecting Antenna "b" to its load/generator. It is further assumed that only a single dominant transmission line mode exists at S_2' so that voltages and currents may be defined. These currents and voltages are then related by impedances Z_b and Z_2 according to

$$V_{2a} = I_{2a} Z_b \tag{3-3}$$

and

$$Z_2 = V_{2b} / I_{2b} \tag{3-4}$$

where

V_{2a}, I_{2a} are the voltage and current produced at the surface S_2' when Antenna "a" is energized; i.e., the voltage and current "received" by Antenna "b"

V_{2b}, I_{2b} are the voltage and current produced on S_2' when Antenna "b" is energized.

The single surface integral in Equation (3-2) can be written as two surface integrals over S_1 and S_2 separately. It can be shown [43] that the only contribution to the integral over S_2 comes from S_2', and the only contribution to that over S_1 comes from the probe aperture S_{ap}. Hence, Equation (3-2) can be rewritten as

$$\int_{S_{ap}} (\underline{E}_a \times \underline{H}_b - \underline{E}_b \times \underline{H}_a) \cdot \hat{z}' dx'dy'$$

$$+ \int_{S_2'} (\underline{E}_a \times \underline{H}_b - \underline{E}_b \times \underline{H}_a) \cdot (-\hat{z}') dx'dy' = 0 \qquad (3\text{-}5)$$

The integral over S_2' can be written in terms of voltages and currents on the transmission line as

$$\int_{S_2'} (\underline{E}_a \times \underline{H}_b - \underline{E}_b \times \underline{H}_a) \cdot (-\hat{z}') dx'dy' = V_{2a} I_{2b} + V_{2b} I_{2a} \qquad (3\text{-}6)$$

Using Equations (3-3) and (3-4) in (3-6) yields

$$V_{2a} I_{2b} + V_{2b} I_{2a} = V_{2a} V_{2b} \left(\frac{Z_2 + Z_b}{Z_2 Z_b}\right) \qquad (3\text{-}7)$$

where V_{2a} is recognized as the voltage $V_1(x_o, y_o, z_o)$ received by the probe when the test antenna is energized. Hence,

$$V_1(x_o, y_o, z_o) = \left[\frac{Z_2 Z_b}{V_{2b}(Z_2 + Z_b)}\right] \int_{S_{ap}} (\underline{E}_a \times \underline{H}_b - \underline{E}_b \times \underline{H}_a) \cdot \hat{z}' dx'dy' \qquad (3\text{-}8)$$

which is one desired result.

Whereas the voltage V_1 is a function of the probe position

(x_o,y_o,z_o), it is assumed that the quantities in the brackets in Equation (3-8) are not; i.e., it is assumed that the two antennas are sufficiently separated and/or present sufficiently small scattering cross-sections such that the effects of scattering on the aforementioned quantities are negligible. Hence, the bracketed term in Equation (3-8) will be treated as a complex constant and absorbed into the voltage V_1; viz.,

$$V_1(x_o,y_o,z_o) = \int_{S_{ap}} (\underline{E}_a \times \underline{H}_b - \underline{E}_b \times \underline{H}_a) \cdot \hat{z}'dx'dy' \qquad (3\text{-}9)$$

The evaluation of Equation (3-9) requires determination of the tangential components of the fields $\underline{E}_a$, $\underline{H}_a$ and $\underline{E}_b$, $\underline{H}_b$ on the probe aperture surface S_{ap}. Let $(x',y',0)$ be the probe coordinates of a point in the probe aperture. Let (x_o,y_o,z_o) be the location in test antenna coordinates of the origin of the probe coordinate system. Let $(x_e,y_e,0)$ be the coordinates of the location of a radiating element in a phased array of such elements as depicted in Figure 3-1. Then for the first orientation of the probe, the point $(x',y',0)$ may be expressed in test antenna coordinates as (x_1,y_1,z_1) where

$$x_1 = x_0 - x' \qquad (3\text{-}10)$$

$$y_1 = y_0 + y' \qquad (3\text{-}11)$$

$$z_1 = z_0 \quad . \qquad (3\text{-}12)$$

The position vector $\underline{r}$ between the radiating element and the point in the probe aperture is given by

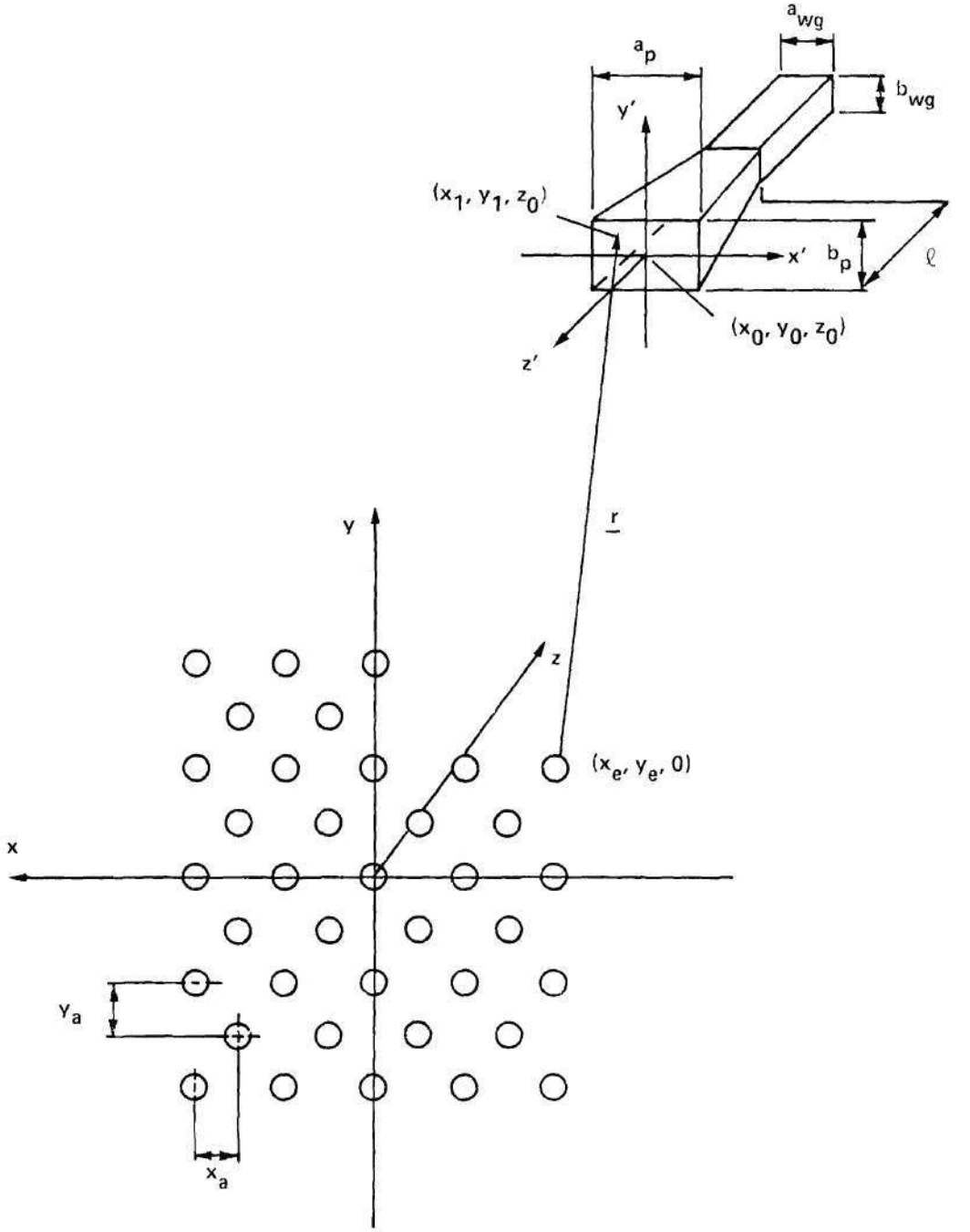

Figure 3-1. Geometry for Analysis of Response of Rectangular Horn Probe in Near Field of Phased Array Test Antenna.

$$\underline{r} = \hat{x}(x_o - x' - x_e) + \hat{y}(y_o - y_e + y') + \hat{z}z_o \qquad (3\text{-}13)$$

From Equation (3-13), the distance $r = |\underline{r}|$ and the direction cosines (k_{xe}, k_{ye}, k_{ze}) may be obtained directly for use below in computing the field at (x',y',0) due to the radiating element.

The integrand in Equation (3-9) may be evaluated by carrying out the vector multiplications with all fields expressed in the probe coordinate system to yield

$$V_1(x_o, y_o, z_o) = \int_{S_{ap}} (-E_{ax}H_{by}, -E_{ay}H_{bx}, -E_{bx}, H_{ay} - E_{by}, H_{ax})dx'dy' \qquad (3\text{-}14)$$

where the test antenna field components E_{ax}, E_{ay}, H_{ax}, H_{ay} are to be evaluated at (x_1, y_1, z_1) given by Equations (3-10) through (3-12). When the probe is rotated ninety degrees, as indicated in Figure 2-1, the received voltage V_2 is given by

$$V_2(x_o, y_o, z_o) = \int_{S_{ap}} (E_{ay}H_{by}, -E_{ax}H_{bx}, -E_{bx}, H_{ax} + E_{by}, H_{ay})dx'dy' \qquad (3\text{-}15)$$

where E_{ax}, E_{ay}, H_{ax}, H_{ay} are to be evaluated at

$$x_2 = x_o + y' \qquad (3\text{-}16)$$

$$y_2 = y_o + x' \qquad (3\text{-}17)$$

$$z_2 = z_o \qquad (3\text{-}18)$$

To clarify matters, it is noted that for the first orientation of the

probe, $\underline{E}_a$ may be written in terms of the probe coordinate system as

$$\underline{E}_a(x_1,y_1,z_1) = -\hat{x}'E_{ax} + \hat{y}'E_{ay} - \hat{z}'E_{az} \tag{3-19}$$

and for the second orientation,

$$\underline{E}_a(x_2,y_2,z_2) = \hat{x}'E_{ay} + \hat{y}'E_{ax} - \hat{z}'E_{az} \tag{3-20}$$

The fields E_{ax}, E_{ay}, H_{ax}, H_{ay} are calculated at $(x',y',0)$ by summing the contributions from each element of the phased array antenna. Let the mn^{th} element be located at $(x_e,y_e,0)$ and have complex excitation coefficient a_{mn}. Let the element radiation (far) field be given by

$$\underline{E}_{eff}(x,y,z) = j2\pi k \frac{e^{-jkr}}{r} [\hat{x}k_{ze}A_{xe} + \hat{y}k_{ze}A_{ye} + \hat{z}(-k_{xe}A_{xe}-k_{ye}A_{ye})] \tag{3-21}$$

where A_{xe}, A_{ye} are the plane wave spectra associated with the element (in a ground plane) and where k_{xe}, k_{ye}, k_{ze} are direction cosines defined by Equation (3-13) for orientation #1, and by

$$\underline{r} = \hat{x}(x_o+y'-x_e) + \hat{y}(y_o+x'-y_e) + \hat{z}z_o \tag{3-22}$$

for orientation #2. For example,

$$k_{ze} = z_o/r \tag{3-23}$$

in both cases. Using the far-field relation

$$\underline{H}_{eff} = \frac{\hat{k}_e \times \underline{E}_{eff}}{\eta} \quad , \tag{3-24}$$

the following expressions for the tangential fields in the probe aperture due to the mn^{th} array element are found:

$$E_{ax}^{mn} = j2\pi k \frac{e^{-jkr}}{r} k_{ze} A_{xe}(k_{xe}, k_{ye}) a_{mn} \tag{3-25}$$

$$E_{ay}^{mn} = j2\pi k \frac{e^{-jkr}}{r} k_{ze} A_{ye}(k_{xe}, k_{ye}) a_{mn} \tag{3-26}$$

$$H_{ax}^{mn} = j2\pi k \frac{e^{-jkr}}{r} a_{mn}[-k_{xe} k_{ye} A_{xe} - (1-k_{xe}^2) A_{ye}] \tag{3-27}$$

$$H_{ay}^{mn} = j2\pi k \frac{e^{-jkr}}{r} a_{mn}[(1-k_{ye}^2) A_{xe} + k_x k_y A_{ye}] \tag{3-28}$$

These field expressions are the primary fields that would exist in the probe aperture in the absence of the probe; i.e., they contain no scattered field components and, hence, consititute a first-order approximation to the actual fields.

Let the fields in the probe aperture when the probe is energized be due to dominant mode excitation of the rectangular waveguide transmission line with y' polarization so that $E_{bx'}$, $H_{by'}$ are identically zero, and $E_{by'}$, $H_{bx'}$ are non-zero. After Silver [44], assume that $E_{by'}$, $H_{bx'}$ are related by

$$H_{bx'} = -\gamma E_{by'} \tag{3-29}$$

where γ is defined by

$$\gamma \triangleq \frac{\sqrt{1-(2\frac{a_{wg}}{\lambda})^{-2}}}{\eta} \frac{(1-\Gamma)}{(1+\Gamma)} \tag{3-30}$$

and where a_{wg} is defined in Figure 3-1 as the wide dimension of the waveguide, and where Γ is the voltage reflection coefficient for the dominant mode wave in the waveguide. Let the probe aperture be subdivided into pq rectangular elements, each of area $\Delta x'\Delta y'$. Then the voltages received by the probe may be approximated by

$$V_1(x_o,y_o,z_o) = \Delta x'\Delta y' \sum_p \sum_q (\gamma E_{ay}^{pq} - H_{ax}^{pq}) E_{by'}^{pq} \tag{3-31}$$

$$V_2(x_o,y_o,z_o) = \Delta x'\Delta y' \sum_p \sum_q (\gamma E_{ax}^{pq} + H_{ay}^{pq}) E_{by'}^{pq} \tag{3-32}$$

where the pq^{th} superscript on E_{ax}, H_{ax}, E_{ay}, H_{ay} indicate total fields at the pq^{th} point due to all radiating elements in the array. The fields $E_{by'}$, $H_{bx'}$ are due only to the dominant mode wave in the waveguide although higher order modes are known to exist; hence, Equations (3-31) and (3-32) constitute first order approximations to the received voltages for the two orientations.

Evaluation of Equations (3-31) and (3-32) require explicit expressions for the field quantities on the surface S_{ap} as presented in the following two sections.

3.3 Mathematic Model of Rectangular Probe Antennas

For small horn antennas and open-end waveguides, it must be assumed that both electric current sources $\hat{z}' \times \underline{H}_b$ and magnetic current sources

$\hat{z} \times \underline{E}_b$ are present to represent the radiating aperture using the equivalence theorem. Using only $\hat{z}' \times \underline{E}_b$ is tantamount to assuming that the radiator is mounted in an infinite ground plane of perfect conductivity over which $\hat{z}' \times \underline{E}_b$ is zero except in the probe aperture. In such case, no x or y component of the radiated electric field is possible in the $z' = 0$ plane and does not conform to physical observations. The use of the electric current sources $\hat{z}' \times \underline{H}_b$ gives rise to such field components as are actually observed. But since $\underline{H}_b$ is assumed related to $\underline{E}_b$ for dominant mode waveguide excitation by

$$\underline{H}_{b_{tan}} = \gamma \hat{z}' \times \underline{E}_{b_{tan}} \quad , \tag{3-33}$$

it follows that only $E_{by'}$ need be known for the probe aperture.

After Collin and Zucker [45], the aperture electric field for a rectangular horn antenna with positive flare angles in both H-plane ($y' = 0$ plane of Figure 3-1) and E-plane ($x' = 0$ plane) and for dominant mode excitation is given by

$$E_{by'} = E_o e^{-j(ky^2/2\rho_y)} \cos\left(\frac{\pi x}{a}\right) e^{-j(kx^2/2\rho_x)} \quad . \tag{3-34}$$

The radii ρ_x and ρ_y are related to the flare length ℓ in Figure 3-1 by

$$\rho_x = \frac{a_p}{2\sin\theta_x} \tag{3-35}$$

$$\rho_y = \frac{b_p}{2\sin\theta_y} \tag{3-36}$$

The flare angles θ_x and θ_y are given by

$$\theta_x = \tan^{-1}\left(\frac{a_p - a_{wg}}{2\ell}\right) \tag{3-37}$$

$$\theta_y = \tan^{-1}\left(\frac{b_p - b_{wg}}{2\ell}\right) \tag{3-38}$$

where the other variables are defined in Figure 3-1.

For a zero or negative flare angle in either plane, the corresponding exponential factor in Equation (3-34) reduces to unity so that the phase of the aperture field becomes uniform in that direction. A zero flare angle corresponds to an open-end waveguide radiator with aperture dimensions $a_p = a_{wg}$, $b_p = b_{wg}$. A negative flare angle corresponds to a dielectric-loaded waveguide with aperture dimensions $a_p < a_{wg}$, $b_p < a_{wg}$ for the case of reductions in both dimensions. For negative flare angles, the parameter γ which relates $E_{by'}$ and $H_{bx'}$ is given by

$$\gamma = \frac{\sqrt{1-\left(\frac{2a_p}{\lambda_\epsilon}\right)^2}}{\eta_\epsilon} \frac{(1-\Gamma)}{(1+\Gamma)} \tag{3-39}$$

where λ_ϵ, η_ϵ are the values in the dielectric material which fills the waveguide; i.e.,

$$\lambda_\epsilon = \frac{\lambda_o}{\sqrt{\epsilon_r}} \tag{3-40}$$

$$\eta_\epsilon = \frac{\eta_o}{\sqrt{\epsilon_r}} \tag{3-41}$$

where ϵ_r is the relative dielectric constant of the waveguide filler material.

The far radiation field of the probe antenna can be found in terms of the Fourier transform of the electric and magnetic aperture fields using the plane wave expansion theory presented in Section 2.2 of the preceding chapter. Dropping the prime on the probe coordinate system, define

$$B_x(k_x,k_y) \triangleq \frac{1}{(2\pi)^2} \int_{S_{ap}} E_x(x,y,0) e^{j(k_x x+k_y y)} dxdy \qquad (3\text{-}42)$$

$$B_y(k_x,k_y) \triangleq \frac{1}{(2\pi)^2} \int_{S_{ap}} E_y(x,y,0) e^{j(k_x x+k_y y)} dxdy \qquad (3\text{-}43)$$

as the usual plane wave spectra associated with E_x, E_y (magnetic current sources). Similarly, define

$$G_x(k_x,k_y) \triangleq \frac{1}{(2\pi)^2} \int_{S_{ap}} H_x(x,y,0) e^{j(k_x x+k_y y)} dxdy \qquad (3\text{-}44)$$

$$G_y(k_x,k_y) \triangleq \frac{1}{(2\pi)^2} \int_{S_{ap}} H_y(x,y,0) e^{j(k_x x+k_y y)} dxdy \qquad (3\text{-}45)$$

as the corresponding plane wave spectra associated with the aperture magnetic fields; i.e., with the electric current sources. Then using Equations (2-19) and (3-24), it is found that the total far fields of the radiating aperture due to both tangential electric and magnetic fields are given by

$$\underline{E}_{ff}(k_x,k_y) = \hat{x}[k_z B_x+\eta k_x k_y G_x+\eta(k^2-k_x^2)G_y]$$

$$+\hat{y}[k_z B_y-\eta(k^2-k_y^2)G_x-\eta k_x k_y G_y]$$

$$\hat{z}[-k_x B_x-k_y B_y+\eta k_y k_z G_x-\eta k_x k_z G_y] \qquad (3\text{-}46)$$

$$\underline{H}_{ff}(k_x,k_y) = \hat{x}[k_z G_x - \frac{k_x k_y}{\eta} B_x - \frac{(k^2-k_x^2)}{\eta} B_y]$$

$$+\hat{y}[k_z G_y + \frac{(k^2-k_y^2)}{\eta} B_x + \frac{k_x k_y}{\eta} B_y]$$

$$+\hat{z}[-k_x G_x - k_y G_y - \frac{k_y k_z}{\eta} B_x + \frac{k_x k_z}{\eta} B_y] \qquad (3\text{-}47)$$

In the special case of dominant mode waveguide excitation where $\underline{E}_b$ and $\underline{H}_b$ are related as in Equation (3-33), the above general expression specialize to the following expressions applicable to the present work:

$$\underline{E}_{ff}(k_x,k_y) = \hat{x}[B_x(k_z+\gamma\eta(k^2-k_x^2) + B_y(-\gamma\eta k_x k_y)]$$

$$+\hat{y}[B_x(-\gamma\eta k_x k_y) + B_y(k_z+\gamma\eta(k^2-k_y^2))]$$

$$+\hat{z}[B_x(-k_x-\gamma\eta k_x k_z) + B_y(-k_y-\gamma\eta k_y k_z)] \qquad (3\text{-}48)$$

$$\underline{H}_{ff}(k_x,k_y) = \hat{x}[B_x(-\frac{k_x k_y}{\eta}) + B_y(-\gamma k_z - \frac{k^2-k_x^2}{\eta})]$$

$$+\hat{y}[B_x(\gamma k_z + \frac{k^2-k_y^2}{\eta}) + B_y(\frac{k_x k_y}{\eta})]$$

$$+\hat{z}[B_x(-\gamma k_y - \frac{k_y k_z}{\eta}) + B_y(\gamma k_x + \frac{k_x k_y}{\eta})] \qquad (3\text{-}49)$$

For the class of rectangular horn probe antennas considered, the plane wave spectra B_x and B_y are given in the case of positive flare angles by [45]

$$B_x(k_x,k_y) \equiv 0 \tag{3-50}$$

$$B_y(k_x,k_y) = I_1(k_{xn})I_2(k_{yn}) \tag{3-51}$$

where

$$I_1(k_{xn}) = \sqrt{\frac{(\rho_x/\lambda)}{2}} \left\{ e^{j\pi(\frac{\rho_x}{\lambda})(k_{xn} + \frac{1}{2(a/\lambda)})^2} [CS(t_2) - CS(t_1)] + e^{j\pi(\frac{\rho_x}{x})(k_{xn} - \frac{1}{2(a/\lambda)})^2} [CS(t_4) - CS(t_3)] \right\} \tag{3-52}$$

and where the t_i are given by

$$t_i = \frac{1}{\sqrt{2(\rho_x/\lambda)}} [(-1)^i \frac{a_p}{\lambda} - 2(\frac{\rho_x}{\lambda})k_{xn} + \delta_i \frac{(\rho_x/\lambda)}{(a_p/\lambda)}] \tag{3-53}$$

with $i = 1,2,3,4$ in turn, and $\delta_i = -1$ for $i = 1,2$, $\delta_i = +1$ for $i = 3,4$; and CS(t) is the complex Fresnel integral [46]

$$CS(t) = C(t) - jS(t) = \int_o^t \cos(\frac{\pi}{2} u^2)du - j \int_o^t \sin(\frac{\pi}{2} u^2)du \quad . \tag{3-54}$$

The function $I_2(k_{yn})$ is given by

$$I_2(k_{yn}) = \sqrt{\frac{\rho_y/\lambda}{2}}\{e^{j\pi(\frac{\rho_y}{\lambda})k_{yn}^2}[CS(u_2) - CS(u_1)]\} \tag{3-55}$$

where

$$u_i = \frac{1}{\sqrt{2(\rho_y/\lambda)}}[(-1)^i \frac{b_p}{\lambda} - 2(\frac{\rho_y}{\lambda})k_{yn}] \quad , \quad i = 1,2 \tag{3-56}$$

In the above expressions for I_1 and I_2, normalized wavenumbers k_{xn}, k_{yn} are used to facilitate normalization of dimensions with respect to wavelength; i.e.,

$$k_{xn} = k_x/k \tag{3-57}$$

$$k_{yn} = k_y/k \tag{3-58}$$

For the case of zero and negative flare angles, the expression for B_y simplifies to

$$B_y(k_{xn},k_{yn}) = \frac{\cos(\pi \frac{a_p}{\lambda} k_{xn})}{1-(2 \frac{a_p}{\lambda} k_{xn})^2} \cdot \frac{\sin(\pi \frac{b_p}{\lambda} k_{yn})}{(\pi \frac{b_p}{\lambda} k_{yn})} \tag{3-59}$$

At $k_{xn} = \pm(2a/\lambda)^{-1}$, the cosine term in this equation evaluates to $+\pi/4$; at $k_{yn} = 0$, the sine term evaluates to unity.

For the case of combinations of negative and nonnegative flare angles, the appropriate factors in Equations (3-51) and (3-59) may be combined to form the correct expression for B_y. For example, for the case of an E-plane sectoral horn and zero flare angle in the H-plane,

the combined expression for B_y is

$$B_y(k_x,k_y) = \frac{\cos(\pi \frac{a}{\lambda} k_{xn})}{1-(2 \frac{a}{\lambda} k_{xn})^2} \cdot I_2(k_{yn}) \qquad (3\text{-}60)$$

Plots of the computed x and y components of the electric field radiated by an open-end waveguide are shown in Figures 3-2 and 3-3. The waveguide dimensions are those for RG-49/U waveguide; viz., $a_{wg} = 1.8720"$ and $b_{wg} = .8720"$. The frequency of operation is 5.62 GHz. In each plot, amplitude is graphed in decibels as a function of normalized wavenumbers k_{xn}, k_{yn} shown in the figures (no subscript n used in the figures); i.e.,

$$k_{xn} = \sin\theta\cos\phi \qquad (3\text{-}61)$$

$$k_{yn} = \sin\theta\sin\phi \qquad (3\text{-}62)$$

where θ is the polar angle (from +z) and ϕ is the azimuthal angle (from +x) in the usual spherical coordinate system. The y component of Figure 3-3 is smoothly varying as expected while the x component peaks up in the forty-five-degree planes containing the corners of the waveguide. Principal plane E-plane ($k_x = 0$) and H-plane ($k_y = 0$) patterns taken as cuts from Figures 3-2 and 3-3 compare favorably to those presented in Figure 10-4 of Silver [44]. The amplitude of $k_z B_x(k_x,k_y)$ in Figure 3-2 is shown relative to its own maximum value. It is offset by +25 dB with respect to the larger maximum value of $k_z B_y(k_x,k_y)$ in Figure 3-3.

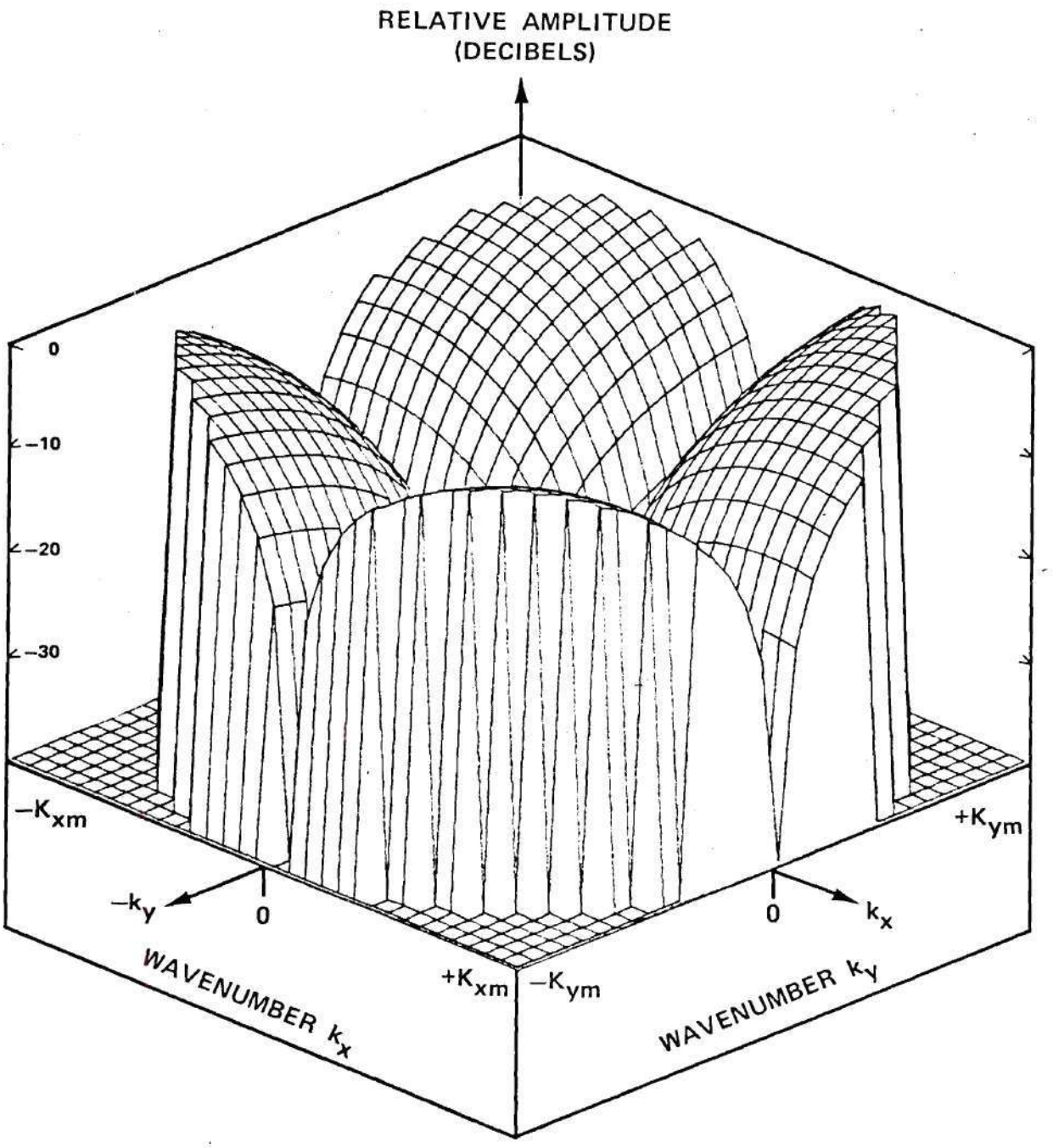

Figure 3-2. Computed Amplitude of $k_z B_x(k_x,k_y)$ for Open-End RG-49 Waveguide (Offset +25 dB).

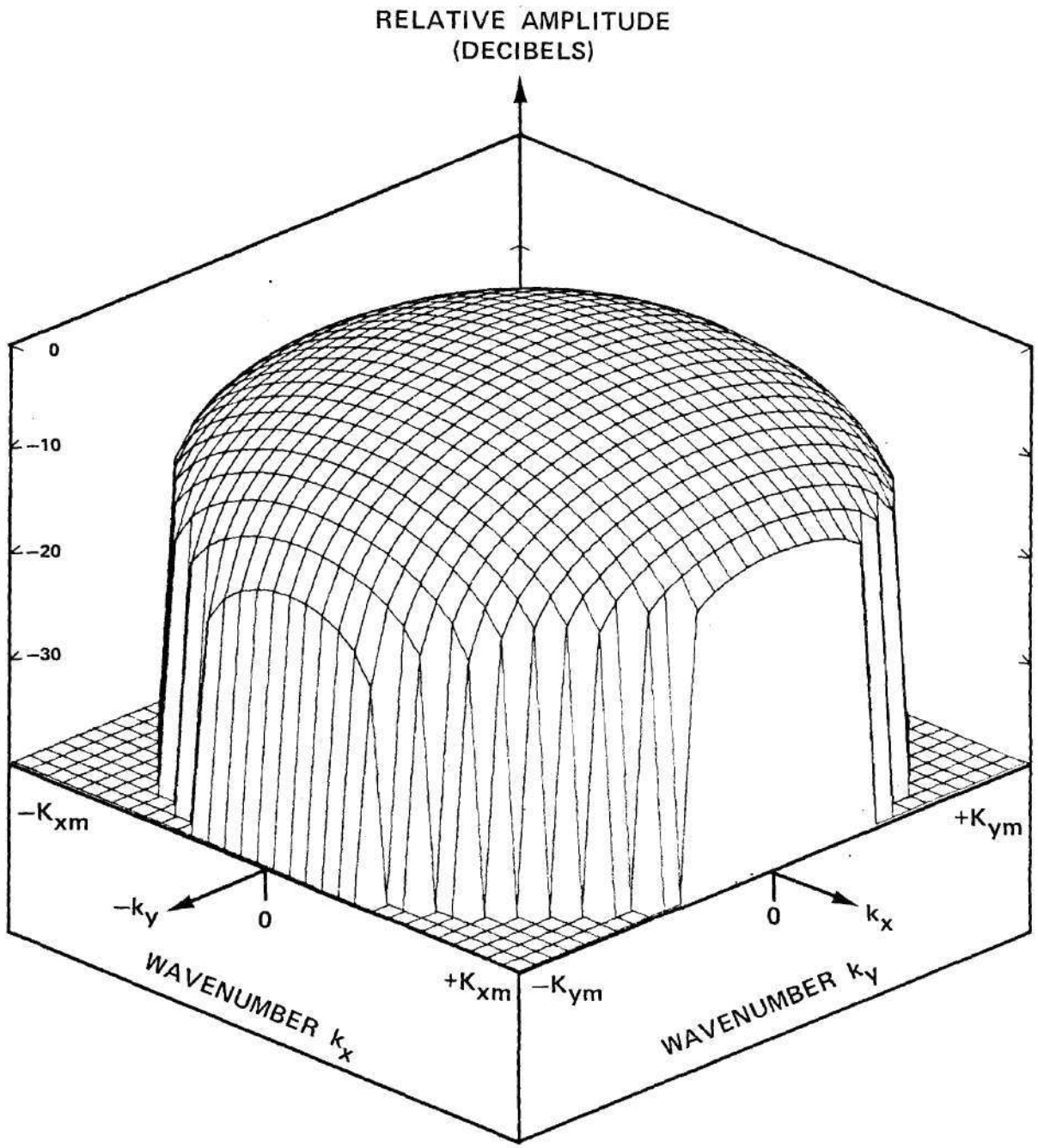

Figure 3-3. Computed Amplitude of $k_z B_y(k_x,k_y)$ for Open-End RG-49 Waveguide.

3.4 Phased Array Antenna Model

The radiated (far) electric field for $z > 0$ of an array of identical elements uniformly spaced in x and y may be written as the product of the element pattern and an array factor [47]; viz.,

$$\underline{E}_{ff}(k_{xn},k_{yn}) = \underline{E}_{eff}(k_{xn},k_{yn}) f(k_{xn},k_{yn}) \tag{3-63}$$

where k_{xn}, k_{yn} are normalized wavenumbers equivalent to direction cosines in the visible region. Let there be N_{xa} elements in each row and N_{ya} elements in each column. Let these integers be odd and let the center element of the array be located at the origin of the coordinate system. Then the array factor may be written as

$$f(k_{xn},k_{yn}) = \sum_{p=1}^{N_{xa}} \sum_{q=1}^{N_{ya}} a_{pq} e^{j2\pi(k_{xn}x_n + k_{yn}y_n)} \tag{3-64}$$

where x_n, y_n designate normalized distances

$$x_n = (p-P-1)(x_a/\lambda) \tag{3-65}$$

$$y_n = (q-Q-1)(y_a/\lambda) \tag{3-66}$$

and where x_a, y_a are the element spacings. The integers P and Q are given by

$$P = (N_{xa}-1)/2 \tag{3-67}$$

$$Q = (N_{ya}-1)/2 \tag{3-68}$$

The phased array actually modeled consists of a triangular lattice of elements as illustrated in Figure 3-1. The excitation coefficients are given by

$$a_{pq} = \cos\left(\frac{\pi\sqrt{x_n^2+y_n^2}}{d_n}\right) e^{-j2\pi(x_n k_{xo}+y_n k_{yo})} \tag{3-69}$$

where $a_{pq} = 0$ for p even and q odd, and $a_{pq} = 0$ for q even and p odd in order to realize the triangular lattice from the rectangular lattice model. In Equation (3-69), the cosine factor provides for amplitude tapering in the array (as found in the space-fed, microwave lens-type phased array antenna used in the measurements). The normalized wavenumbers k_{xo}, k_{yo} are used to specify the relative phasing of the elements and thereby produce a main beam of radiation in the direction specified by (k_{xo},k_{yo}). The actual number of nonzero elements in the array is given approximately by the product of P and Q.

Both the far-field model of Equation (3-63) and the near-field model of Equations (3-25) through (3-28) require the far-field model of the circular waveguide element of radius a, mounted in a ground plane, and operating in the dominant TE_{11} mode (y polarized). After Silver [48], the tangential electric field in the aperture of the element, assumed to be identical to that in the unperturbed circular waveguide, is (inverse) Fourier transformed to obtain the plane wave spectra A_{xe}, A_{ye} required; viz.,

$$A_{xe}(\theta,\phi) = -j \frac{\eta k(1+\Gamma)\kappa_{11} a\pi \sin 2\phi}{2k^2[(\frac{\kappa_{11}}{k})^2 - \sin^2\theta]} \{\kappa J_2(\kappa_{11}a)[J_1(\kappa a) - J_3(\kappa a)]$$

$$-\kappa_{11} J_2(\kappa_a)[J_1(\kappa_{11}a) - J_3(\kappa_{11}a)]\} \qquad (3\text{-}70)$$

$$A_{ye}(\theta,\phi) = j \frac{\eta(1+\Gamma)\kappa_{11} a\pi}{(\frac{\kappa_{11}}{k})^2 - \sin^2\theta} \{-(\frac{\kappa}{k}) J_o(\kappa_{11}a) J_1(\kappa a)$$

$$+ (\frac{\kappa_{11}}{k}) J_1(\kappa_{11}a) J_o(\kappa a) + \frac{\cos 2\phi}{2} [(\frac{\kappa}{k}) J_2(\kappa_{11}a)(J_1(\kappa a) - J_3(\kappa a))$$

$$- (\frac{\kappa_{11}}{k}) J_2(\kappa a)(J_1(\kappa_{11}a) - J_3(\kappa_{11}a))]\} \qquad (3\text{-}71)$$

where $\kappa_{11}a = 1.84$ is the first root of $J_1'(\kappa a) = 0$ and where $J_m(\kappa a)$ is the Bessel function of the first kind of integer order m. The spherical coordinate angles θ,ϕ are related to the normalized wavenumbers k_{xn}, k_{yn} by

$$\sin\theta = \sqrt{k_{xn}^2 + k_{yn}^2} \qquad (3\text{-}72)$$

$$\tan\phi = k_{yn}/k_{xn} \qquad (3\text{-}73)$$

The phased array model was implemented on a digital computer as part of the simulation of the near-field measurement technique. Three dimensional plots of the amplitudes of the x and y far field components of a circular waveguide element of radius a = .4531" at 5.62 GHz in a ground plane are shown in Figure 3-4 and 3-5. Similar computations made

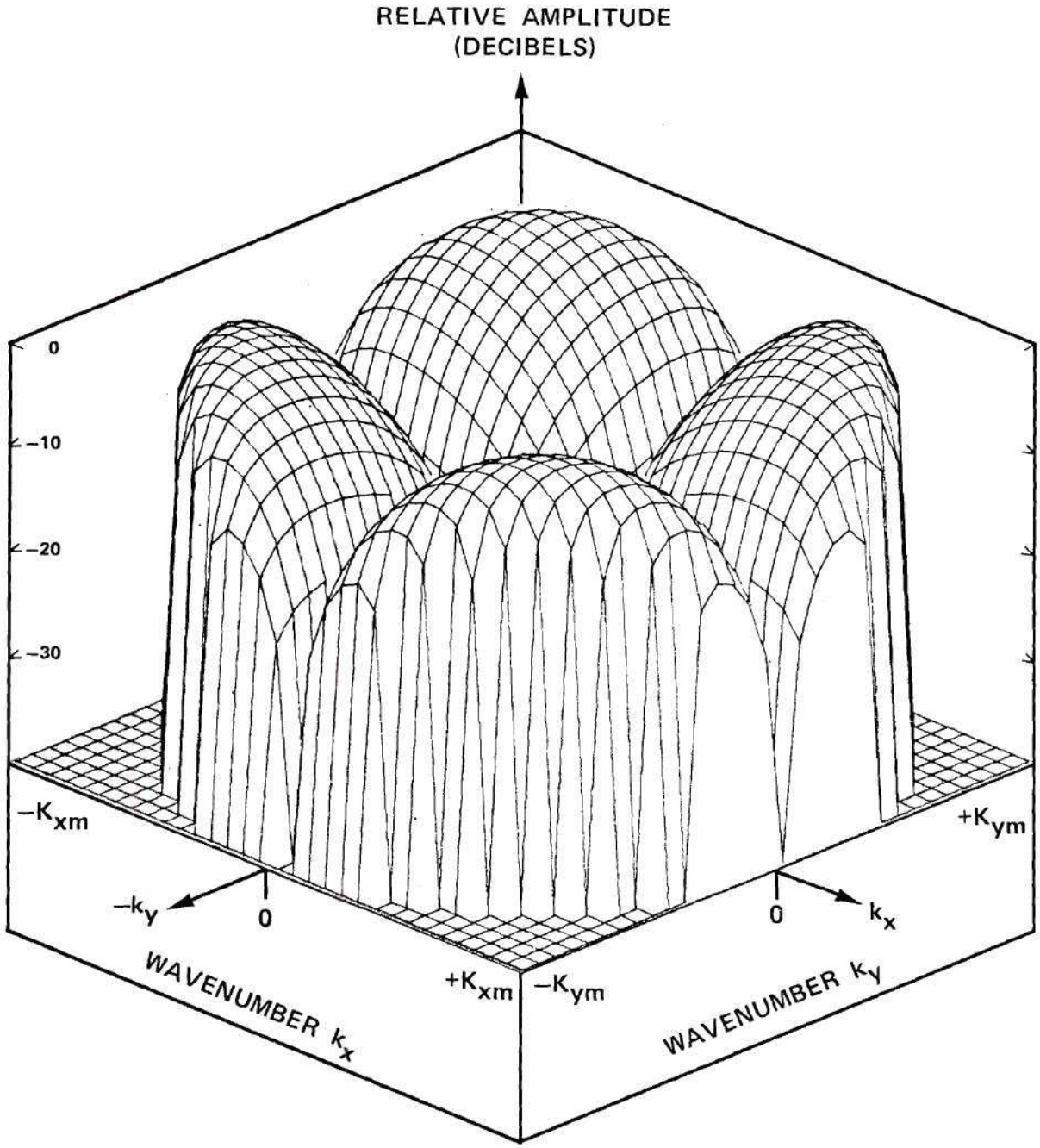

Figure 3-4. Computed Amplitude of $B_x(k_x,k_y)$ for Circular Waveguide Element of Radius $a = .22\lambda$ in Ground Plane.

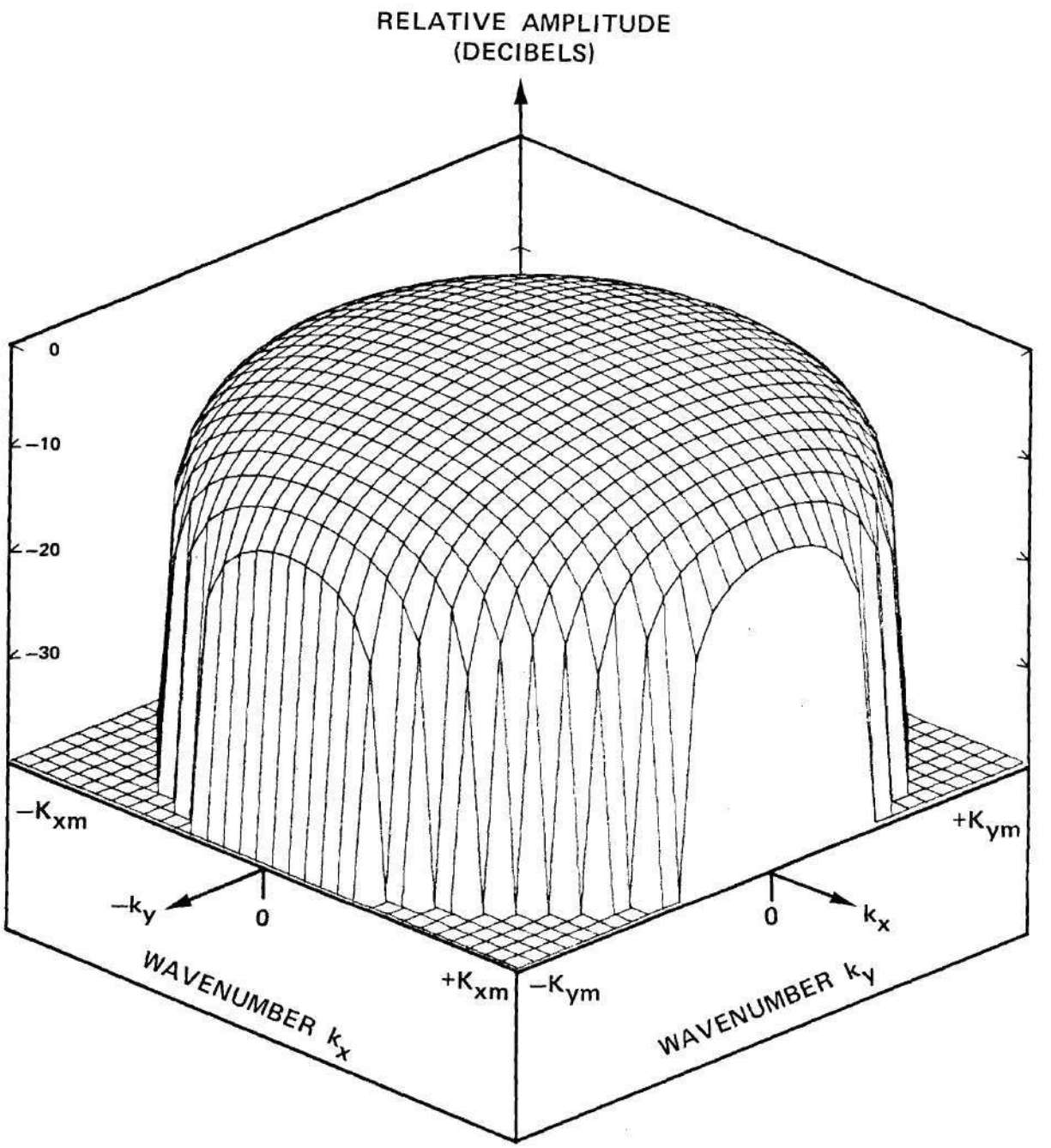

Figure 3-5. Computed Amplitude of $B_y(k_x,k_y)$ for Circular Waveguide Element of Radius $a = .22\lambda$ in Ground Plane.

without a ground plane compare favorably in the principal planes with those shown in Figure 10.2 of Silver [48].

Figure 3-6 and 3-7 show the computed principal plane radiation patterns of a phased array having $N_{xa} = 9$ elements per row and $N_{ya} = 17$ elements per column, and element spacings of $x_a = 1.074"$ and $y_a = .620"$ at a frequency of 5.62 GHz. Since every other element has a zero excitation coefficient in order to realize a triangular lattice, the actual number of elements is approximately one-fourth of the product $N_{xa}N_{ya}$. The phases of the excitation coefficients were chosen to produce a main beam of radiation at 45 degrees in the H-plane, which explains the shift in the pattern in Figure 3-6. The reduced amplitude of the E-plane pattern of Figure 3-7 is due to the fact that the beam is scanned. In each case, the elevation component of the far field is shown and normalized with respect to the peak of the main beam shown in Figure 3-6.

3.5 Results of Computer Simulation

A computer simulation of the near-field measurement was carried out to determine the design parameters of a rectangular horn probe antenna which produced the most concentrated near-field response to the phased array antenna model just described. The design parameters of the rectangular probes were restricted to the aperture dimensions a_p and b_p. The flare length ℓ (see Figure 3-1) was held constant at 8.0 inches, at an operating frequency of 5.62 GHz. The values of $a_{wg} = 1.8720"$ and $b_{wg} = .8720"$ are those for standard RG-49 waveguide. Values of a_p ranged from $.25\lambda$ to 1.25λ for a fixed value of $a_p = .892\lambda = a_{wg}$. Three additional probe aperture sizes were also examined, corresponding to those of the

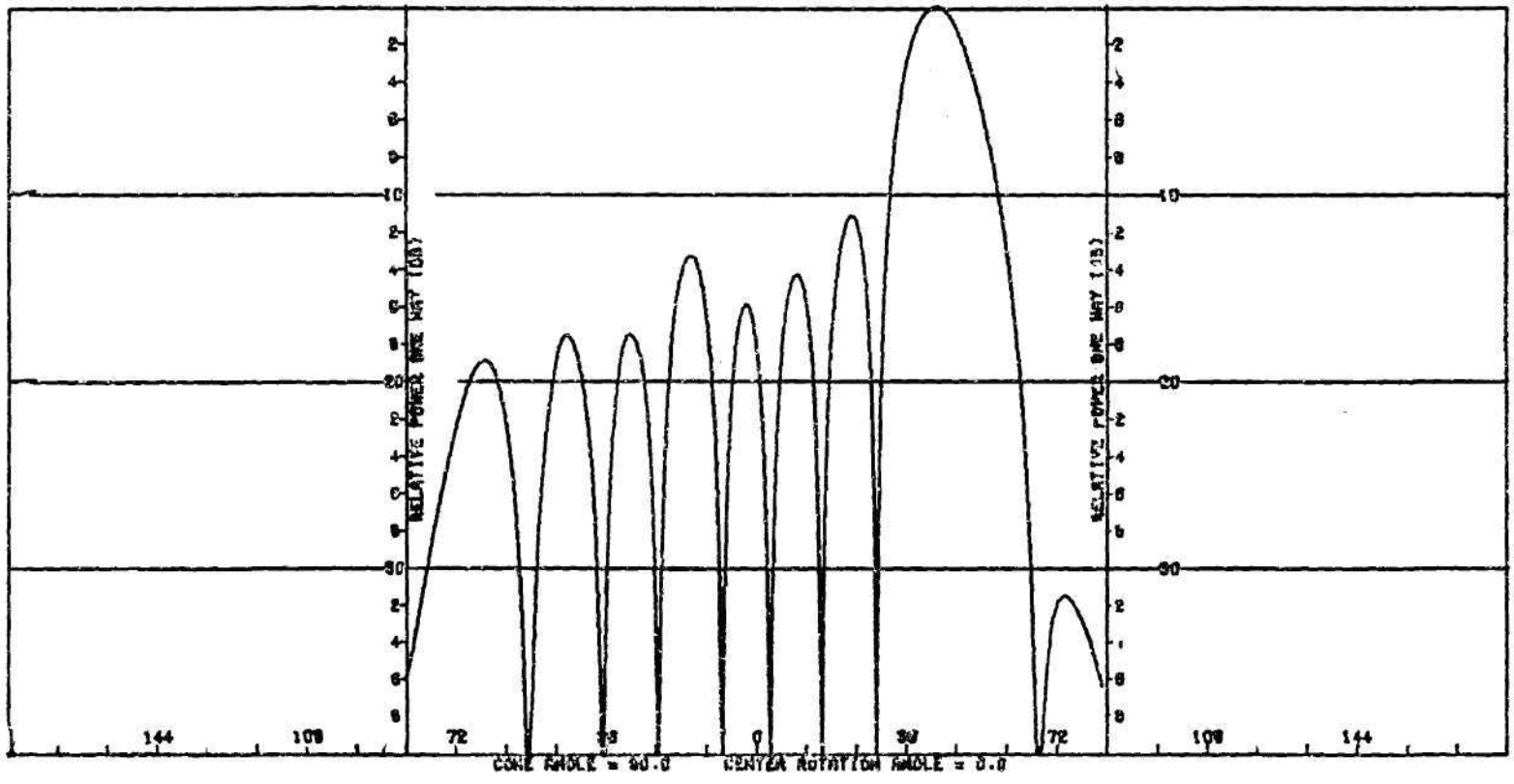

Figure 3-6. Computed H-Plane Power Pattern for Phased Array. Antenna Model When Scanned to 45° in Azimuth.

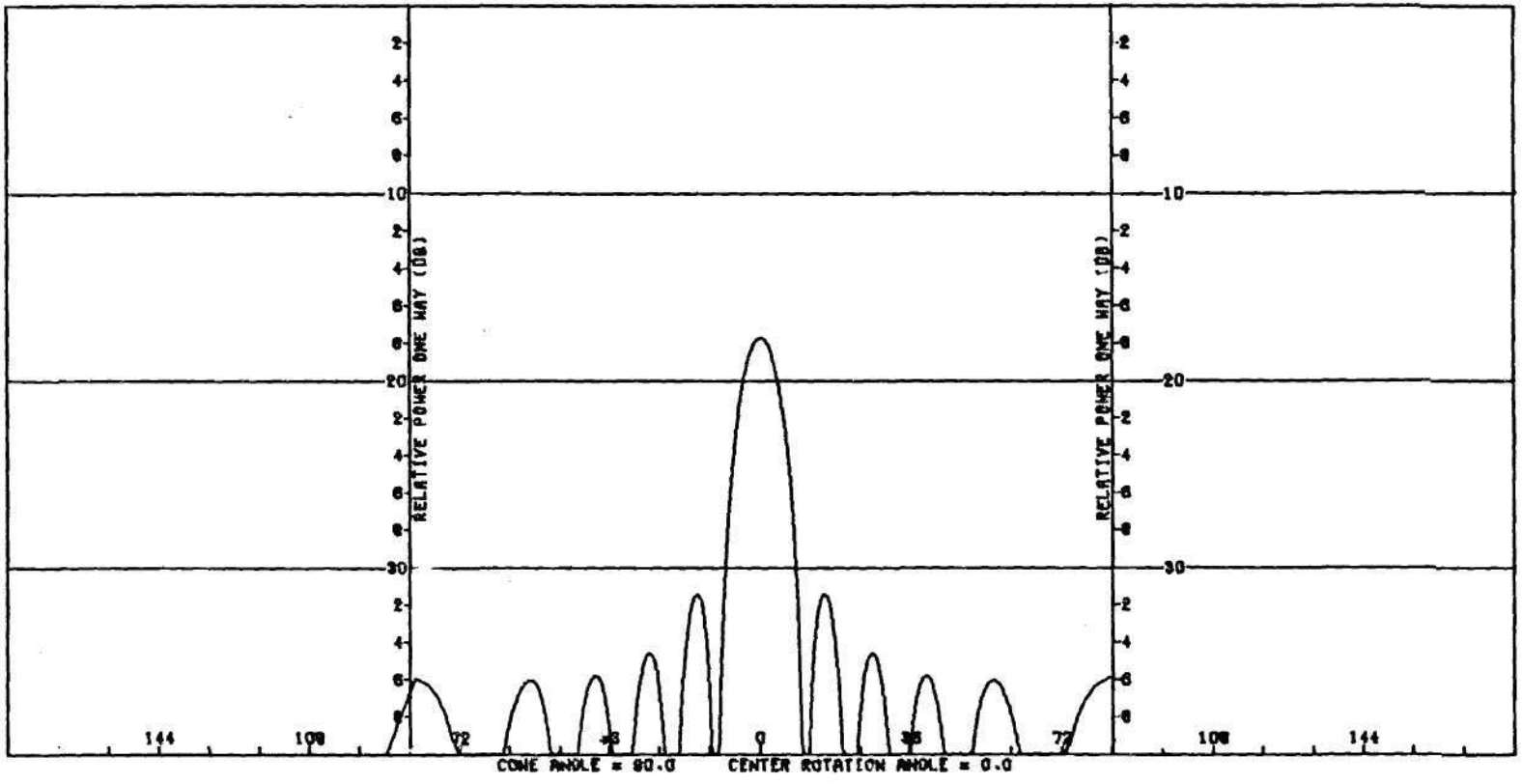

Figure 3-7. Computed E-Plane Power Pattern for Phased Array. Antenna Model When Scanned to 45° in Azimuth.

three probes used in the experimental work. The separation between probe and test antenna was $z_o = 1.0\lambda$ in all cases.

The phased array antenna model used in the simulation employed a reduced number of elements; viz., $N_{xa} = 5$, $N_{ya} = 9$. Such a reduction was found to be necessary because of computation time requirements and the desire to examine a large number of probe designs. Some typical computation times for each position of the probe antenna are shown in Table 3-1. The number of points N_{xp}, N_{yp} used in the surface integration over the probe aperture also influenced computation time as indicated in the table. The values of N_{xp}, N_{yp} were selected according to the size of the aperture such that sampling in the aperture was no greater than $.20\lambda$. Also shown in Table 3-1 are the computation times in minutes for computing the probe response at $64 \times 64 = 4096$ points as would be required in a complete simulation.

The probe design data were obtained by computing the response of each probe in Orientation #1 at 64 sample points spaced one-third wavelength apart along the two lines $x = 0$ and $y = 0$. Two cases of test antenna phasing were considered: in one case, a main beam of radiation was formed at 45 degrees in the H-plane (xz-plane); in the other case, the main beam was formed at 45 degrees in the E-plane (yz-plane). In each case, one aperture dimension of the probe was held constant, and responses were computed for five values of the other aperture dimension. The simulation was not repeated for Orientation #2 of the probe since the response of the probe in the second position is so much reduced as to be much less affected by changes in the probe design parameters as compared to the first orientation.

Table 3-1. Computation Times for Near-Field Simulation

N_{xa}	N_{ya}	N_{xp}	N_{yp}	Run Time	
				Per Point (sec.)	64 x 64 Points (min.)
5	9	3	3	.1339	9.7
5	9	5	3	.2199	15.0
5	9	5	5	.3649	24.9
5	9	5	7	.4502	30.7
5	9	7	7	.6921	47.0
9	17	5	3	.5971	40.8

The results of the simulation for the case of the main beam of the phased array scanned to 45 degrees in azimuth (H-plane) are presented graphically in Figures 3-8 through 3-11. It is seen from Figures 3-8 and 3-9 that for b_p held constant, increases in a_p result in increased concentration of response in the H-plane and a decrease in concentration in the E-plane; however, the increase in concentration in the H-plane is somewhat more marked than is the decrease in the E-plane.

Figures 3-10 and 3-11 show the effects on concentration of response of five values of b_p while a_p is held constant. In Figure 3-10, it is seen that changes in b_p produce insignificant changes in the concentration of probe response in the H-plane. But in the E-plane, increases in b_p up to 1.0λ produce significant increases in the concentration of probe response. For $b_p = 1.25\lambda$, however, the response is less concentrated than for $b_p = 1.0\lambda$ for values of distance $|y| > 4\lambda$ as seen in Figure 3-11. Hence, there is a reversal in the trend of increasing concentration with increasing b_p at $b_p = 1.0\lambda$. This reversal in trend is even more apparent in the next case.

The graphical results of the simulation for the case when the main beam of the phased array is scanned to 45 degrees in elevation (E-plane) are presented in Figures 3-12 through 3-15. Referring to Figure 3-12, it is seen that increases in b_p of the probe at fixed a_p result in small decreases in the concentration of the probe response in the H-plane. However, significant increases in concentration occur in the E-plane response when b_p is increased up to 1.0λ as seen in Figure 3-13. A further increase in b_p to 1.25λ results in a significant decrease in concentration of response for this case.

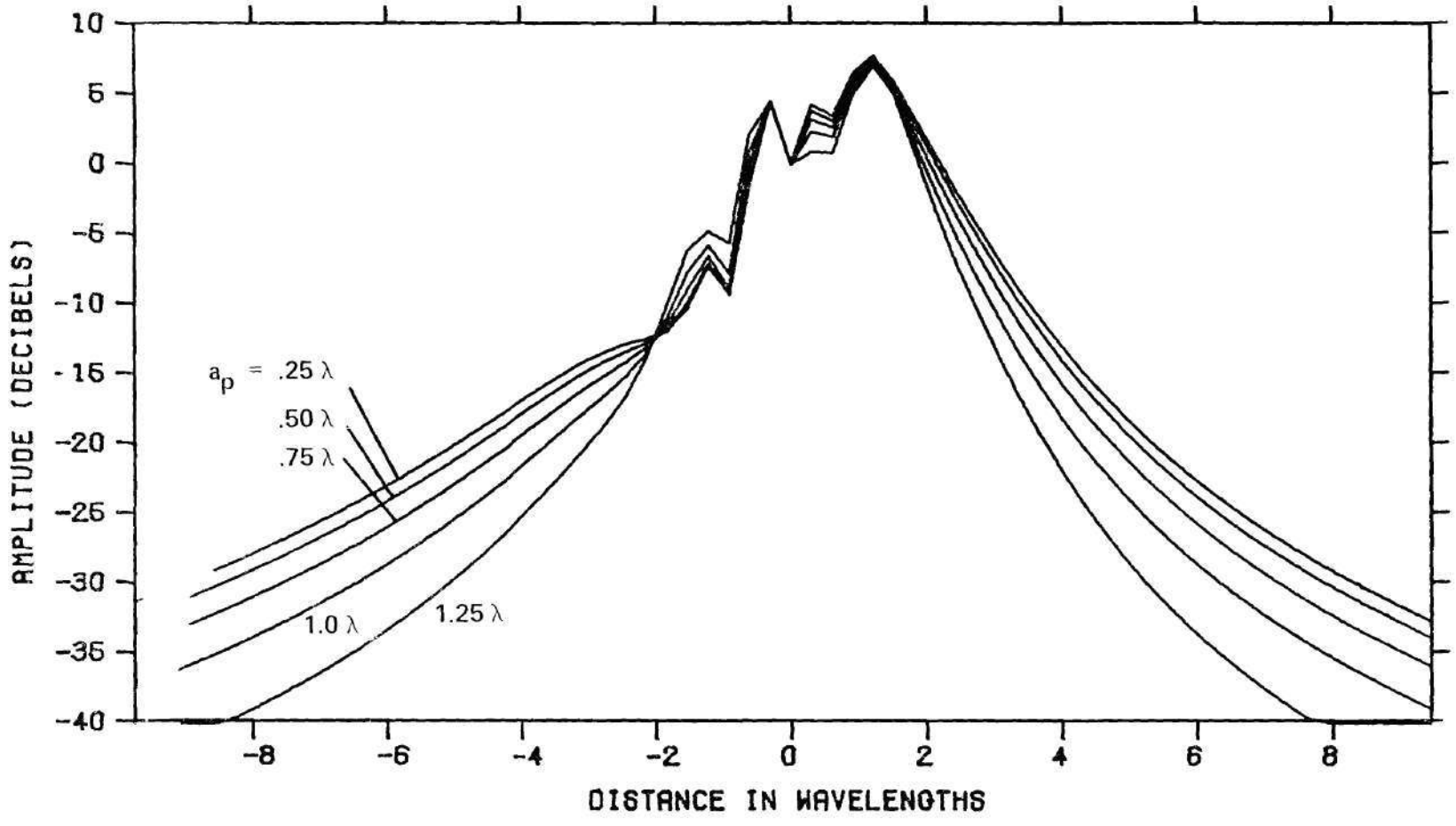

Figure 3-8. Computed Probe Response Versus x at y=0 for Rectangular Probes with b_p = .415λ and Five Values of a_p When Phased Array is Scanned to 45° in Azimuth.

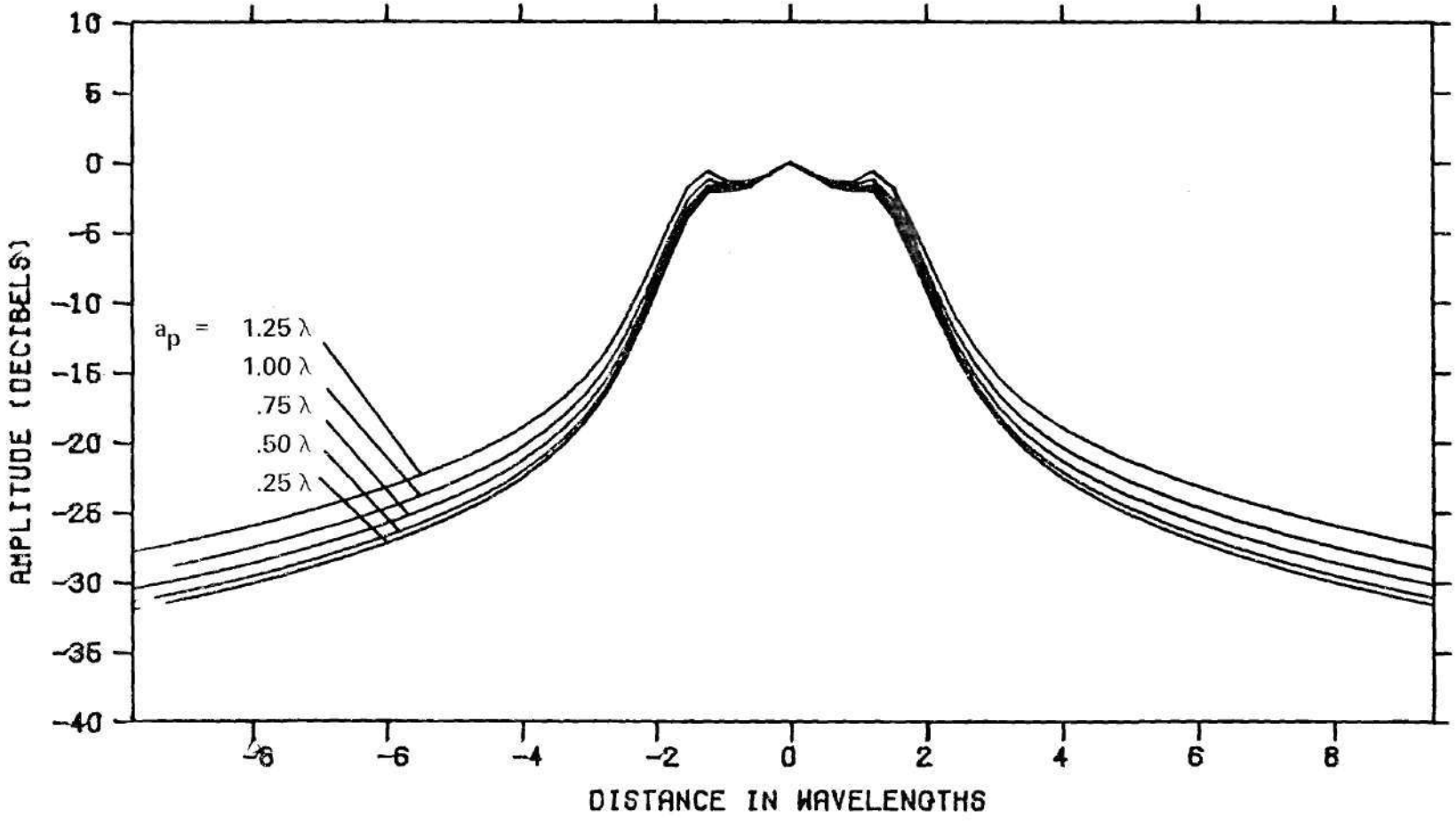

Figure 3-9. Computed Probe Response Versus y at x=0 for Rectangular Probes with b_p = .415λ and Five Values of a_p When Phased Array is Scanned to 45° in Azimuth.

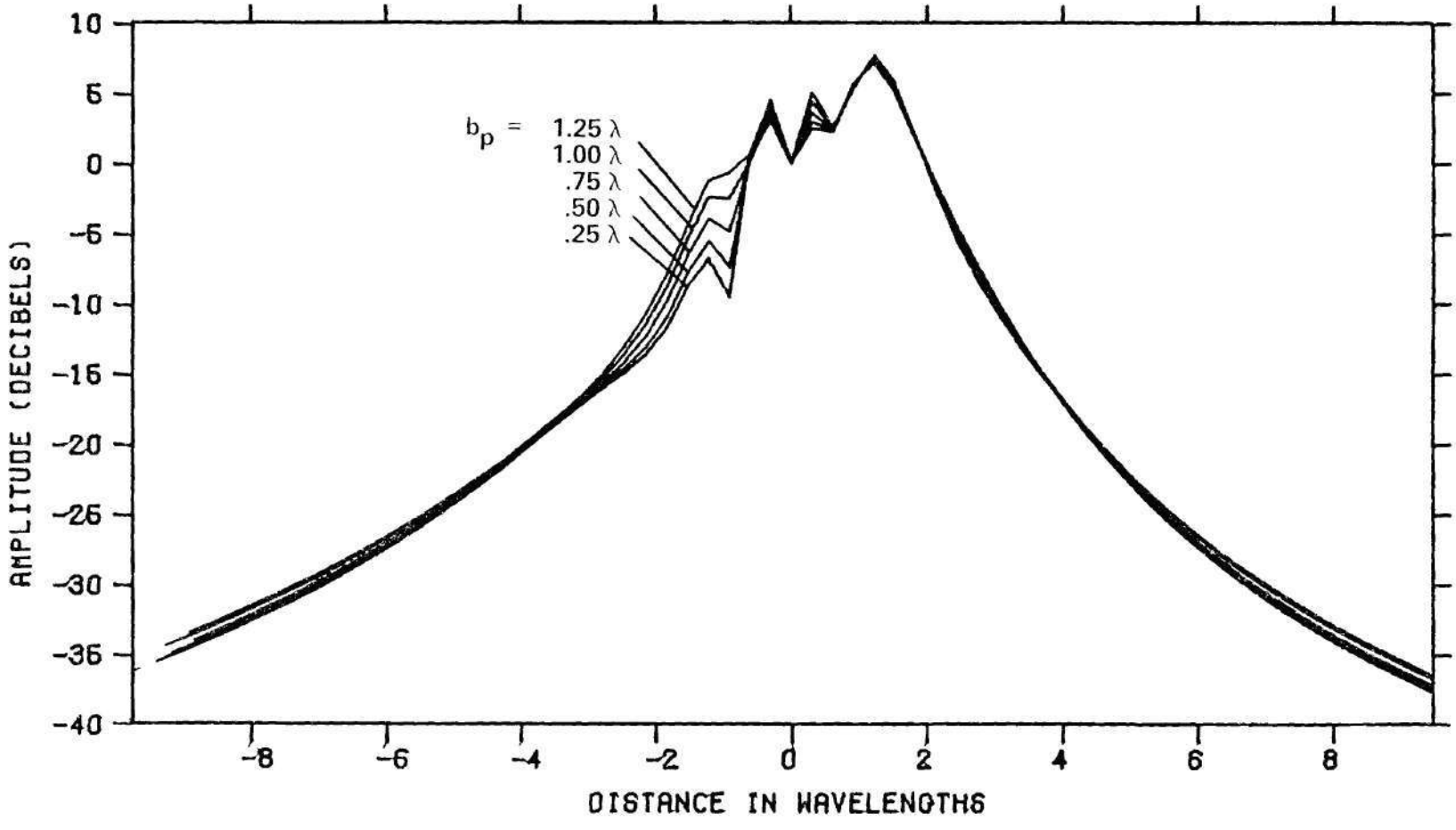

Figure 3-10. Computed Probe Response Versus x at y=0 for Rectangular Probes With a_p = .892λ and Five Values of b_p When Phased Array is Scanned to 45° in Azimuth.

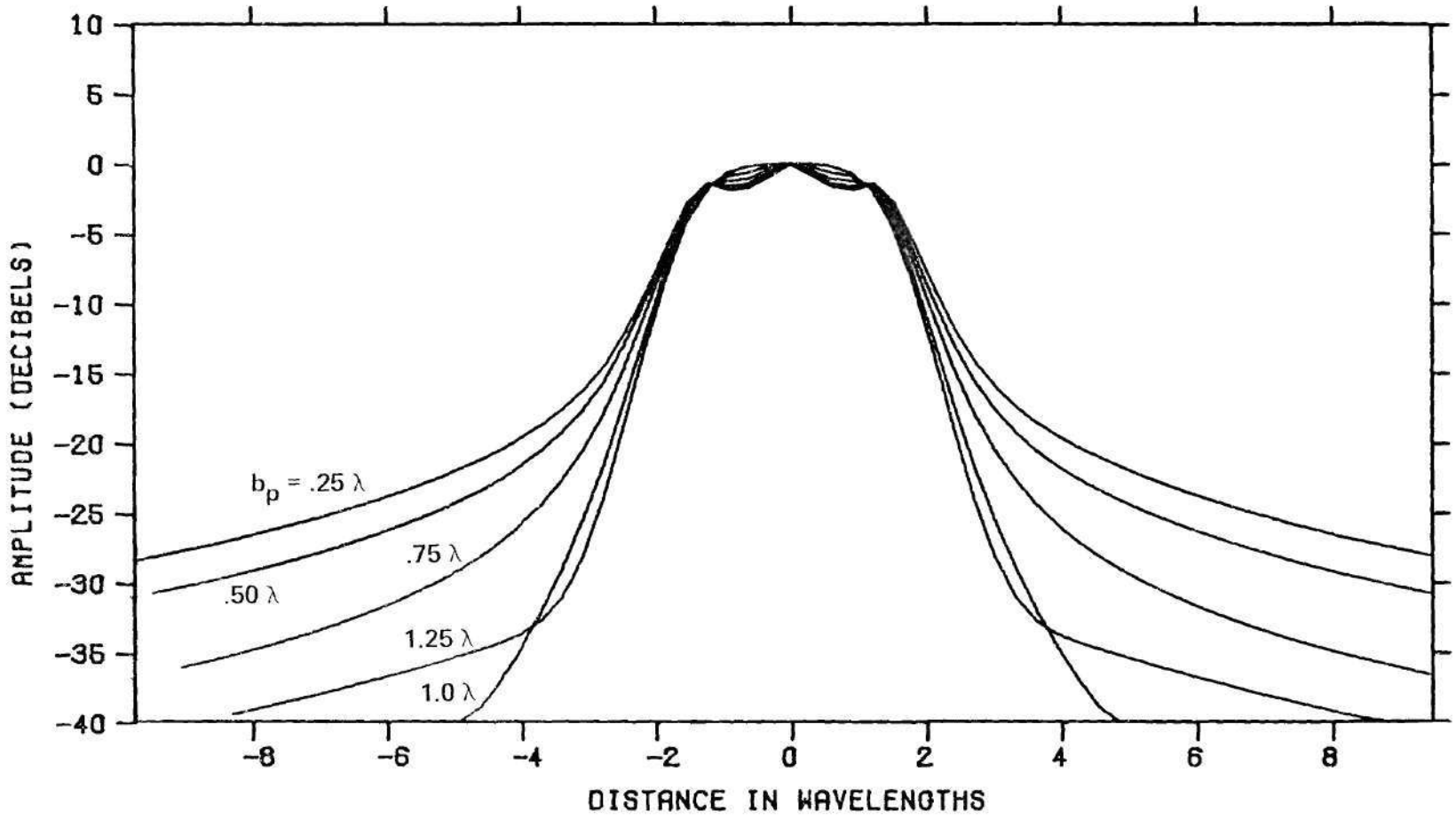

Figure 3-11. Computed Probe Response Versus y at x=0 for Rectangular Probes With a_p = .892λ and Five Values of b_p When Phased Array is Scanned to 45° in Azimuth.

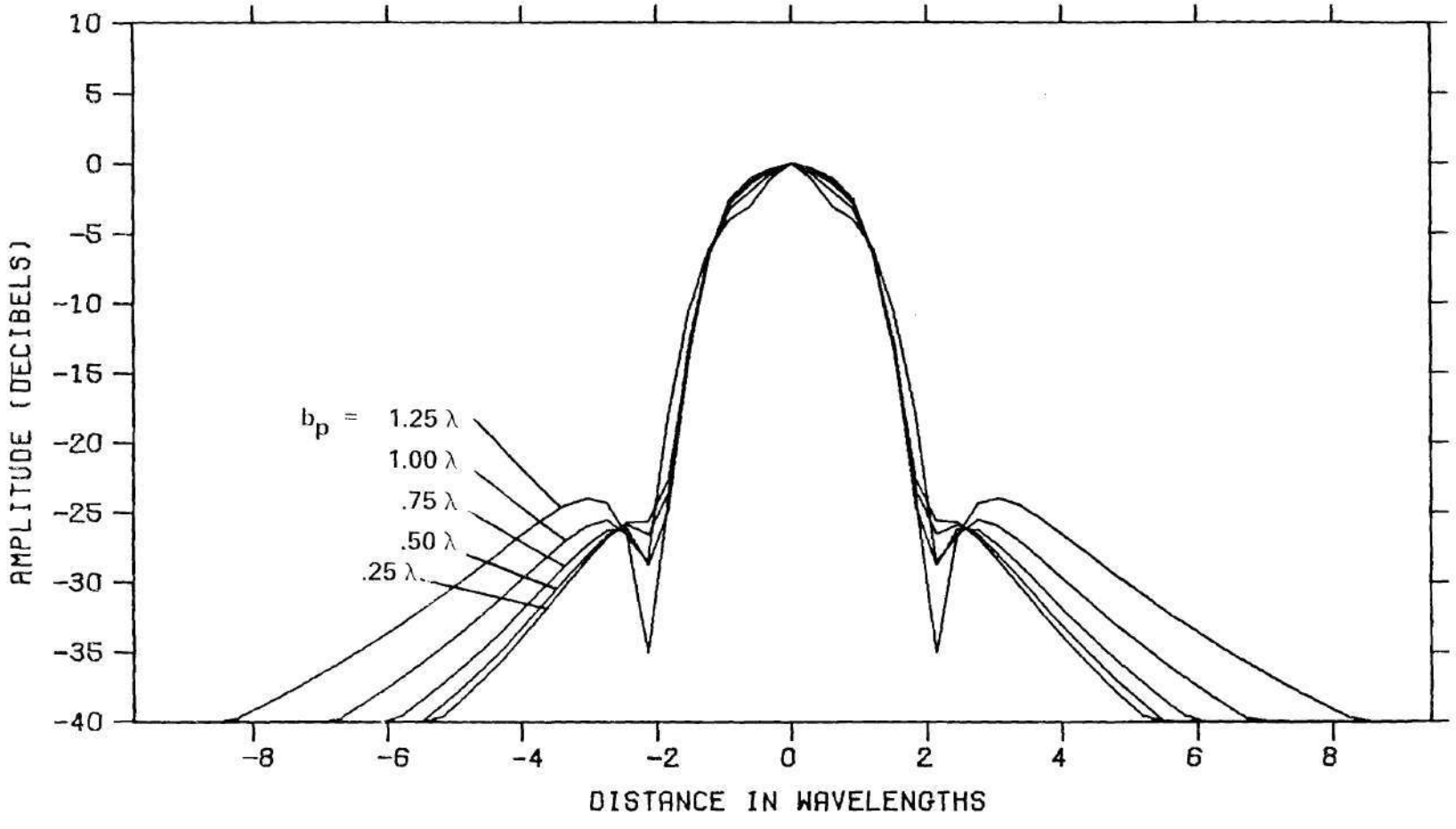

Figure 3-12. Computed Probe Response Versus x at y=0 for Rectangular Probes with a_p = .892λ and Five Values of b_p When Phased Array is Scanned to 45° in Elevation.

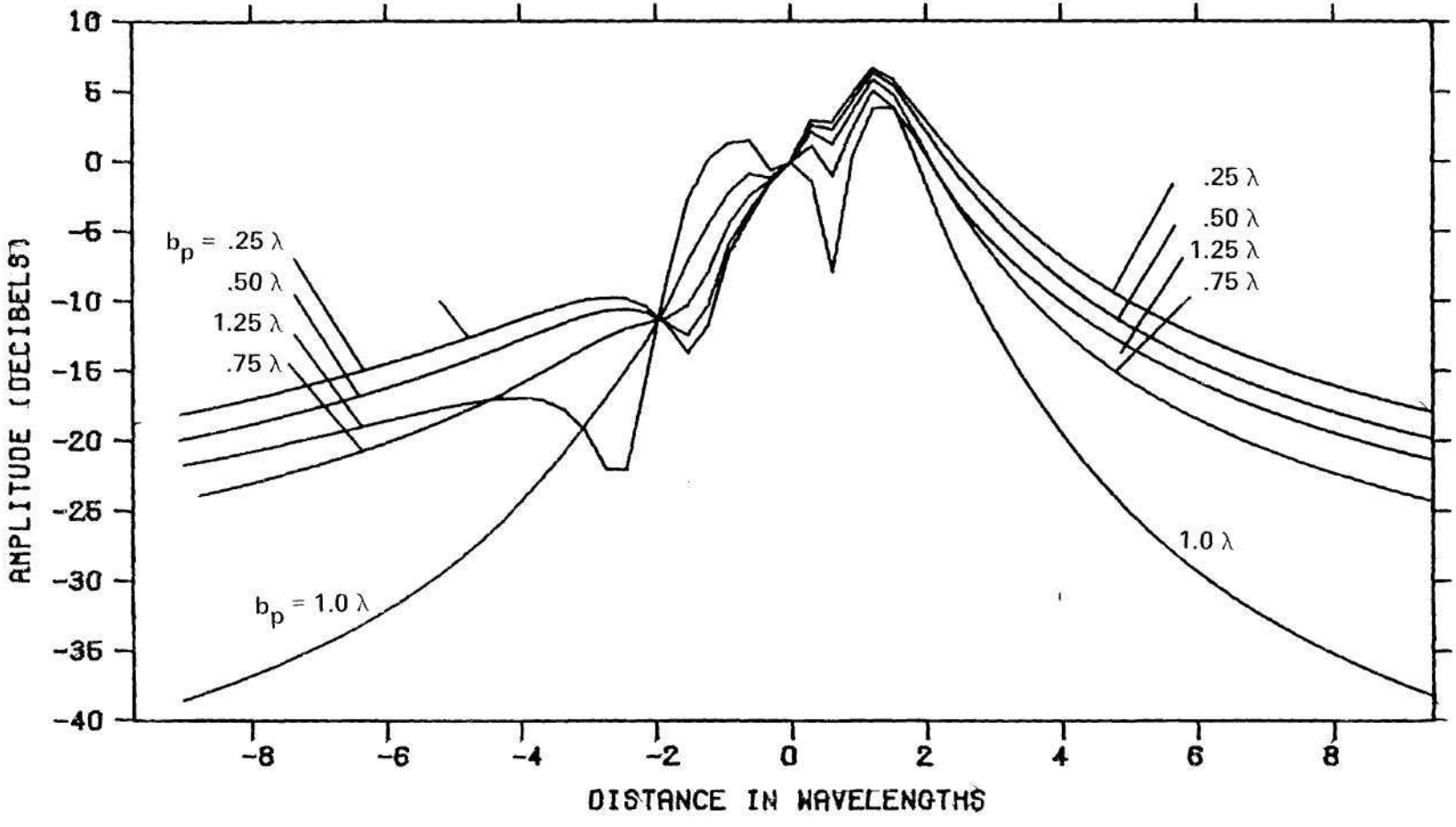

Figure 3-13. Computed Probe Response Versus y at x=0 for Rectangular Probes With a_p = .892λ and Five Values of b_p When Phased Array is Scanned to 45° in Elevation.

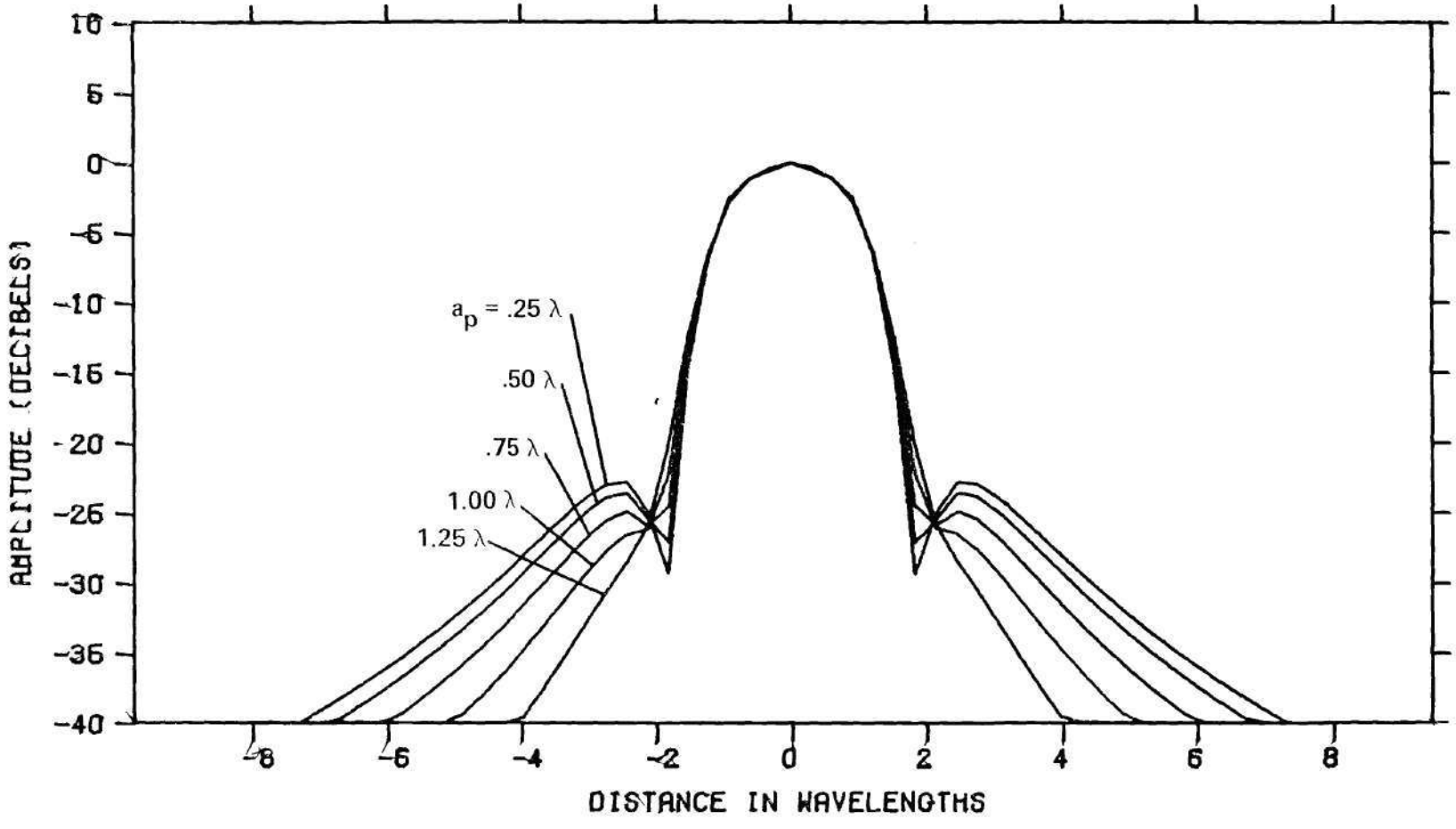

Figure 3-14. Computed Probe Response Versus x at y=0 for Rectangular Probes with b_p = .415λ and Five Values of a_p When Phased Array is Scanned to 45° in Elevation.

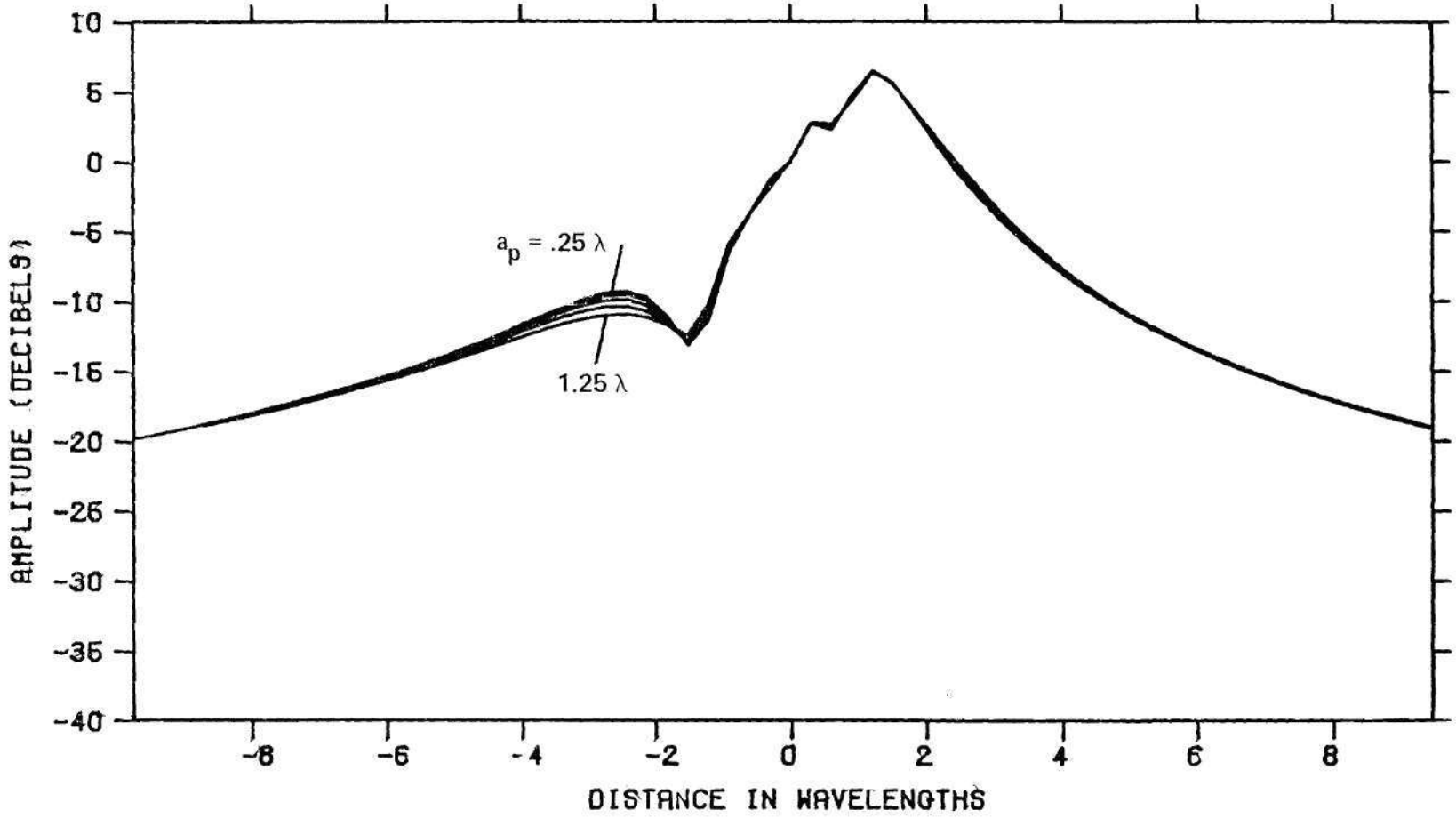

Figure 3-15. Computed Probe Response Versus y at x=0 for Rectangular Probes With b_p = .415λ and Five Values of a_p When Phased Array is Scanned to 45° in Elevation.

The effects of increases in probe aperture dimension a_p at fixed b_p are shown in Figures 3-14 and 3-15. Referring to the former, it is seen that an increased concentration of H-plane response results from increases in a_p. There is no trend reversal at $a_p = 1.0\lambda$. In the E-plane results of Figure 3-15, no significant changes in the response are apparent.

The salient qualitative observations made for the cases of azimuth and elevation scan of the main beam are presented quantitatively in Figures 3-16 through 3-18. For example, Figure 3-16 is a graph of the one-dimensional concentration factor ϵ_x^2 defined by

$$\epsilon_x^2 = 1 - \frac{\int_{-x_{max}}^{x_{max}} |V_1(x,0)|^2 dx}{\int_{-\infty}^{\infty} |V_1(x,o)|^2 dx} \tag{3-74}$$

A similar definition holds for ϵ_y^2 when x=0. The abscissa of the graph is defined by

$$\sin\theta_{max} = \frac{d_m - d_a}{\sqrt{z_o^2 + (d_m - d_a)^2}} \tag{3-75}$$

where the variables are defined on the inset of Figure 3-16 for a test antenna aperture dimension $2d_a$ and a measurement interval dimension $2d_m$. The angle θ_{max} so defined has been put forth as the angular limit beyond which far-field predictions cannot be relied upon for accuracy [16,17].

The graph of Figure 3-16 shows that the concentration of the probe response in the H-plane continues to increase for increases in a_p, even

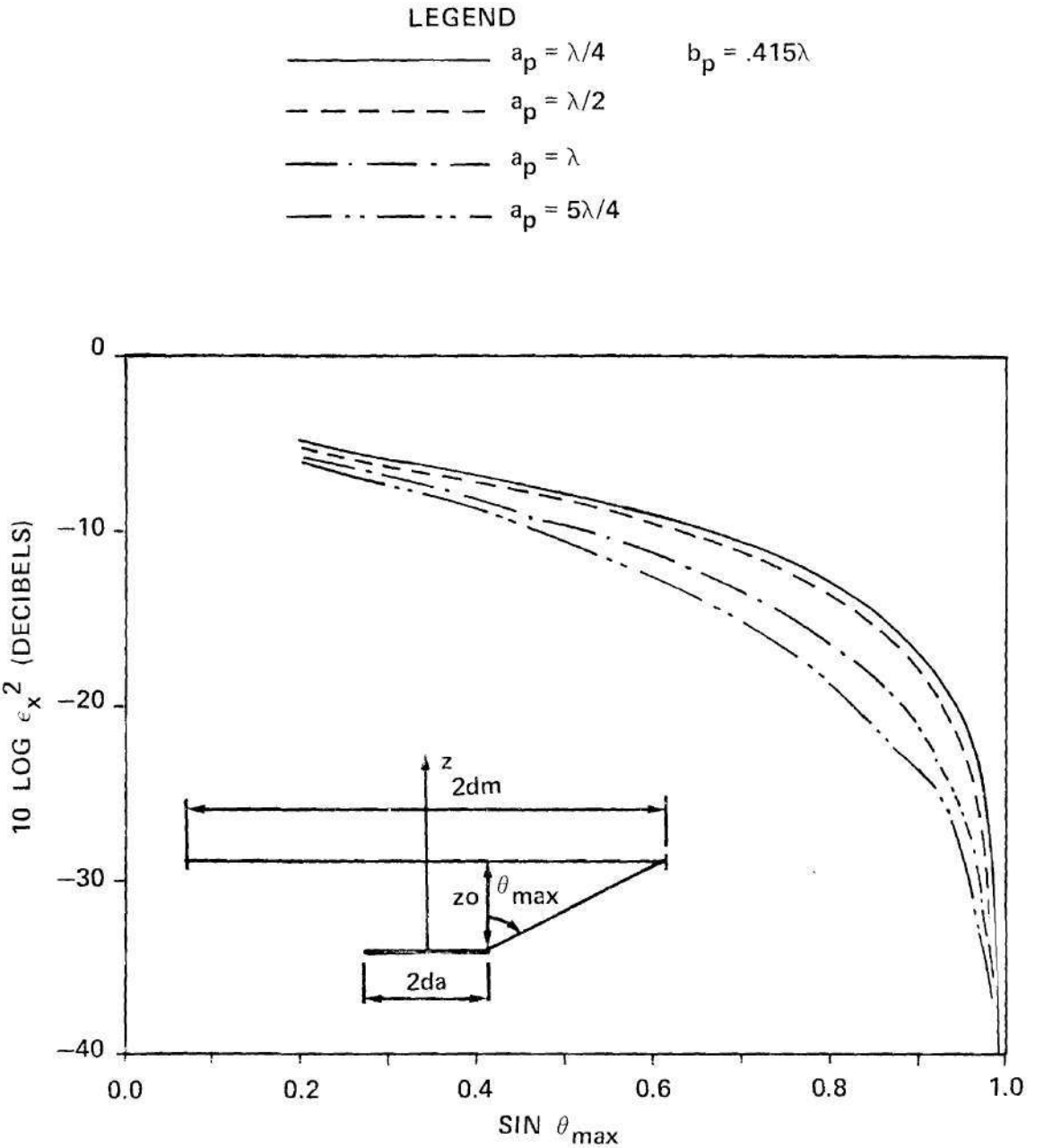

Figure 3-16. Computed Values of Concentration Factor ϵ_x^2 Versus $\sin\theta_{max}$ for Four Values of Probe. Dimension a_p for Case of Main Beam of Phased Array Scanned to 45 Degrees in Azimuth.

beyond the value of $a_p = 1.0\lambda$. This behavior is attributed in some measure to the cosinusoidal x-variation of the probe aperture field as given by Equation (3-24). Such an aperture function and increases in a_p yield a continued decrease in the far-field H-plane beamwidth with the appearance of only miniscule sidelobes for $a_p > 1.0\lambda$.

The significant effects of values of b_p on the concentration factor ϵ_y^2 for the case of elevation scan of the main beam of the test antenna is shown in Figure 3-17. The greatest concentration of probe response is obtained for $b_p = 1.0\lambda$ for all values of θ_{max}. The significant decrease in concentration for $b_p = 1.25\lambda$ is attributed to the approximately uniform excitation of the probe aperture in the y-direction as given in Equation (3-34). Such uniform excitation produces the far-field E-plane response of the form $\sin(ck_y)/k_y$ given explicitly in Equation (3-59). The sidelobes which appear for $b_p > 1.0\lambda$ have significant amplitude and contribute to increasing the near-field probe response at larger angles θ_{max}.

The data in the foregoing figures are presented in Figure 3-18 in a form which accentuates the effects of b_p on the concentration factor ϵ_y^2. Referring to Figure 3-18, it is seen that maximum concentration occurs at values of b_p slightly larger than 1.0λ for the two smaller values of θ_{max} shown. For the largest value of $\theta_{max} = 83$ degrees, $b_p = 1.0\lambda$ produces the most concentrated response of all. This behavior is again attributed to the appearance of sidelobes in the E-plane pattern of the probe such that the nulls in the pattern coincide with the values of θ_{max}. At larger values of b_p, the pattern nulls occur at angles less than θ_{max} such that the sidelobes contribute to increased probe response and, hence,

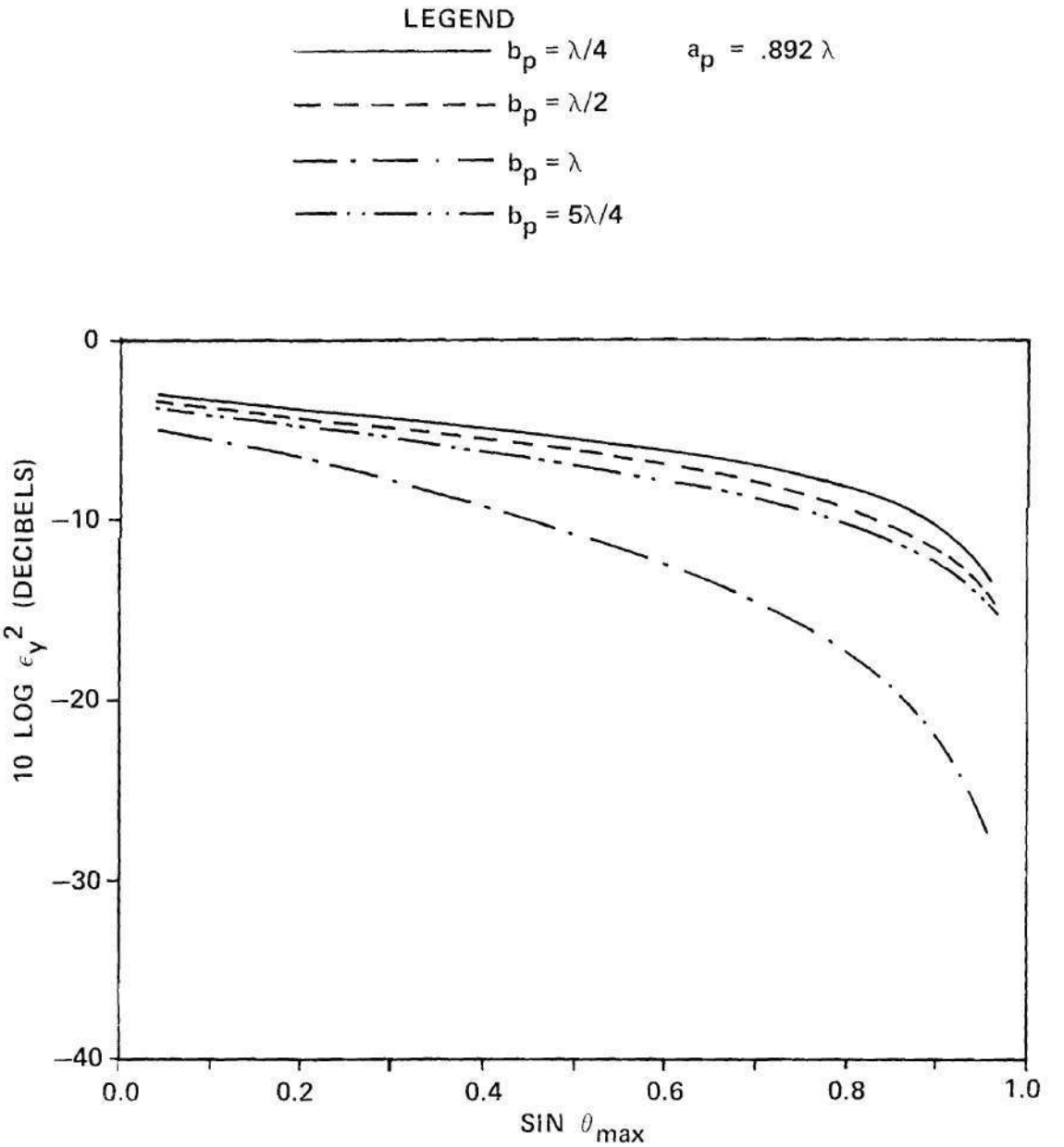

Figure 3-17. Computed Values of Concentration Factor ϵ_x^2 Versus $\sin\theta_{max}$ for Four Values of Probe Dimension b_p for Case of Main Beam of Phased Array Scanned to 45 Degrees in Elevation.

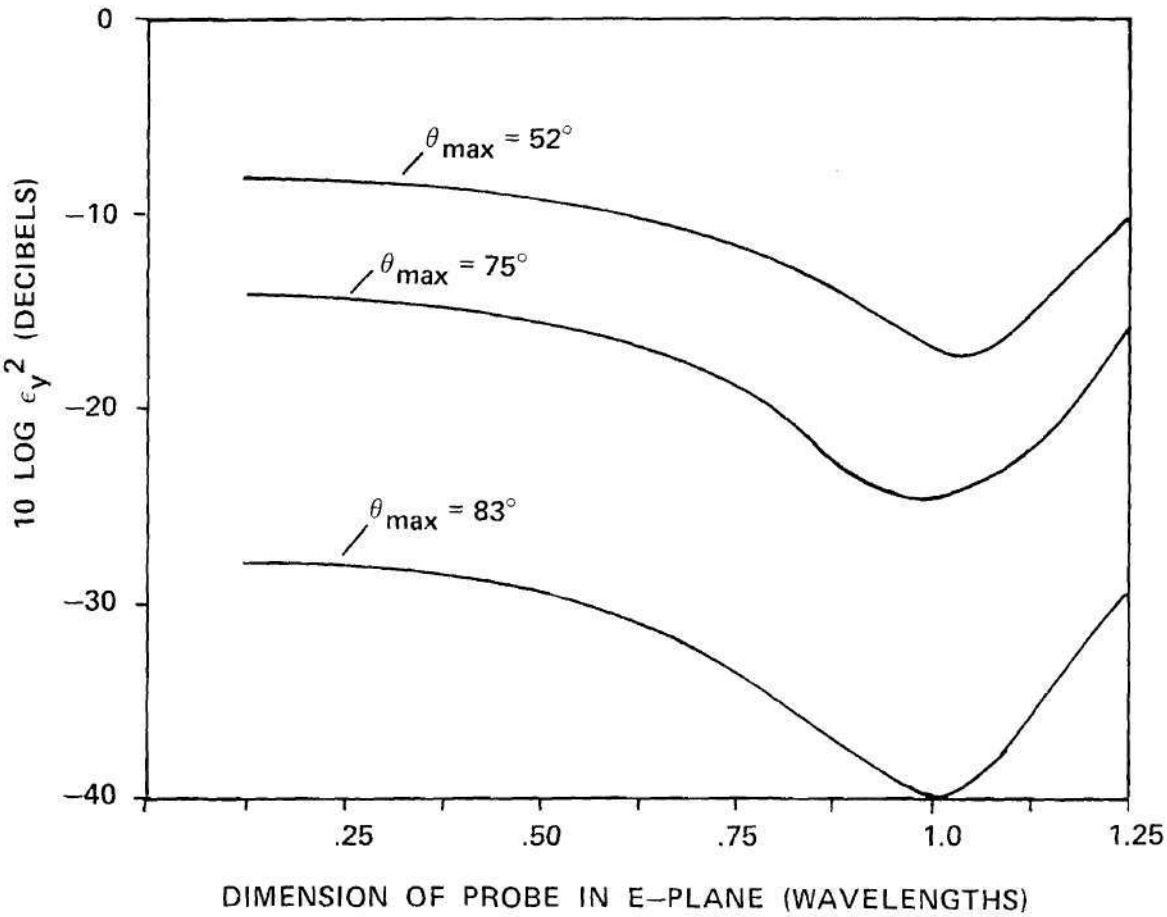

Figure 3-18. Computed Values of Concentration Factor ϵ_x^2 Versus Dimension b_p of Probe Aperture in E-plane for Three Values of θ_{max} When Main Beam of Phased Array is Scanned to 45 Degrees in Elevation.

decreased concentration.

It is concluded from the computer simulation results that the optimum aperture dimensions of the rectangular probe are approximately one wavelength on each side. The design is more sensitive to changes in the E-plane dimension b_p of the probe than to changes in the H-plane dimension a_p. Furthermore, there is a definite maximization of the concentration of response for $b_p \approx 1.0\lambda$. Whereas increases in a_p beyond 1.0λ yield continued increases in concentration in the H-plane, the attendant decreases in concentration in the E-plane suggest that a value of $a_p \approx 1.0\lambda$ also be chosen for this probe dimension as well.

The computed responses of three probe aperture sizes corresponding to those used in the experimental verification are presented in Figures 3-19 through 3-22 for the two cases of main beam locations. The $.23\lambda \times .107\lambda$ ($a_p \times b_p$) aperture corresponds to a dielectric loaded, undersize waveguide probe similar to that described by Richmond and Tice [38]. The $.89\lambda \times .415\lambda$ aperture is that of an open-end RG-49 waveguide probe. The $.89\lambda \times 1.0\lambda$ aperture is that of an E-plane sectoral horn formed by flaring RG-49 waveguide in the b dimension while maintaining $a_p = a_{wg} = .892\lambda$. Examination of these figures shows the real advantage offered by the E-plane horn insofar as concentration of response is concerned. The actual advantages offered by this probe insofar as accuracy in the measured spectra and predicted far fields are concerned are presented in Chapter V following the description of the equipment and procedures used to carry out the experimental work.

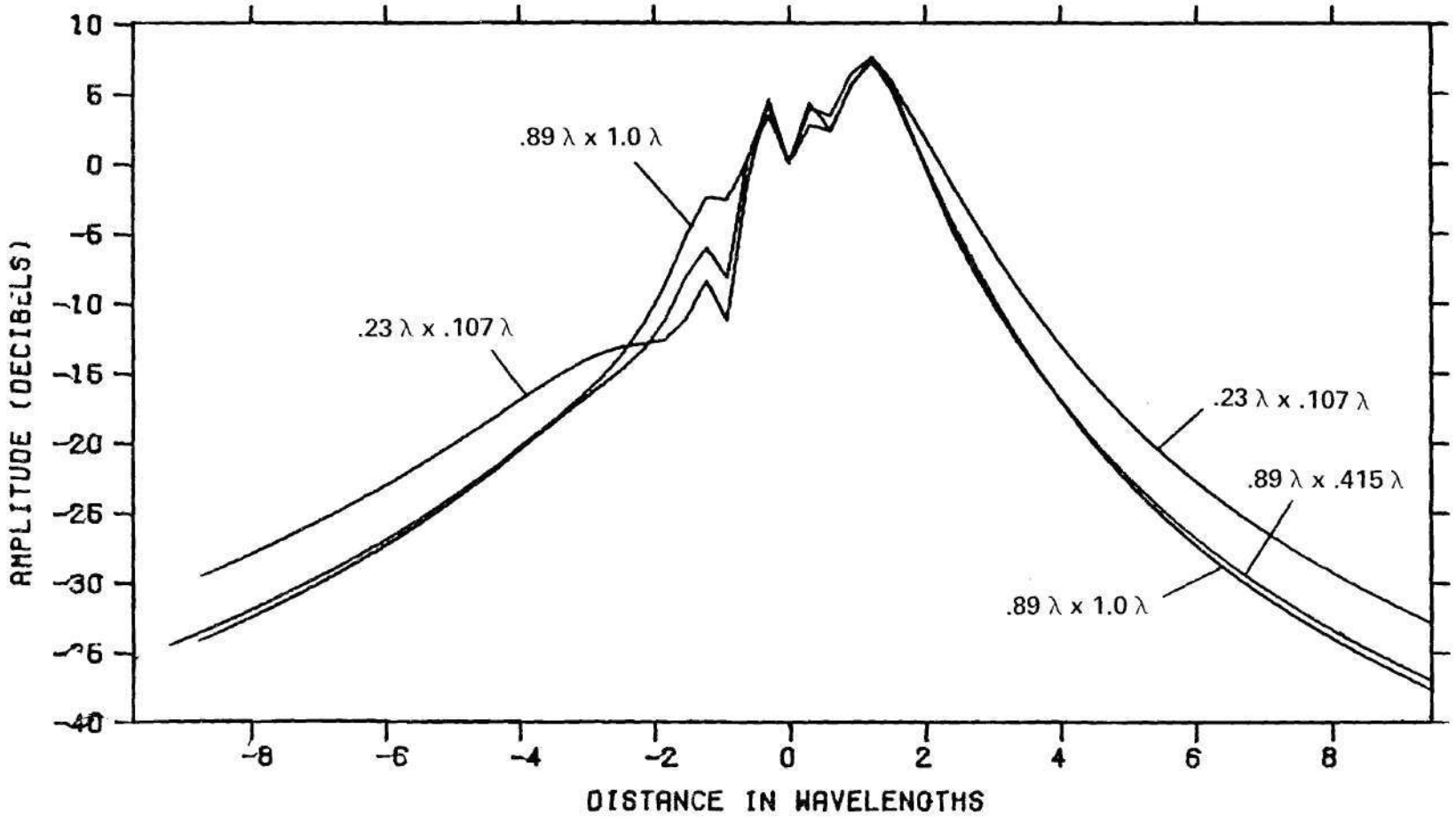

Figure 3-19. Computed Probe Response Versus x at y=0 for Rectangular Probes with Three Aperture Dimensions a_p x b_p When Phased Array is Scanned to 45° in Azimuth.

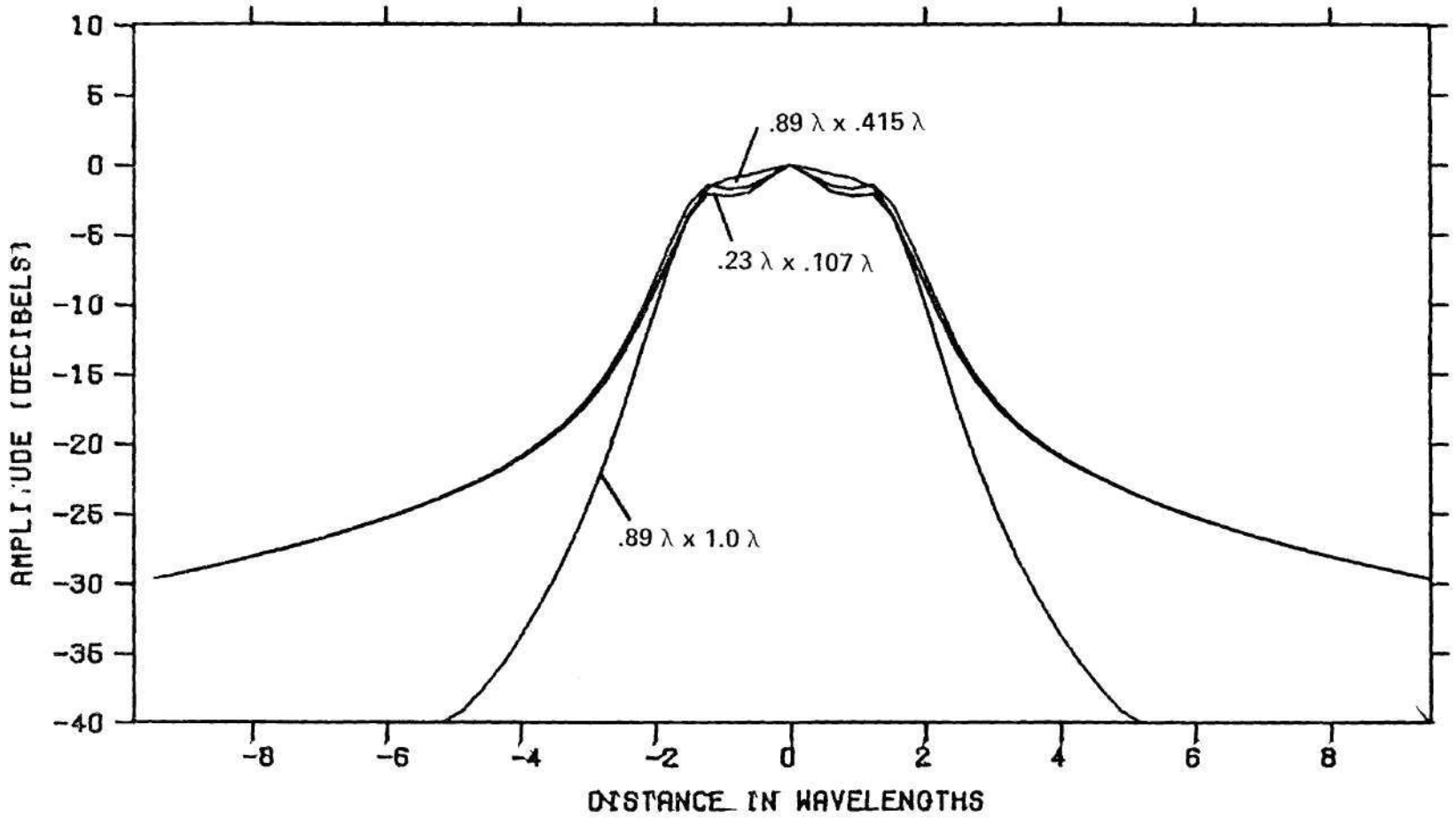

Figure 3-20. Computed Probe Response Versus y at x=0 for Rectangular Probes with Three Aperture Dimensions a_p x b_p When Phased Array is Scanned to 45° in Azimuth.

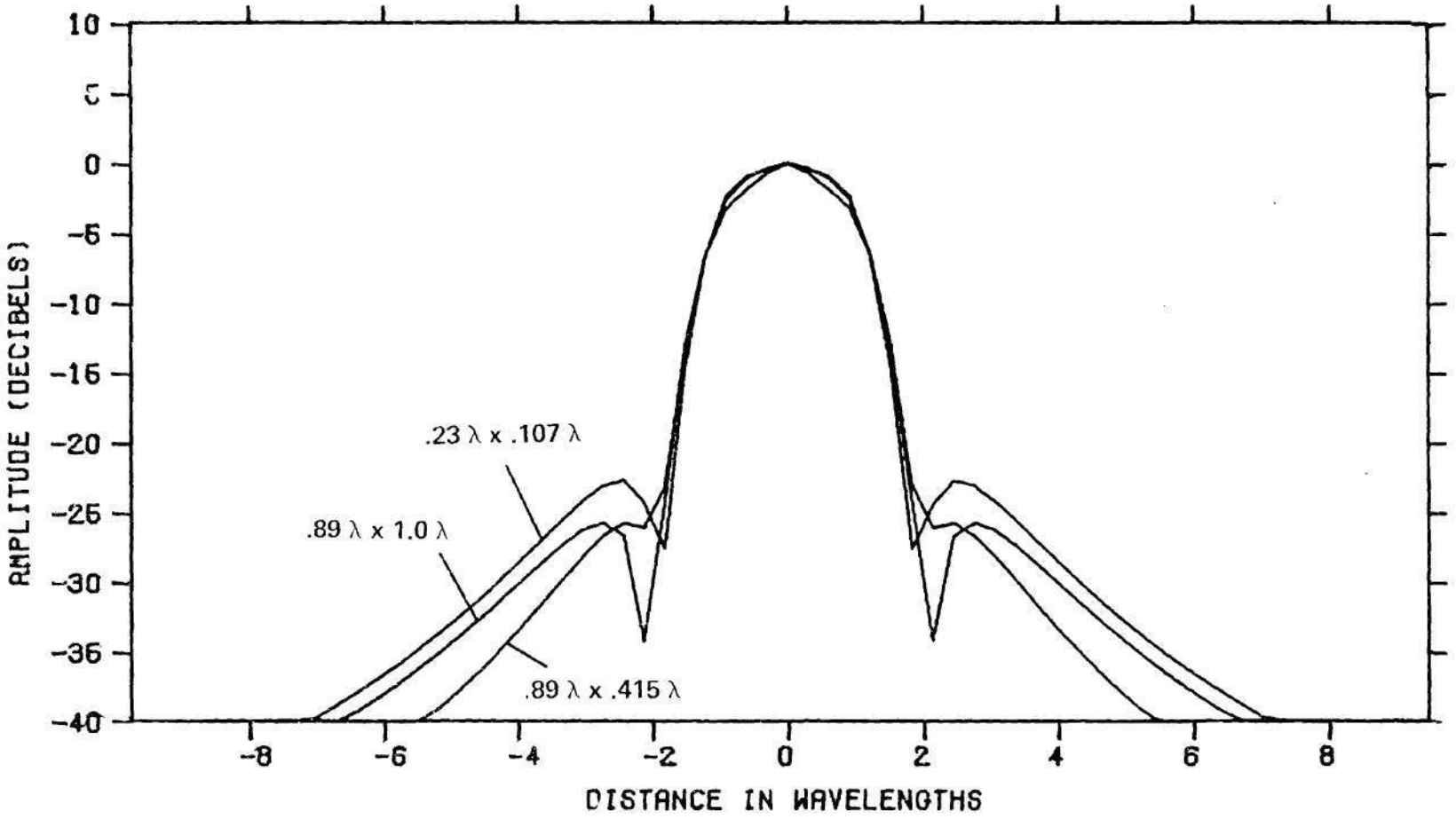

Figure 3-21. Computed Probe Response Versus x at y=0 for Rectangular Probes With Three Aperture Dimensions a_p x b_p When Phased Array is Scanned to 45° in Elevation.

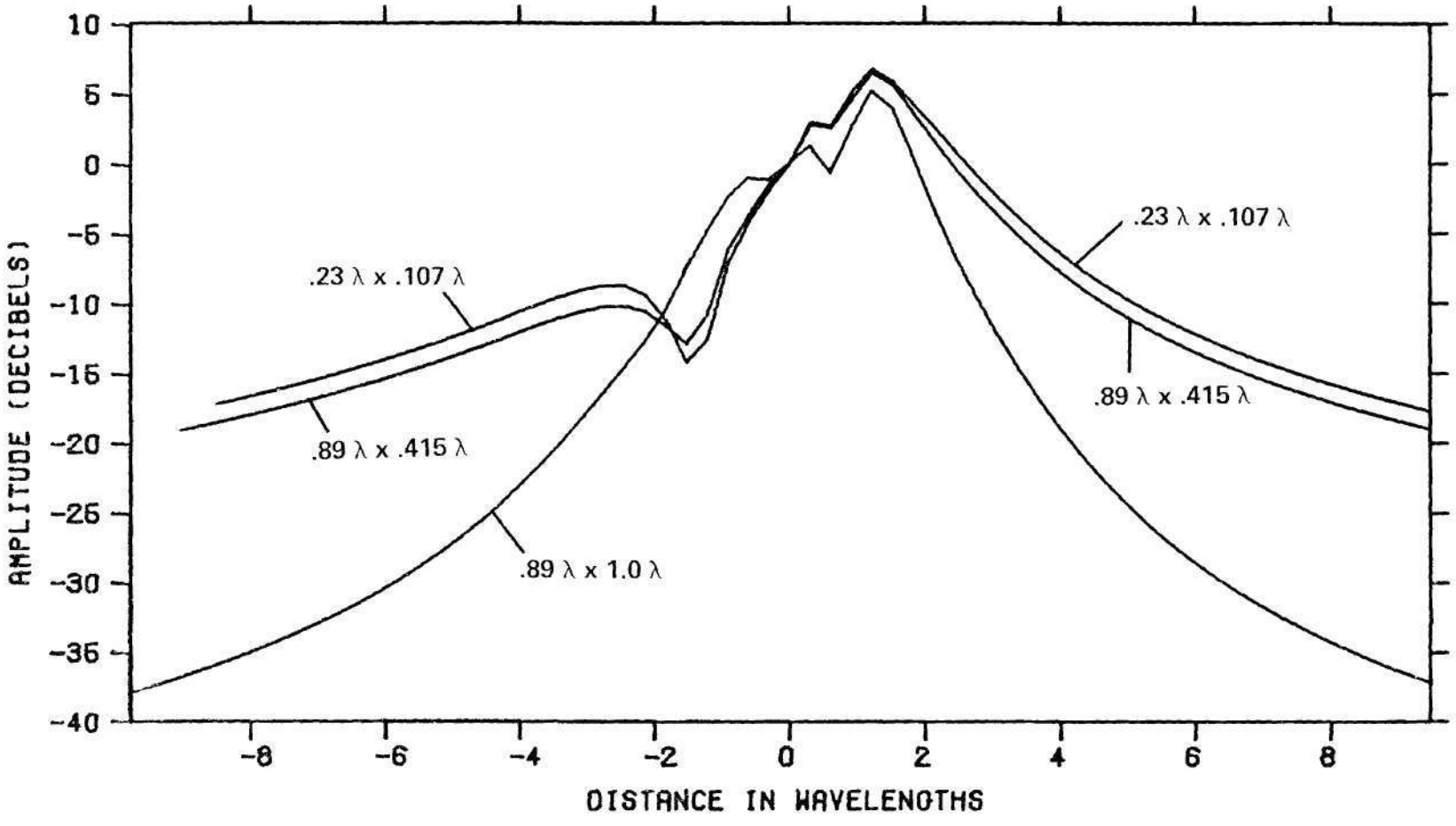

Figure 3-22. Computed Probe Response Versus y at x=0 for Rectangular Probes with Three Aperture Dimensions a_p x b_p When Phased Array is Scanned to 45° in Elevation.

CHAPTER IV

INSTRUMENTATION AND EQUIPMENT

4.1 Introduction

The apparatus used in the experimental verification of the research is described in this chapter. The design of the three probe antennas and positioner used to measure their far fields are described in the first two sections. The phased array test antenna and the automated near-field measurement facility used for both far-field probe measurements and near-field measurements on the test antenna are described in the two succeeding sections.

4.2 The Probe Antennas

The three rectangular probe antennas used in the experimental work are shown in Figure 4-1(a). Each probe consists of a UG-149/u cover flange, a section of RG-49 copper waveguide, and appropriate modifications to form three different aperture sizes. Each probe has an overall length of nine inches for compatibility with the probe positioner and measurement system. The salient dimensions of the probes are presented in Table 4.1.

The three probes were chosen on the basis of expected concentration of near-field response. The undersize waveguide probe had the smallest aperture that could be conveniently fabricated, and was expected to produce the least concentrated response. The open-end waveguide was selected for its simplicity and was expected to produce a moderately concentrated response. The E-plane horn probe was designed using the results

of the computer simulation and was expected to produce the most concentrated response; i.e., the optimum rectangular probe antenna.

The undersize waveguide probe was designed to operate over the same frequency band as standard RG-49 waveguide. The Emerson and Cuming Stycast^{R} HiK dielectric material used in the undersize section possesses a dielectric constant of $\epsilon_r = 15.0$. The dimensions a_p, b_p scale according to the following relations to produce the dimensions shown in Table 4.1:

$$a_p = \frac{a_{wg}}{\sqrt{\epsilon_r}} \tag{4-1}$$

$$b_p = \frac{b_{wg}}{\sqrt{\epsilon_r}} \tag{4-2}$$

The length of the transition section was scaled from the dimension used for the X-band probe described by Richmond and Tice [38]. The Stycast dielectric was uniformly tapered in both dimensions over the length of the transition section. The transition section was later filled with melted paraffin to fill all air pockets, seal the snug-fitting Stycast in place, and to improve coupling from the RG-49 waveguide to the dielectric-loaded waveguide section.

The open-end waveguide probe consists of a section of standard RG-49 waveguide, soft-soldered into the UG-149/u cover flange. The aperture end of the probe was milled square; i.e., no beveled edges were used.

The E-plane horn probe was fabricated from a section of RG-49

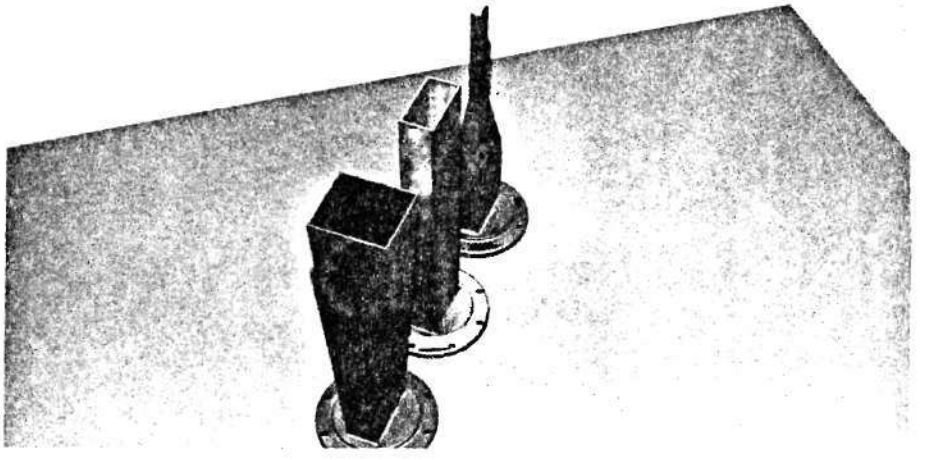

(a) Undersize Waveguide, Open-End Waveguide, and E-Plane Horn Probes.

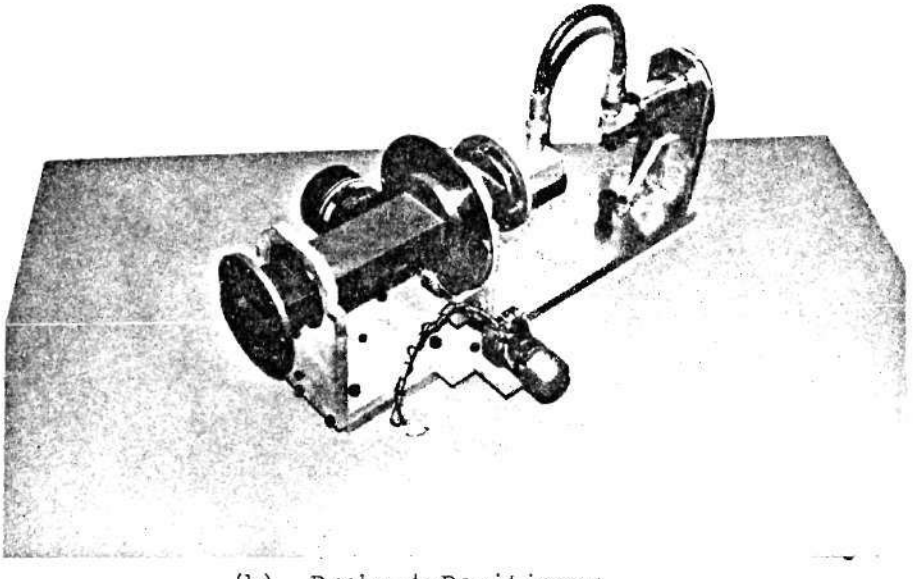

(b) Probe ϕ-Positioner

Figure 4-1. Experimental Probe Antennas and Positioner.

Table 4.1. Physical Characteristics of Rectangular Probes.

NAME	a_p[1]	b_p	ℓ	ϵ_r	a_{wg}	b_{wg}
Undersize Waveguide	.483	.225	3.50[2]	15.00	1.8720	.8720
Open-End Waveguide	1.872	.872	∞	1.00		
E-Plane Horn	1.872	2.05	8.00	1.00		

1. Inside dimensions; waveguide wall thickness = .064" in all cases.
2. Length of undersize waveguide section; length of tapered transition section = 2.50"; length of RG-49 section = 3.00".

waveguide by removing the sidewalls, flaring the top and bottom walls, and soft-soldering two new sidewall pieces into place to produce the desired flare. The b_p dimension of the horn was chosen to be approximately one wavelength at the expected operating frequency of 5.75 GHz in accordance with the results of the computer simulation. The a_p dimension was selected to be that of the waveguide because of simplicity of fabrication and insensitivity of the concentration of response to this parameter.

4.3 Probe Positioner

The positioner used to measure the far fields of the three probe antennas is shown in Figure 4-2. This two-axis positioner was used to accurately position the probe in the spherical coordinate system of Figure 4-3. The ϕ-positioner, also shown in Figure 4-1(b), rotates about a horizontal axis to select a specified ϕ = constant plane. Once the ϕ plane is selected, the entire upper assembly in Figure 4-2 is rotated about the vertical axis of the Scientific-Atlanta Model 5303-1-R azimuth-over-elevation positioner. This rotation provides the required variation of zero to 90° in the polar angle θ of Figure 4-3.

The probe antenna was used as a transmitting antenna with microwave power being provided by RG-9B coaxial cable through two Scientific-Atlanta Model 10-1 (dc to 12.4 GHz) coaxial rotary joints. A receiving antenna was located approximately six feet away on level with the probe antenna as shown in Figure 4-4. This antenna, a small E-plane horn, was also equipped with a rotary joint so that rotation through 90 degrees could be done to measure both V_θ and V_ϕ indicated in Figure 4-3 while maintaining the relative phase reference in the process. As evident in

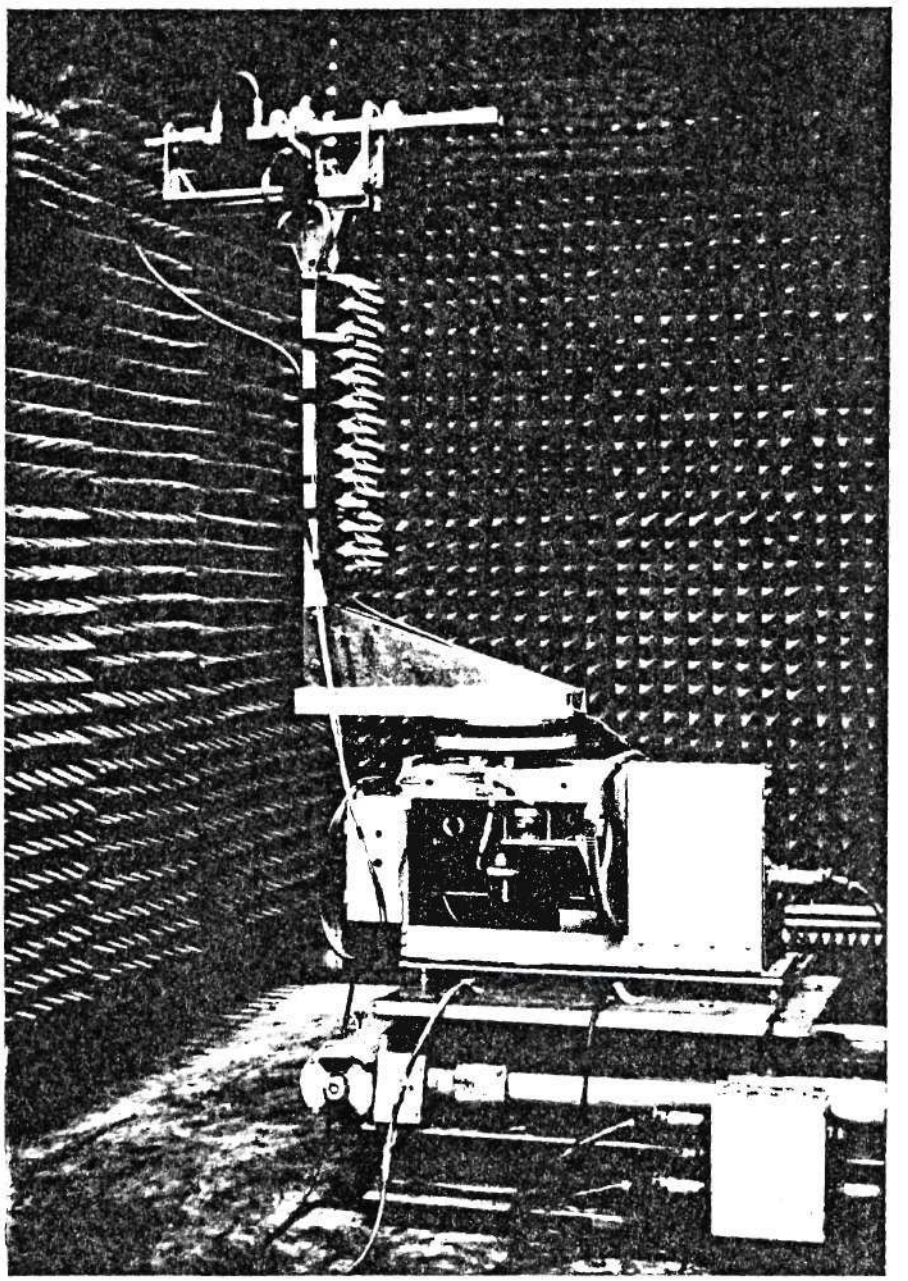

Figure 4-2. Automated Probe Positioner.

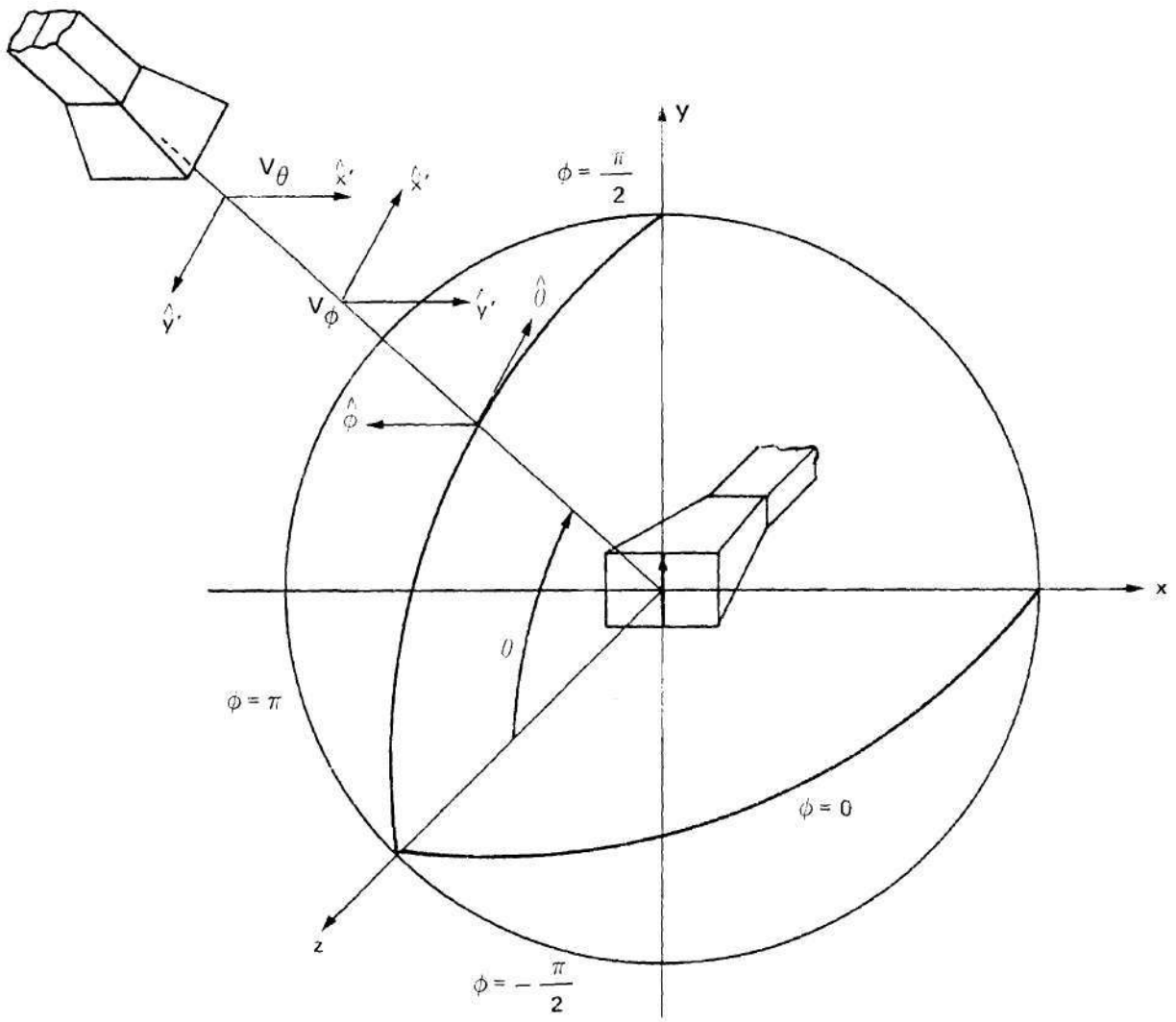

Figure 4-3. Coordinate System Used For Measuring Far Fields of Probe Antennas Showing Two Orthogonal Orientations of the Measuring Antenna to Produce Received Voltages V_θ and V_ϕ.

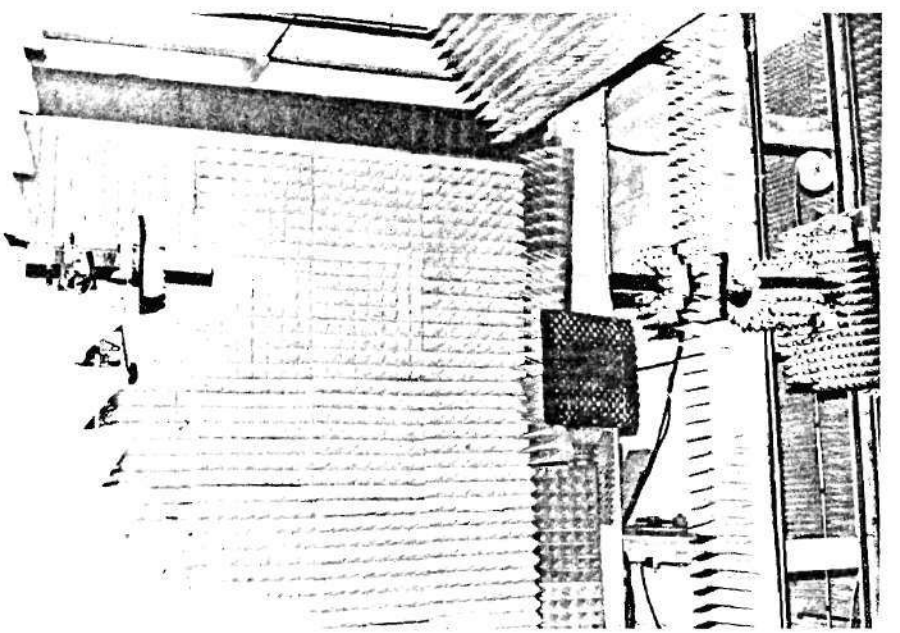

Figure 4-4. Probe Positioner (Left) and XY Positioner (Right).

Figure 4-4, the xy probe positioner was held stationary and used as the receiving antenna.

The ϕ-positioner is an original design and was fabricated in the Main Machine Shop at Georgia Tech. It consists of a 10.0-inch section of RG-49 waveguide onto which two brass bearing surfaces have been soldered and accurately turned about the centered longitudinal axis of the waveguide. Two Kaydon KA-25ARO Reli-Slim^{R} ball bearings are mounted snugly on the bearing surfaces, along with a Pic #Q1-13, 64 pitch, 5.625-inch pitch diameter worm wheel. Cover flanges (UG-149/u) were installed on each end of the waveguide section, and the complete assembly mounted in the upright bearing blocks as shown in Figure 4-1(b). The worm wheel meshes with a Pic #Q2-3, 64 pitch worm gear such that one revolution of the smaller worm gear produces 1° rotation of the worm wheel and waveguide assembly. A waveguide-to-coaxial adapter UG-149/NF and short length of RG-9B coaxial cable are used to make the microwave connection to the coaxial rotary joint at the rear of the positioner. (The rotary joint is necessary to maintain phase reference when the waveguide assembly rotates.) One-half inch aluminum plate was used for all horizontal base pieces, and 3/8-inch aluminum plate was used for vertical pieces to ensure a rigid structure with the least weight.

The ϕ-positioner was equipped for automatic operation by installing a small 27 vdc permanent magnet motor (Delco 5069230, 145 rpm) on one end of the 1/4-inch shaft of the worm gear. On the other end of the common shaft, a Renco Model 25LE-6/4 IN, Option 5D1-S, optical encoder was mounted. Oldham couplers, Pic #T7-3, were used to rigidly couple the

motor and encoder to the shaft while allowing for slight misalignments of up to one degree. The output of the encoder consists of two TTL-compatible signals in quadrature. Each channel produces one hundred pulses for each revolution of the encoder shaft. Hence, the resolution provided on the angular location of the waveguide assembly was 0.01 degree.

The θ-positioner consisted of the Scientific-Atlanta 5303-1-R azimuth positioner and L-shaped boom shown in Figure 4-2. The boom was made from 2" x 2" x .125" square aluminum tube and 1/4-inch aluminum plate. It is fastened to the azimuth turntable by three 3/8" steel bolts which are also used to align the boom with respect to the axis of rotation of the azimuth turntable. The complete positioner is secured to a one-inch steel baseplate of the z-positioner by four 3/8" steel bolts which are also used to level the positioner. The ϕ-positioner is mounted on top of the boom as shown in Figure 4-2. Provisions are made for small adjustments of the positioner with respect to the boom so that the ϕ-positioner with probe can be leveled and so that the probe can be accurately located with respect to the vertical axis of rotation.

The Scientific-Atlanta positioner was modified in two ways to facilitate automatic operation of the complete positioner. First, the standard synchro transmitters were removed from the azimuth positioner, and a Renco optical encoder was installed. Pic gears G26-36 and G24-216 were installed to give a turns ratio which yielded ten pulses per degree of rotation of the azimuth turntable; i.e., 0.1 degree resolution in θ. The second modification consisted of disconnecting the elevation drive motor of the positioner and connecting the elevation motor armature

voltage through a voltage-dropping rhoestat to the 27 vdc motor on the ϕ-positioner. In this way, the standard Scientific-Atlanta Model 4112 Positioner Control Unit was used to control the θ- and ϕ-positioner motors. This control unit is also used to control the xy positioner motors as seen in the next section.

4.4 Automated Measurement Facility

A block diagram of the automated measurement facility is shown in Figure 4-5. This facility is located in the Electronics Research Building at Georgia Tech. Its function is to provide automatic, computer-controlled probe positioning, spatial sampling, and data recording of the microwave signal received by the xy probe. The same facility may be used for far-field probe measurements and for near-field measurements on a stationary test antenna. A list of the commercial equipment referred to in the block diagram is presented in Table 4.2.

A 2K43 klystron is used as a stable microwave power source. To further increase the frequency (and phase) stablity, a feedback control system consisting of a microwave stabilizer, harmonic generator with crystal oscillator input, and klystron power supply is used. A portion of the klystron signal is mixed with the output of the harmonic generator which consists of a "comb" of frequencies spaced 30 MHz apart over the microwave frequency band of interest. The klystron is manually tuned until its output frequency coincides with one of the comb frequencies. The 30-MHz difference frequency at the output of the crystal mixer is then detected by the narrow-band, 30 MHz IF amplifier of the stabilizer. Any subsequent drift in the frequency of the klystron output is detected by the stabilizer and corrected via control of the klystron reflector

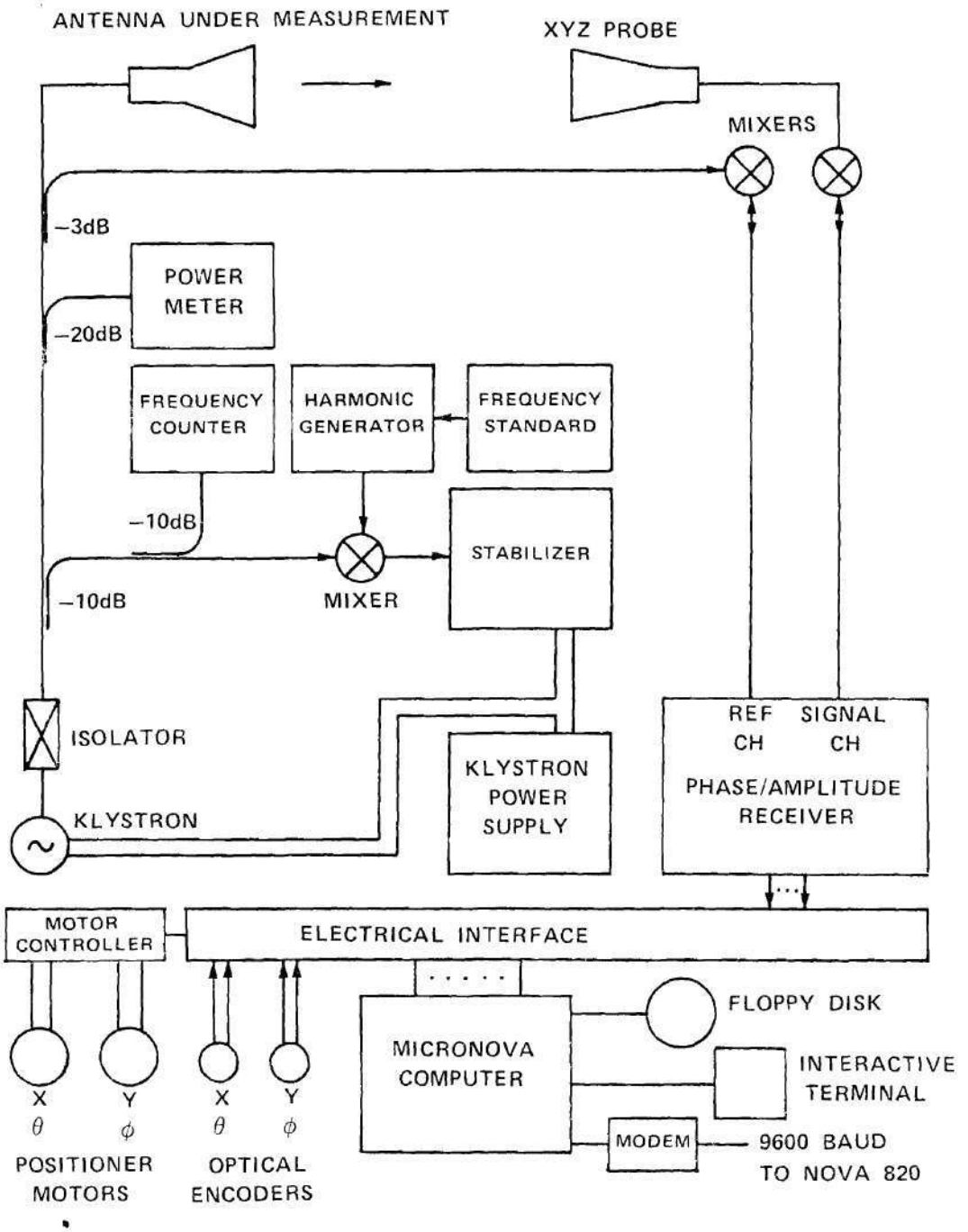

Figure 4-5. Block Diagram of Instrumentation Used to Measure Far Fields of Probes and Near Fields of Test Antenna.

Table 4-2. Commercial Equipment Used in Experiment

Data General MicroNova with 6038 Diskette Drive
Gandalf LDS 120 Modem
Beehive CRT Terminal w/Graphics Expansion Module
Scientific-Atlanta Model 5303-1-R Positioner
Scientific-Atlanta XYZ Positioner, 100" x 100"
Scientific-Atlanta Positioner Control Unit Model 4112
Scientific-Atlanta Series 1750 Phase/Amplitude Receiver
Hewlett-Packard 431B Power Meter w/Thermistor 478A
Hewlett-Packard 537A Wave Meter
Hewlett-Packard 5245L Frequency Counter w/5257A Transfer Oscillator
Hewlett-Packard 105A Quartz Oscillator
Varian 2K43 Klystron Microwave Tube
Narda 438 Klystron Power Supply
Microwave Systems PLM-1x5/100 Harmonic Generator
Micro-Now Model 211-A1 Frequency Stabilizer
Miscellaneous: Coaxial couplers, isolator, cooling fan, crystal mixers, RG-214 coaxial cable, electrical interfaces

voltage; i.e., the klystron is phased locked to the stable reference frequency provided by a quartz crystal frequency standard. A frequency counter is used to give a visual indication of the frequency. A power meter is used to monitor the output power of the klystron, particularly during the tuning process.

The output of the klystron is fed to the antenna under test as shown in the block diagram of Figure 4-5. Power transmitted by the antenna is received by the xy probe antenna. A portion of the transmitted signal is mixed with the local oscillator of the reference channel of the phase/amplitude receiver. Another crystal mixer is located close to the xy probe where mixing with the local oscillator frequency of the signal channel takes place. The receiver continuously measures the amplitude (55 dB dynamic range) and phase (±0.2°) of the signal in the signal channel with respect to that in the reference channel and provides electrical outputs to the computer interface.

The microcomputer controls the acquisition and recording of data. The interactive terminal is used to enter measurement parameters such as number of samples, sampling distance, starting point, etc. Once started, the program controls the probe position via the electrical interface and motor controller. As the positioner motors turn, the optical encoders provide pulses to up/down counters in the interface which maintain position information on two axes. As the probe reaches a position corresponding to a sample point, the program causes the output of the receiver to be sampled and fed into the computer. Periodically, the computer records the sampled data on a FD32-1000 diskette via the 6038 diskette drive. When all data have been recorded, they can be transferred

from the diskette to another computer for processing via the 9600 baud modem shown.

The xy positioner shown in Figure 4-4 provides for precise positioning of the xy probe to within .005" over a 100" x 100" planar surface with a maximum (z) normal deviation of ±.025". Optical encoders installed on the positioner provide relative positioning information to the electrical interface with a resolution of .005". Direct current, separately excited motors provide a maximum traverse rate of 10 inches/second in either the horizontal (x) or vertical (y) direction. A typical traverse rate during measurements is 2.5 inches/second.

An arrangement of constant-length arms and coaxial rotary joints is used to prevent phase changes that would otherwise occur from flexing of the microwave coaxial cables. The crystal mixer for the signal channel is mounted on the moveable probe fixture so that only the difference frequency derived from the test frequency and the local oscillator need be passed unaffected through the rotary joints.

Automation of the probe $\theta\phi$-positioner was accomplished simply by disconnecting the xy motors and encoders and connecting the $\theta\phi$ devices in their stead. Sampling distances in θ and ϕ were entered into the program using equivalent x and y parameters, where each pulse from the x or y encoder corresponds to .005", each pulse from the θ encoder equals 0.1°, and each pulse from the ϕ encoder equals .01°. The parameter values used in the program for collecting probe data over a hemisphere are shown in Table 4-3.

Table 4-3. Program Input Values Used to Collect Probe Data

Starting $x(\theta)$:	- 4.64" (-92.8°)
$\Delta x(\Delta\theta)$:	.145" (2.9°)
Number of Points:	64
Error Tolerance:	.01" (.2°)
Stopping $x(\theta)$:	4.495" (89.9°)
Starting $y(\phi)$:	-45.0" (-90°)
$\Delta y(\Delta\phi)$:	1.41" (2.82°)
Number of Points:	64
Error Tolerance:	.05" (.1°)
Stopping $y(\phi)$:	43.83" (87.66°)

4.5 Test Antenna

The test antenna used in the experimental portion of this research was a modification of the feed array built originally for the AGILTRAC antenna by Raytheon Corporation, Bedford, Massachusetts, and later donated to Georgia Tech for general research use. This array, shown in Figure 4-6, forms a microwave lens, space-fed by a two-plane monopulse feed horn and comparator with sum and difference ports. These ports are visible at the rear of the array in Figure 4-6(a). Only the sum port was used in this research.

The original antenna consisted of 499 interchangable circular waveguide elements. Each element is dielectric loaded with a radius of a = .4531". The elements are arranged in a triangular lattice with spacings of y_a = .620" and x_a = 1.074", which is slightly less than one-half wavelength at the operating frequency. Each element has a fixed phase shift corresponding to one of eight values spaced 45° apart over the zero to 360 degree range. Appropriate elements can be arranged to produce a main beam pointing in some specified direction. The array is approximately 30 inches in diameter.

The array was modified as shown in Figure 4-6 by removing many outer elements to form the smaller 9 x 17 array shown. The elements were phased to produce a main beam at 45° in the H-plane. A ground plane was made from 1/16" aluminum plate and carefully cut to fit around the rectangular array of elements. It was held in place by special screw fasteners which fitted through four holes vacated by other elements. On the back side of the lens, microwave absorber (Eccosorb AN-74) was used to cover the unused portion of the lens as shown in Figure 4-7 so that

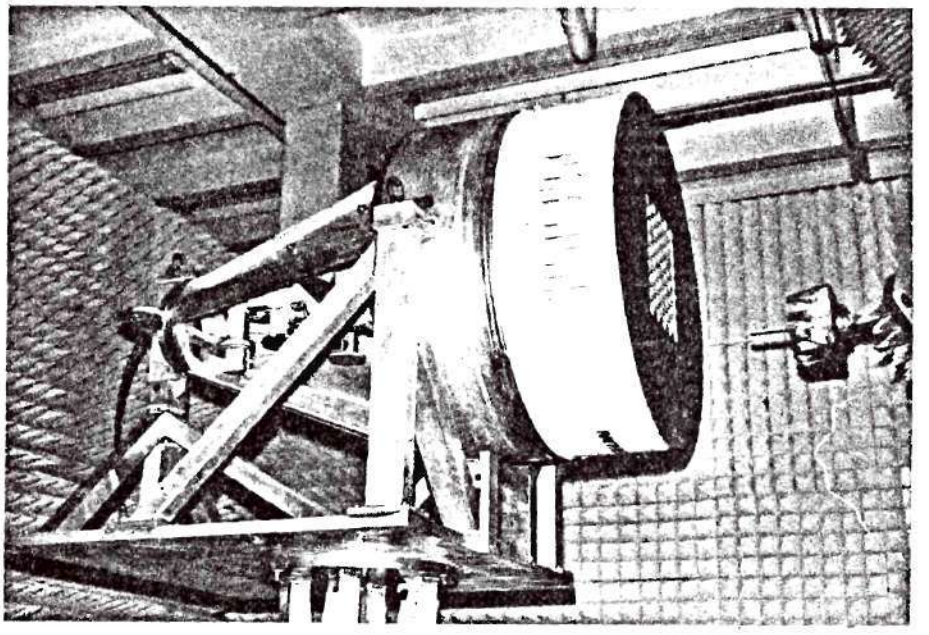

(a) Phased Array Antenna

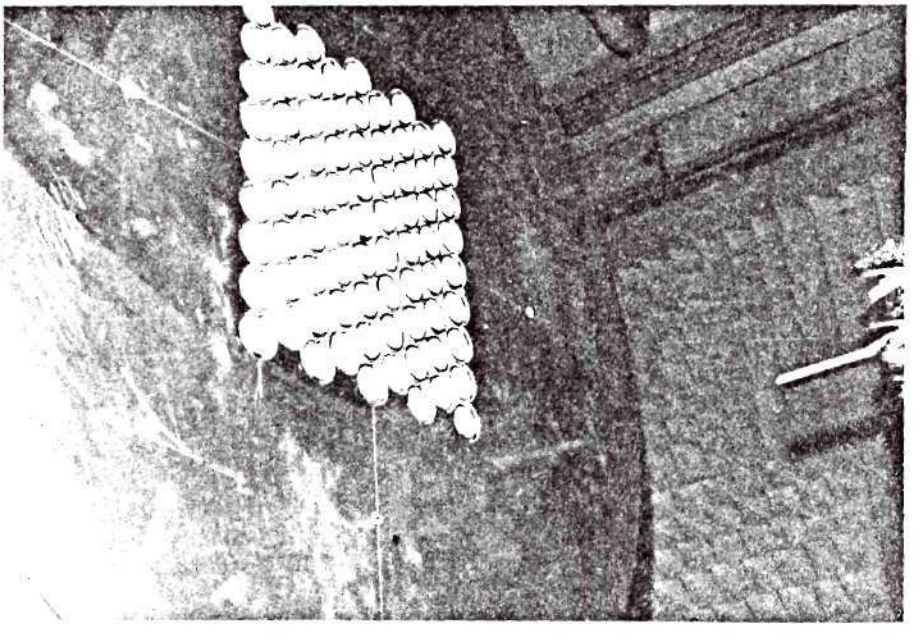

(b) Close-up View of Phased Array Elements

Figure 4-6. Test Antenna Used in Measurements.

reflections would be minimized. Side panels, including microwave absorber, were installed around the rear feed structure to prevent direct radiation by the feed structure.

In Figure 4-6, the y-axis of the test antenna coordinate system (see Figure 2-1) is vertical and pointing toward the ceiling of the room. The z-axis is normal to the array and points toward the xy probe also visible in the photographs. The x-axis follows from application of the right-hand rule. It is noted that the direction of positive x movement of the probe as recorded by the data acquisition system is opposite to the +x direction established for the test antenna.

A reduced-size array was selected so that accurate far-field predictions at wide angles could be obtained by using the full 100" x 100" xy measurement area; i.e., so that ~100% of the energy in the near-field probe response would be obtained within this area. This was a very important consideration as explained in the experimental procedures.

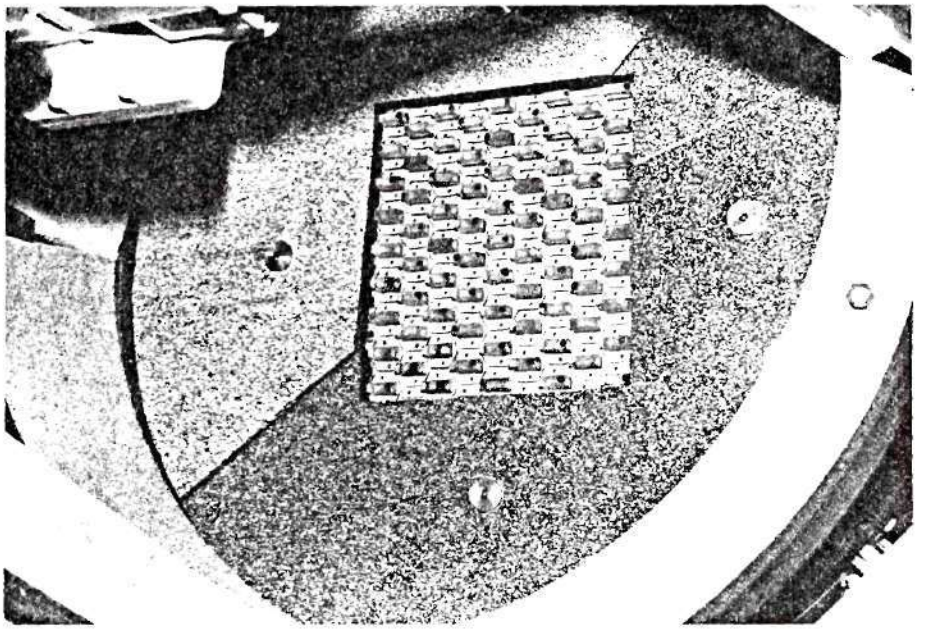

Figure 4-7. Rear View of Microwave Lens.

CHAPTER V

EXPERIMENTAL RESULTS

5.1 Introduction

The experimental procedures used and results obtained to verify the theoretical aspects of optimum probe design are presented in this chapter. The far fields of three probe antennas were measured using the $\theta\phi$ positioner and automated measurement facility. These data were processed for subsequent use in probe-compensation of the measured near-field data. The near-field response of each probe to the phased array antenna was measured using the xy positioner and the same automated facility. The near-field data for each probe were then processed to determine the relative effects of truncating the measurement area on the accuracies of the measured spectra and predicted far-field patterns.

The experiment was designed to accentuate the effects of truncating the measurement area and thereby introducing aliasing errors into the measured spectra obtained by inverse Fourier transformation of measured probe response. Consequently, the test antenna was phased to produce a main beam at 45 degrees in the xz plane (H-plane) so that significant radiation would occur at wide angles greater than θ_{max} determined by the relative sizes of the test antenna and measurement area. Also, the undersize waveguide probe was selected for its broad angular response so that maximum aliasing errors would occur when its expectedly unconcentrated near-field response was truncated and transformed. The E-plane horn antenna was selected to demonstrate the importance of probe design

in producing a maximally concentrated response and, hence, the least error in the measured spectrum when a smaller measurement area is used. The open-end waveguide probe was selected as an alternate for the undersize waveguide probe and to provide intermediate reference data.

The experiment was also designed for complete accommodation by the automated xy measurement facility. That is, the least-concentrated near-field response was to be such that essentially 100 percent of the power in the response would be contained within the 100" x 100" maximum measurement area of the xy positioner. In such case, the true values of the measured spectra and predicted far fields of the test antenna would be obtained directly from the near-field response of each probe over the maximum measurement area. This procedure obviated the necessity of performing measurements on the test antenna using a bonafide far-field measurement range with its attendant errors due to range reflections and other environmental factors. Moreover, it was well known that the sidelobe structure of the far-field patterns of the phased array antenna varied considerably with variations in the ambient temperature such as occur on the outdoor far-field range [14]. The air-conditioned environment of the near-field facility minimized such temperature variations as required for valid detection and comparison of errors due to the probes themselves.

5.2 Data Processing Procedures

Certain procedures involving data acquisition and processing were common to both near-field and far-field (probe) measurements. The steps indicated by the left side of the flow diagram in Figure 5-1 represent such procedures. The steps on the right side of Figure 5-1 pertain to

the processing of the near-field data wherein the probe data are also used. These steps are explained below.

The first step in the process is the acquisition and recording on diskette of the amplitude and phase of the microwave signal received by the xy probe. This is true for either the near-field or far-field probe characterization configuration of the automated measurement facility. One diskette (floppy disk) has capacity for one 128 x 128 data array or two 64 x 64 data arrays, where amplitude and phase are recorded for each spatial sample point. The order of data recording, together with initial input data, serve to identify the location (x,y) of each data point.

Data arrays for probe characterization measurements contained 64 x 64 data samples. The time required to measure each data array was approximately 1-3/4 hours. Data arrays for the near-field measurements contained 128 x 128 data samples. The measurement time required for each near-field array was approximately 3-3/4 hours.

The objective of the next three steps shown in Figure 5-1 is to transfer the measured data onto the disk files of the central campus computer (Cyber 70, Control Data Corporation Model 70-74) for processing and display. Data was transferred from the diskette at the MicroNova (Program SEND) to a Nova 820 (Program MTALK) via a dedicated telephone line and 9600 baud modems. The Nova 820 minicomputer stored the data on a removable disk pack. The disk pack was subsequently installed on a Nova Eclipse minicomputer system which also had a magnetic tape drive. Using the program WTAPE, data on the disk pack was transferred to a nine-track, 800 bits per inch magnetic tape compatible with the Cyber 70.

The nine-track magnetic tape containing six 64 x 64 probe data

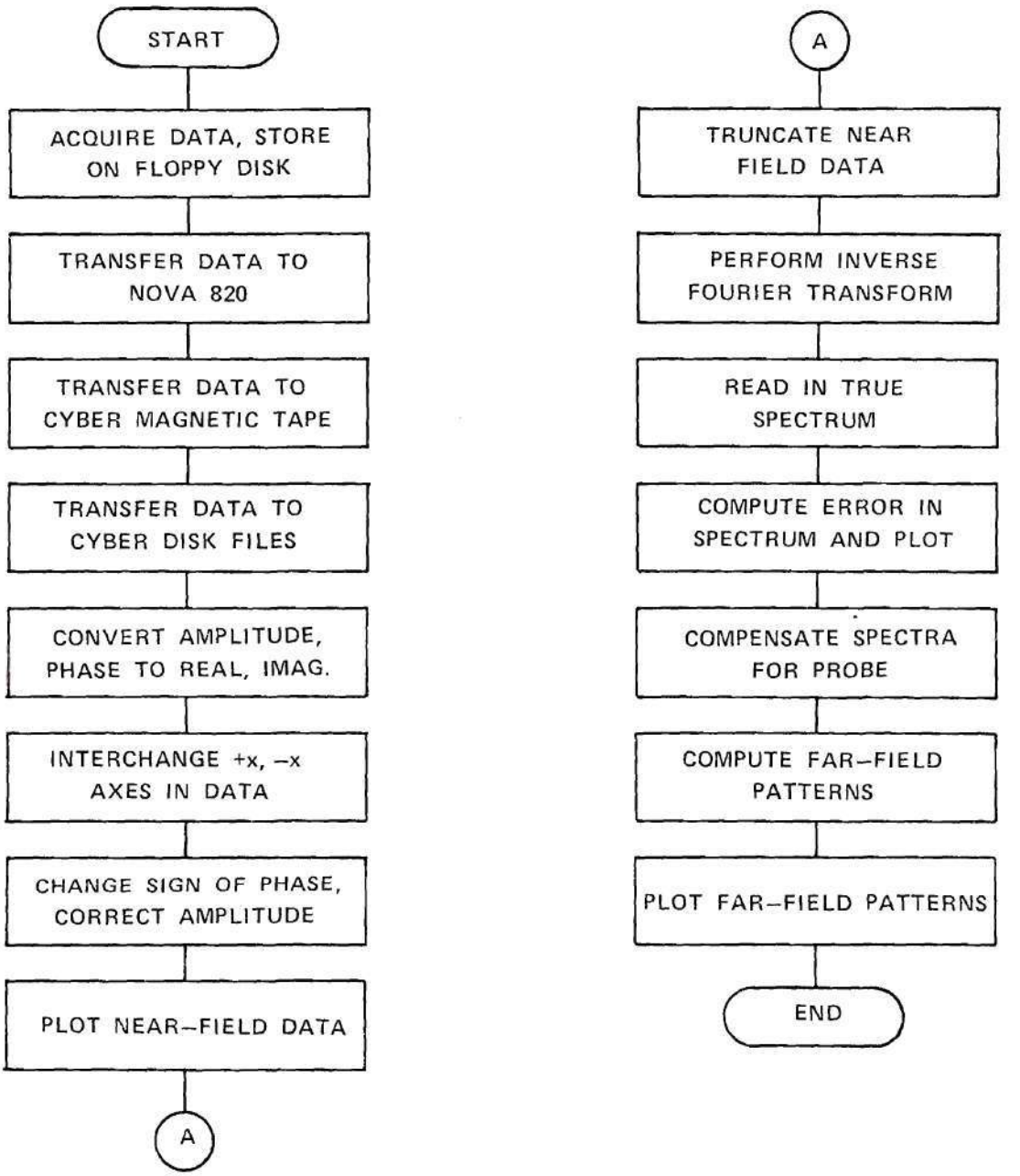

Figure 5-1. Flow Diagram of Data Collection and Processing.

arrays and six 128 x 128 near-field data arrays was placed in the tape library of the central computer facility. The data were transferred from the tape to the Cyber disk files using the program TLATE. In this process, the program BNOVCYB was used to convert the data from the ASCII format used on the tape to standard CDC format. Also, program TLIST was used to convert the amplitude and phase information to real and imaginary parts in conformance to standard Fortran programming. The final data arrays were stored on disk as unformatted (binary), direct access files.

The next two steps in the data processing were to correct known errors in the data. The program FLIPX was used to interchange the data in the near-field data arrays about the column corresponding to x=0 of the test antenna coordinate system. This step corrected the error caused by the x-encoder mentioned earlier in Section 4.4. The program FLIP was next used to change the sign of the phase in all data arrays to correct for the B→A setting used on the Scientific-Atlanta receiver. (A→B should have been used.) Program CRCT was next used to correct the measured amplitude in all arrays for deliberate offsets (to enhance dynamic range) and according to the calibration data shown in Table 5-1. These data were obtained by recording the output of the amplitude displayed by the automated measurement system for known settings on a precision attenuator placed to control the microwave power input to the test antenna. Finally, the measured data, corrected for the x reversal, phase reversal, amplitude errors and deliberate offsets were plotted for examination.

The six near-field data arrays, corresponding to orientations #1 and #2 of each probe, were processed as shown in the seven steps on the right hand side of the flow diagram in Figure 5-1. Initially, and not

Table 5-1. Amplitude Calibration Data

Measured Amp (dB)	True Amplitude (dB)
0.00	0.00
- 2.00	- 1.65
- 4.00	- 3.42
- 6.00	- 5.35
- 8.00	- 7.31
-10.00	- 9.32
-12.00	-11.38
-14.00	-13.45
-16.00	-15.59
-18.00	-17.78
-20.00	-19.98
-22.00	-22.21
-24.00	-24.50
-26.00	-26.81
-28.00	-29.21
-30.00	-31.65
-32.00	-34.20
-34.00	-36.78
-36.00	-39.21
-38.00	-41.91
-40.00	-44.40
-42.00	-46.92
-44.00	-49.37
-46.00	-51.72
-48.00	-54.06
-50.00	-56.34
-52.00	-58.60
-54.00	-60.82
-56.00	-63.00
-58.00	-65.17
-60.00	-67.30

shown on the diagram, each near-field data array was inverse Fourier transformed using the Fast Fourier Transform algorithm. The central portion of the resulting 128 x 128 complex array was extracted to form a 81 x 81 complex array which contained all the data corresponding to radiating waves for which probe compensation was to be applied. These 81 x 81 arrays were stored on disk for later use in steps three and four to compute the errors in the measured spectra due to truncation of the measurement area.

A truncated measurement area corresponding to 32 x 32 near-field samples spaced approximately one-third wavelength apart in x and y was selected when processing the data to generate aliasing errors in the measured spectra. For the approximately two wavelength separation between probe and test antenna, the maximum angle of confidence in far-field predictions was calculated from Equation (3-75) to be θ_{max} = 54 degrees. The measurement area truncation was implemented by setting to zero all measured data outside the central 32 x 32 portion of each 128 x 128 near-field data array. The resulting 128 x 128 array was then inverse Fourier transformed to produce the erroneous measured spectrum with exactly the same resolution as present in the true spectrum. The error was computed by performing a point-by-point subtraction of the values in the erroneous spectrum from the true values in the corresponding 81 x 81 array. Only those errors corresponding to wavenumbers k_x, k_y such that $k_x^2 + k_y^2 < k^2$ were retained and plotted. No significance is attached to errors that may be produced in the data corresponding to the invisible region $(k_x^2 + k_y^2 > k^2)$.

The final outputs of the data processing were plots of the

far-field patterns of the phased array antenna as predicted from the near-field responses of each probe, with and without truncation of the measurement area. For each probe, these patterns were computed at an increased resolution of sixteen times using Fourier interpolation in the measured spectrum. Each measured spectrum was then probe-compensated using Equations (2-35) and (2-36) and the measured probe data. From the plane wave spectra A_x, A_y which resulted, the far-field patterns were computed according to Equation (2-19). The true far-field patterns were assumed to be those predicted by using all of the data in the measured near-field arrays.

Probe-compensation of the measured spectra required a computer program which converted the measured vector components in $\theta\phi$ space for the probe to x and y components in k_x, k_y space. This conversion and interpolation procedure is described in the next section.

5.3 Probe Characterizations

The transmitted far-fields of the three probe antennas were measured using the $\theta\phi$ positioner and automated test facility. The two vector components corresponding approximately to E_θ and E_ϕ of Figure 4-3 were measured for each probe by using two orthogonal positions of the linearly polarized receiving antenna. The resulting voltage responses V_θ and V_ϕ were depolarized to produce E_θ and E_ϕ by using the three-antenna method described by Joy and Paris [49]. The measured probe data were then plotted for examination in different formats. The resulting probe characterization data are presented in this section and in Appendices B and C.

The probe positioner was aligned to produce a vertical axis of θ rotation and a horizontal ϕ axis of rotation. A precision level was used to level the azimuth positioner turntable to produce the vertical axis of rotation. The four leveling/mounting bolts which secured the positioner to the z-positioner baseplate were used to accomplish this. Next, the level and the three leveling bolts which secured the L-shaped boom to the turntable were used to level the ϕ-positioner mounted on top of the boom. A plumb bob was suspended from the end of the nine-inch probe installed on the ϕ-positioner, and the lateral position of the ϕ-positioner was adjusted until the plane of the probe aperture and its center of symmetry coincided with the vertical axis of rotation. Finally, the axis of symmetry of the receiving antenna (xy probe) was carefully aligned with that of the probe by sighting optically through the 10-inch waveguide section of the ϕ-positioner and by adjusting the position of the xy probe using the xy positioner motors.

Amplitude and phase data were recorded for each probe at 64 points spaced 2.9 degrees apart in θ, and at 64 points spaced 2.82 degrees in ϕ. The response V_ϕ was obtained when the receiving antenna was vertically polarized. The V_θ response was obtained when the receiving antenna was rotated clockwise by 90 degrees (for an observer standing behind the receiving antenna and looking toward the transmitting antenna). Depolarization of the measured responses to produce E_θ and E_ϕ was carried out according to the following equations for $\pi/2 \leq \phi < 3\pi/2$:

$$E_\theta = \frac{R_1 V_\phi - V_\theta}{R_1^2 + 1} \qquad (5\text{-}1)$$

$$E_\phi = \frac{-R_1 V_\theta - V_\phi}{R_1^2 + 1} \tag{5-2}$$

For values of ϕ in Figure 4-3 such that $-\pi/2 \leq \phi < \pi/2$,

$$E_\theta = \frac{-R_1 V_\phi + V_\theta}{R_1^2 + 1} \tag{5-3}$$

$$E_\phi = \frac{R_1 V_\theta + V_\phi}{R_1^2 + 1} \tag{5-4}$$

where R_1 is the complex polarization ratio determined from the measurements described by Joy and Paris [49] and shown using their notation in Table 5-2. The resulting value of polarization ratio (on-axis) for the receiving antenna is given in the table. The necessity for the two pairs of equations above is due to the definitions of E_θ, E_ϕ and the orientation of the receiving antenna used.

The conversion of the E_θ, E_ϕ components at a point (θ,ϕ) to rectangular vector components E_x, E_y at the point (k_{xn},k_{yn}) is required for probe-compensation of the near-field data. The normalized wavenumbers and angles are related by

$$\sin\theta = \sqrt{k_{xn}^2 + k_{yn}^2} \tag{5-5}$$

$$\cos\phi = \frac{k_{xn}}{\sqrt{k_{xn}^2 + k_{yn}^2}} \tag{5-6}$$

$$\sin\phi = \frac{k_{yn}}{\sqrt{k_{xn}^2 + k_{yn}^2}} \tag{5-7}$$

Table 5-2. Polarization Ratio Measurements

Probe Combination	S_A	S_B
Rcvg/E-Plane Horn (1,2)	-1.75dB/0°	-41.36dB/72.5°
Rcvg/Open-End WG (1,3)	-1.70dB/2.5°	-54.00dB/96°
E-Plane Horn/Open-End WG (2,3)	-3.14dB/-11.5°	-72.25dB/83.1°
Polarization Ratio: $R_1(0,0) = (.15127 + j.60241) \times 10^{-2}$		

The far-field rectangular components E_x, E_y follow from spherical-to-rectangular coordinate conversions as [50]

$$E_x = \frac{k_{xn} k_{zn} E_\theta - k_{yn} E_\phi}{\sqrt{k_{xn}^2 + k_{yn}^2}} \tag{5-8}$$

$$E_y = \frac{k_{yn} k_{zn} E_\theta + k_{xn} E_\phi}{\sqrt{k_{xn}^2 + k_{yn}^2}} \tag{5-9}$$

The measured amplitudes of the x and y far-field components of the three probes are presented in Figures 5-2 through 5-7. The voltage amplitude in each graph is plotted in decibels relative to the maximum amplitude of E_y for each probe. The abscissas of each three dimensional graph are normalized wavenumbers k_{xn}, k_{yn} such that the central circular region corresponds to the visible region; i.e., $k_{xn}^2 + k_{yn}^2 \leq 1$. As expected from consideration of aperture sizes, the far-fields of the E-plane horn are more directive than those of the other two probes, especially E_y. The x component of each probe exhibits very low (< -40 dB) values in the principal planes corresponding to $k_x=0$ (E-plane) and $k_y=0$ (H-plane). Examinations of the phase plots in Appendix B for these amplitude plots show that the sign of the x component changes from quadrant to quadrant. The plots in Figures 5-4 and 5-5 also are in general agreement with the theoretical predictions for the open-end waveguide presented earlier in Figures 3-2 and 3-3.

The graphs of the measured phase of the three probes are presented

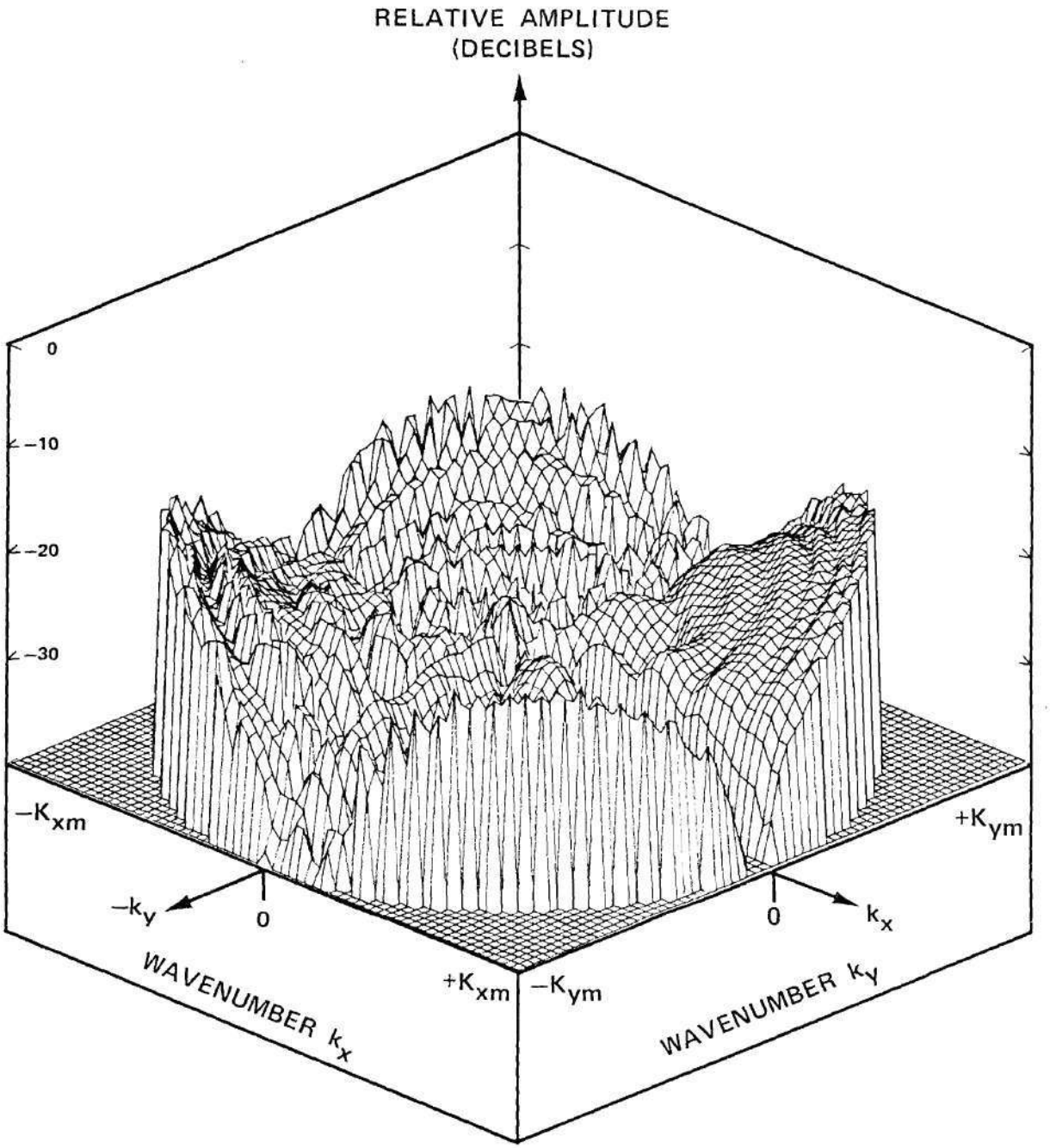

Figure 5-2. Measured Amplitude of $E_{xff}(k_x,k_y)$ of Undersize Waveguide Probe.

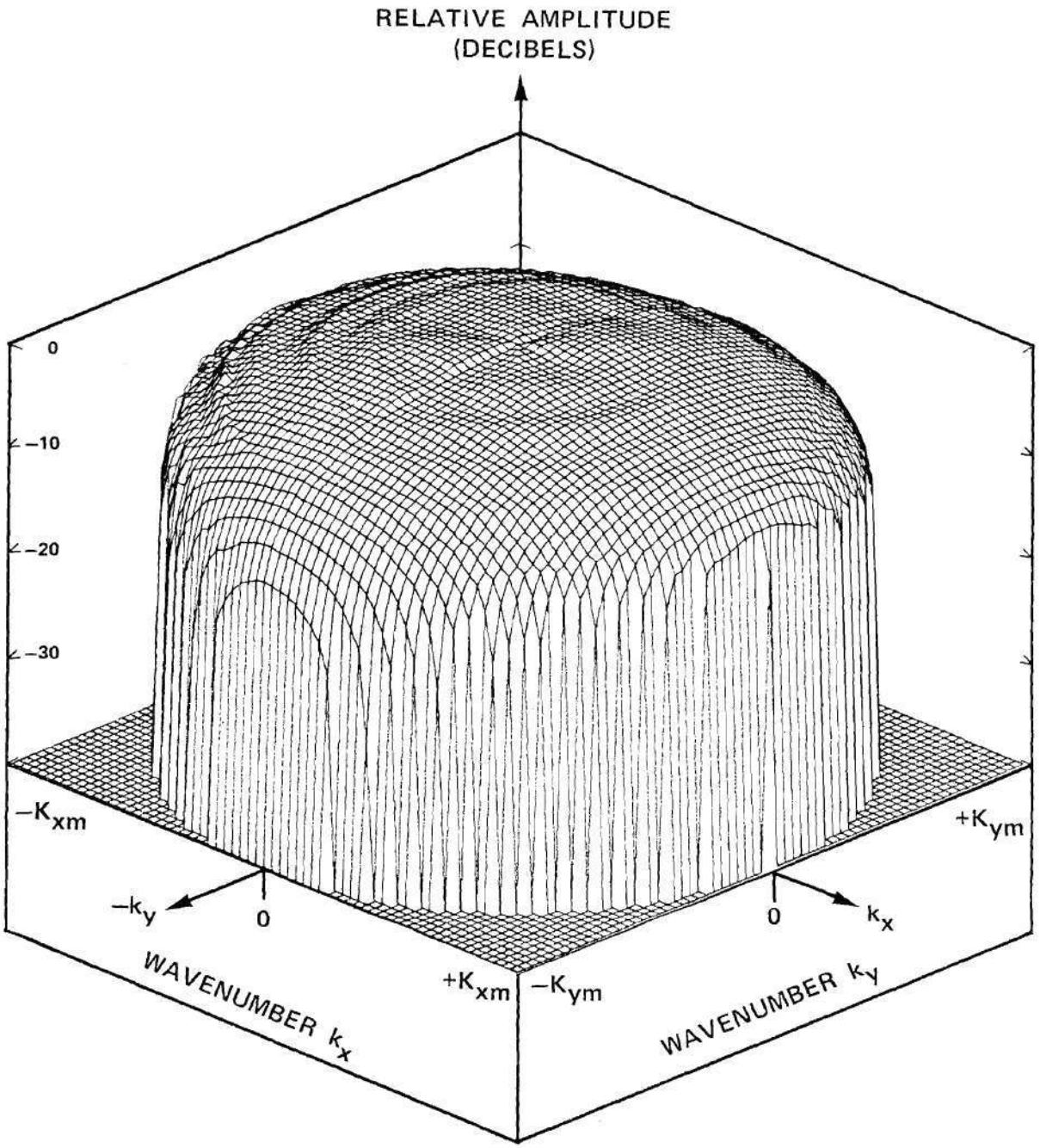

Figure 5-3. Measured Amplitude of $E_{yff}(k_x,k_y)$ for Undersize Waveguide Probe.

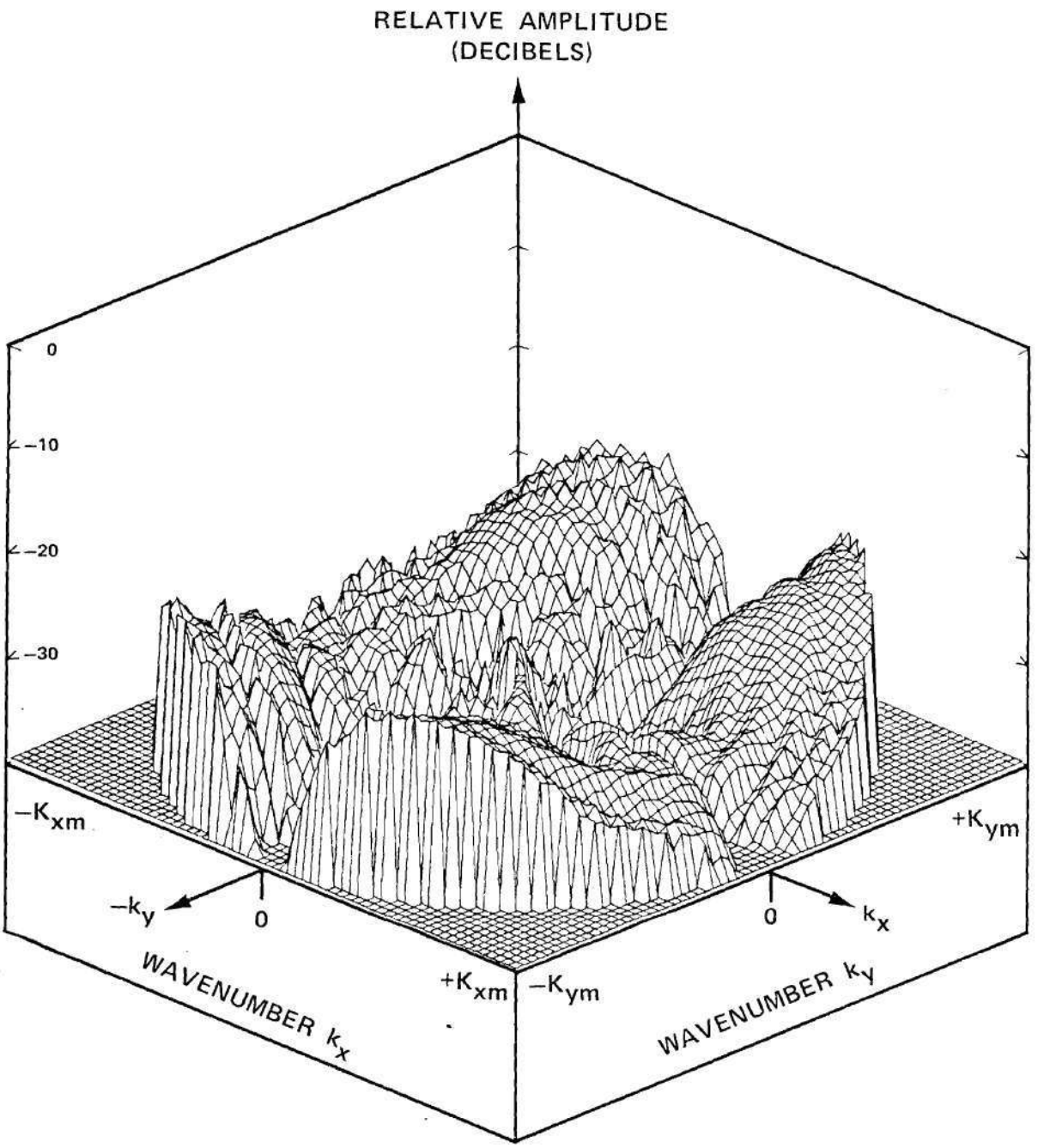

Figure 5-4. Measured Amplitude of $E_{xff}(k_x,k_y)$ for Open-End Waveguide Probe.

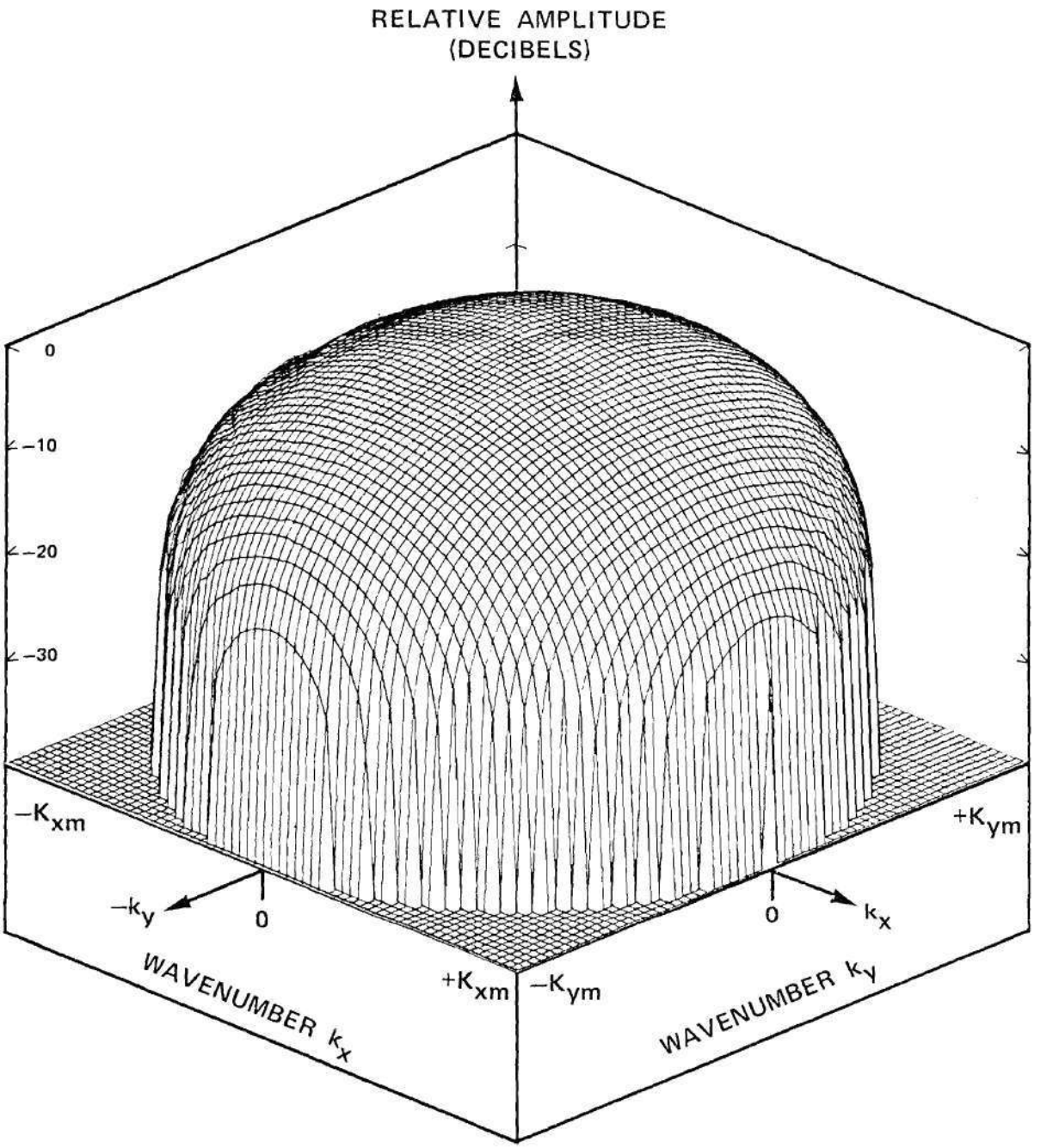

Figure 5-5. Measured Amplitude of $E_{yff}(k_x,k_y)$ of Open-End Waveguide Probe.

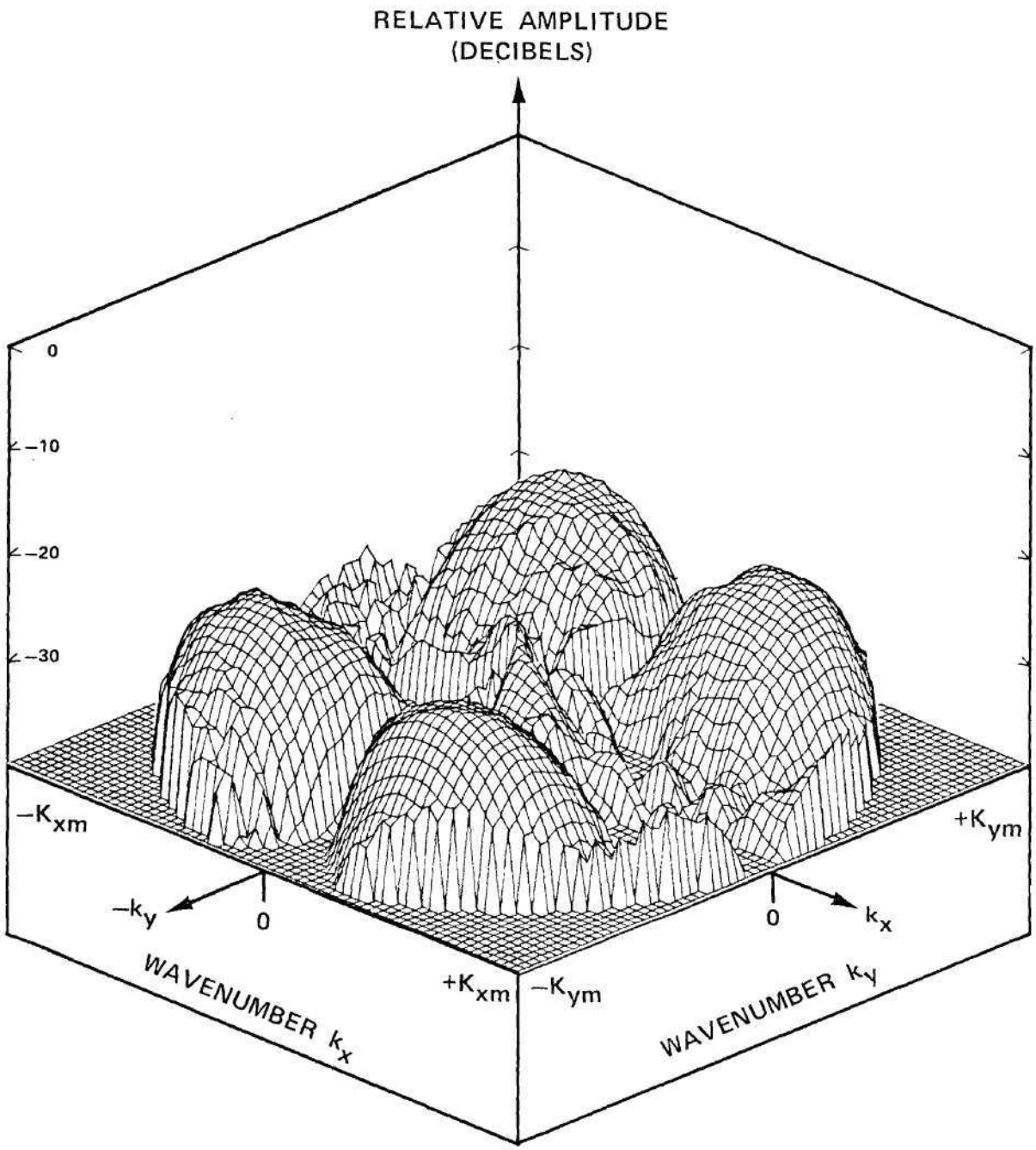

Figure 5-6. Measured Amplitude of $E_{xff}(k_x,k_y)$ for E-Plane Horn Probe.

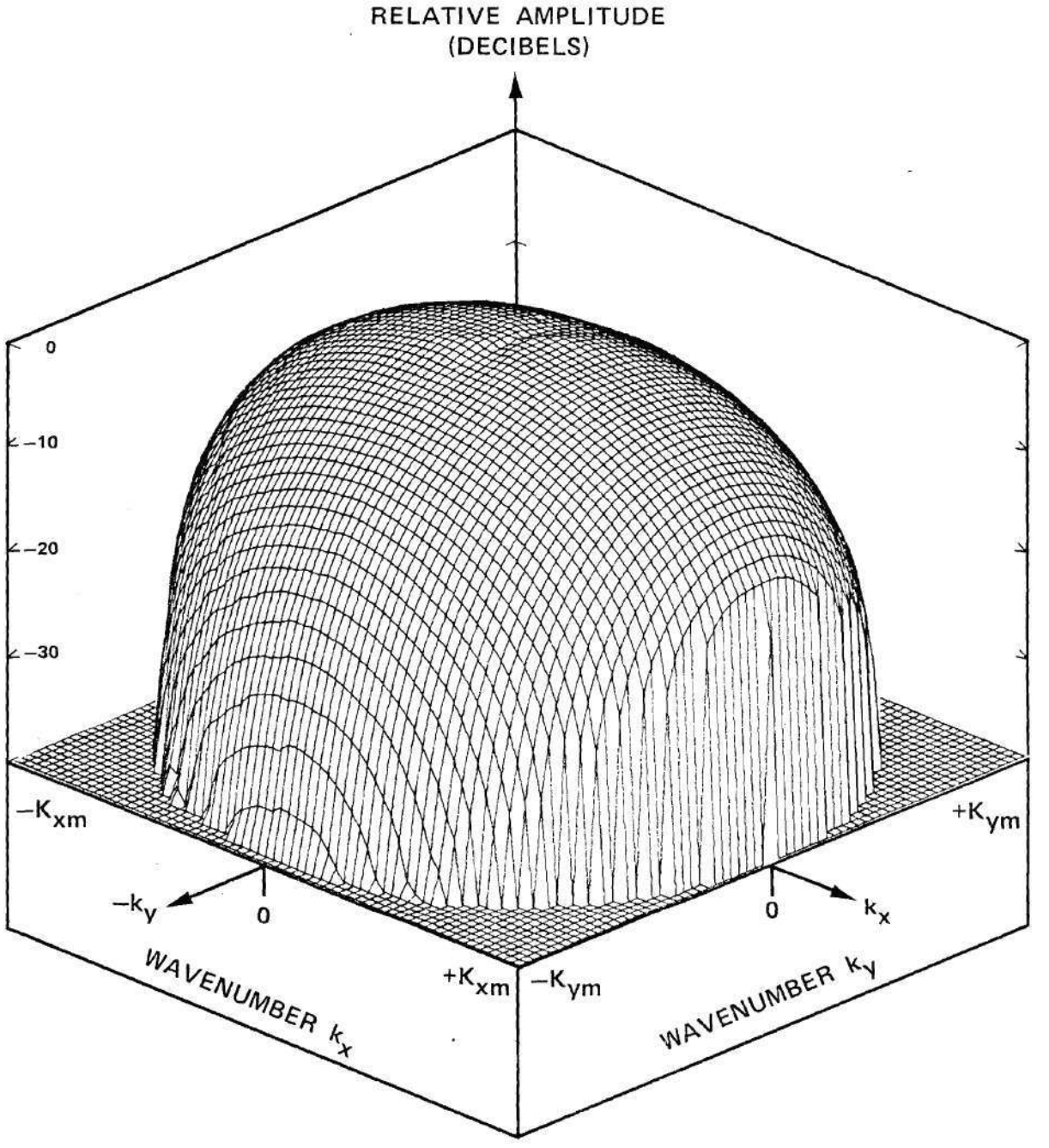

Figure 5-7. Measured Amplitude of $E_{yff}(k_x,k_y)$ of E-Plane Horn Probe.

in Figures B-1 through B-6 of Appendix B for completeness. Examination of the phase plots for the y component in each case shows that there is a slight mismatch at $k_x=0$. This mismatch is caused by a systematic change during measurement in the measured phase from its value at the starting time and position of the probe to its final value at the ending time and position. For the procedure used, the ϕ-positioner was rotated through almost 180 degrees from starting to ending position. Since phase drifts during the measurement were observed to be less than two degrees, and since no mechanical misalignment would explain the mismatch, the mismatch is attributed to the rotary joint at the rear of the ϕ-positioner. No calibration data was taken so that this error could have been removed. The effects of the mismatch on the predicted far fields were minor, as will be seen.

The original measured probe data are presented in Appendix C for completeness. It was from these amplitude and phase data that the graphs in Figures 5-2 through 5-7 (and in Appendix B) were generated using Equations (5-5) through (5-9). The data in Appendix C have been corrected for amplitude errors as specified in Table 5-1, and depolarization has been applied; i.e., the data are that for E_θ and E_ϕ. These data for E_θ, E_ϕ were used as input data for the probe compensation procedure used in predicting the far fields of the test antenna from the measured near-field data described in the next section.

5.4 Near-Field Measurements

The near-field responses of the three probes to the phased array test antenna were measured using the automated test facility. Amplitude and phase data were recorded for each probe in two orthogonal orientations as required for probe-compensated near-field measurements. The square measurement area used was 81.28 inches on each side. Sample points were spaced .305λ apart in x and y, and 128 rows of data were taken. Each row contained 128 data samples. Other parameters of the near-field measurement are cited in Table 5-3.

The test antenna was mounted on a special pedestal to elevate the center of the array of elements to the approximate center of the xy scan area. The pedestal and test antenna were securely bolted together and to the z-positioner baseplate. The plane of the array was aligned by sight approximately parallel to the measurement plane that is described by the probe aperture as the probe is moved in x and y. The nine-inch long open-end waveguide probe was installed on the xy positioner, and the z-positioner was actuated to adjust the probe/test antenna separation to 4.10 inches, corresponding to approximately two wavelengths. This separation corresponds to an attenuation of the evanescent plane waves by approximately 142 dB [4].

The probe was aligned in the first orientation (y' vertical) using a precision level placed on the broad wall of the waveguide section of the probe. Alignment in the second orientation was accomplished by rotating the probe clockwise through ninety degrees until the level placed on the narrow wall indicated a level condition. The probe fixture was securely clamped in each position by tightening four 3/8" bolts provided

Table 5-3. Parameters of Near-Field Measurements

	x	y
Starting Position	-40.96"	-40.96"
Sample Distance	.64"	.64"
Number of Samples	128	128
Error Tolerance	.05"	.05"
Stopping Position	40.32"	40.32"
Maximum Wavenumber (Normalized)	1.64	1.64
Probe/Test Antenna Separation:	z_o = 4.10"	
Frequency:	f = 5.62334 GHz	

for this purpose in the rotation assembly. The xy positioner was positioned initially so that the center of the probe aperture coincided with the center of the center element in the phased array. The position indicated on the syncho read-outs provided on the positioner controller were recorded for re-positioning reference, and the encoder counters were cleared to initialize the origin (x=0, y=0) of the test antenna coordinate system for data acquisition.

In orientation #1, the probe response was of larger amplitude since the test antenna and probe were both vertically polarized. Preliminary measurements were made in x for y=0 to determine the location of the maximum response. With the probe located at this point, the receiver gain controls were set so that the automated facility displayed an amplitude of approximately -2.0 decibels. These gain settings ensured the best dynamic range in measuring amplitude. The probe was then moved to the (0,0) position, and the phase was set equal to zero using the receiver controls. The measured amplitude and phase at the origin were recorded before and after the near-field measurement to preclude non-detection of gross errors. Typically, the amplitudes before and after the 3-3/4 hour measurement scan differed by no more than .4 dB, and the phases differed by no more than two degrees. When the measurement for orientation #1 was completed, the probe was rotated 90 degrees for the second measurement.

Graphs of the measured amplitude of the near-field response of each probe are presented in Figures 5-8 through 5-13. The second figure in each pair is the graph of the amplitude of the response for the second orientation of the probe, and it is shown relative to the maximum value

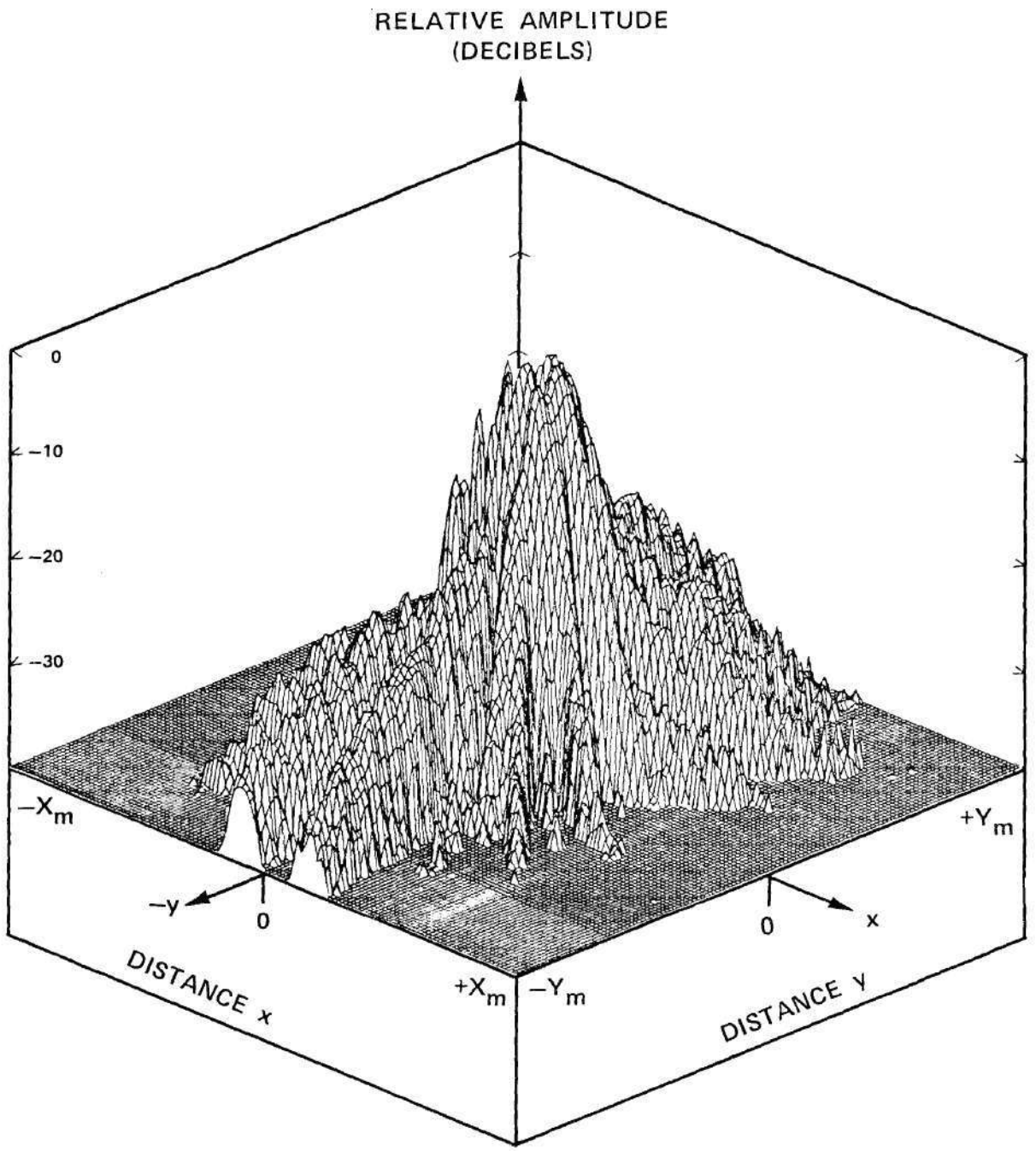

Figure 5-8. Measured Amplitude of Near-Field Response of Undersize Waveguide Probe for Orientation #1.

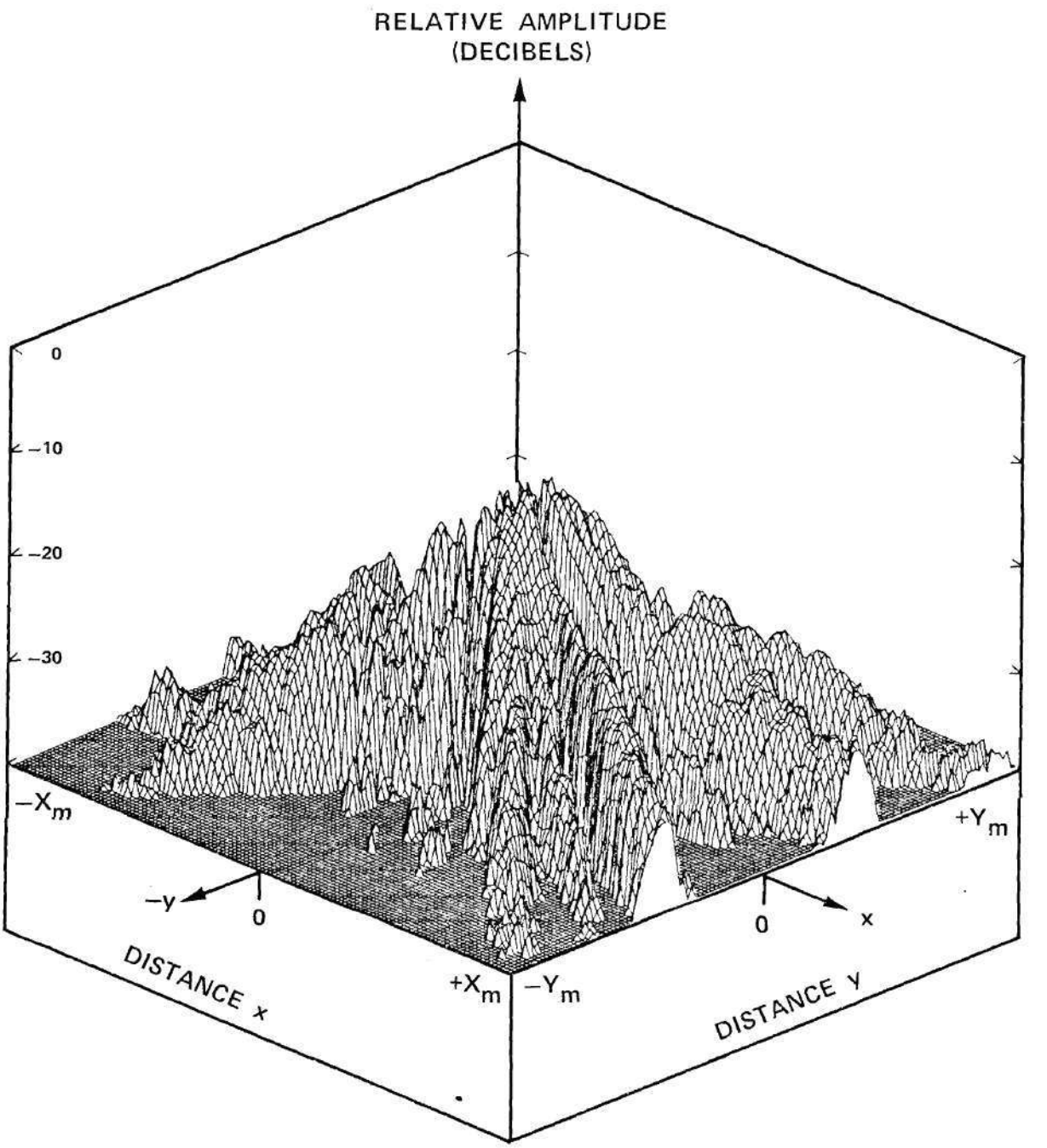

Figure 5-9. Measured Amplitude of Near-Field Response of Undersize Waveguide Probe for Orientation #2.

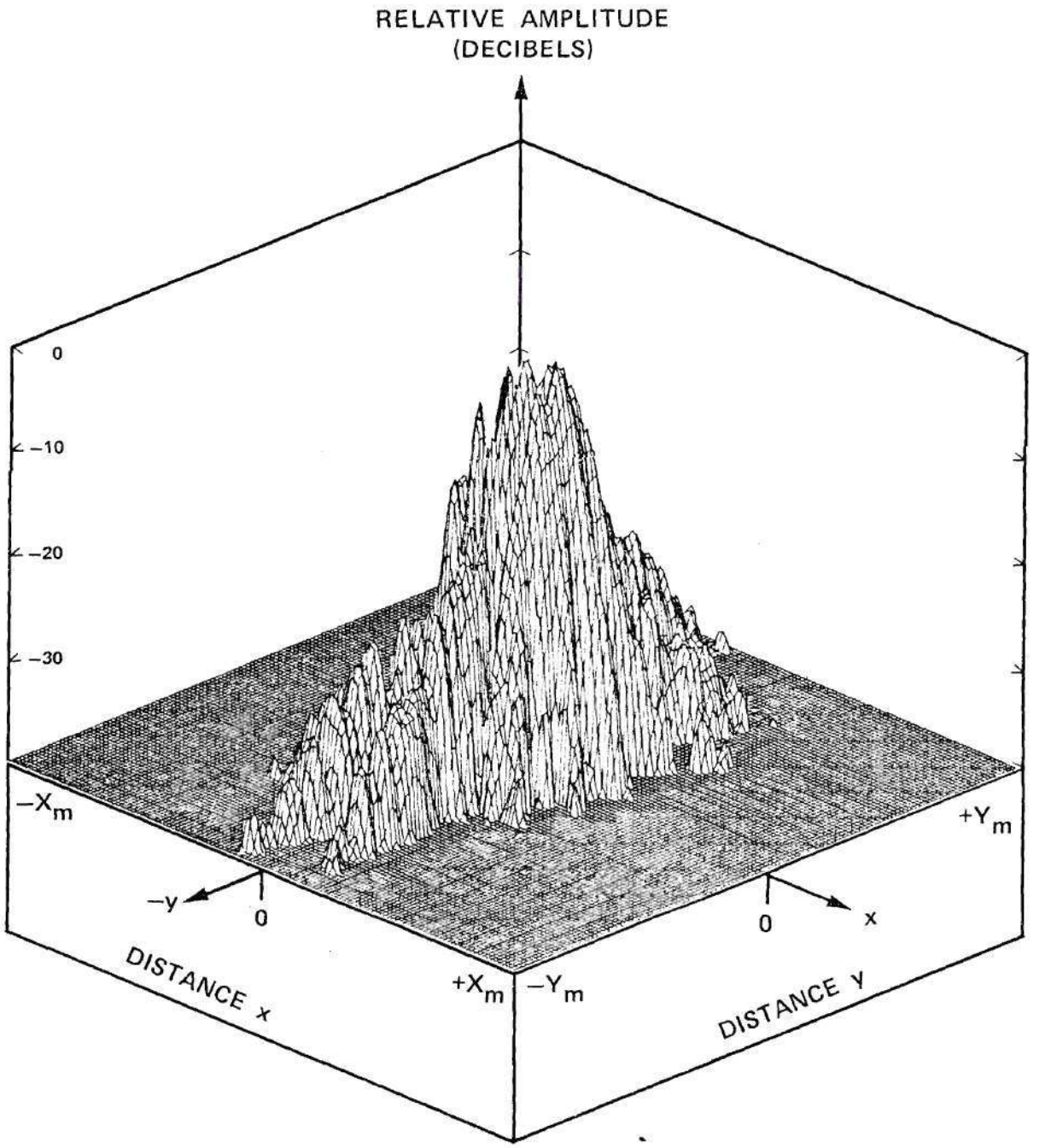

Figure 5-10. Measured Amplitude of Near-Field Response of Open-End Waveguide Probe for Orientation #1.

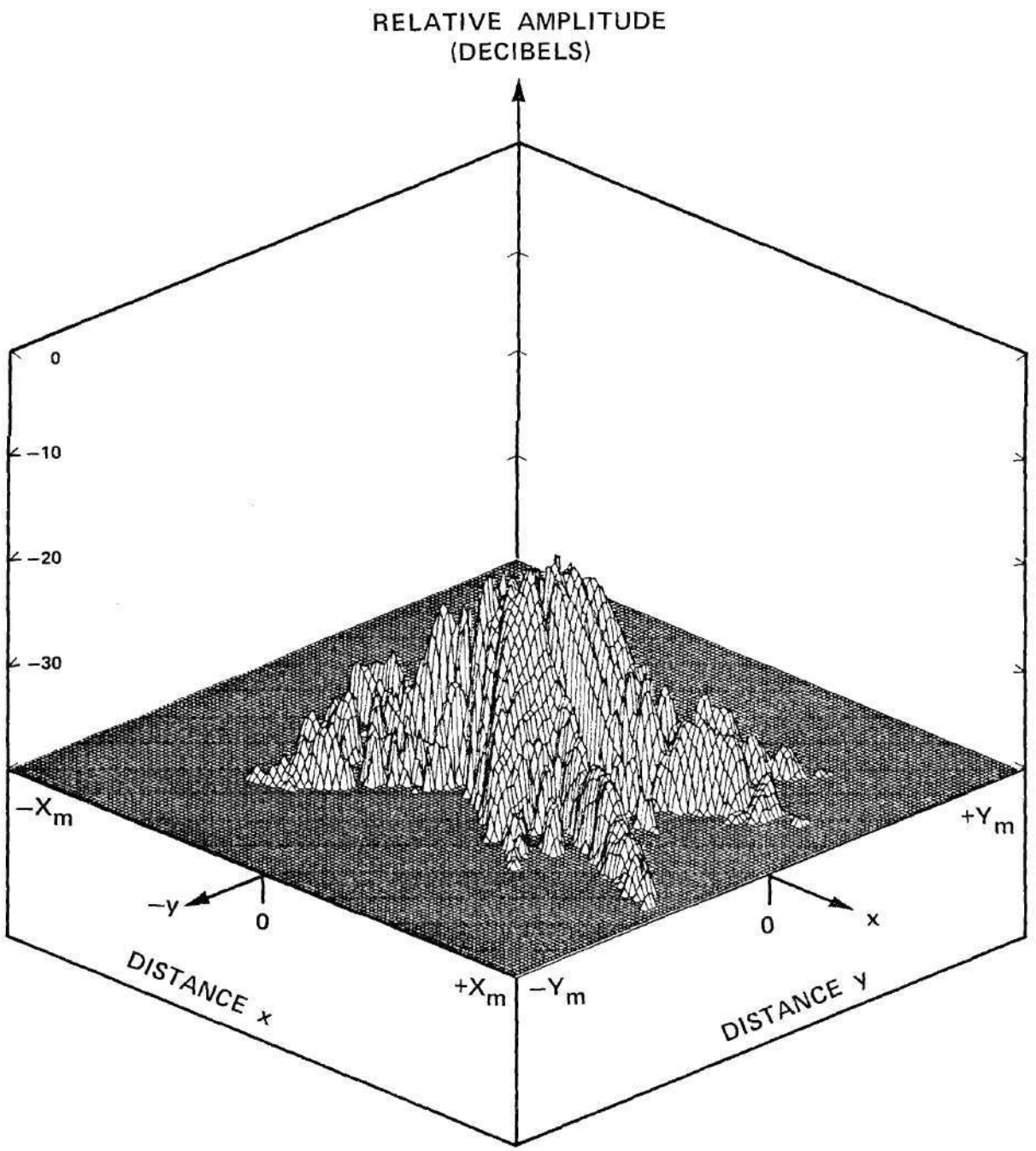

Figure 5-11. Measured Amplitude of Near-Field Response of Open-End Waveguide Probe for Orientation #2.

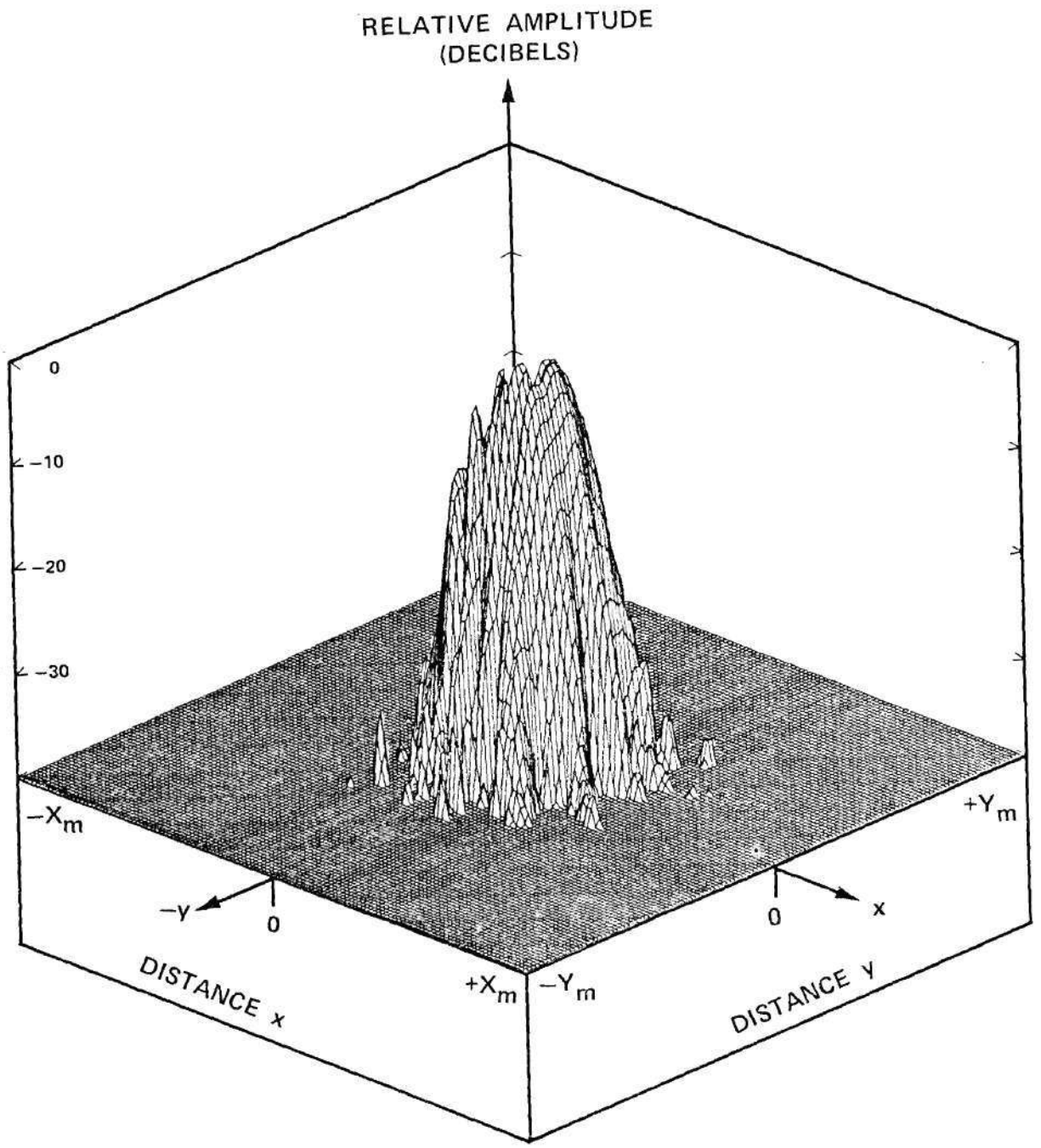

Figure 5-12. Measured Amplitude of Near-Field Response of E-Plane Horn Probe for Orientation #1.

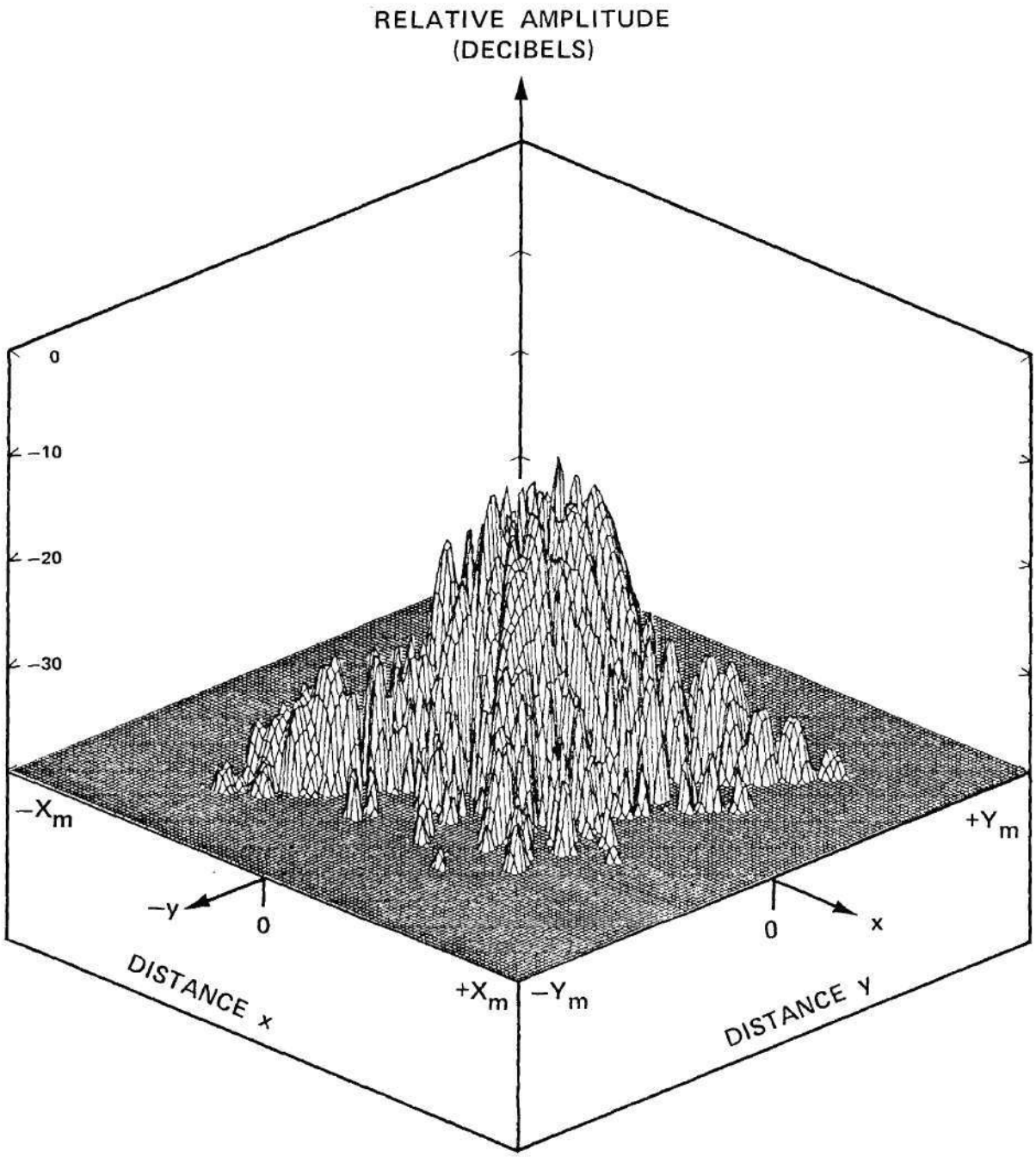

Figure 5-13. Measured Amplitude of Near-Field Response of E-Plane Horn Probe for Orientation #2.

obtained for orientation #1. The abscissas in the graphs represent distances x and y in the test antenna coordinate system. The maximum values and increments indicated in the graphs are presented in Table 5-3.

Comparisons of the graphs in Figures 5-8 through 5-13 reveal that the concentration of the near-field response increases with increasing probe aperture size as expected. The undersize waveguide probe produced the least concentrated response while the E-plane horn produced the most concentrated response. For the two smaller probes, the near-field response is more concentrated in the x direction than in y. Comparison of Figures 5-8 and 5-12 shows the significant effect of the b_p dimension in controlling the concentration in y. The amplitude of the response of each probe for orientation #2 is somewhat less concentrated than that for the first orientation.

For completeness, three dimensional graphs of the measured phase of each probe response are presented in Appendix D. The phase data are somewhat incomprehensible due to the scanned condition of the phased array test antenna.

Quantitative descriptions of the concentrations of the probe responses are presented in Figures 5-14 and 5-15. The former presents the percent of signal power contained within a square region centered on x=0, y=0 of the measurement area, where the size of the square region is determined by θ_{max} and Equation (3-75). It is assumed in each case that 100% of the signal power is contained within the complete measurement area corresponding to the 128 x 128 data array. From Figure 5-14, it is clear that the E-plane horn produces the most concentrated response for both orientations. The graph also shows that at θ_{max} = 45 degrees, the

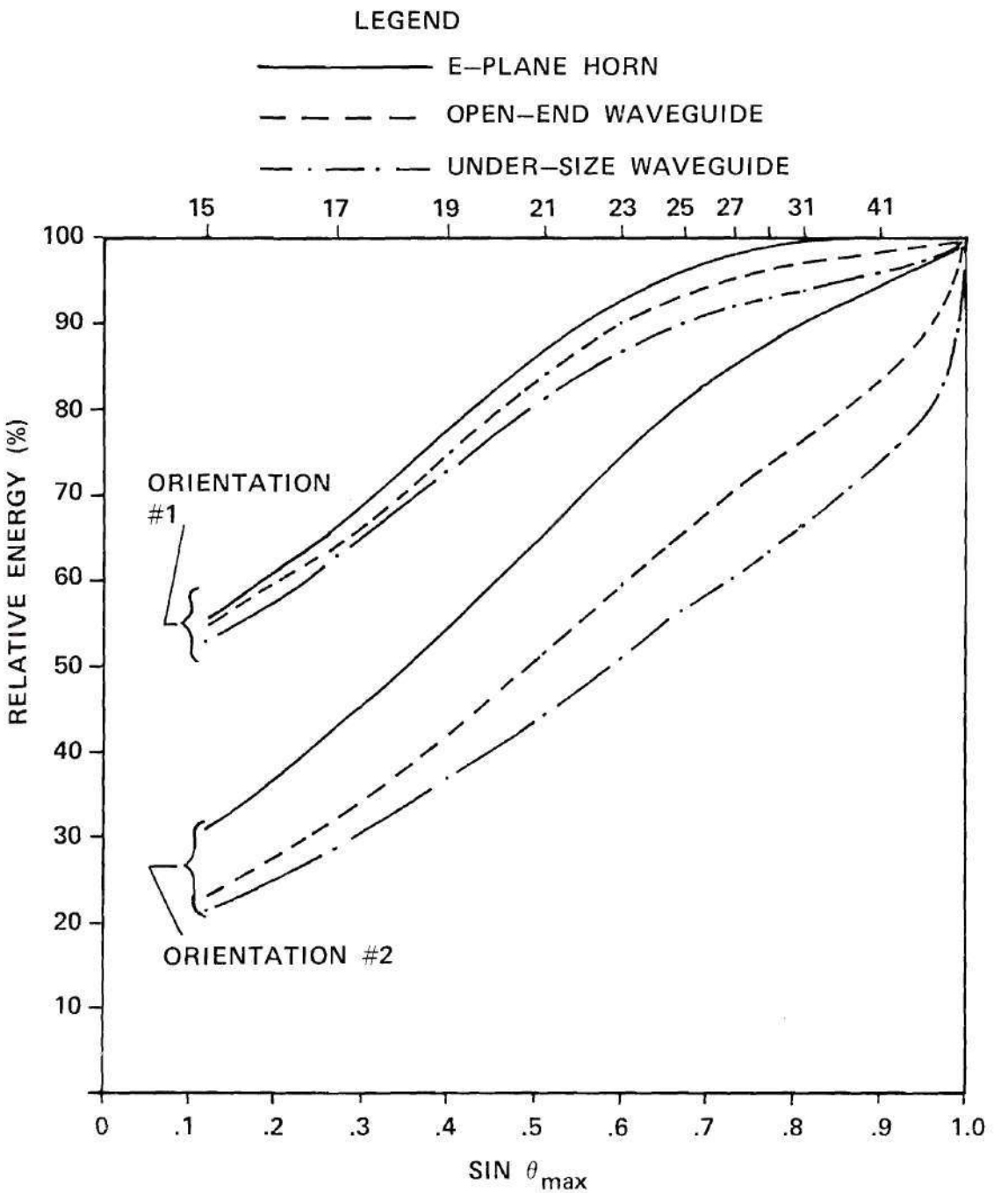

Figure 5-14. Graph of Measured Values of Relative Signal Energy Versus $\sin\theta_{max}$ for Near Field Responses of Three Probes for Two Orientations.

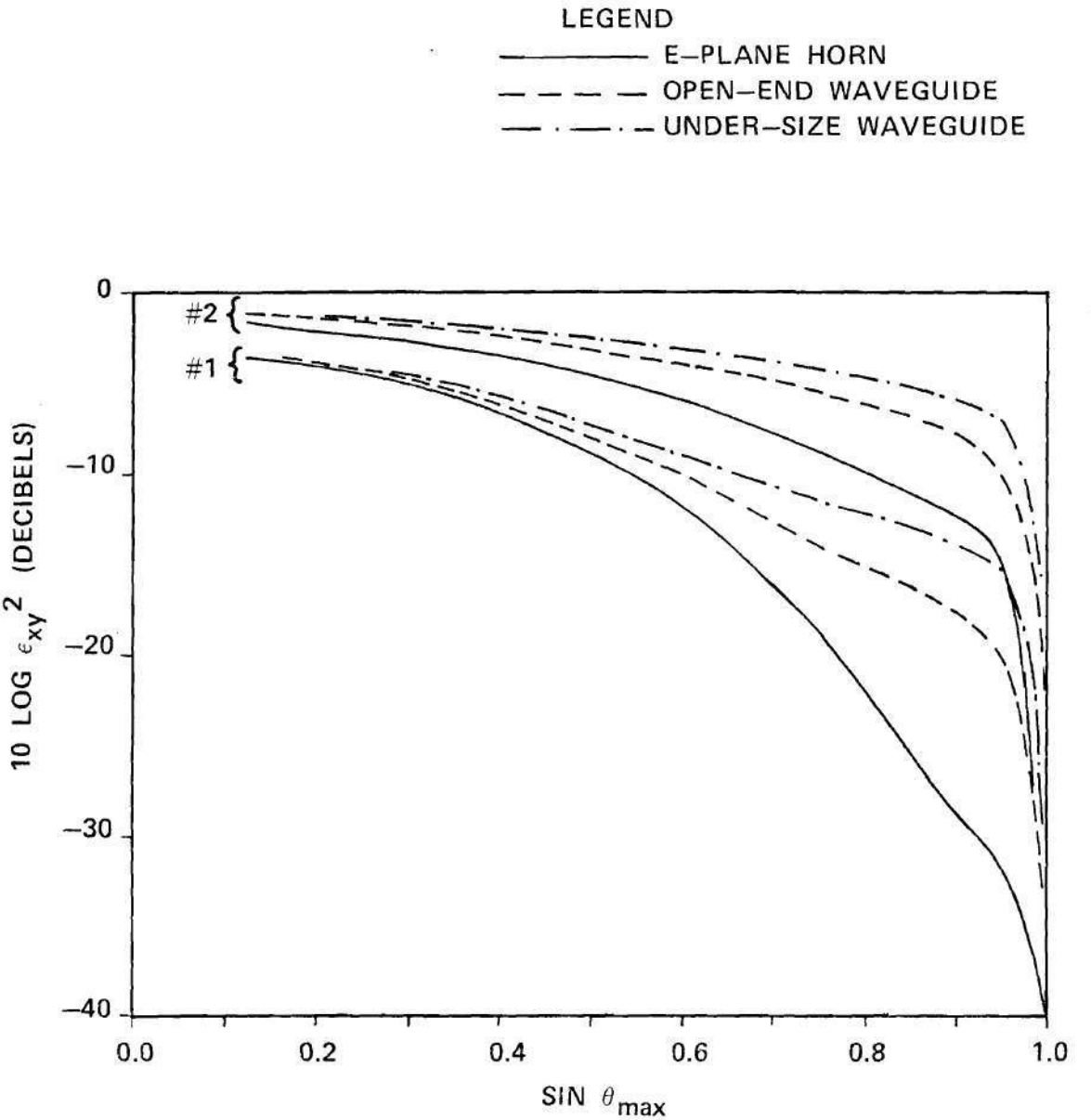

Figure 5-15. Graph of Measured Values of Concentration Factor ϵ_{xy}^2 Versus $\sin\theta_{max}$ for Near Field Responses of Three Probes Used to Measure the Phased Array Test Antenna (Orientations #1 and #2).

relative power is greater than 90% for orientation #1 of all three probes, but ranges from 59% to 84% for the other orientation.

Figure 5-15 presents the same concentration data in the form of the concentration factor ϵ_{xy}^2 defined by Equation (2-99). The ordinate of the graph is in decibels, where zero decibels corresponds to a value of unity and indicates the least possible concentration. Values of ϵ_{xy}^2 less than -10 decibels in Figure 5-15 correspond to relative power greater than 90% in Figure 5-14. It is noted that the mean square error in the measured spectrum is assumed to be proportional to ϵ_{xy}^2 as indicated in Equation (2-117).

The integers along the top of the graph in Figure 5-14 indicate the number of data samples in each row of the square measurement area specified by θ_{max}. The example, a measurement area consisting of 32 x 32 sample points in x and y, corresponds to a value of $\sin\theta_{max} = .83$; i.e., $\theta_{max} = 56$ degrees.

5.5 Results Derived From the Measurements

To demonstrate the effects of probe design and concentration of response on the measured spectra and predicted far fields, the near-field data arrays were truncated to simulate a smaller measurement area as illustrated in Figure 5-16. The reduced size area corresponded to a data array of 32 x 32 samples as may be used in practice. The maximum angle of confidence for far-field predictions was computed from Equation (3-75) to be 56 degrees. Each truncated array was inverse Fourier transformed to obtain the measured spectrum. Errors due to aliasing and lack of concentration were then determined in each case by direct comparison to the

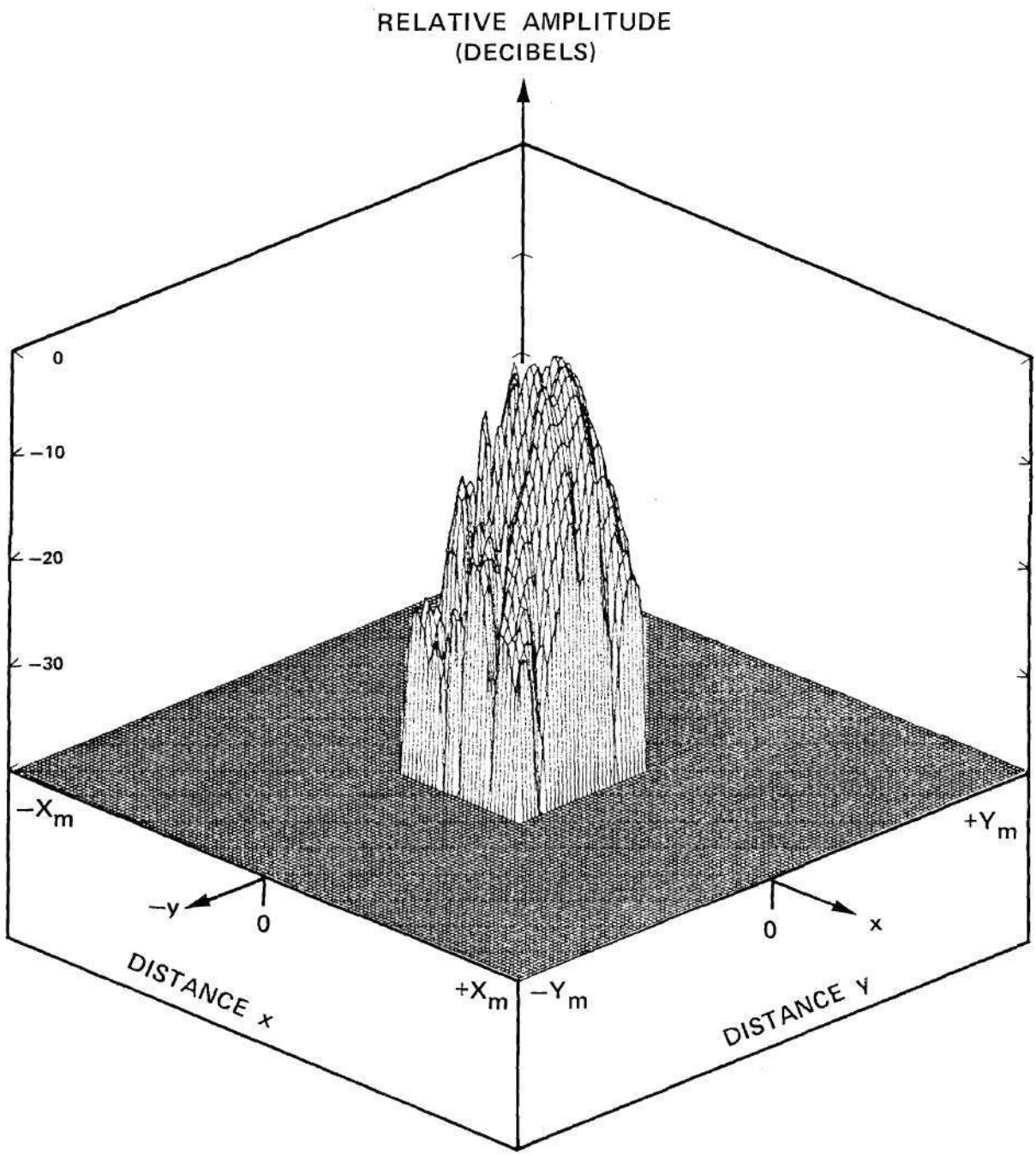

Figure 5-16. Measured Amplitude of Near-Field Response of Undersize Waveguide Truncated to 32 x 32 Measurement Area.

true spectrum. In addition, the far fields of the test antenna were predicted from the near-field probe responses over the 32 x 32 measurement area and compared to the true far fields as determined using the complete 128 x 128 data arrays. These data are presented below.

Graphs of the amplitude of the errors produced in the measured spectra are presented in Figures 5-17 through 5-22. The abscissas in these three dimensional graphs represent normalized wavenumbers, and the central circular region corresponds to real angles. The ordinate of each graph is the amplitude, in decibels, of the error relative to the maximum amplitude of the measured spectrum for orientation #1. Comparisons of these graphs show that the spectra for the E-plane horn probe exhibit significantly less error than do those of the undersize waveguide probe. The errors in the spectra for the open-end waveguide occupy an intermediate position relative to those of the other two probes. These results are in conformance with expectations based on the theoretical development of Chapter 2 and on the observed concentration of response of the three probes. Quantitative measures of the mean square error in the spectra of Figures 5-17 through 5-22 are presented in Table 5-4.

It has been tacitly assumed throughout that the probe which produces the least error in the measured spectrum will also produce the least error in the predicted far fields. The extent to which this tacit assumption is true is illustrated in Figures 5-23 through 5-28. The first three figures in this group are H-plane ($k_{yn}=0$) far-field power patterns of the test antenna as predicted from the near-field responses of the three probes. The next three figures are E-plane power patterns for which $k_{xn}=0$ and $|k_{yn}| \leq 1$. The patterns in all cases are those for

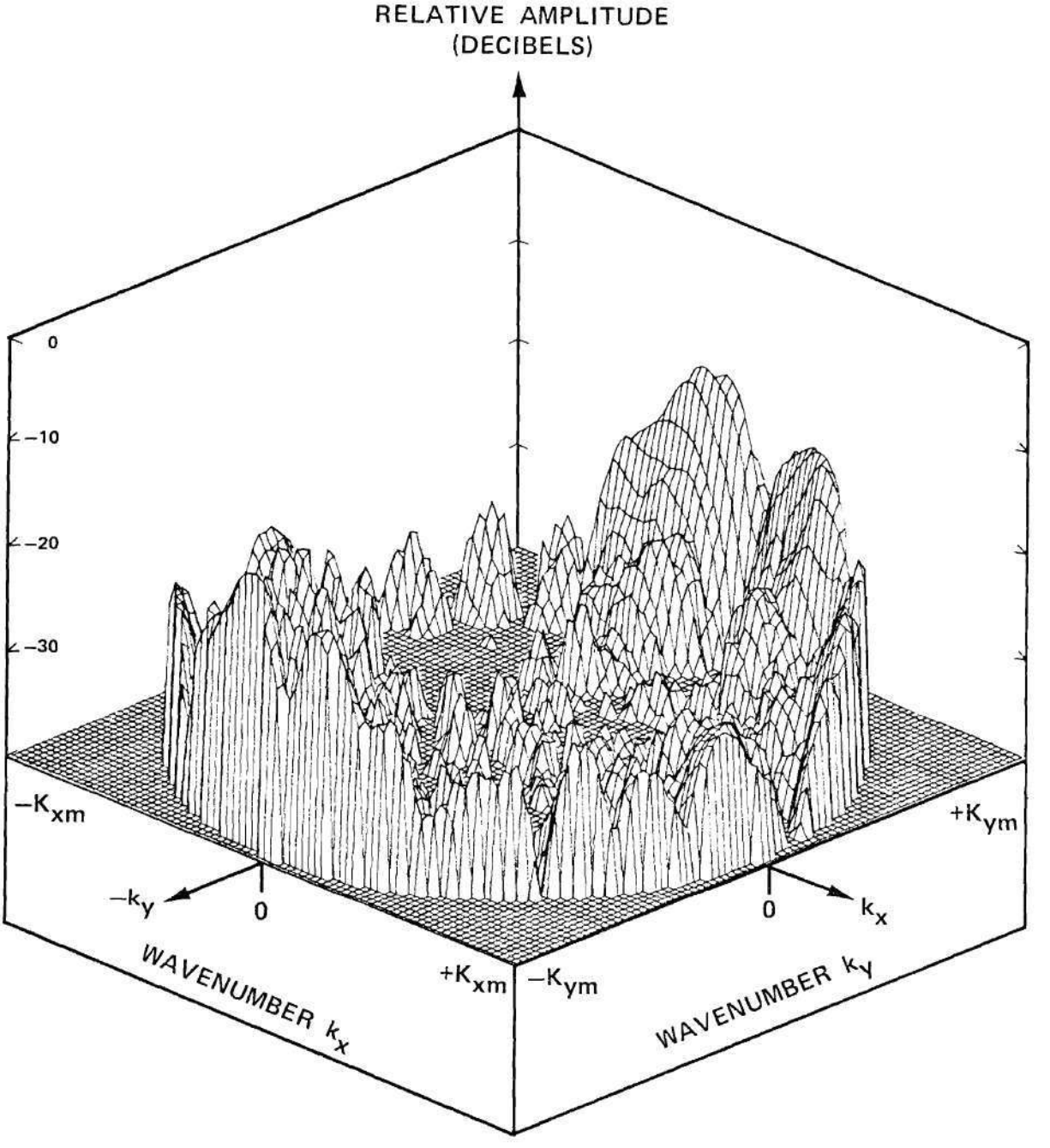

Figure 5-17. Amplitude of Error in Measured Spectrum for Undersize Waveguide Probe in Orientation #1 Due to Reduced Measurement Area.

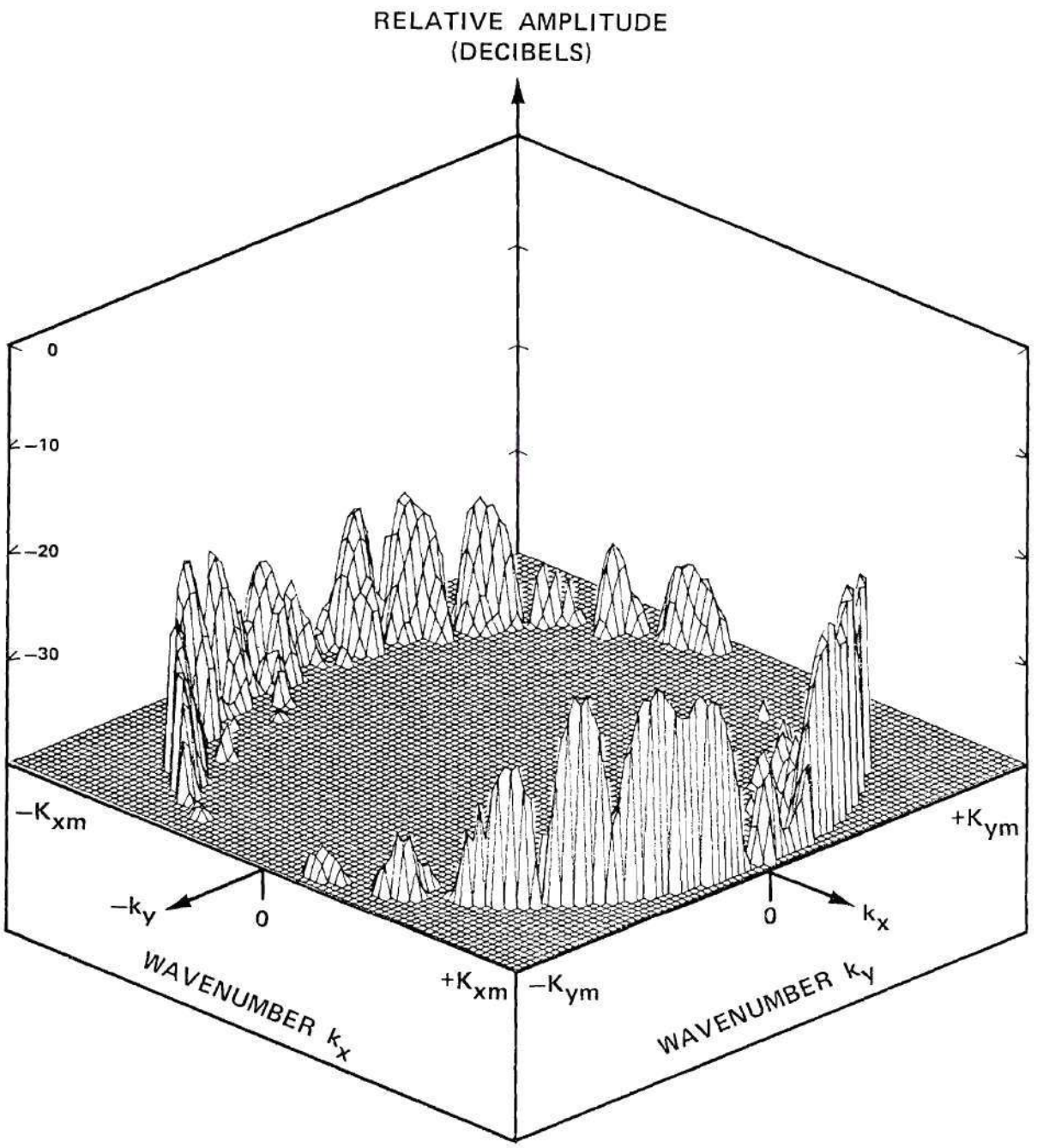

Figure 5-18. Amplitude of Error in Measured Spectrum for Undersize Waveguide Probe in Orientation #2 Due to Reduced Measurement Area.

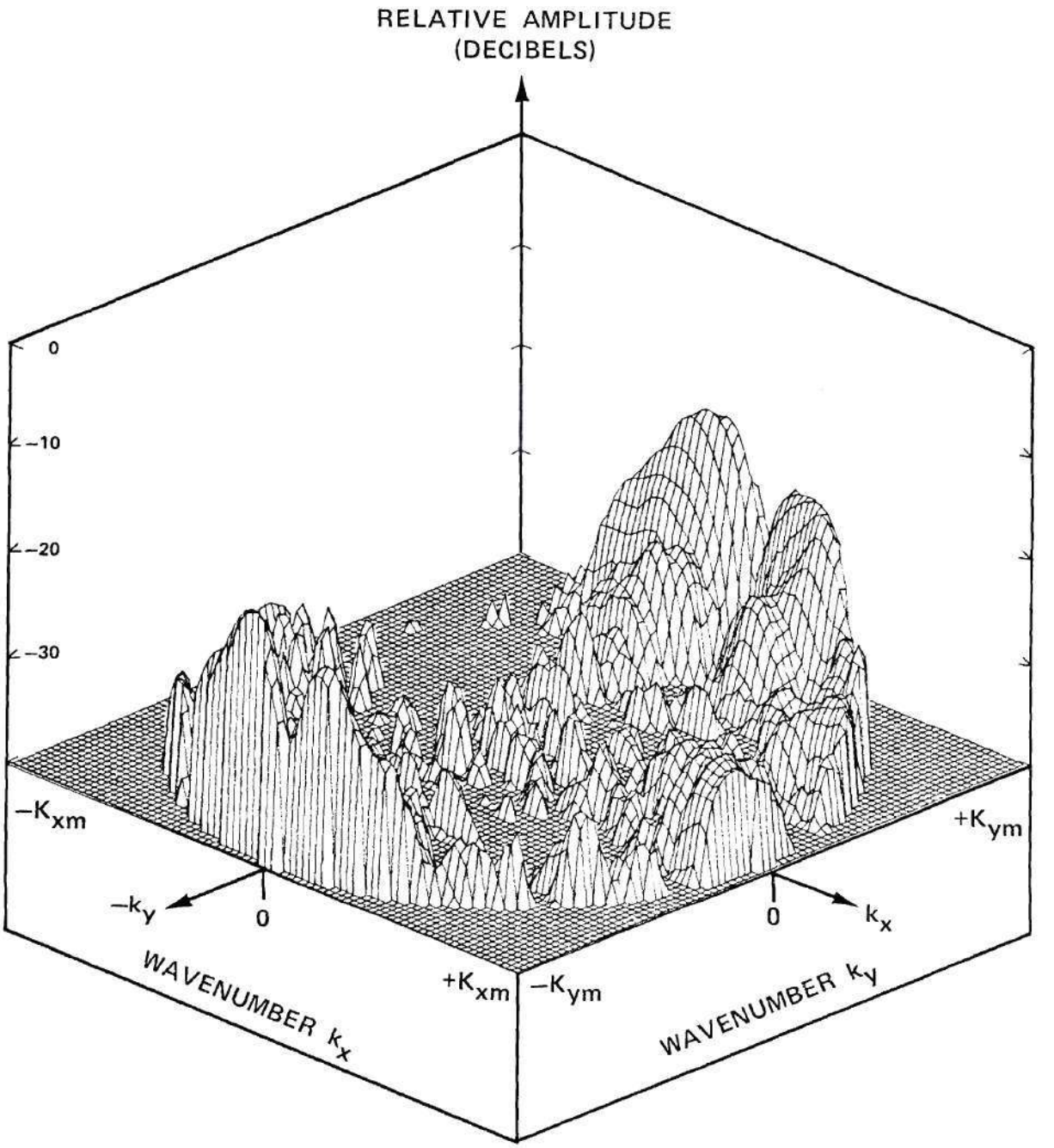

Figure 5-19. Amplitude of Error in Measured Spectrum for Open-End Waveguide Probe in Orientation #1 Due to Reduced Measurement Area.

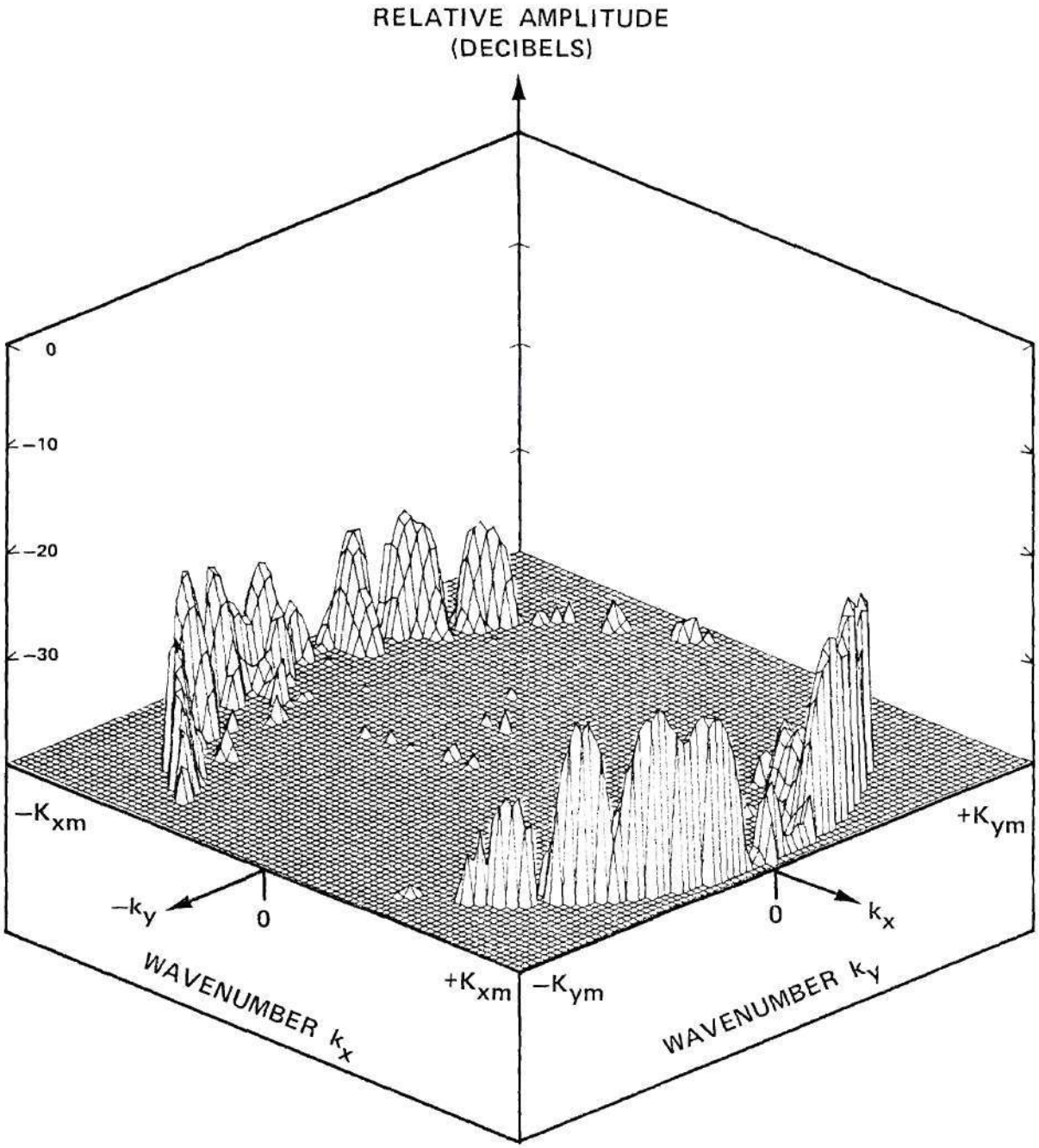

Figure 5-20. Amplitude of Error in Measured Spectrum for Open-End Waveguide Probe in Orientation #2 Due to Reduced Measurement Area.

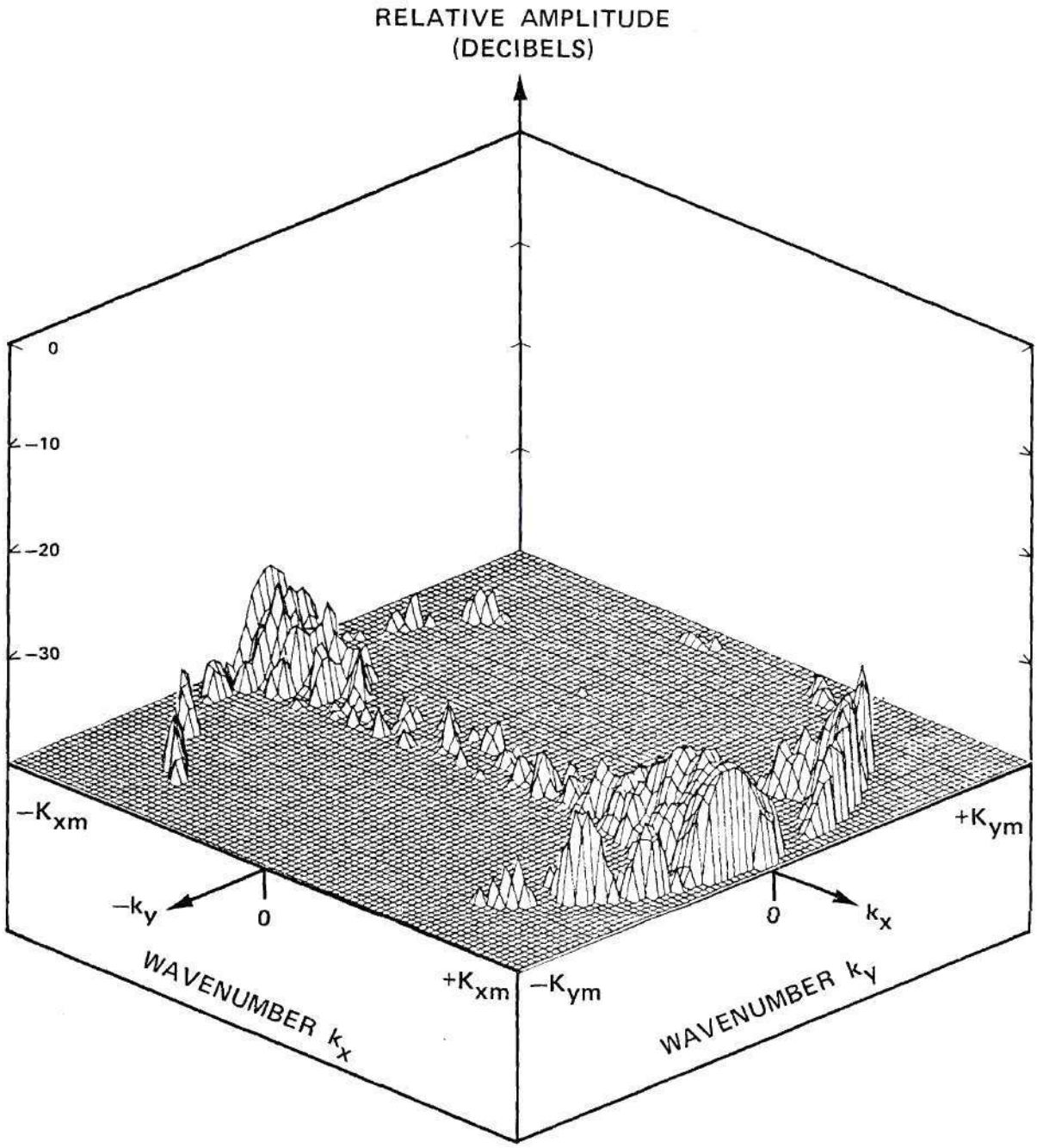

Figure 5-21. Amplitude of Error in Measured Spectrum for E-Plane Horn Probe in Orientation #1 Due to Reduced Measurement Area.

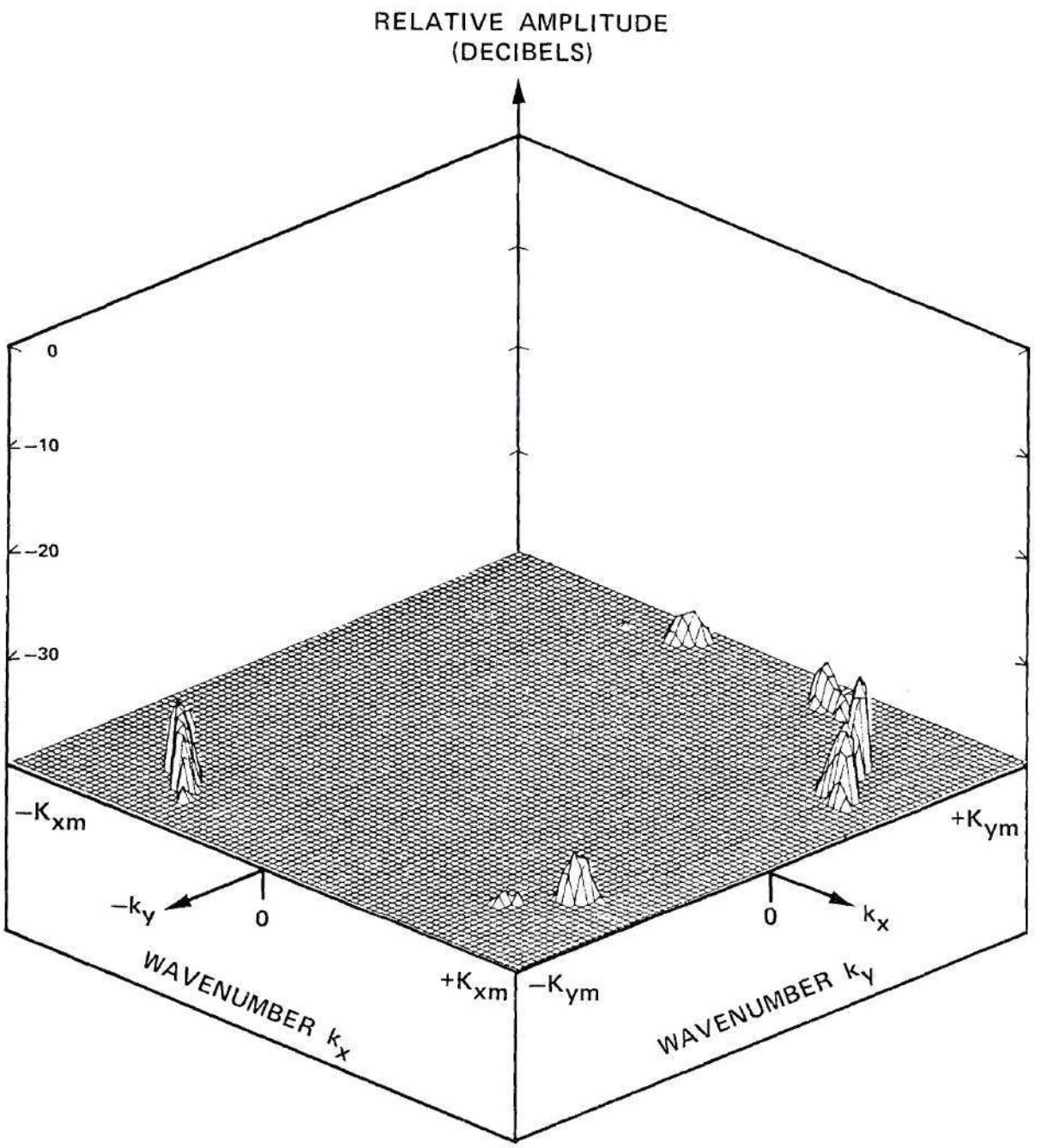

Figure 5-22. Amplitude of Error in Measured Spectrum for E-Plane Horn Probe in Orientation #2 Due to Reduced Measurement Area.

Table 5-4. Mean Square Errors in Measured Spectra

Probe	Mean Square Error	
	A_1	A_2
Undersize Waveguide	.0458	.267
Open-End Waveguide	.0224	.182
E-Plane Horn	.00387	.0765

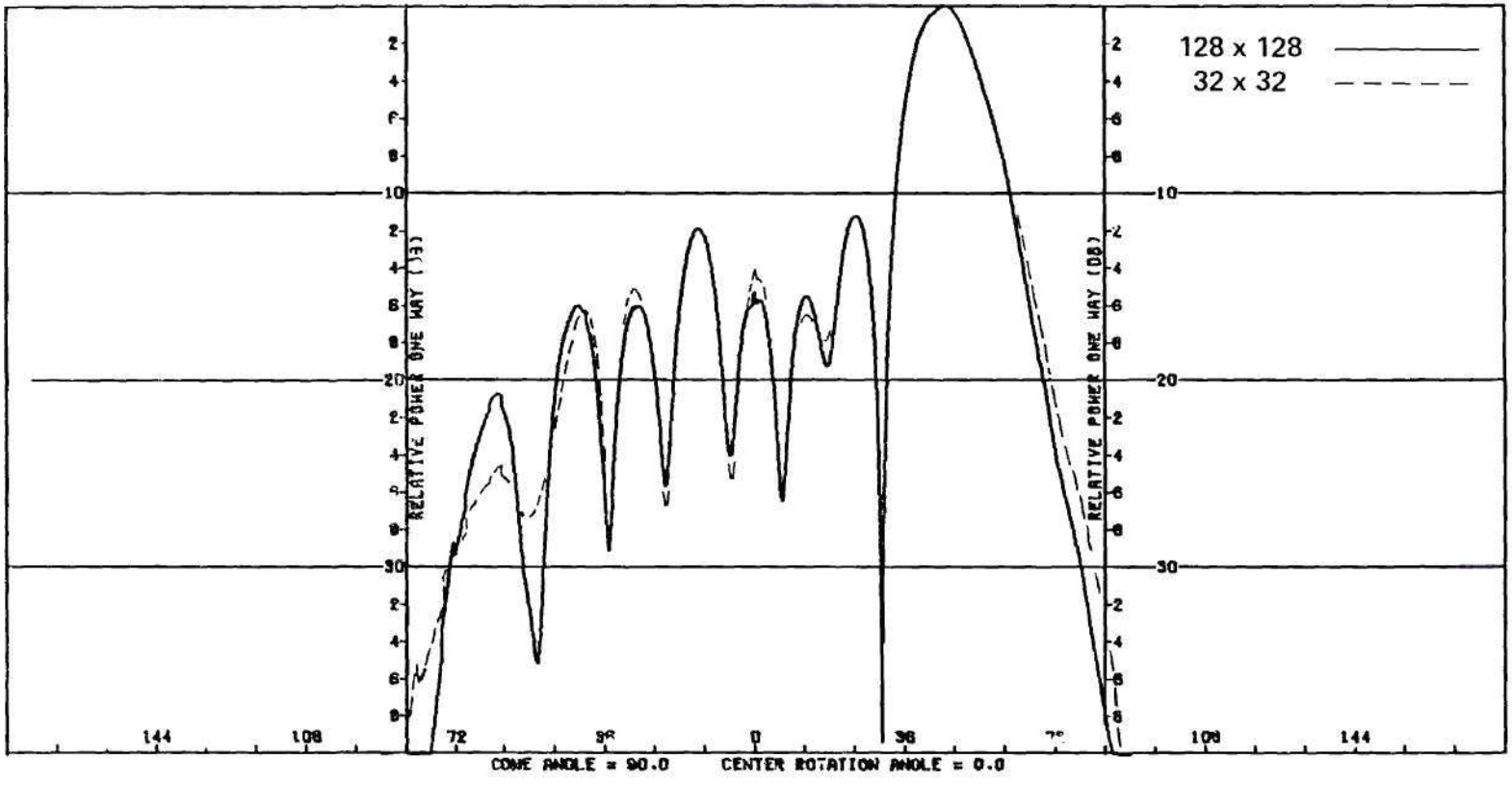

Figure 5-23. H-Plane Power Patterns Predicted From Near-Field Measurements Using Undersize Waveguide Probe (Elevation Components).

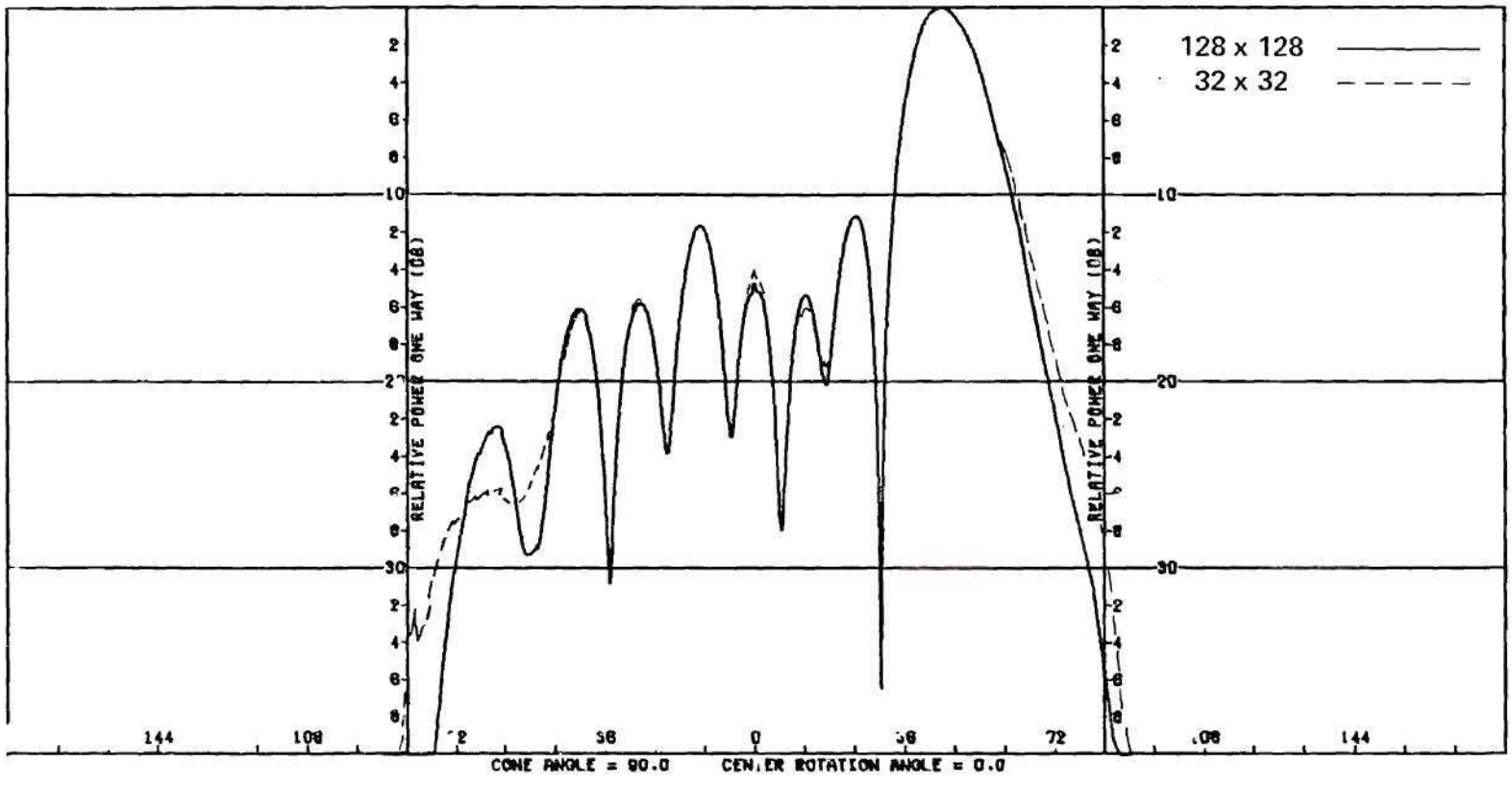

Figure 5-24. H-Plane Power Patterns Predicted From Near-Field Measurements Using Open-End Waveguide Probe (Elevation Components).

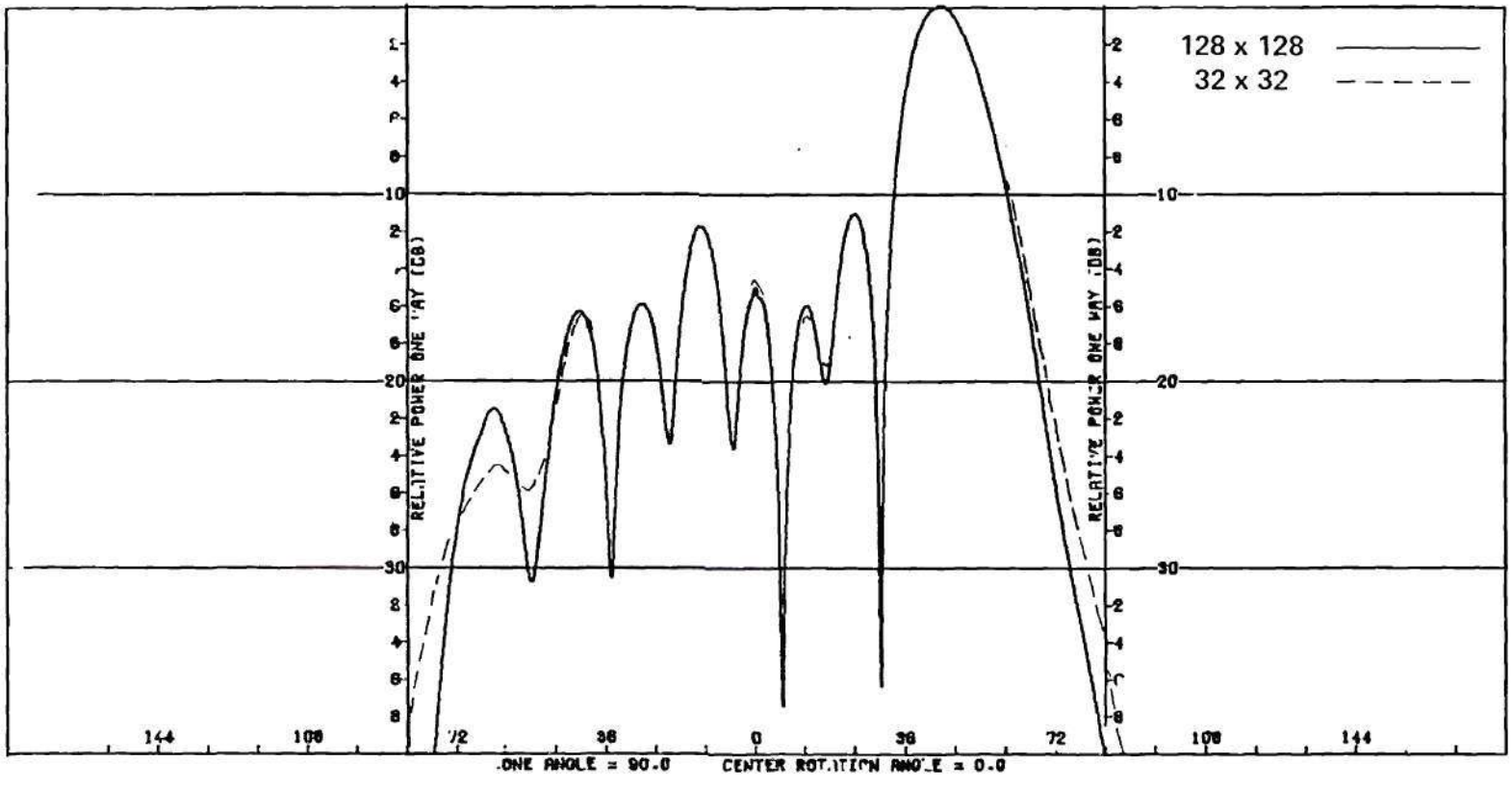

Figure 5-25. H-Plane Power Patterns Predicted From Near-Field Measurements Using E-Plane Horn Probe (Elevation Component).

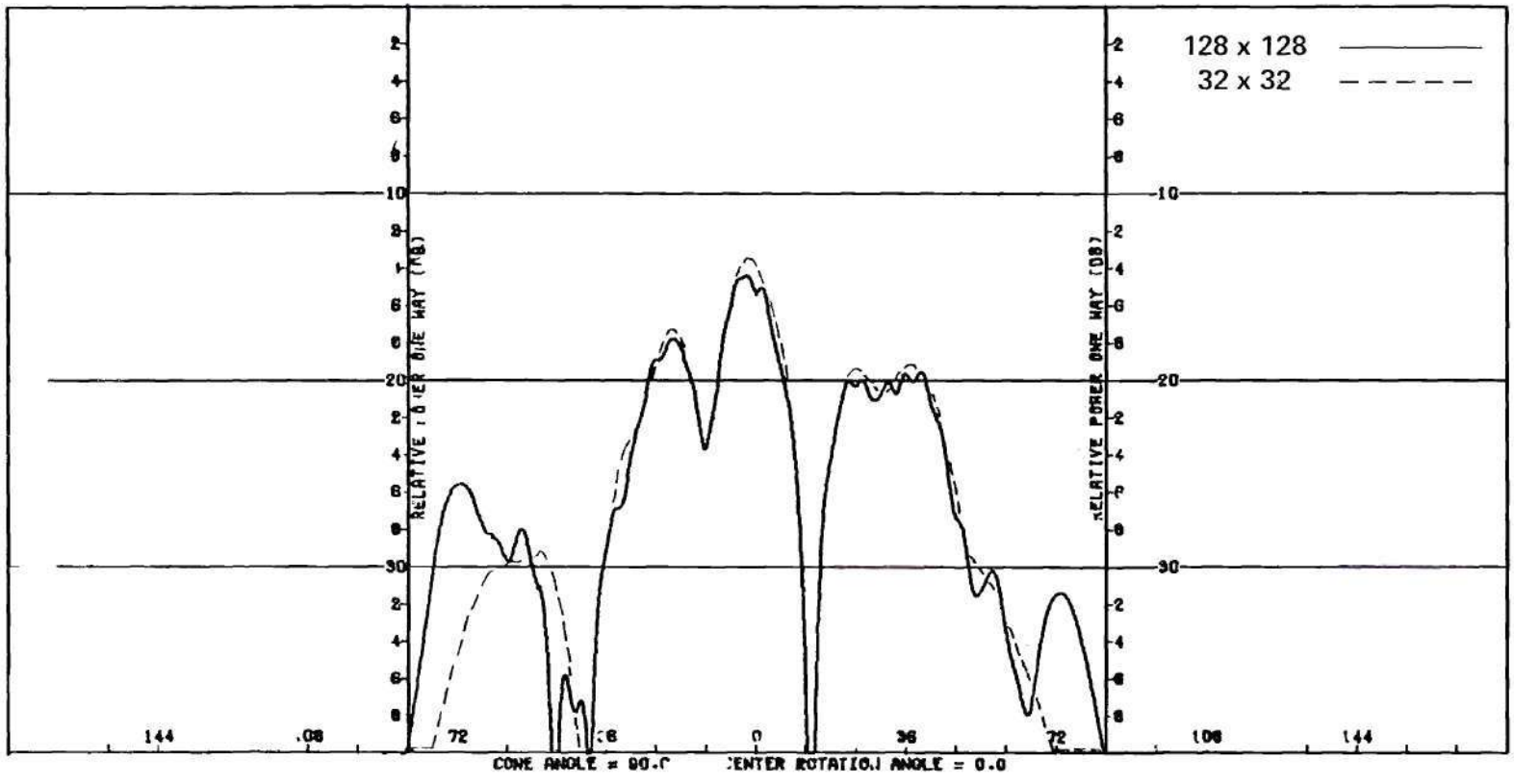

Figure 5-26. E-Plane Power Patterns Predicted From Near-Field Measurements Using Undersize Waveguide Probe (Elevation Component).

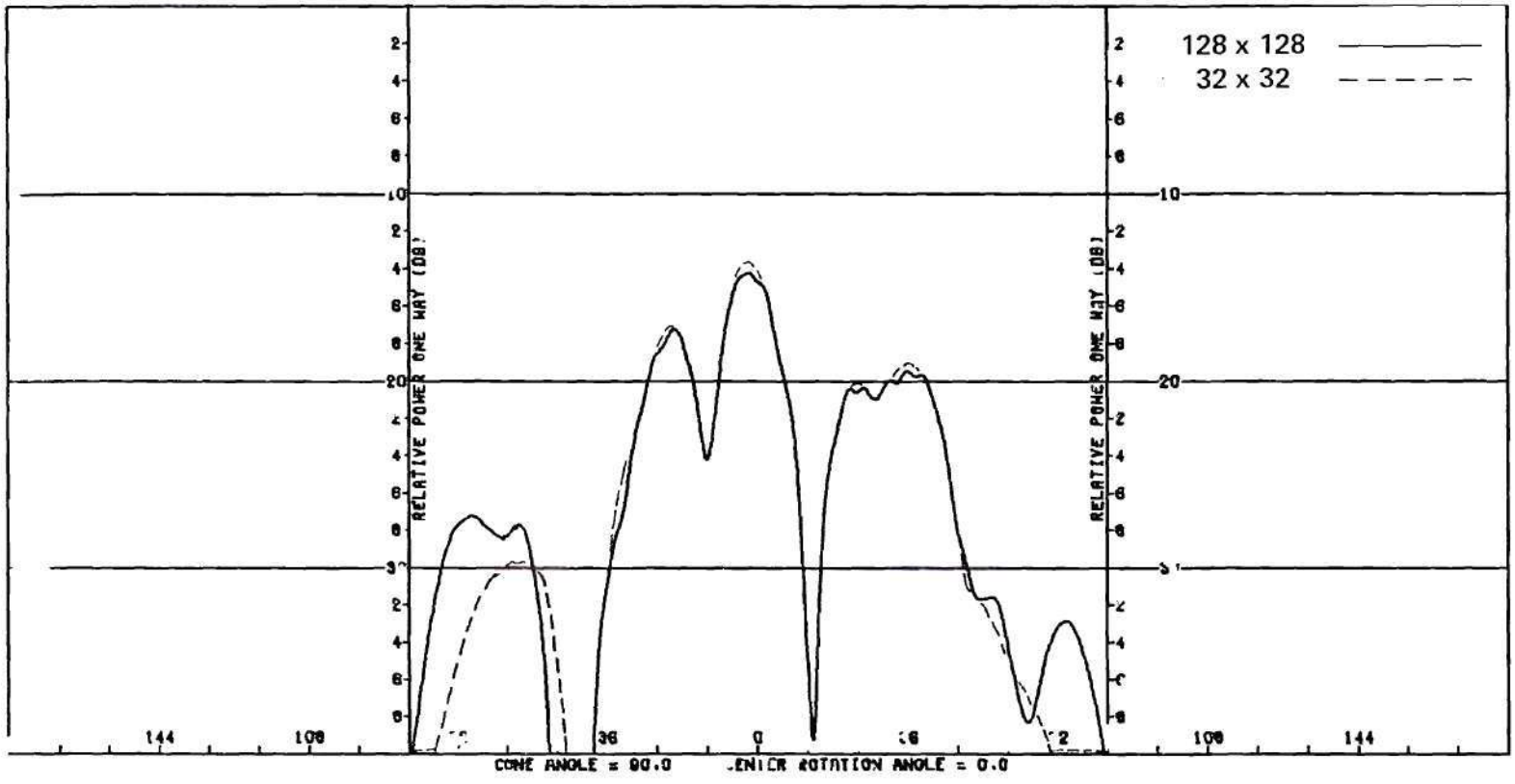

Figure 5-27. E-Plane Power Patterns Predicted From Near-Field Measurements Using Open-End Waveguide Probe (Elevation Component).

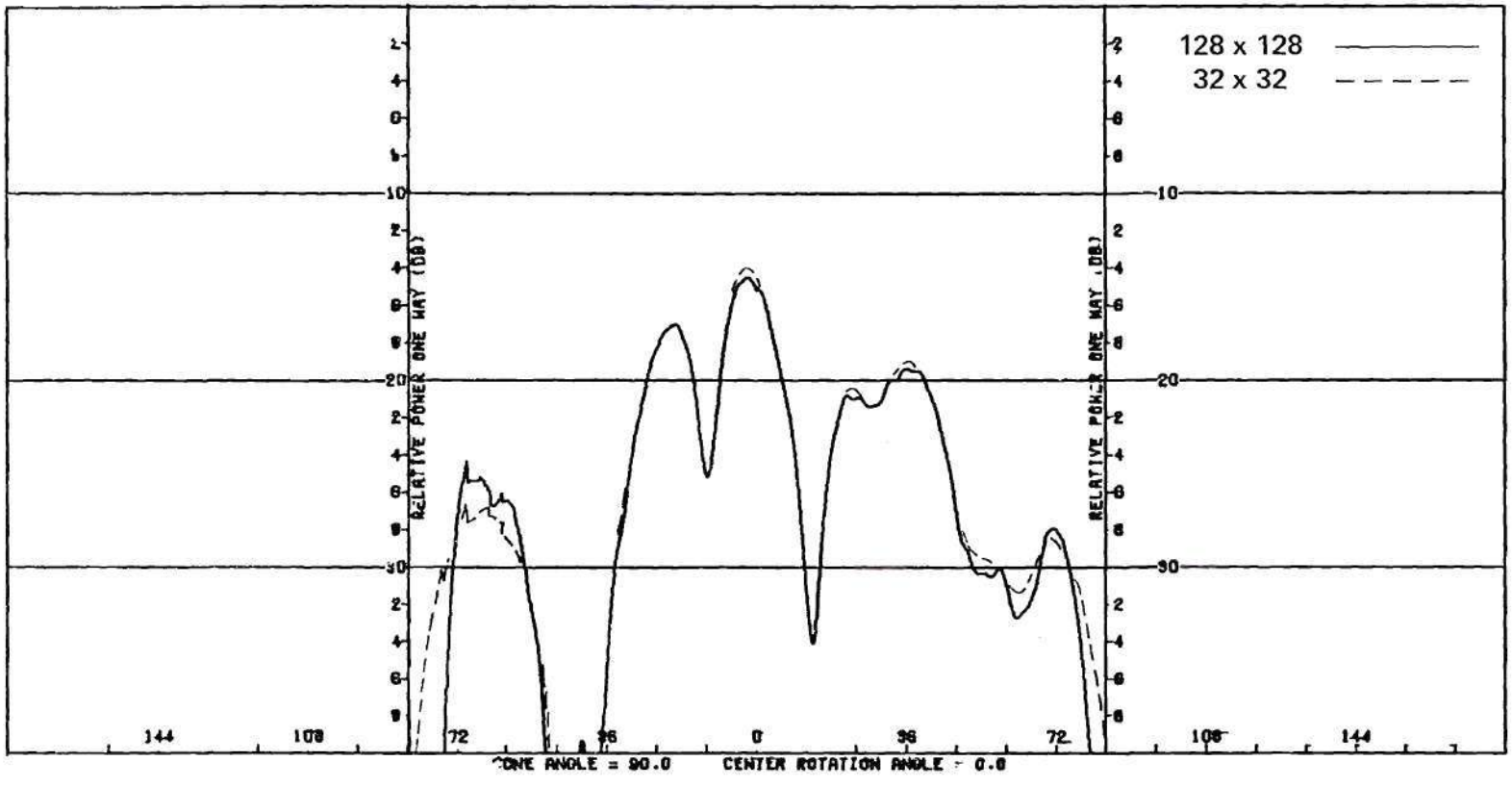

Figure 5-28. E-Plane Power Patterns Predicted From Near-Field Measurements Using E-Plane Horn Probe (Elevation Component).

the power density in the elevation component of the total electric field. Additional power patterns for the orthogonal azimuth component and for conical cuts are presented in Appendix F for completeness. The vertical scale ranges from zero to -40 decibels, and all patterns are shown relative to the peak of the main beams located at 45 degrees in Figures 5-23 through 5-25 for the respective probes.

Close examination of the H-plane power patterns in Figures 5-23 through 5-25 reveals that within the angular region defined by $|\theta_{max}| \leq 56$ degrees, the E-plane horn probe produces a slightly more accurate result than does the undersize waveguide probe or the open-end waveguide probe. The differences in accuracies, however, are not nearly as dramatic as those seen in the measured spectra of Figures 5-17 through 5-22. But closer examination of the errors in the spectra reveal that larger errors occur along the line $k_x=0$ (E-plane) than along $k_y=0$ (H-plane). Such would be expected since all three probes produced near-field responses that were more concentrated in x than in y.

Figures 5-26 through 5-28 present E-plane power patterns predicted from the three probe responses. Again, the E-plane horn probe produces a somewhat more accurate far-field prediction for $|\theta| \leq \theta_{max}$ than do the other two probes. The E-plane results show more clearly the effects of the probes than do the H-plane results as expected from the distributions of errors in the spectra.

The power patterns for the azimuth components and for conical pattern cuts through the main beam at $k_{xn} = .707$ presented in Appendix F show the same general trend; i.e., the E-plane horn probe yields a slightly more accurate far-field prediction when the measurement area is

truncated than do the other two probes.

It is noted in all cases that the predicted pattern deviates from the true pattern for angles outside of the region defined by $|\theta| \leq \theta_{max}$. This result is expected and corroborates the approximate maximum angle prediction of Crawford and Newell [17].

It is also noted that the true patterns in Figures 5-23 through 5-25, and those in Figures 5-26 through 5-28, do not agree exactly; i.e., the three probes produced three slightly different results even when all the data were used. For example, the right sidelobe at 36 degrees in Figure 5-26 exhibits more ripples than the same sidelobe in Figure 5-28.

These slight differences are attributed to reflections in the measurement environment. The undersize waveguide probe has a less directive pattern and is, therefore, more responsive to reflected signals than are the other two, more directive probes. It may be concluded, on the basis of this reasoning, that the less directive probe may also be less desirable, especially in measurement environments where reflections are significant.

The far-out sidelobes in the E-plane pattern of Figure 5-28 as predicted by the E-plane horn probe are somewhat different than those predicted by the other two probes. These differences, as well as the "glitches" in the pattern at -72 degrees, are attributed to errors in the characterization of the E-plane horn probe. Examination of the graph in Figure 5-7 along the line $k_{xn} = 0$ and near $k_{yn} = -1$ reveals a slight discrepancy in the probe data at low signal levels. These observations reinforce the importance of accurate probe characterization in making accurate far-field predictions.

As a final note, it is important to identify the reason for the rather small improvement in accuracy in the predicted far fields afforded by the E-plane horn when the errors in the measured spectra of Figures 5-17 through 5-22 would seem to indicate a much large improvement. The E-plane horn probe produced the most concentrated near-field response which, when sampled, truncated, and Fourier transformed, produced the measured spectrum having the least mean square error (Table 5.4) and the least absolute error (Figures 5-21 and 5-22). The far field of the E-plane horn is also the most directive as indicated in Figure 5-7. The directive properties of this probe tend to suppress those signal components at wavenumbers corresponding to wide angles in order to produce the desired concentrated near-field response. When the transformed data are corrected for the probe, the small errors are enhanced by the probe correction. The enhancement is greater for the more directive probe and smaller for the less directive probe. The net effects are manifested in the far-field predictions as only a slight improvement in accuracy for the case of the E-plane horn.

Equivalently, if probe correction were applied to the error spectra in Figures 5-17 through 5-22, it is expected that the graphs of the errors would then become very similar for all three probes. The errors for the E-plane horn would, however, be somewhat less than those for the other two probes in order to produce the more accurate far-field predications.

The experimental results confirm the theoretical expectation that the probe which produces the most concentrated near-field response also produces the measured spectra having the least error. This probe also

produces the most accurate predicted far-field patterns from near-field data contained within a reduced-size measurement area. In measurement situations where more power is radiated at wide angles by the test antenna and/or the measurement area is severely restricted in size, it is expected that even greater advantages of the optimum probe will be realized.

CHAPTER VI

CONCLUSIONS AND RECOMMENDATIONS

It is concluded that an optimum probe for near-field antenna measurements on a planar surface of finite size is one which maximizes the concentration of the power of its near-field response within the measurement area. For the class of rectangular horn probes, including dielectric-loaded, open-end waveguide probes, the E-plane dimension of the probe is the more critical and should be approximately one wavelength in size to ensure maximum concentration of response to a linearly polarized test antenna. The H-plane dimension of the probe has less effect on the concentration of response, and a size of approximately one wavelength will ensure an adequate concentration of response.

It is also concluded that the degree of improvement offered by the optimum probe in the accuracy of the predicted far-field patterns may be small in cases where the test antenna radiates insignificant amounts of power at angles far from the normal to the measurement plane. In such cases, the differences in concentrations of responses of suboptimum and optimum probes for practical size measurement areas may be so slight as to produce only insignificant differences in either the measured spectra or predicted far fields; i.e., the probe is indeed arbitrary. In those other cases where the measurement area is restricted in size, and/or the antenna under test radiates significant power at wide angles, it is expected that the optimally designed probe will offer significant improvements.

The optimum design of other probe configurations may be determined by applying the maximum power criterion. Mathematical models of the probe and test antenna of interest may be used in an analytical procedure based on the reciprocity theorem to determine the response of the probe to the test antenna as a function of probe position on the measurement plane. The design parameters of the probe, such as aperture size, flare length, and polarization, are then varied until a maximum in the concentration of the power in the response is obtained. Only the amplitude of the response need be calculated. For simplicity, only principal plane near-field responses need be used to evaluate the concentration of response. Ideally, a single probe design would serve to maximize the concentrations of response for both probe orientations; however, such is not expected to be the case in general. A compromise design, or two distinct, independent probes, will then be indicated.

From theoretical consideration of the measurement equations, it is concluded that either a short electric or magnetic dipole constitutes an ideal probe for near-field measurements on a plane; i.e., a probe for which no compensation is required. This conclusion is based on the assumption that the measured spectra may be obtained without error by inverse Fourier transformation of the measured probe response over the measurement area. Since an ideal dipole responds to the field at a point, its response would be less concentrated than that of a more directive probe. The experimental results obtained show a direct correlation between probe directivity and concentration of near-field response. Furthermore, these results show that the less concentrated the near-field response, the larger the mean square error in the measured spectrum.

Hence, any advantages in simplicity of computations that may accrue from use of an ideal probe may be offset by the errors introduced as a result of the finite measurement area and spatial sampling of the probe response over it.

Inasmuch as the present investigation has taken no account of the effects of random noise on the measured response of the probe, it is recommended that this be done. It is anticipated that the optimality criterion defined in the present work would be modified somewhat to guarantee a specified signal-to-noise ratio in the predicted far fields for a given signal-to-noise ratio in the measurements. The analytical procedures developed in the current work would be applicable to the probe design.

It is also recommended that additional probe configurations be investigated to determine any advantages which may be offered. In particular, conical horn antennas, as fashioned from circular waveguides, should be considered. Moreover, the use of left-hand and right-hand circular polarized probes should be investigated since the amplitudes of the response of the probes would ideally be identical; hence, the concentration of the response would be maximized for both independent measurements required. Any difficulties that may be encountered in the probe compensation procedure as a result of responses which differ only in phase should be identified at the outset.

The alternative method of analysis which utilizes the plane wave spectra of the probe and test antenna to determine the near-field probe response should be implemented. It is anticipated that significant savings in computation time would be realized so that a complete analysis

of probe response would be possible. In addition, direct computation of errors produced in the measured spectra and predicted far fields would become feasible in the computer simulation and probe design procedure. It is also recommended that oversampling of the near-field response be investigated using the computer simulation to determine the merits of this means of reducing aliasing errors as compared to the use of an optimum probe.

With regard to the measurement procedure, it is recommended that the A and Q channels of the optical encoder for the x position of the near-field probe be interchanged. The measured near-field data would then be recorded in the coordinate system of the test antenna so that no correction would be required in the data processing. Also, it is recommended that the phase reference control on the receiver be set to the A→B position so that no phase correction would be necessary during the data processing. Finally, it is recommended that a power leveling device be installed in the measurement system so that the effects of drifts in the power output of the klystron tube be minimized.

APPENDIX A

SPHEROIDAL FUNCTIONS [22-29]

A.1 The Functions S_{on}

The angular prolate spheroidal wave functions of zero order $S_{on}(c,\eta)$ satisfy the differential equation

$$(1 - \eta^2)\frac{d^2u}{d\eta^2} - 2\eta\frac{du}{d\eta} + (\chi + c^2\eta^2)u = 0 \qquad \text{(A-1)}$$

in the closed η interval $[-1,1]$ only for certain discrete real positive values

$$0 < \chi_o(c) < \chi_1(c) < \ldots \qquad \text{(A-2)}$$

of the parameter χ. Corresponding to each eigenvalue χ_n, $n = 0,1,\ldots,$ there is a unique solution $S_{on}(c,\eta)$ such that $S_{on}(c,0) = P_n(0)$ where $P_n(\eta)$ is the n^{th} Legendre polynomial. The eigenvalues χ_n are continuous functions of c and $\chi_n(0) = n(n+1)$, $n = 0,1,\ldots$

The functions $S_{on}(c,\eta)$ also satisfy the integral equation

$$\nu_n(c)S_{on}(c,\eta) = \int_{-1}^{1} S_{on}(c,\alpha)e^{jc\alpha\eta}d\alpha \qquad \text{(A-3)}$$

for discrete eigenvalues $\nu_n(c)$, $n = 0,1,\ldots,$ which correspond to χ_n. Equation (A-3) is valid for all η, real and complex and reveals the similarity to the Fourier integral as elucidated below.

The functions $S_{on}(c,\eta)$ are entire functions of η, they have no zeros at $\eta = \pm 1$, they are real for real η, and they have exactly n zeros in the interval (-1,1). They are even or odd functions of η, according to whether n is even or odd. The functions $\{S_{on}(c,\eta)\}$ are doubly orthogonal on the intervals (-1,1) and $(-\infty,\infty)$, and form complete sets with respect to square integrable functions and functions having bounded support, respectively as discussed below.

A second set of functions $R_{on}^{(1)}(c,\eta)$, $n = 0,1,\ldots$, called radial prolate spheroidal wave functions, which differ from the angular functions only by a real scale factor,

$$R_{on}^{(1)}(c,\eta) = k_n(c) S_{on}(c,\eta) \tag{A-4}$$

are also solutions to Equation (A-1). The eigenvalues $\nu_n(c)$ of Equation (A-3) are related to $R_{on}^{(1)}(c,\eta)$ at $\eta = 1$ by

$$\nu_n(c) = 2j^n R_{on}^{(1)}(c,1) \tag{A-5}$$

where $R_{on}^{(1)}(c,1)$ is real. Hence, the eigenvalues $\nu_n(c)$ are real for n even, and imaginary for n odd; i.e.,

$$\nu_n(c) = j^n \left| \nu_n(c) \right| \quad . \tag{A-6}$$

The functions $S_{on}(c,\eta)$ also satisfy the integral equation, for $|\eta| < 1$,

$$\nu_n(c)\gamma_n(c)S_{on}(c,\eta) = \int_{-\infty}^{\infty} S_{on}(c,\alpha)e^{jc\alpha\eta}d\alpha \qquad (A-7)$$

where $\gamma_n(c)$ is a proportionality constant which relates the normalization on $(-\infty,\infty)$ to that on $(-1,1)$ as seen below.

The orthogonality relation on $(-1,1)$ can be arbitrarily designated by [22]

$$\int_{-1}^{1} S_{om}(c,\eta)S_{on}(c,\eta)d\eta = \lambda_n\delta_{mn} \qquad (A-8)$$

where δ_{mn} is the Kronecker delta and where $\{\lambda_n(c)\}$ is a set of arbitrary positive numbers. On the other interval $(-\infty,\infty)$, it can be shown that

$$\int_{-\infty}^{\infty} S_{om}(c,\eta)S_{on}(c,\eta)d\eta = \gamma_n(c)\lambda_n(c)\delta_{mn} \qquad (A-9)$$

i.e., the normalization constants on $(-\infty,\infty)$ are proportional to the arbitrarily chosen normalization constants $\{\lambda_n(c)\}$ on $(-1,1)$, where the proportionality constants $\{\gamma_n(c)\}$ are real positive numbers.

In keeping with established convention, the normalization on $(-\infty,\infty)$ will be chosen to be unity; i.e.,

$$\gamma_n(c)\lambda_n(c) = 1 \quad . \qquad (A-10)$$

As consequences, it is found that [22]

$$\gamma_n(c) = \frac{2\pi}{c|\nu_n|^2} \qquad (A-11)$$

and

$$\lambda_n(c) = \frac{1}{\gamma_n} = \frac{c|\nu_n|^2}{2\pi} \quad . \tag{A-12}$$

The spheroidal functions $S_{on}(c,\eta)$ can be expanded in terms of Gegenbaur polynomials $T_k^0(\eta)$ [31,42]

$$S_{on}(c,\eta) = \sum_{k=0,1}^{\infty}{}' d_k(c|0n) T_k^0(\eta) \tag{A-13}$$

where the prime denotes summation over only even or odd values of k depending on whether n is even or odd, respectively. The expansion (A-13) converges rapidly everywhere inside of the interval (-1,1), but outside it converges more and more slowly with increasing values of η.

An alternative expansion is in terms of Bessel functions [21,31]

$$S_{on}(c,\eta) = \frac{j^n(2\pi)^{\frac{1}{2}}}{\nu_n(c)} \sum_{k=0,1}^{\infty}{}' a_k(c|0n) \frac{J_{k+\frac{1}{2}}(c\eta)}{(c\eta)^{\frac{1}{2}}} \tag{A-14}$$

where the coefficients a_k are related to d_k by

$$a_k(c|0n) = j^{k-n} \frac{\Gamma(k+1)}{k!} d_k(c|0n) \tag{A-15}$$

The coefficients a_k and d_k are real and have been tabulated for certain values of c and n [25,31].

The functions $S_{on}(c,\eta)$ also satisfy the integral equations

$$\nu_n^*(c) S_{on}(c,\eta) = \int_{-1}^{1} S_{on}(c,\alpha) e^{-jc\alpha\eta} d\alpha \tag{A-16}$$

for all η, real and complex, and

$$\nu_n^*(c)\gamma_n S_{on}(c,\eta) = \int_{-\infty}^{\infty} S_{on}(c,\eta)e^{-jc\alpha\eta} \tag{A-17}$$

for $|\eta| \leq 1$. The first of these equations is established by integrating both sides of Equation (A-3) to give

$$\int_{-1}^{1} \nu_n S_{on}(c,\eta)e^{-jc\chi\eta}d\eta = \int_{-1}^{1} e^{-jc\chi\eta}[\int_{-1}^{1} S_{on}(c,\alpha)e^{jc\alpha\eta}d\alpha]d\eta \tag{A-18}$$

Interchanging the order of integration on the right hand side yields

$$I = \int_{-1}^{1} \nu_n S_{on}(c,\eta)e^{-jc\chi\eta}d\eta = \int_{-1}^{1} S_{on}(c,\alpha)[\int_{-1}^{1} e^{jc\eta(\alpha-\chi)}d\eta]d\alpha \tag{A-19}$$

Carrying out the integration in brackets yields

$$I = \frac{2\pi}{c}\int_{-1}^{1} S_{on}(c,\alpha)\ \frac{\sin c(\alpha-\chi)}{\pi(\alpha-\chi)}\ d\alpha \tag{A-20}$$

But [22],

$$\int_{-1}^{1} S_{on}(c,\alpha)\ \frac{\sin c(\alpha-\chi)}{\pi(\alpha-\chi)}\ d\alpha = \lambda_n S_{on}(c,\chi) \tag{A-21}$$

Using Equation (A-12) and the relation $|\nu_n|^2 = \nu_n\nu_n^*$ in Equation (A-20) yields

$$\int_{-1}^{1} \nu_n S_{on}(c,\eta)e^{-jc\chi\eta}d\eta = \nu_n\nu_n^* S_{on}(c,\chi) \tag{A-22}$$

from which Equation (A-16) follows by the simple redefinition of variables η and χ in Equation (A-22) to α and η, respectively.

Equation (A-17) can be established by using the orthogonality condition on $(-\infty,\infty)$

$$\int_{-\infty}^{\infty} S_{on}(c,\eta)S_{on}(c,\eta)d\eta = \gamma_n\lambda_n \qquad \text{(A-23)}$$

and the Equations (A-3) and (A-8). Substituting for the first $S_{on}(c,\eta)$ in Equation (A-23) the integral representation in Equation (A-16) gives

$$\int_{-\infty}^{\infty} [\frac{1}{\nu_n^*}\int_{-1}^{1} S_{on}(c,\alpha)e^{-jc\alpha\eta}d\alpha]S_{on}(c,\eta)d\eta = \gamma_n\lambda_n \quad . \qquad \text{(A-24)}$$

Interchange the order of integration to yield

$$\int_{-1}^{1} [\frac{1}{\nu_n^*}\int_{-\infty}^{\infty} S_{on}(c,\eta)e^{-jc\alpha\eta}d\eta]S_{on}(c,\alpha)d\alpha = \gamma_n\lambda_n \quad . \qquad \text{(A-25)}$$

In order for Equation (A-25) to be the identity Equation (A-8), the bracketed expression must equal $\gamma_n S_{on}(c,\eta)$, and Equation (A-17) is established.

A.2 The Functions $\psi_n(c,t)$, $\psi_n(c,f)$

It is desirable to generalize the above results to arbitrary intervals on the familiar axes of time t and frequency f. Make the changes of variables

$$\alpha = 2t/T \qquad \text{(A-26)}$$

$$\eta = f/W \tag{A-27}$$

in Equation (A-3) to yield

$$\nu_n S_{on}(c,2t/T) = \int_{-W}^{W} \frac{S_{on}(c,f/W)}{W} e^{j\frac{2c}{WT}ft} df \quad . \tag{A-28}$$

To make this relation conform to the Fourier integral, set

$$\frac{c}{WT} = \pi \tag{A-29}$$

Define the constant b such that

$$\int_{-W}^{W} b^2 S_{on}^2(c,f/W)df = \lambda_n \tag{A-30}$$

After integrating, b is found to be

$$b = \sqrt{\frac{1}{W}} \tag{A-31}$$

Define

$$\psi_n(c,f) = \sqrt{\frac{1}{W}}\, S_{on}(c,f/W) \tag{A-32}$$

$$\psi_n(c,t) = \sqrt{\frac{2}{T}}\, S_{on}(c,2t/T) \tag{A-33}$$

and substitute into Equation (A-28) to yield

$$\nu_n \sqrt{\frac{T}{2}}\ \psi_n(c,t) = \int_{-W}^{W} \frac{\psi_n(c,f)}{\sqrt{W}} e^{j2\pi ft} df \qquad \text{(A-34)}$$

Combining all constants on the left side yields

$$j^n \sqrt{\lambda_n}\ \psi_n(c,t) = \int_{-W}^{W} \psi_n(c,f) e^{j2\pi ft} df \qquad \text{(A-35)}$$

where the relations in Equations (A-6), (A-12), and (A-29) have been used to obtain

$$\nu_n \sqrt{\frac{WT}{2}} = j^n \sqrt{\lambda_n} \qquad \text{(A-36)}$$

Equation (A-35) states that the function

$$g(t) = j^n \sqrt{\lambda_n}\ \psi_n(c,t) \qquad \text{(A-37)}$$

is bandlimited as given by the inverse Fourier transform of $\psi_n(c,f)$ multiplied by the rectangular window function $p_w(f) = 1$ for $|f| \leq W$, $= 0$ otherwise; i.e.,

$$j^n \sqrt{\lambda_n}\ \psi_n(c,t) = F^{-1}\{\psi_n(c,f) p_w(f)\} \quad . \qquad \text{(A-38)}$$

By the inversion integral,

$$\psi_n(c,f) p_w(f) = \int_{-\infty}^{\infty} j^n \sqrt{\lambda_n}\ \psi_n(c,t) e^{-j2\pi ft} dt \qquad \text{(A-39)}$$

where $p_w(f)$ is used to denote the fact that this integral equation is valid only for $|f| \leq W$.

Another useful relation occurs for the case where $\psi_n(c,t)$ is known only over the finite interval $(-T/2,T/2)$. From Equation (A-35) there results

$$(-j)^n\sqrt{\lambda_n}\,\psi_n(c,f) = \int_{-T.2}^{T/2} \psi_n(c,t)e^{-j2\pi ft}dt \quad . \tag{A-40}$$

Multiply both sides by $j^n\sqrt{\lambda_n}$ to yield

$$\lambda_n\psi_n(c,f) = \int_{-T/2}^{T/2} j^n\sqrt{\lambda_n}\,\psi_n(c,t)e^{-j2\pi ft}dt \quad . \tag{A-41}$$

Equation (A-41) states that when the bandlimited function $j^n\sqrt{\lambda_n}\,\psi_n(c,t)$ is truncated to the finite interval $(-T/2,T/2)$, its Fourier transform $\lambda_n\psi_n(c,f)$ in the interval $-W \leq f \leq W$ differs only by a constant factor λ_n from that of the original function; however, since $j^n\sqrt{\lambda_n}\,\psi_n(c,t)p_{T/2}(t)$ is of finite duration, the corresponding transform $\lambda_n\psi_n(c,f)$ is no longer limited to the interval $-W \leq f \leq W$.

Apply Parseval's theorem to Equation (A-38) to yield the "energy" in the signal as

$$E = \int_{-\infty}^{\infty} |g(t)|^2dt = \int_{-\infty}^{\infty} |G(f)|^2df \tag{A-42}$$

$$E = \int_{-\infty}^{\infty} |j^n\sqrt{\lambda_n}\,\psi_n(c,t)|^2dt = \int_{-\infty}^{\infty} |\psi_n(c,f)p_w(f)|^2df \tag{A-43}$$

$$E = \lambda_n^2\gamma_n = \lambda_n \tag{A-44}$$

since by Equation (A-12) $\gamma_n = 1/\lambda_n$. When Parseval's theorem is applied to to Fourier transform pair Equation (A-41), there results

$$E' = \int_{-\infty}^{\infty} |\lambda_n \psi_n(c,f)|^2 df = \int_{-\infty}^{\infty} |j^n \sqrt{\lambda_n}\, \psi_n(c,t) p_{T/2}(t)|^2 dt \qquad \text{(A-45)}$$

$$E' = \lambda_n^2 \quad . \qquad \text{(A-46)}$$

Hence, truncating the bandlimited function $j^n \sqrt{\lambda_n}\, \psi_n(c,t)$ has the effect of diminishing its total energy by a factor of λ_n. The energy of the truncated function contained in the interval $-W \le f \le W$ is λ_n^3.

A.3 The Functions $\psi_n(c,k_x)$, $\psi_n(c,x)$

Near-field techniques consider wavenumber-limited functions $\psi_n(c,x)$ defined by

$$\psi_n(c,x) = a \int_{-k_{max}}^{k_{max}} \psi_n(c,k_x) e^{-jk_x x} dk_x \qquad \text{(A-47)}$$

where the constant of proportionality is to be determined. Make the change of variables

$$\eta = \frac{x}{x_{max}} \qquad \text{(A-48)}$$

$$\alpha = \frac{k_x}{k_{max}} \qquad \text{(A-49)}$$

in Equation (A-16) to yield

$$\nu_n^*(c) S_{on}(c, \frac{x}{x_{max}}) = \int_{-k_{max}}^{k_{max}} S_{on}(c, \frac{k_x}{k_{xmax}}) e^{-jc \frac{k_x x}{x_{max} k_{max}}} \frac{dk_x}{k_{max}} \qquad \text{(A-50)}$$

To make Equation (A-50) correspond to the Fourier integral, set

$$c = x_{max} k_{max} \quad . \qquad \text{(A-51)}$$

Define

$$\psi_n(c,k_x) = \sqrt{\frac{1}{k_{max}}} S_{on}(c,k_x/k_{max}) \qquad \text{(A-52)}$$

$$\psi_n(c,x) = \sqrt{\frac{1}{x_{max}}} S_{on}(c,x/x_{max}) \qquad \text{(A-53)}$$

Substitute these definitions into Equation (A-50) to yield

$$\nu_n^*(c) \sqrt{x_{max}} \psi_n(c,x) = \int_{-k_{max}}^{k_{max}} \frac{\psi_n(c,k_x)}{\sqrt{k_{max}}} e^{-jk_x x} dk_x \qquad \text{(A-54)}$$

Combine all constants onto the left side to give

$$(-j)^n \sqrt{2\pi\lambda_n} \psi_n(c,x) = \int_{-k_{max}}^{k_{max}} \psi_n(c,k_x) e^{-jk_x x} dk_x \qquad \text{(A-55)}$$

where the relation

$$\sqrt{\nu_n^{*2} c} = (-j)^n \sqrt{2\pi\lambda_n} \qquad \text{(A-56)}$$

has been used. There results the Fourier transform pair

$$(-j)^n\sqrt{2\pi\lambda_n}\ \psi_n(c,x) = F\{\psi_n(c,k_x)p_{k_{max}}(k_x)\} \tag{A-57}$$

By the inversion integral,

$$\psi_n(c,k_x)p_{k_{max}}(k_x) = \frac{1}{2\pi}\int_{-\infty}^{\infty}(-j)^n\sqrt{2\pi\lambda_n}\ \psi_n(c,x)e^{+jk_x x}dx \tag{A-58}$$

Also, interchange x and k_x, j and -j, in Equation (A-55) to yield

$$j^n\sqrt{2\pi\lambda_n}\ \psi_n(c,k_x) = \int_{-x_m}^{x_m}\psi_n(c,x)e^{+jk_x x}dx \tag{A-59}$$

Multiply both sides by $(-j)^n\sqrt{2\pi\lambda_n}$ to yield the inversion formula

$$\lambda_n\psi_n(c,k_x) = \frac{1}{2\pi}\int_{-x_m}^{x_m}(-j)^n\sqrt{2\pi\lambda_n}\ \psi_n(c,x)e^{jk_x x}dx \tag{A-60}$$

which is useful when G(x) is known only over the interval $|x| \le x_{max}$. Parseval's theorem for this case is

$$\frac{1}{2\pi}\int_{-\infty}^{\infty}|G(x)|^2dx = \int_{-\infty}^{\infty}|g(k_x)|^2dk_x \quad . \tag{A-61}$$

A.4 Expansion of Wavenumber-Limited Functions

Since the wavenumber-limited function G(x) is an entire function, it can, in principle, be extrapolated exactly to find its values outside the interval $|x| \le x_{max}$. A Taylor series could be used to do this extrapolation, but the approximation to G(x) for large x would generally be poor when only a finite number of terms is used. Such an approximation

is not wavenumber-limited.

The functions $\{\psi_n(c,x)\}$ are doubly orthogonal and complete on the intervals $(-x_{max},x_{max})$ and $(-\infty,\infty)$; hence, they can be used in a series expansion of G(x); i.e.,

$$G(x) = \sum_{n=0}^{\infty} a_n \psi_n(c,x) \tag{A-62}$$

where

$$a_n = \int_{-\infty}^{\infty} G(x)\psi_n(c,x)dx \tag{A-63}$$

$$\sum_{n=0}^{\infty} |a_n|^2 = \int_{-\infty}^{\infty} |G(x)|^2 dx \tag{A-64}$$

and convergence is in the mean square sense

$$\lim_{N \to \infty} \int_{-\infty}^{\infty} \left| G(x) - \sum_{n=0}^{N} a_n \psi_n(c,x) \right|^2 dx = 0 \tag{A-65}$$

By the orthogonality on $(-x_{max},x_{max})$, the coefficients are also given by

$$a_n = \frac{1}{\lambda_n} \int_{-x_{max}}^{x_{max}} G(x)\psi_n(c,x)dx \tag{A-66}$$

An approximation for G(x) is obtained by using only N terms in the series Equation (A-62)

$$G_N(x) = \sum_{n=0}^{N} a_n \psi_n(c,x) \tag{A-67}$$

with the a_n given by Equation (A-66). This approximation is itself wavenumber-limited since each function $\psi_n(c,x)$ is wavenumber-limited. The mean square error is

$$MSE_{\infty} = \int_{-\infty}^{\infty} |G(x) - G_N(x)|^2 dx = \sum_{n=N+1}^{\infty} |a_n|^2 \qquad (A-68)$$

The error in the fit of G_N to G in the interval $|x| \leq x_{max}$ is

$$MSE_{xmax} = \int_{-x_{max}}^{x_{max}} |G(x) - G_N(x)|^2 dx = \sum_{n=N+1}^{\infty} |a_n|^2 \lambda_n \qquad (A-69)$$

The inverse Fourier transform of G(x) has bounded support on the interval $|k_x| \leq k_{xmax}$ and is given by

$$g(k_x) = \frac{1}{2\pi} \int_{-\infty}^{\infty} G(x) e^{jk_x x} dx = \frac{1}{2\pi} \sum_{n=0}^{\infty} a_n \int_{-\infty}^{\infty} \psi_n(c,x) e^{jk_x x} dx \qquad (A-70)$$

where the order of integration and summation have been interchanged. From Equation (A-58)

$$g(k_x) = \sum_{n=0}^{\infty} \frac{a_n}{(-j)^n \sqrt{2\pi\lambda_n}} \psi_n(c,k_x) p_{k_{max}}(k_x) \qquad (A-71)$$

The transform can be approximated by using only N terms in the summation to yield

$$g_N(k_x) = \sum_{n=0}^{N} b_n \psi_n(c,k_x) p_{k_{max}}(k_x) \qquad (A-72)$$

where the relation between a_n and b_n is obvious. Since g and g_N are each

non-zero only over the interval $|k_x| \leq k_{max}$, the mean square error is

$$MSE_{\infty} = \int_{-k_{max}}^{k_{max}} |g(k_x) - g_N(k_x)|^2 dk_x \qquad \text{(A-73)}$$

Substitute Equations (A-71) and (A-72) into (A-73) to yield

$$MSE_{\infty} = \int_{-k_{max}}^{k_{max}} \left| \sum_{n=0}^{\infty} b_n \psi_n(c,k_x) - \sum_{n=0}^{N} b_n \psi_n(c,k_x) \right|^2 dk_x \qquad \text{(A-74)}$$

Combine the summations to give

$$MSE_{\infty} = \int_{-k_{max}}^{k_{max}} \left| \sum_{n=N+1}^{\infty} b_n \psi_n(c,k_x) \right|^2 dk_x \qquad \text{(A-75)}$$

Rewrite the magnitude of the summation as itself multiplied by its conjugate to yield

$$MSE_{\infty} = \int_{-k_{max}}^{k_{max}} \left(\sum_{n=N+1}^{\infty} b_n \psi_n \right) \left(\sum_{p=N+1}^{\infty} b_p \psi_p \right)^* dk_x \qquad \text{(A-76)}$$

Form an equivalent double summation and interchange the order of integration and summation to give

$$MSE_{\infty} = \sum_{n=N+1}^{\infty} \sum_{p=N+1}^{\infty} b_n b_p^* \int_{-k_{max}}^{k_{max}} \psi_n(c,k_x) \psi_p^*(c,k_x) dk_x \qquad \text{(A-77)}$$

which, from the orthogonality condition and Equation (A-30),

$$MSE_{\infty} = \sum_{n=N+1}^{\infty} \frac{|a_n|^2}{2\pi\lambda_n} \lambda_n = \frac{1}{2\pi} \sum_{n=N+1}^{\infty} |a_n|^2 \quad . \qquad \text{(A-78)}$$

Equation (A-78) is merely a statement of Parseval's theorem in Equation (A-61); more importantly, Equation (A-73) and (A-78) state that the true spectrum $g(k_x)$ and its estimate $g_N(k_x)$ are both confined to the interval $|k_x| \leq k_m$, and that the mean square error in the estimate is equal to $(2\pi)^{-1}$ of the mean square error in the estimate $G_N(x)$ averaged over the interval $|x| < \infty$. Therefore, if an upper bound on the error in $G_N(x)$ can be established (and it can), then it applies equally to the error in $g_N(k_x)$.

APPENDIX B

GRAPHS OF MEASURED PHASE OF PROBE ANTENNAS

This appendix presents graphs of the measured phases of the three probe antennas for the rectangular far-field components E_{xff}, E_{yff} as functions of normalized wavenumber k_{xn}, k_{yn}. The vertical scale corresponds to ±180 degrees as shown. The circular region indicated in each graph corresponds to real directions; i.e., $k_{xn}^2 + k_{yn}^2 \leq 1$.

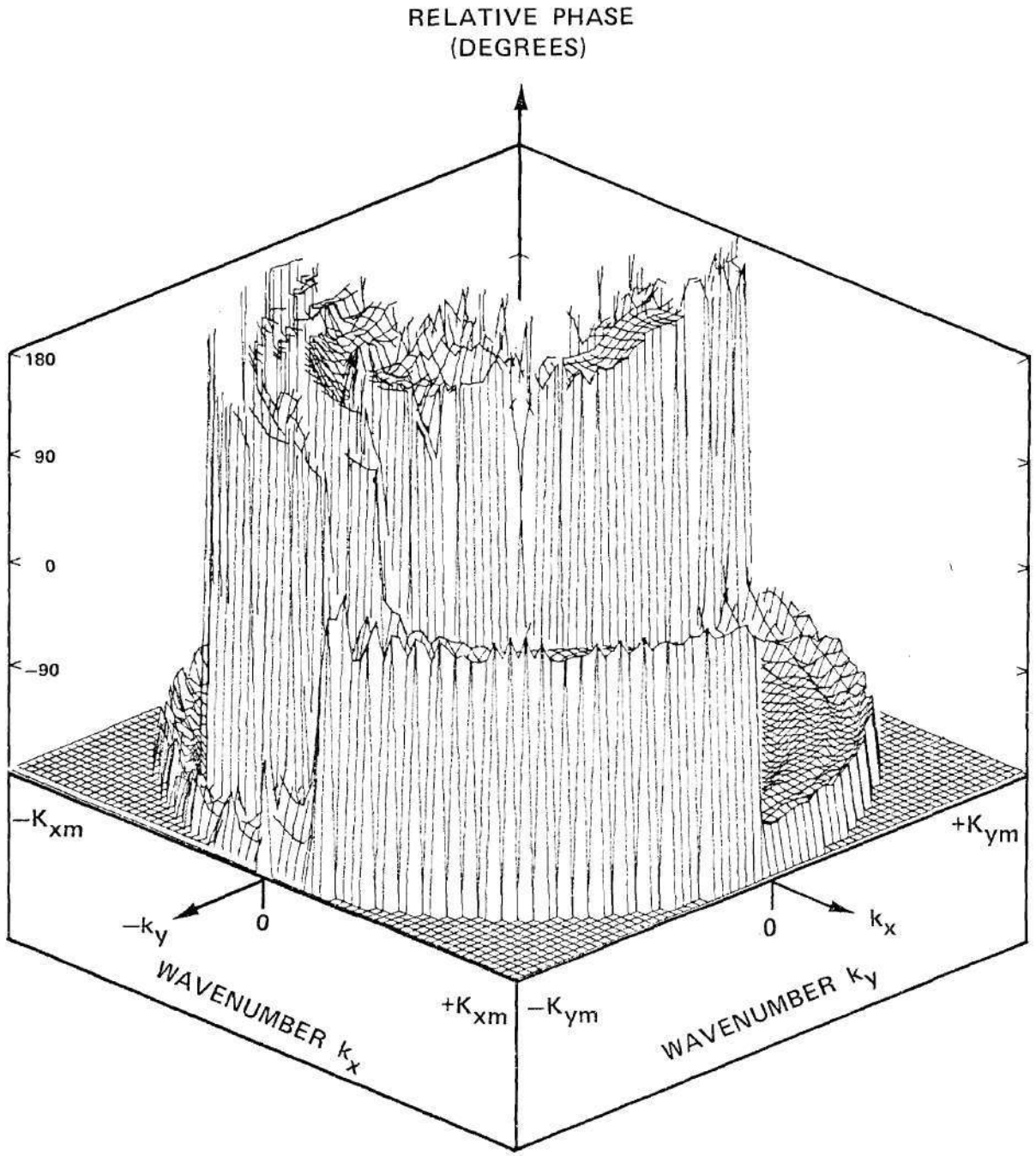

Figure B-1. Measured Phase of $E_{xff}(k_x,k_y)$ for Undersize Waveguide Probe.

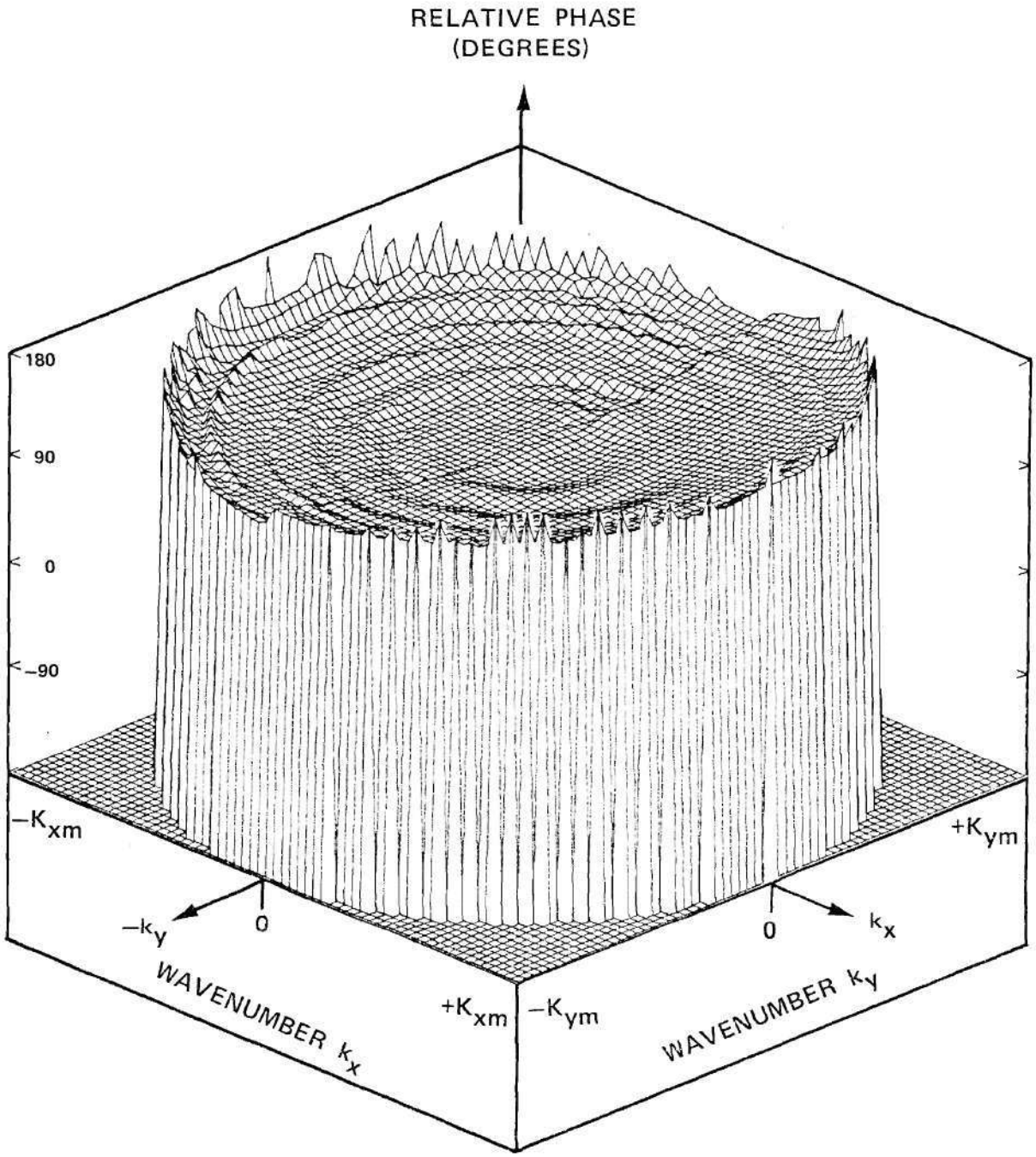

Figure B-2. Measured Phase of $E_{yff}(k_x,k_y)$ for Undersize Waveguide Probe.

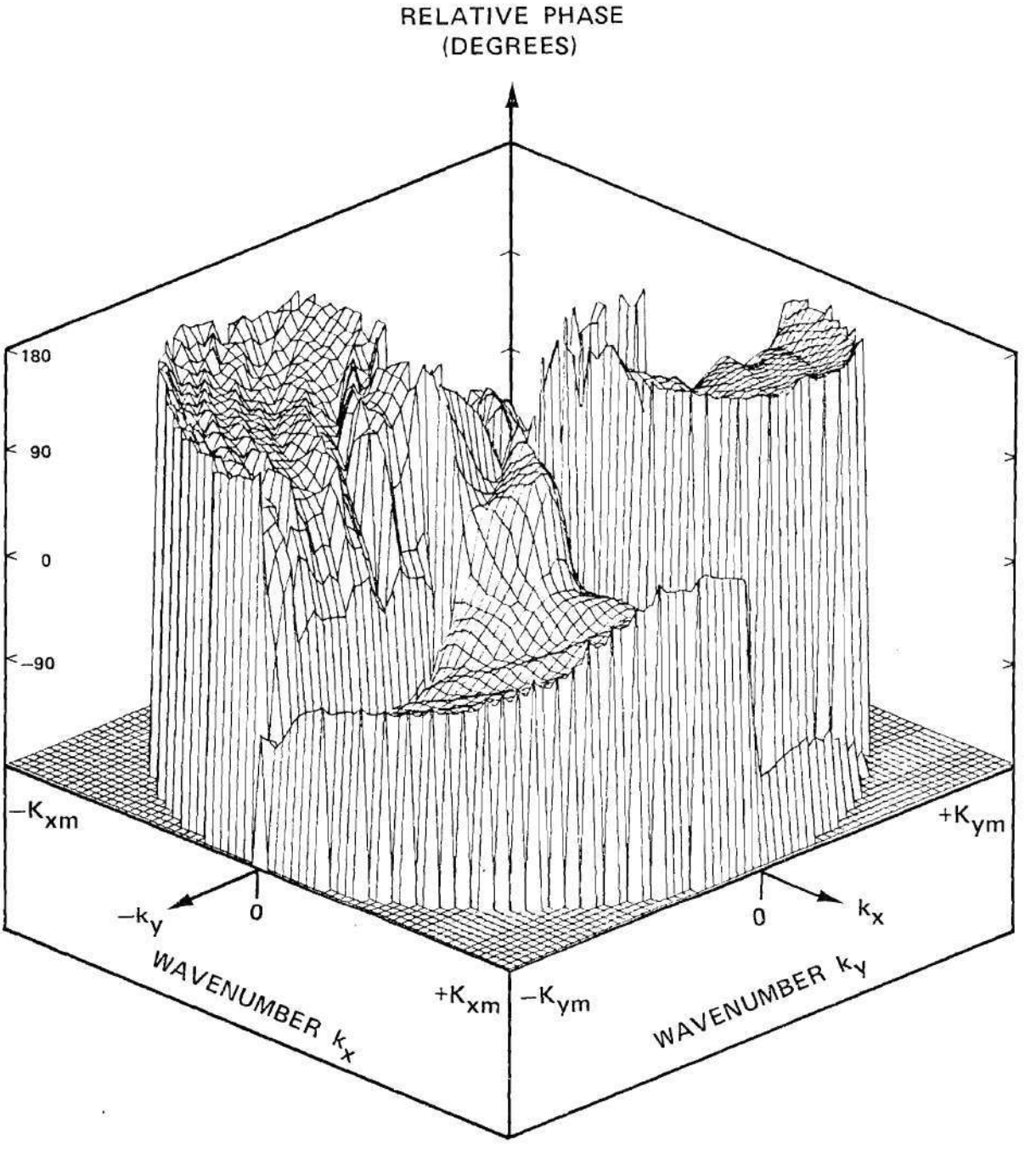

Figure B-3. Measured Phase of $E_{xff}(k_x,k_y)$ for Open-End Waveguide Probe.

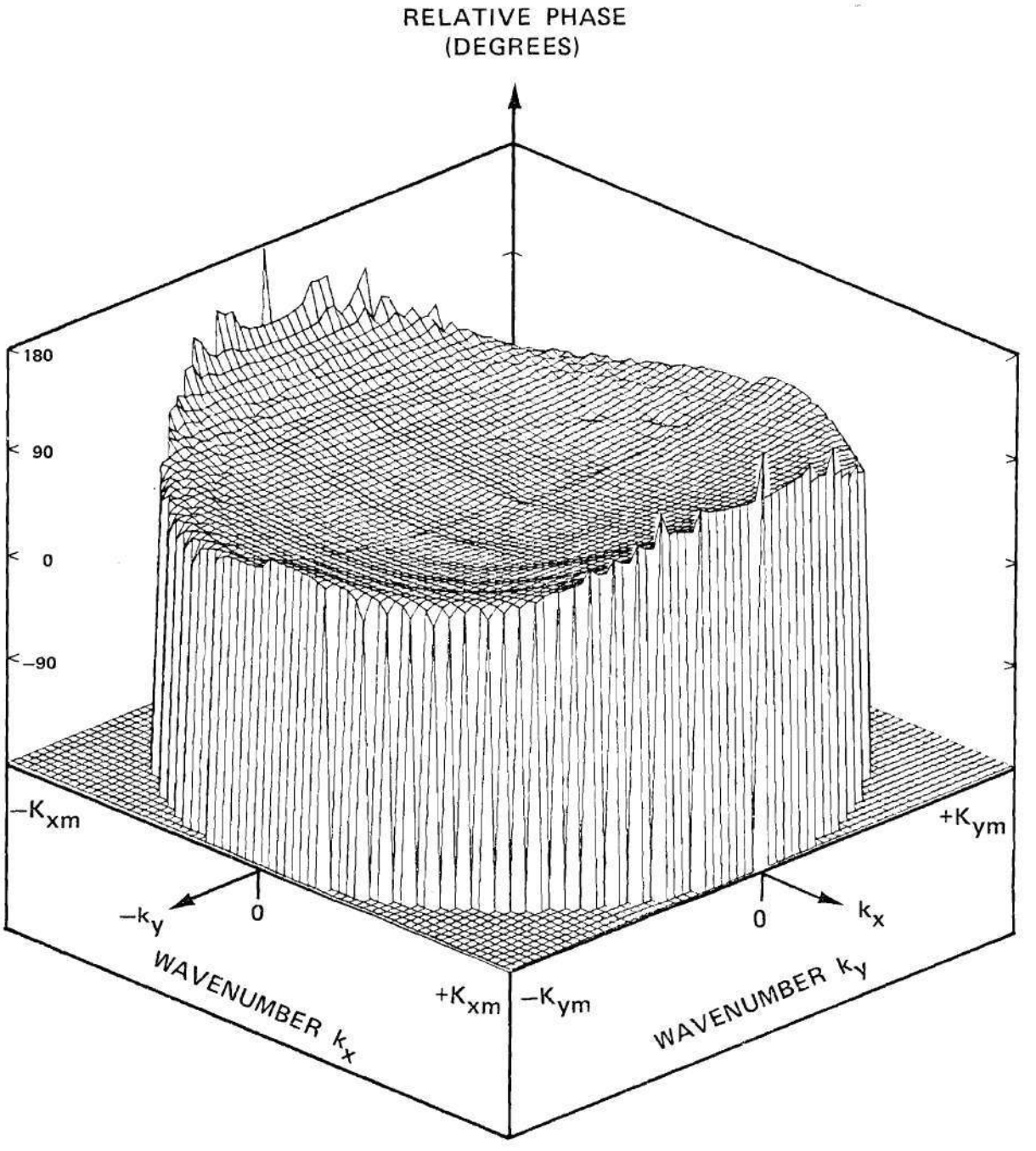

Figure B-4. Measured Phae of $E_{yff}(k_x,k_y)$ for Open-End Waveguide Probe.

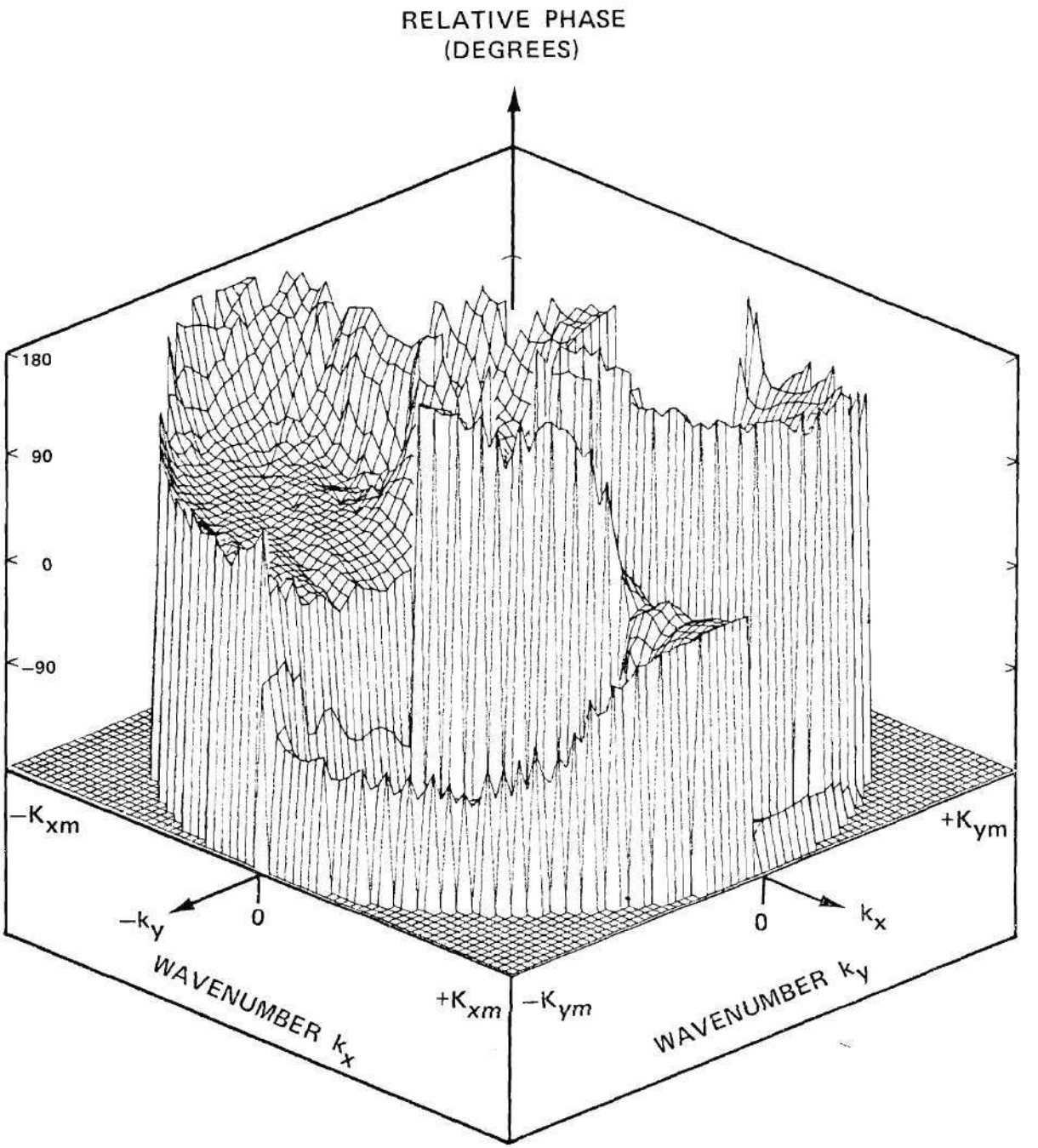

Figure B-5. Measured Phase of $E_{xff}(k_x,k_y)$ for E-Plane Horn Probe.

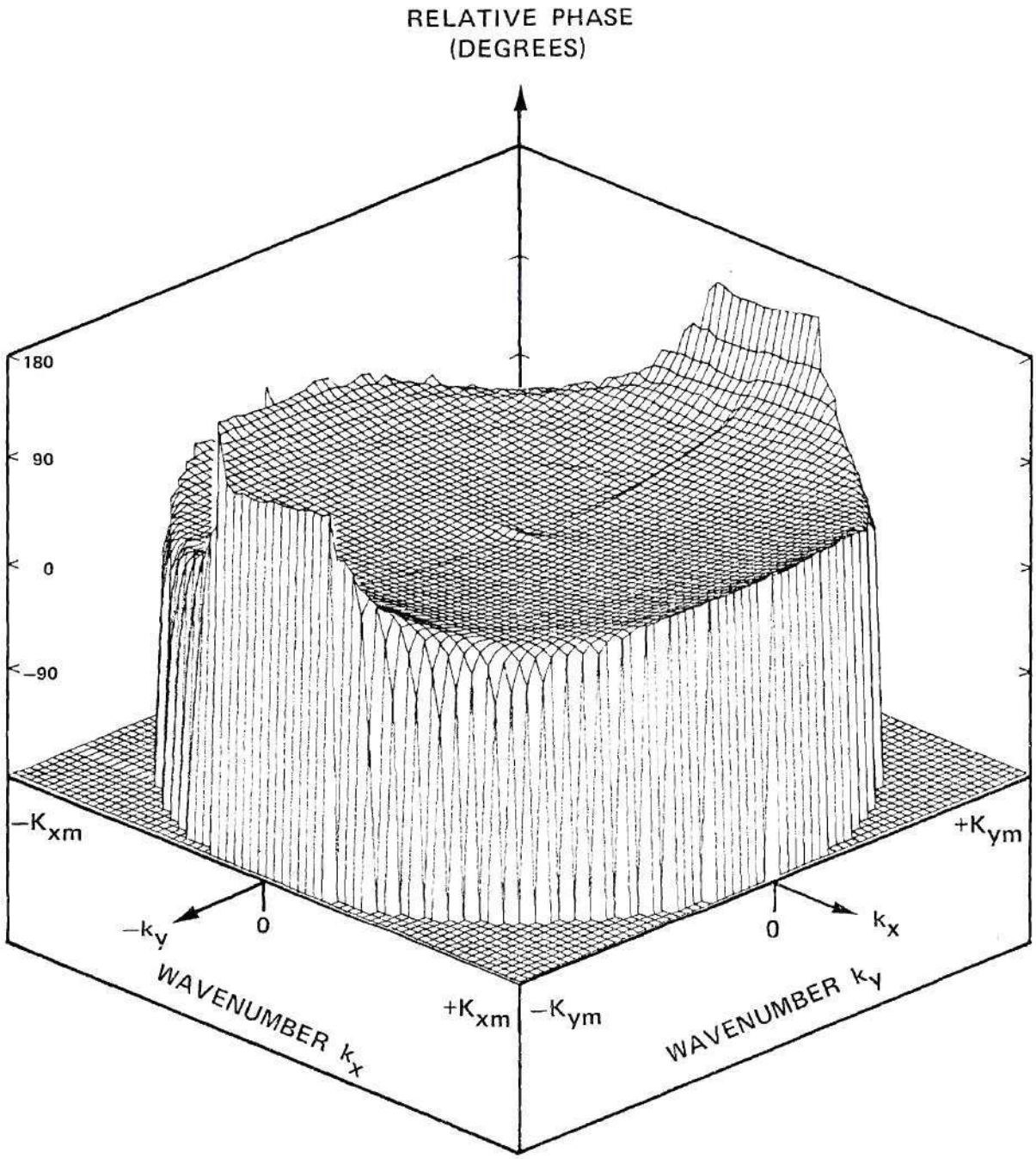

Figure B-6. Measured Phase of $E_{yff}(k_x, k_y)$ for E-Plane Horn Probe.

APPENDIX C

MEASURED PROBE FAR FIELDS E_θ AND E_ϕ

This appendix presents graphs of the amplitudes and phase of the measured far fields E_θ and E_ϕ of the three probe antennas. The amplitude is plotted in decibels from 0 dB to -40 dB relative to the maximum value in each graph. The phase vertical scale ranges from -180 degrees to +180 degrees. The abscissas in each graph represent angles θ and ϕ as shown and as defined in Figure 4-3 of the text. Note that the angle ϕ is such as to make the data periodic in ϕ with period 2π. The angle θ is always non-negative. The angles θ and ϕ take on values corresponding to the hemisphere $z > 0$ in Figure 4-3. Note that the plane in each graph for $\theta = 0$ corresponds to the z-axis in Figure 4-3. Rapid changes in the phase data merely reflect the fact that +180° and -180° are the same point on the unit circle.

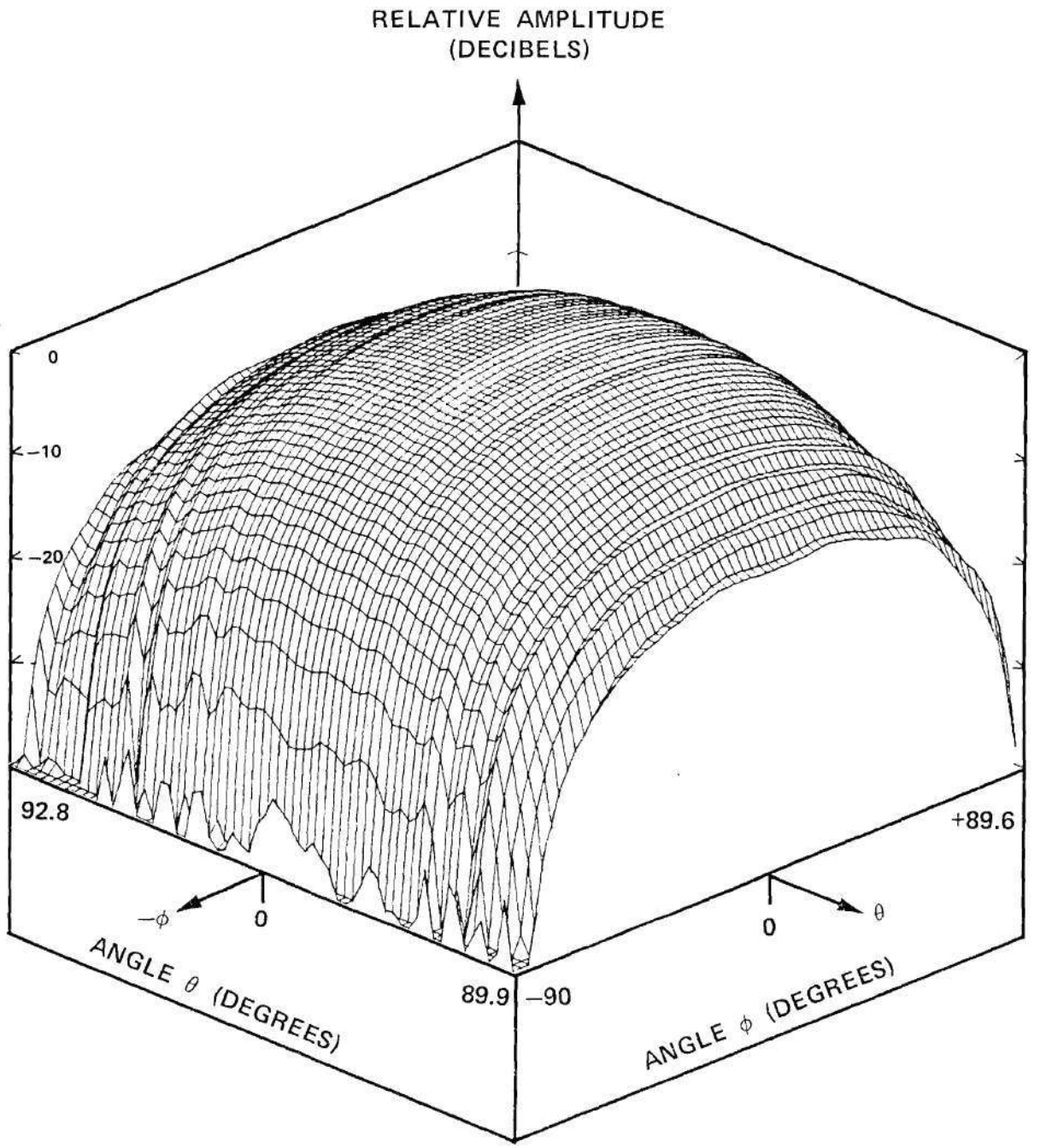

Figure C-1. Measured Amplitude of E_ϕ for Undersize Waveguide Probe.

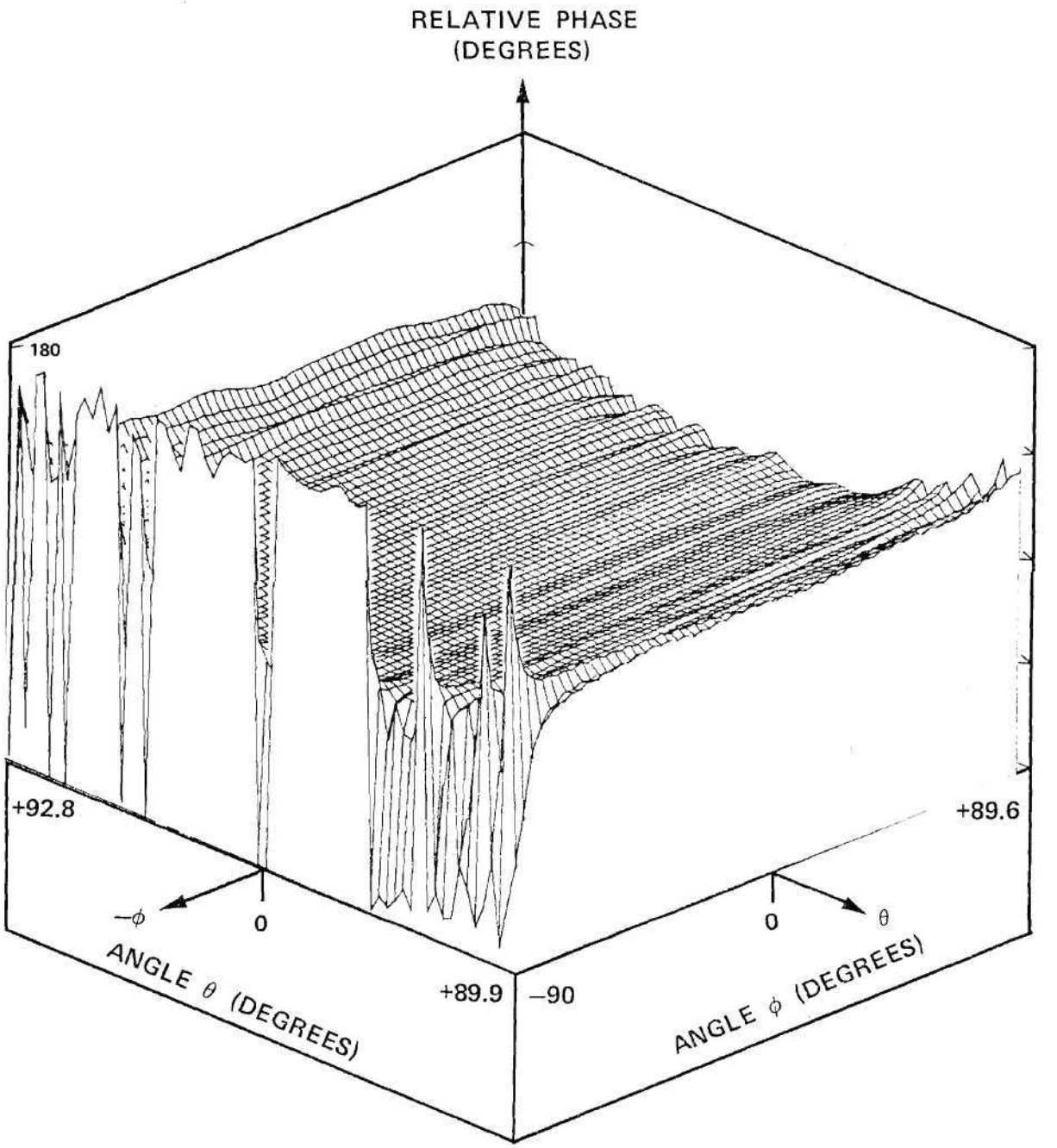

Figure C-2. Measured Phase of E_ϕ for Undersize Waveguide Probe.

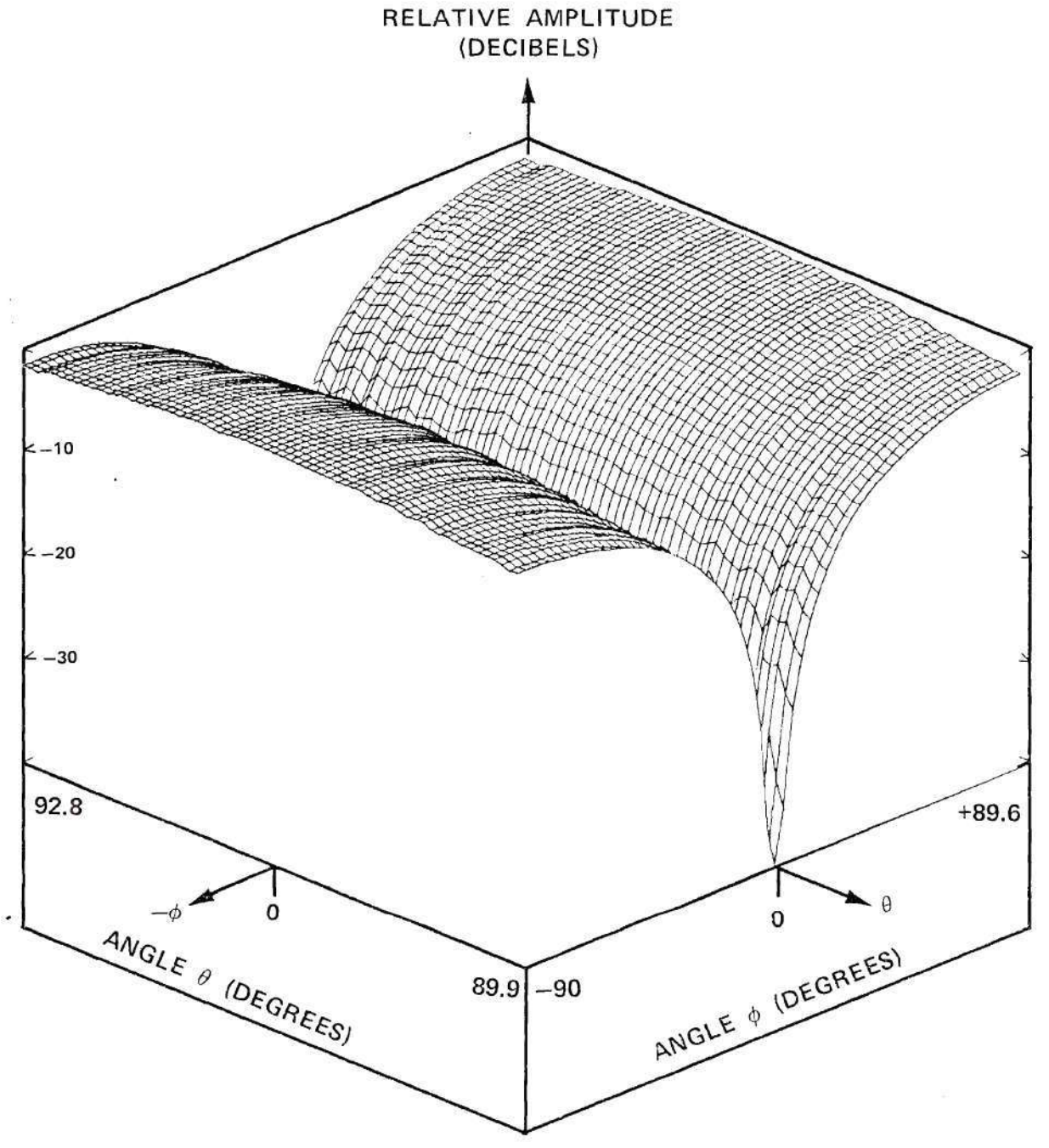

Figure C-3. Measured Amplitude of E_θ for Undersize Waveguide Probe.

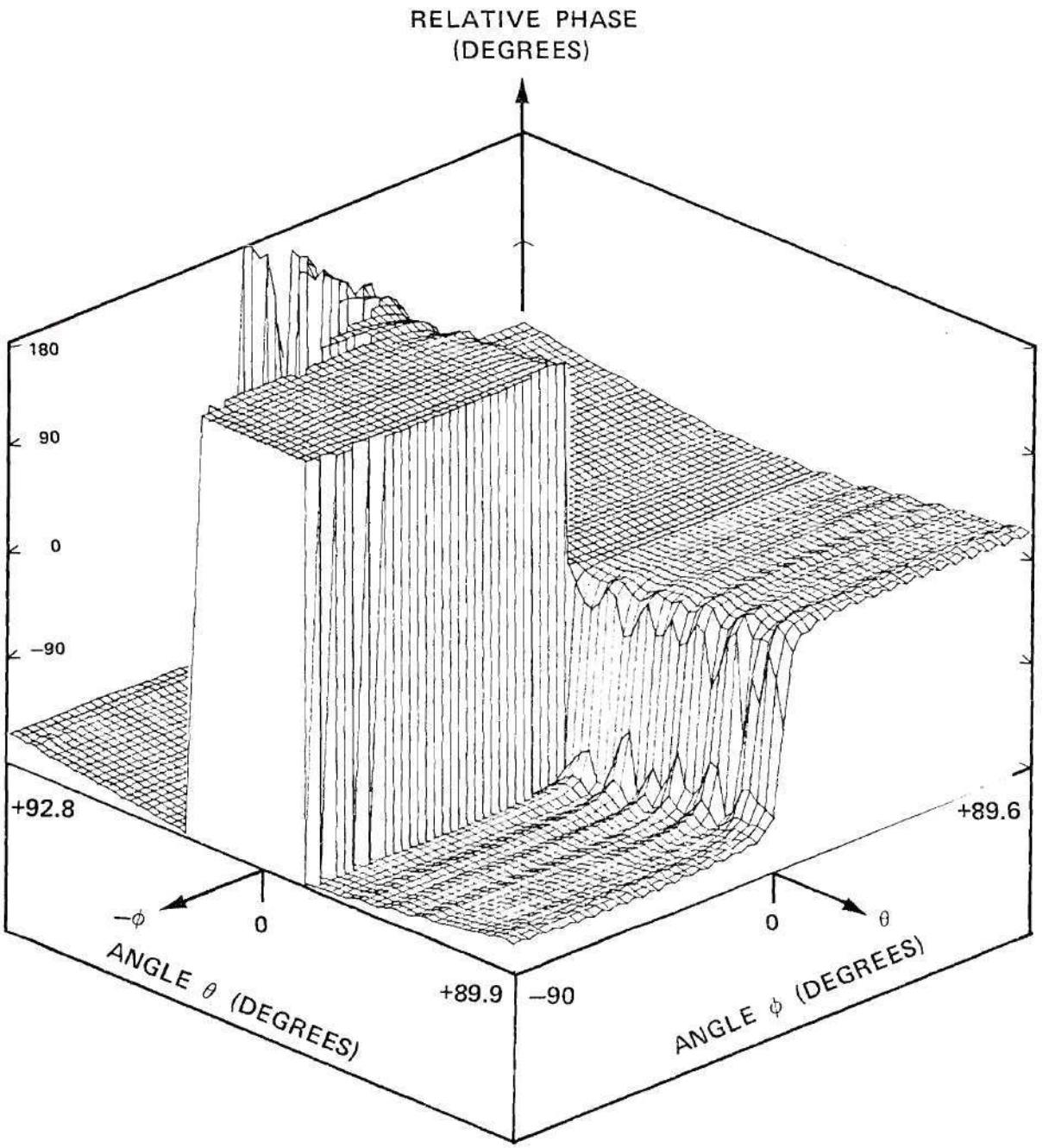

Figure C-4. Measured Phase of E_θ for Undersize Waveguide Probe.

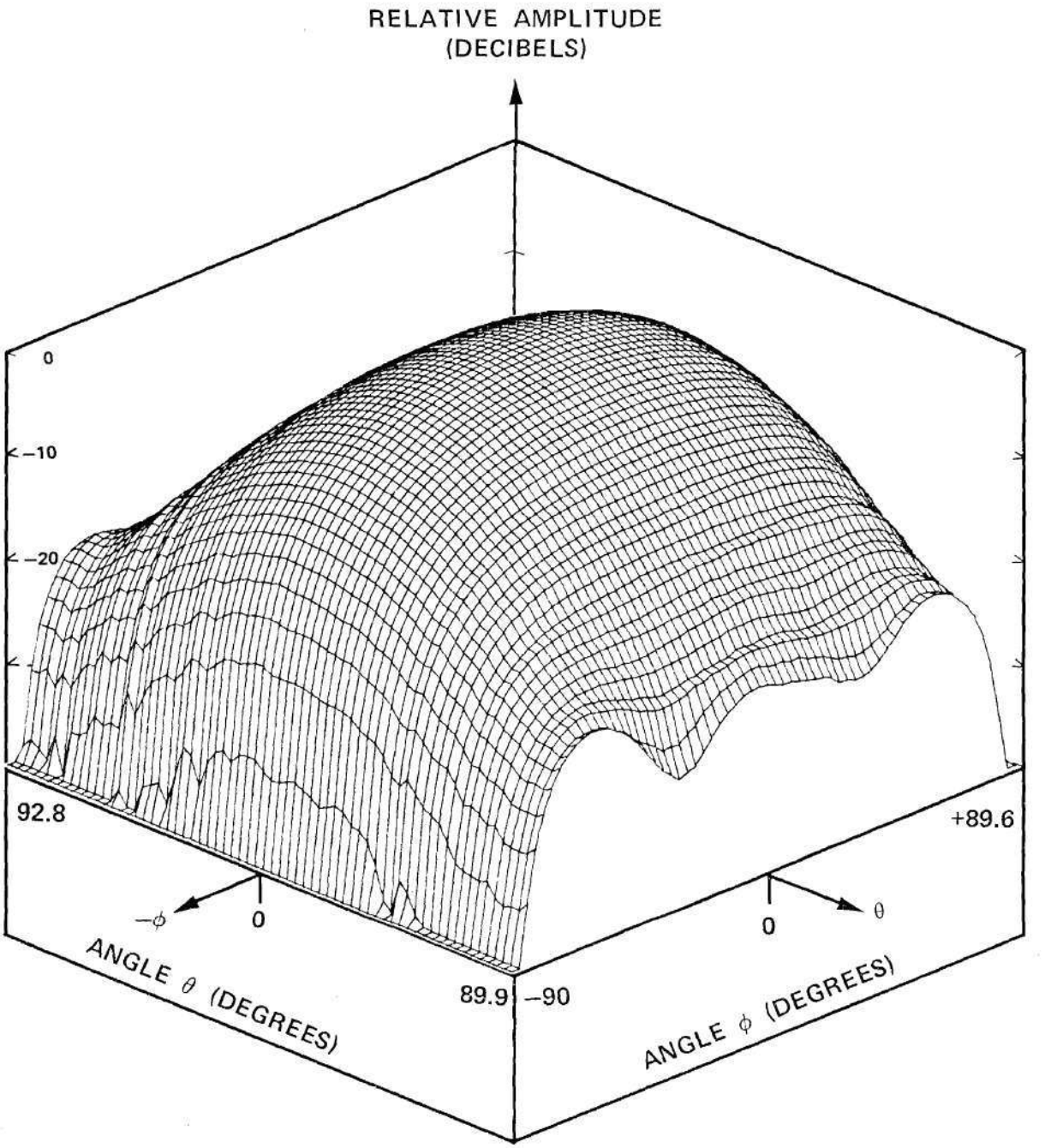

Figure C-5. Measured Amplitude of E_ϕ for Open-End Waveguide Probe.

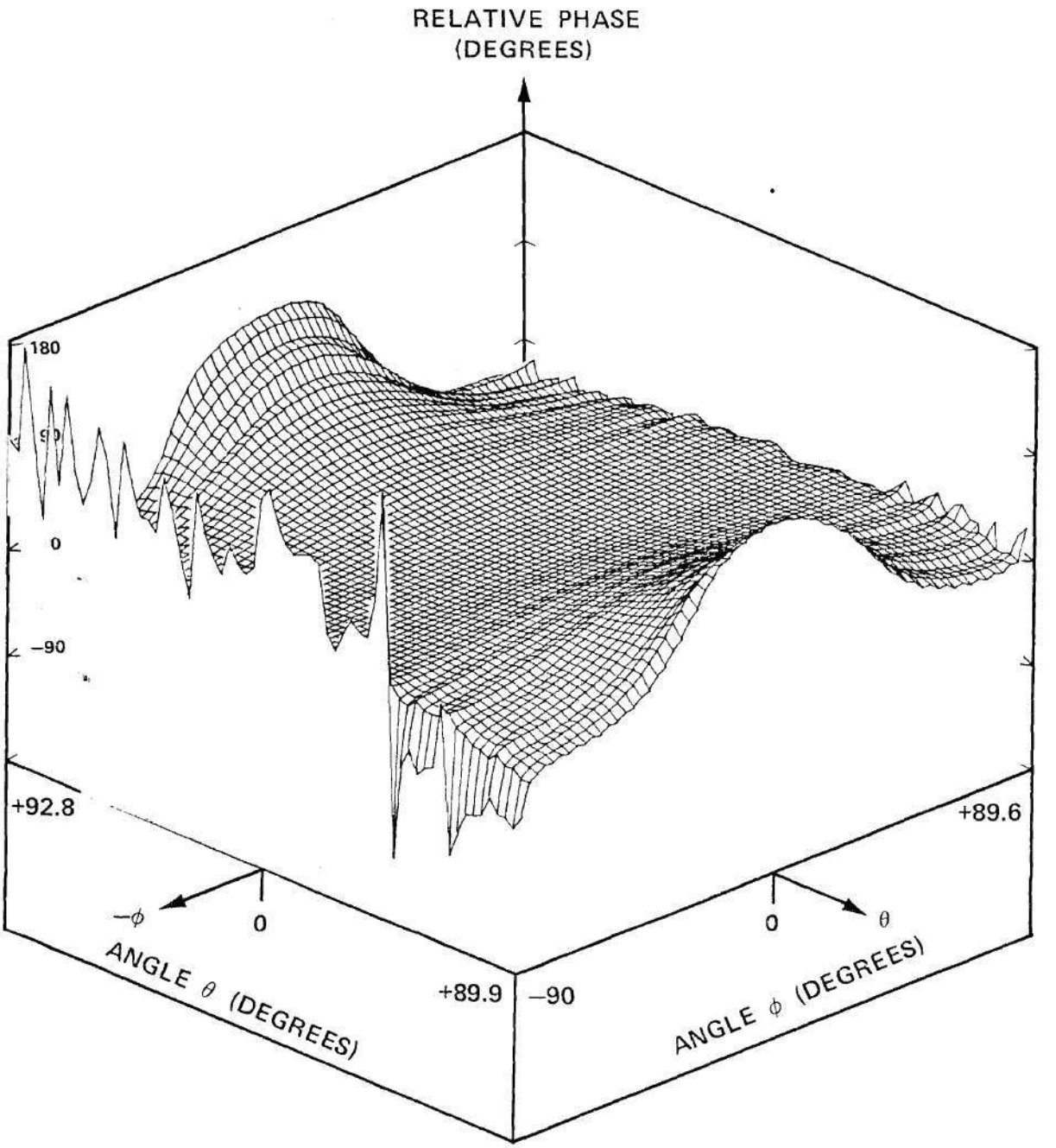

Figure C-6. Measured Phase of E_ϕ for Open-End Waveguide Probe.

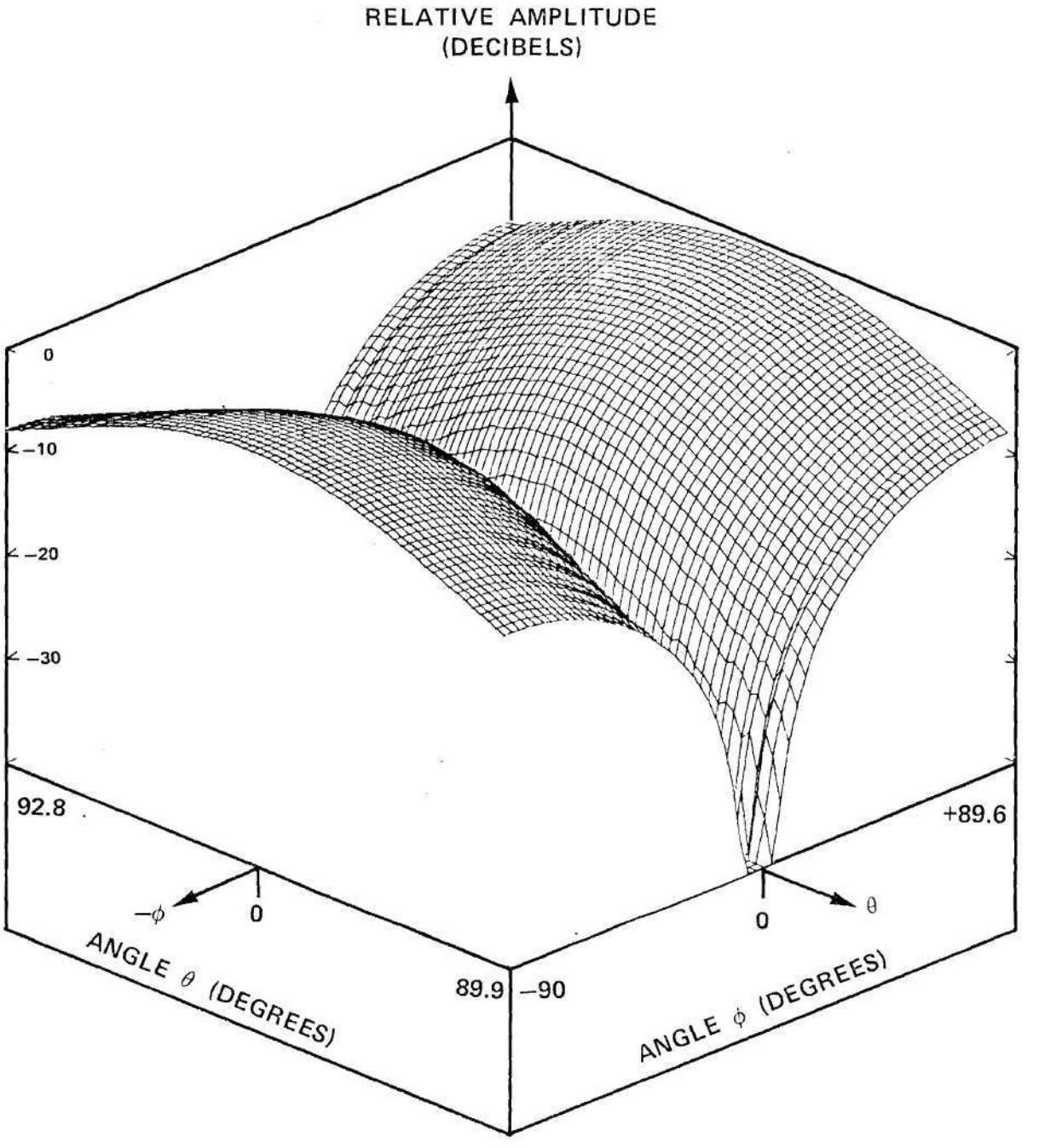

Figure C-7. Measured Amplitude of E_θ for Open-End Waveguide Probe.

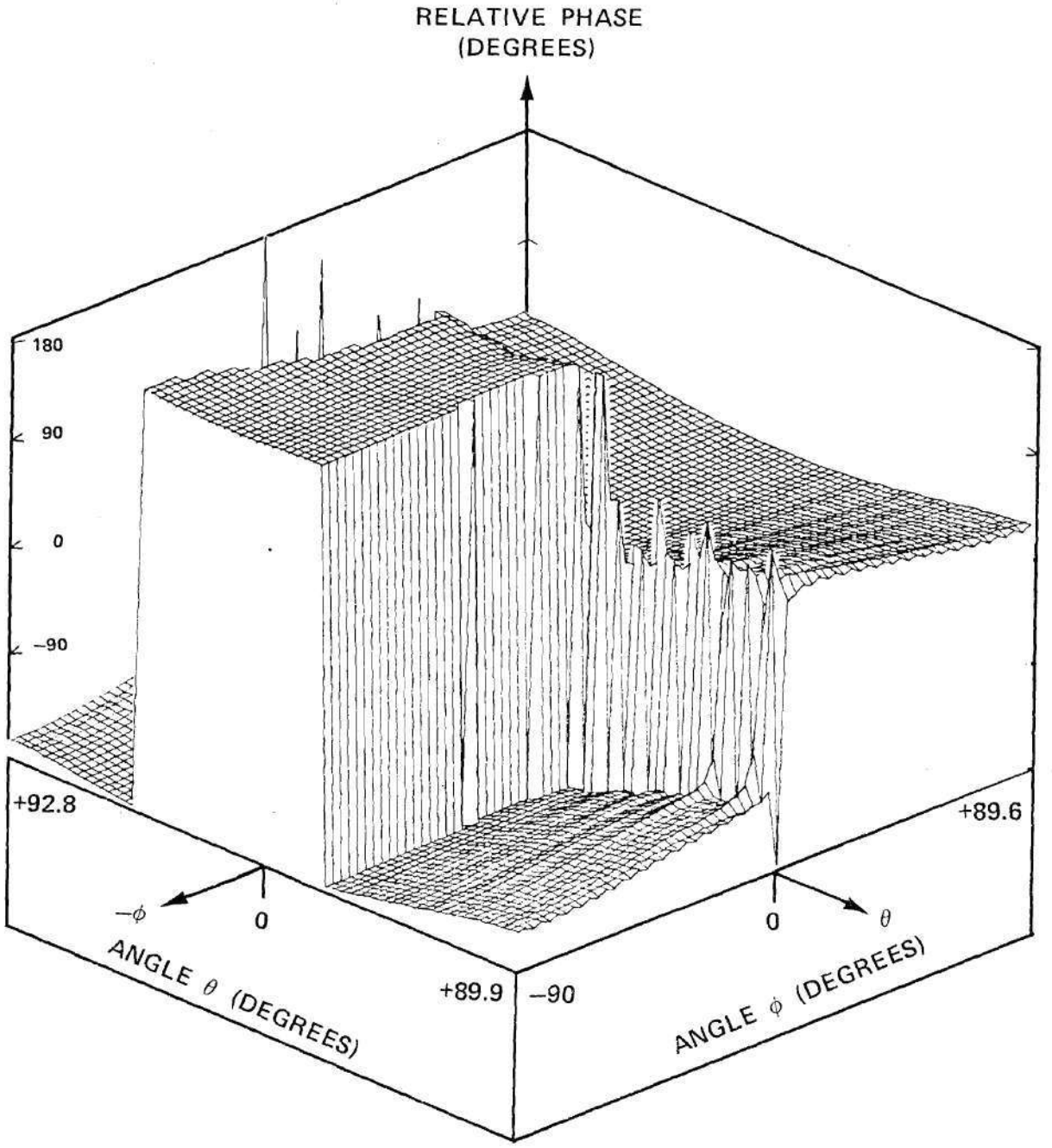

Figure C-8. Measured Phase of E_θ for Open-End Waveguide Probe.

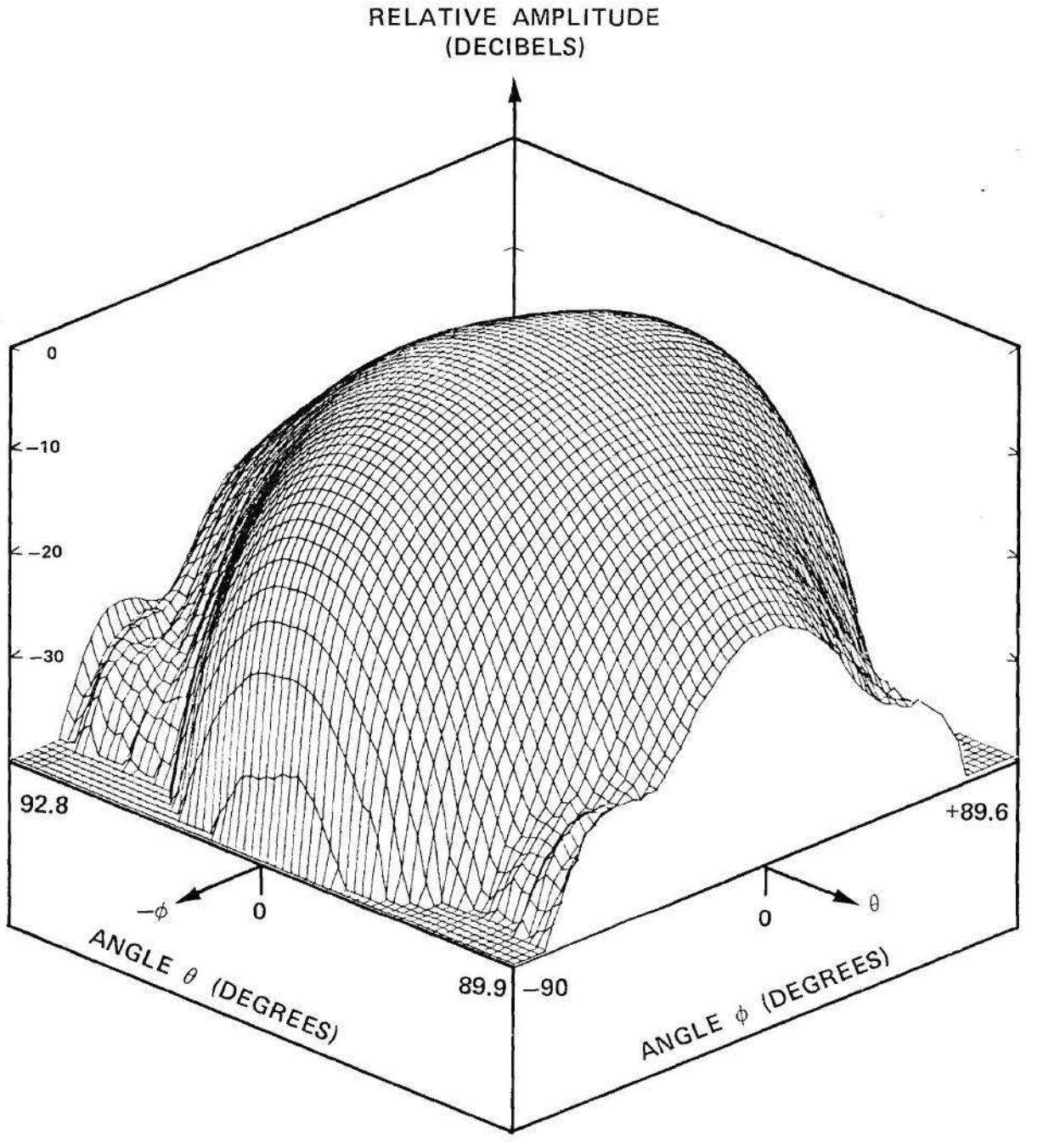

Figure C-9. Measured Amplitude of E_ϕ for E-Plane Horn Probe.

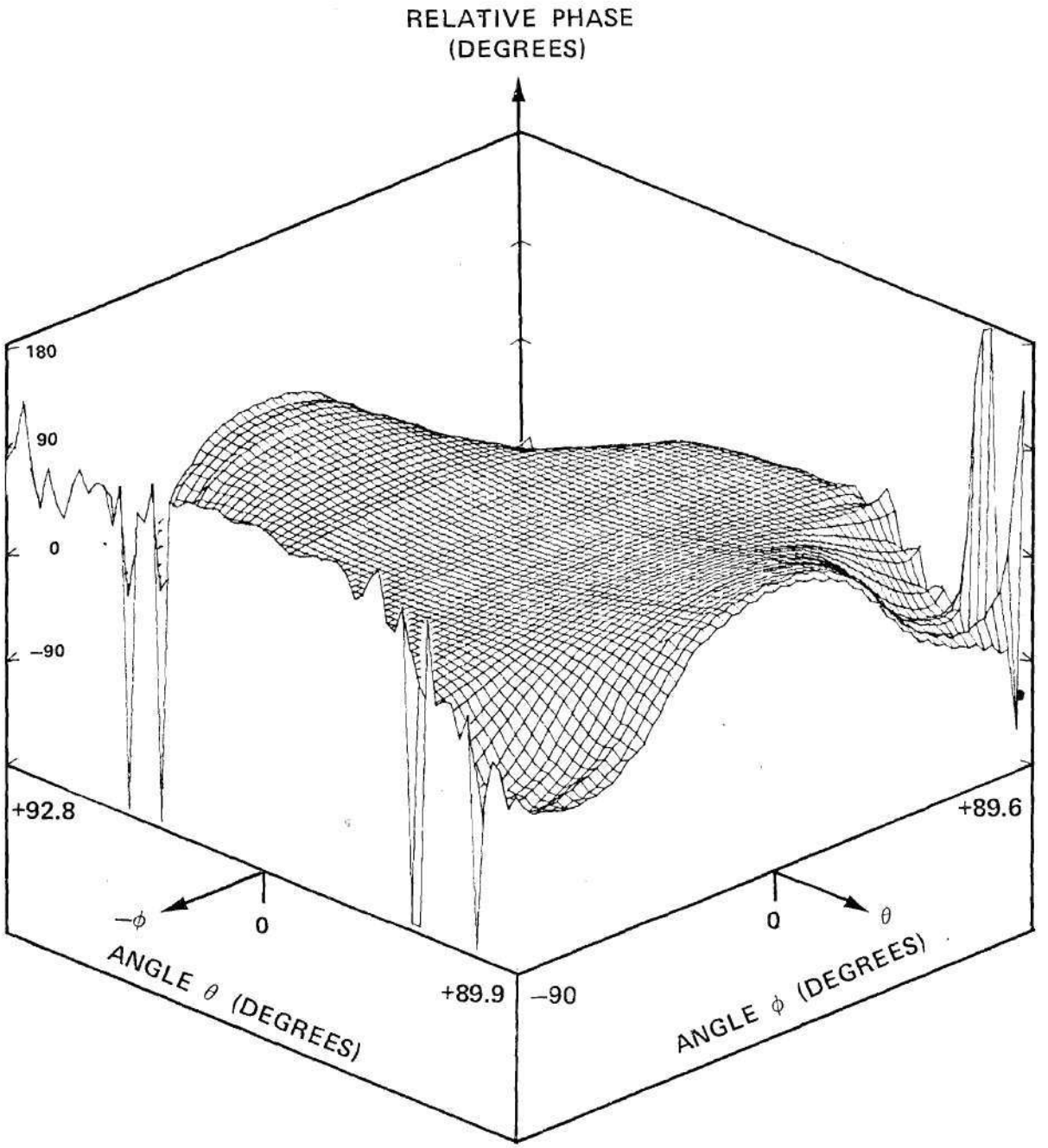

Figure C-10. Measured Phase of E_ϕ for E-Plane Horn Probe.

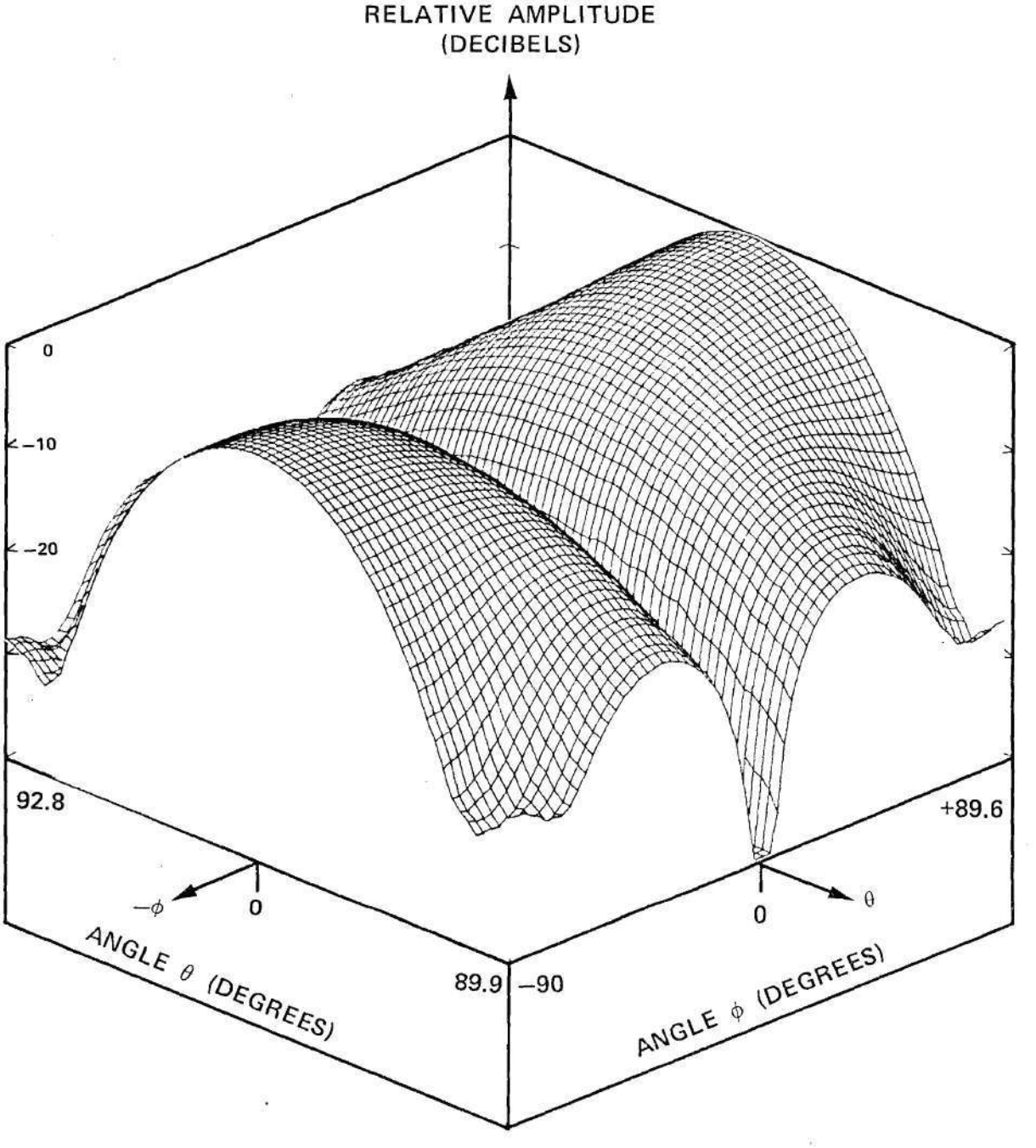

Figure C-11. Measured Amplitude of E_θ for E-Plane Horn Probe.

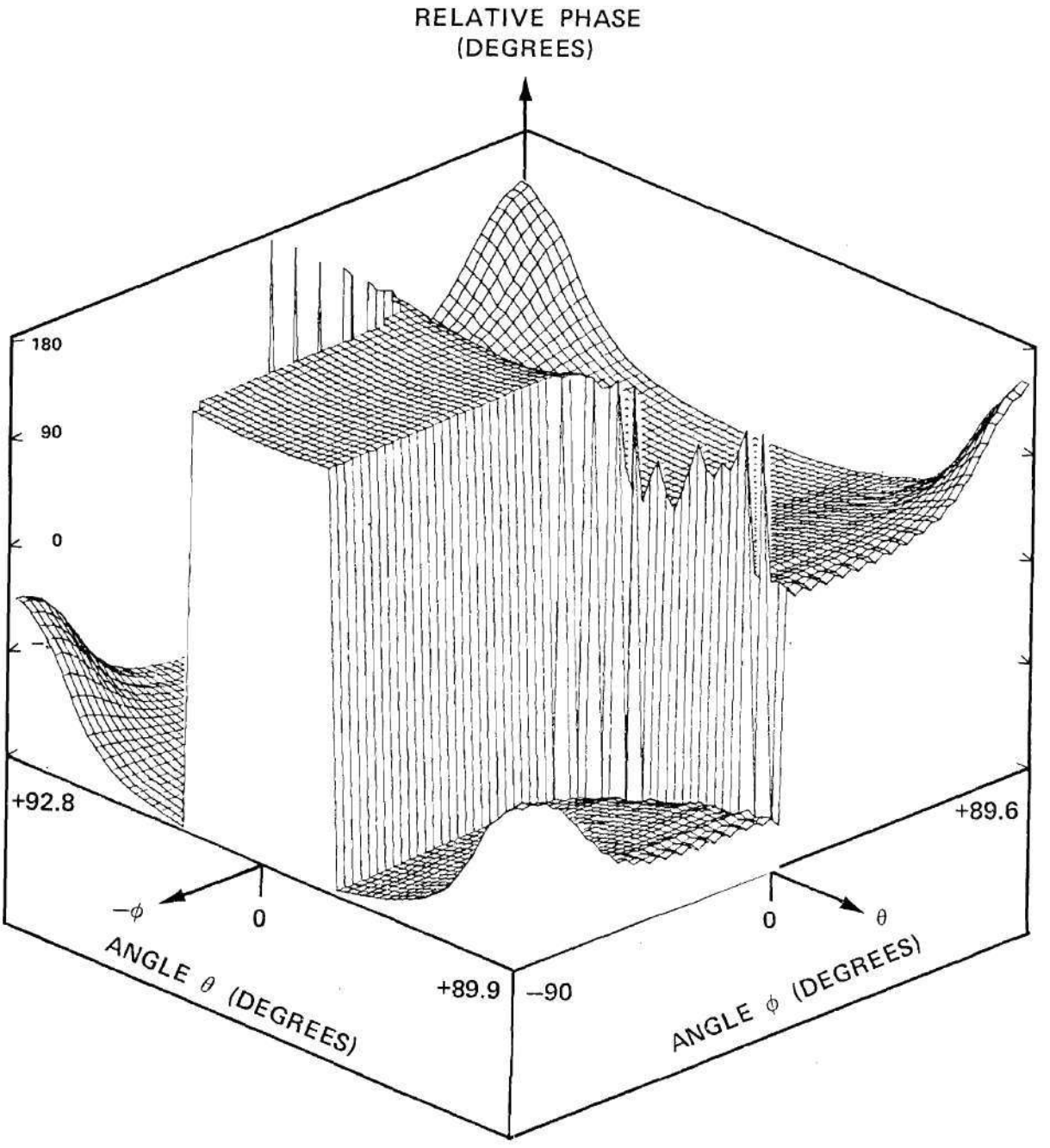

Figure C-12. Measured Phase of E_θ for E-Plane Horn Probe.

APPENDIX D

MEASURED NEAR-FIELD PHASE DATA

This appendix presents three dimensional graphs of the measured phase of the near-field response for each of the three probes to the phased array test antenna. The vertical scale on each graph ranges from -180 degrees to +180 degrees. The abscissas are distances x and y in the test antenna coordinate system of Figure 2-1. The values of the ranges and increments of the abscissas are given in Table 5-3 of the text. The phase graphs are somewhat incomprehensivle because of the scanned condition of the phased array antenna and because +180° and -180° are the same point on the unit circle.

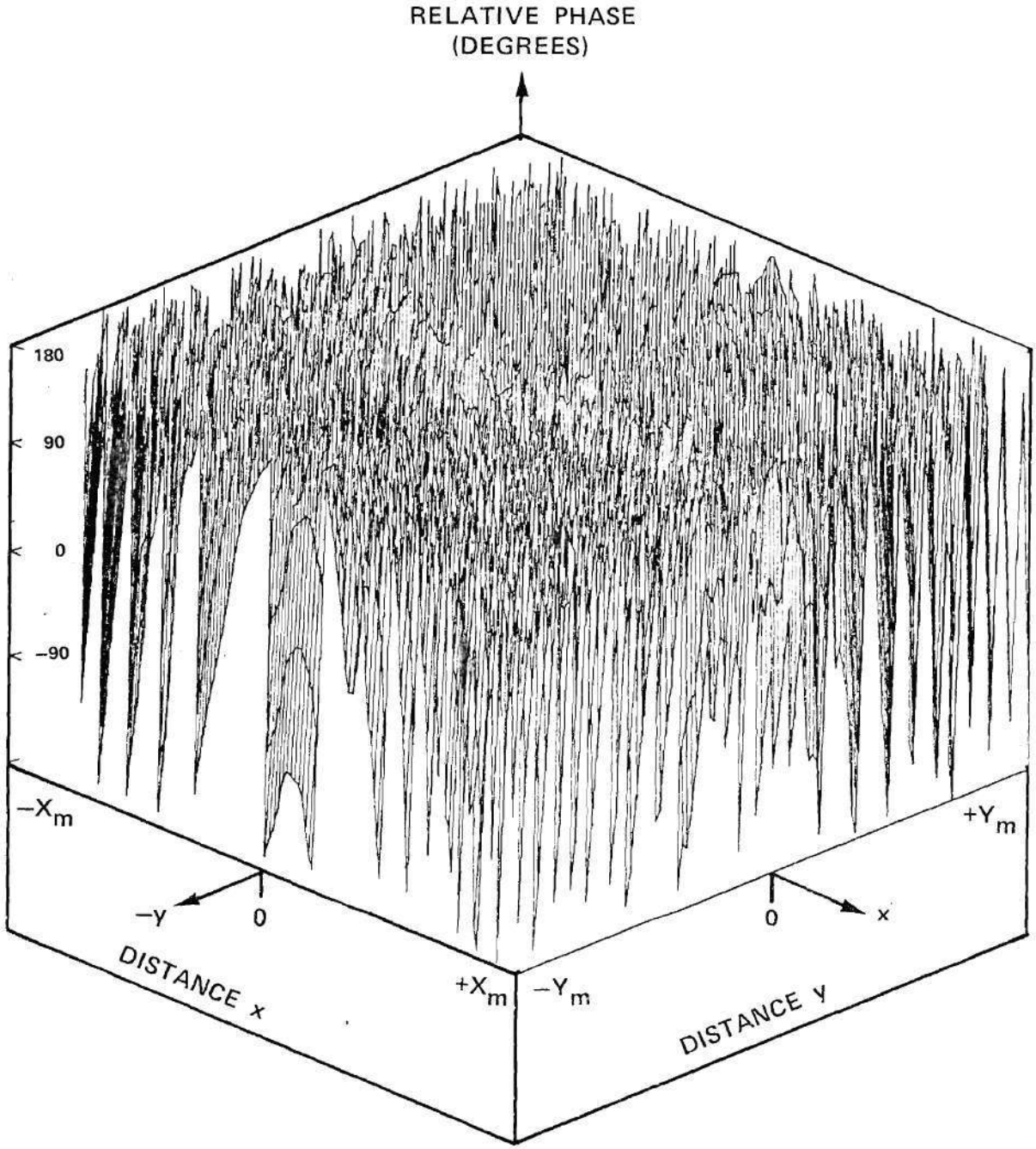

Figure D-1. Measured Phase of Near-Field Response of Undersize Waveguide Probe in Orientation #1.

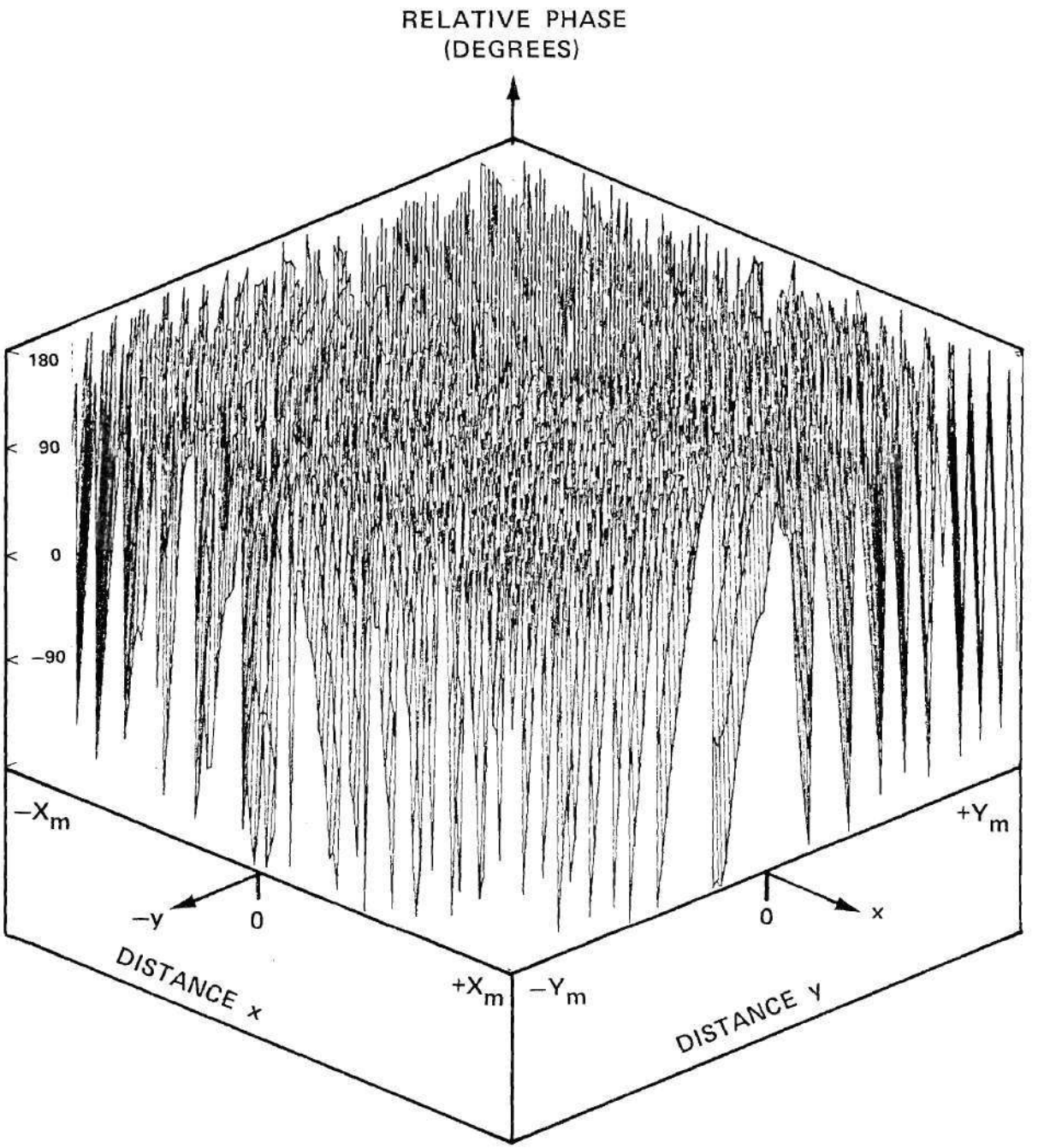

Figure D-2. Measured Phase of Near-Field Response of Undersize Waveguide Probe in Orientation #2.

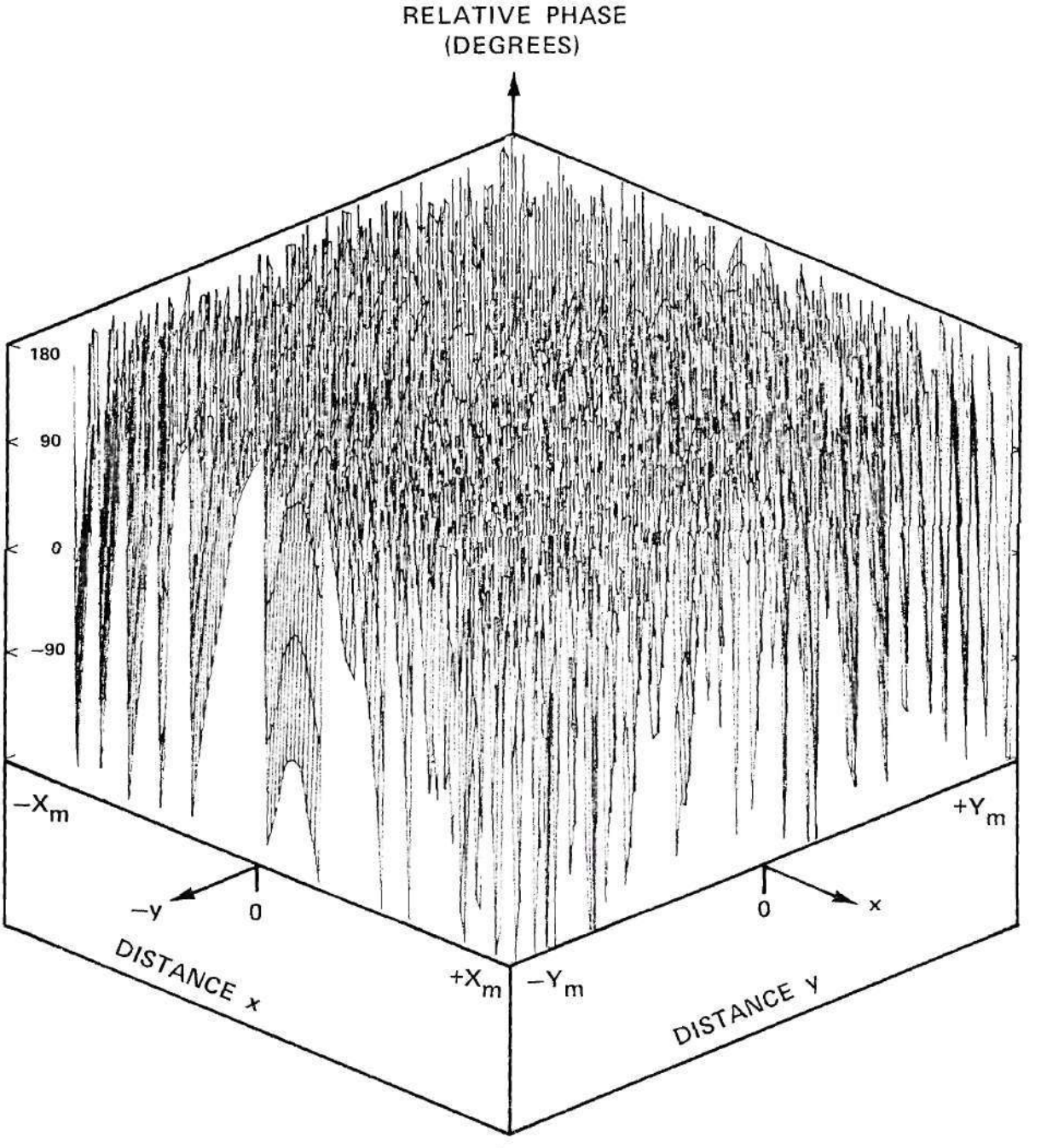

Figure D-3. Measured Phase of Near-Field Response for Open-End Waveguide Probe in Orientation #1.

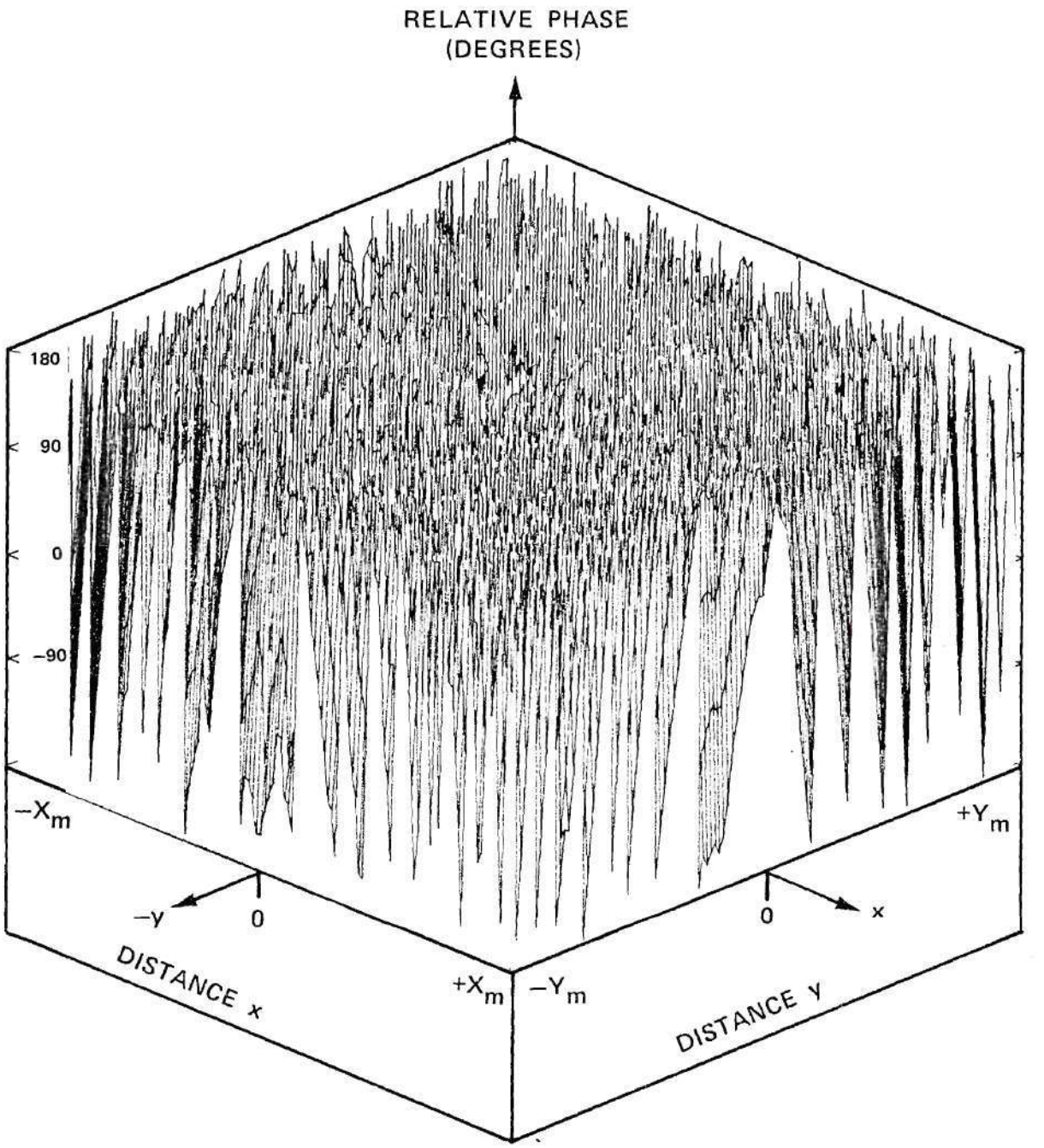

Figure D-4. Measured Phase of Near-Field Response for Open-End Waveguide Probe in Orientation #2.

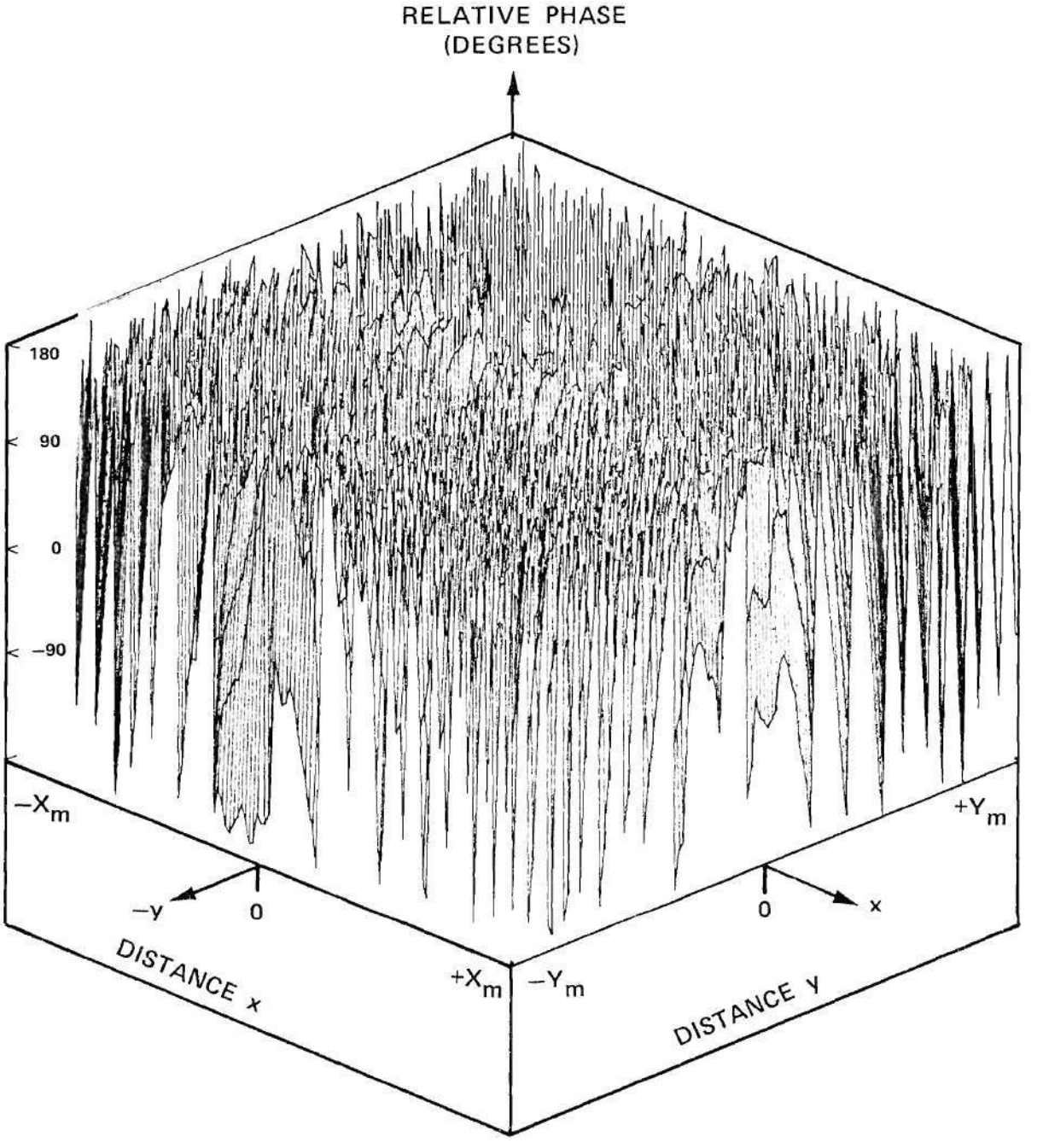

Figure D-5. Measured Phase of Near-Field Response for E-Plane Horn Probe in Orientation #1.

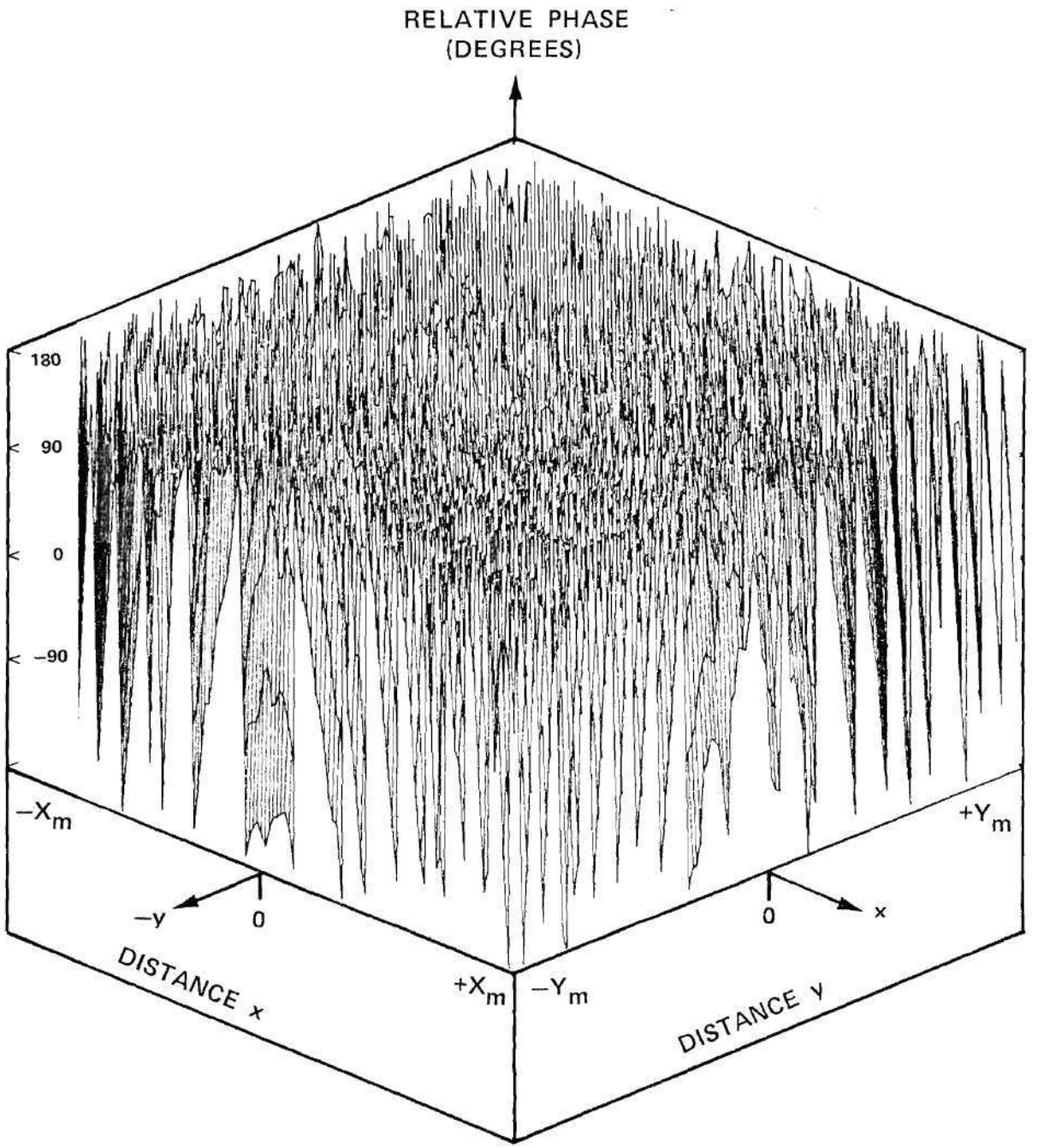

Figure D-6. Measured Phase of Near-Field Response for E-Plane Horn Probe in Orientation #2.

APPENDIX E

MEASURED PLANE WAVE SPECTRA

This appendix presents three dimensional graphs of the measured plane wave spectra obtained by inverse Fourier transformation of the measured near-field probe responses. Only amplitude data are presented. The vertical scale is in decibels (0 to -40 dB). The amplitude is shown relative to the maximum amplitude of that obtained for orientation #1 for each probe. The abscissas are normalized wavenumbers ranging from -1.64 to +1.64 in both k_x and k_y. The central circular region in each plot corresponds approximately to the visible region. The number of data points in the data array for each graph is 128 x 128. The wavenumber-limited character of the data is quite evident in the graphs.

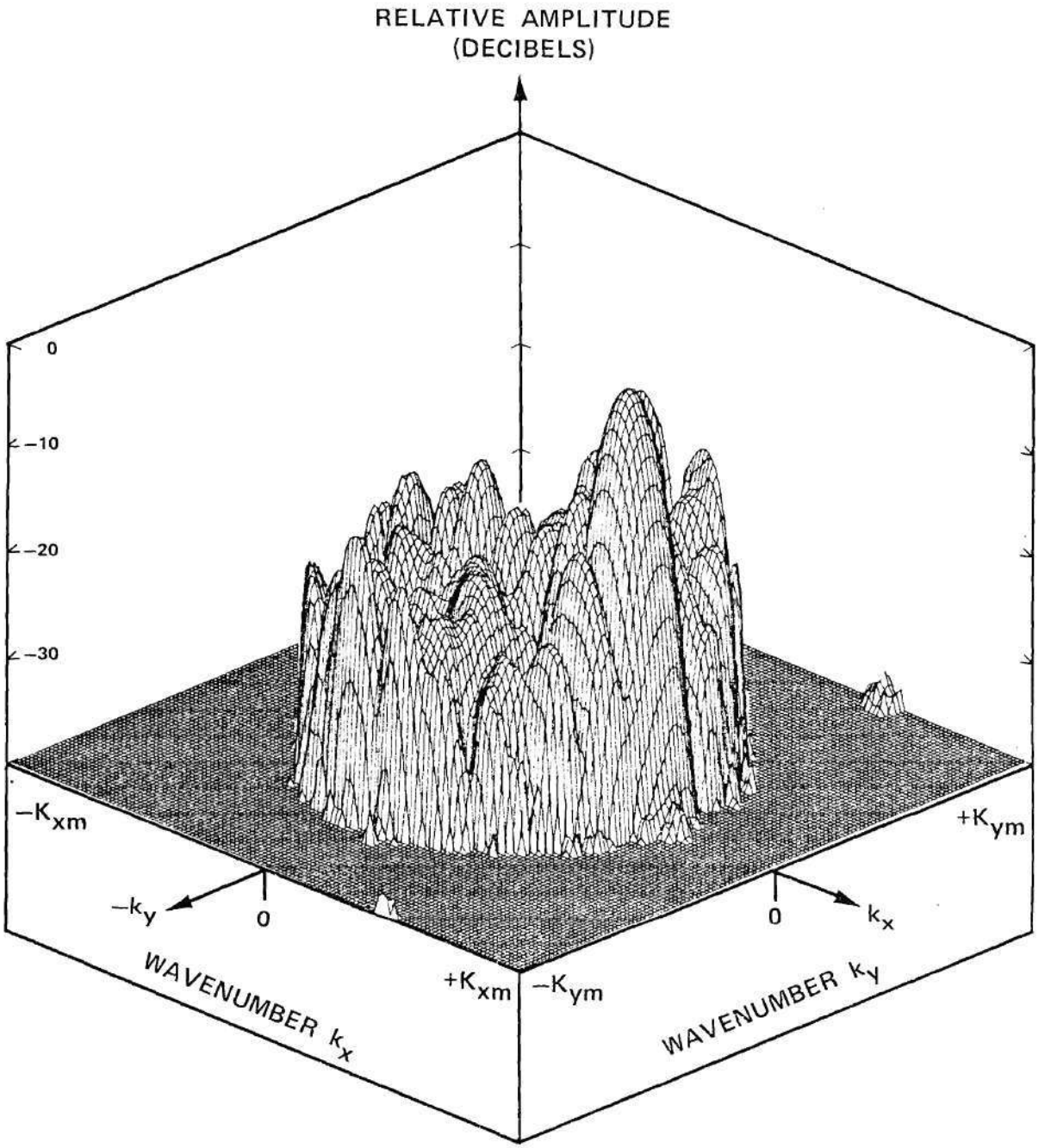

Figure E-1. Amplitude of Measured Spectrum for Undersize Waveguide Probe in Orientation #1.

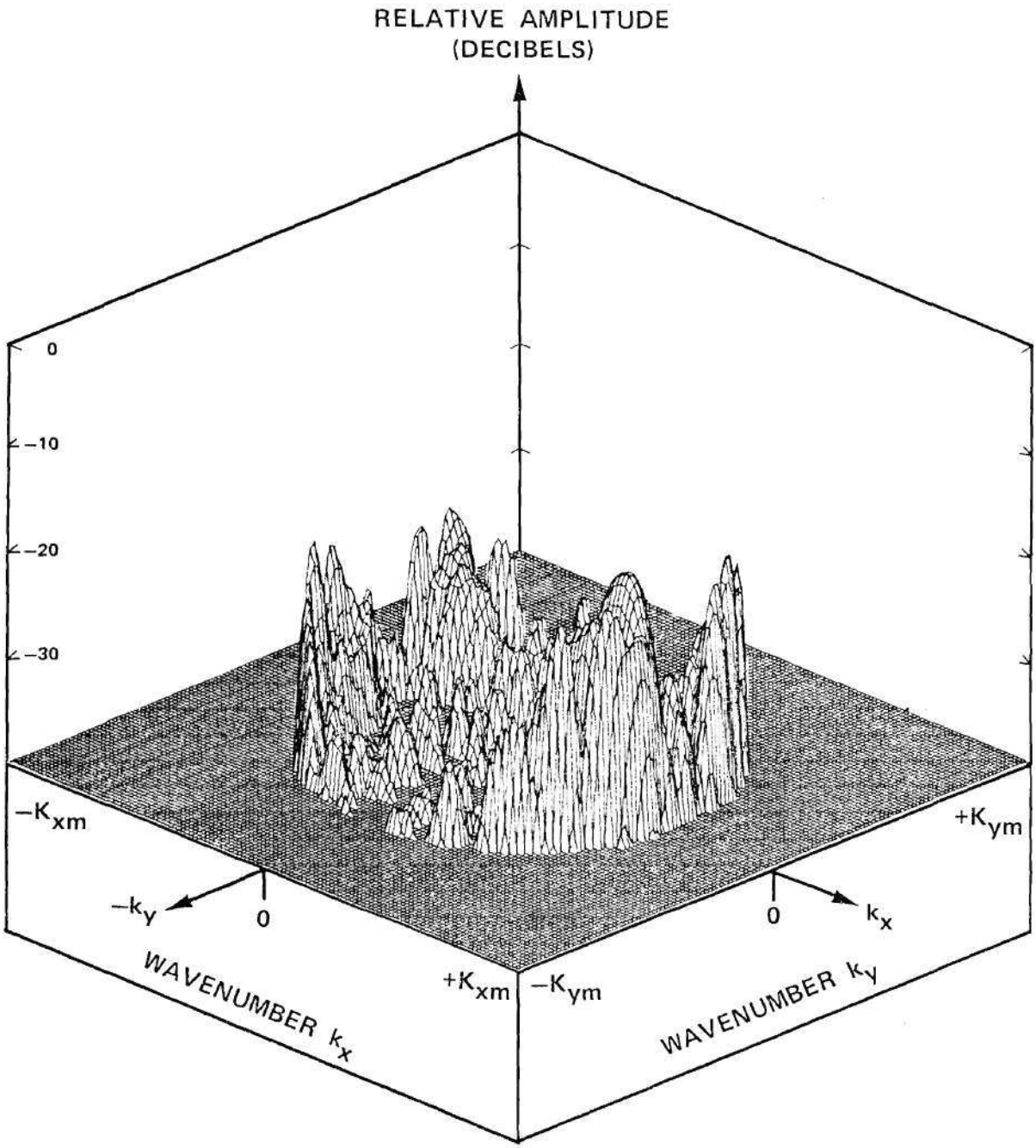

Figure E-2. Amplitude of Measured Spectrum for Undersize Waveguide Probe in Orientation #2.

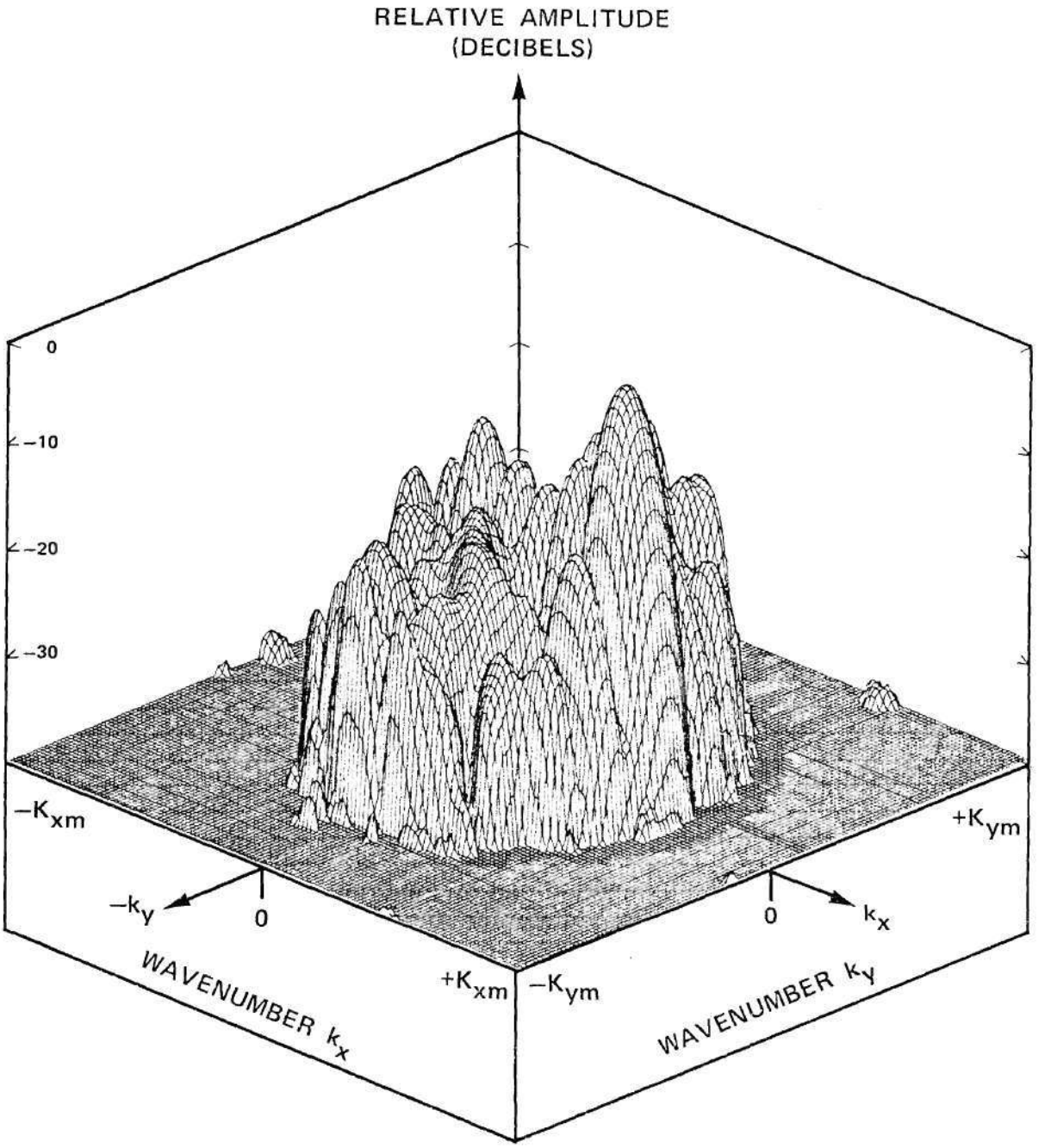

Figure E-3. Amplitude of Measured Spectrum for Open-End Waveguide Probe in Orientation #1.

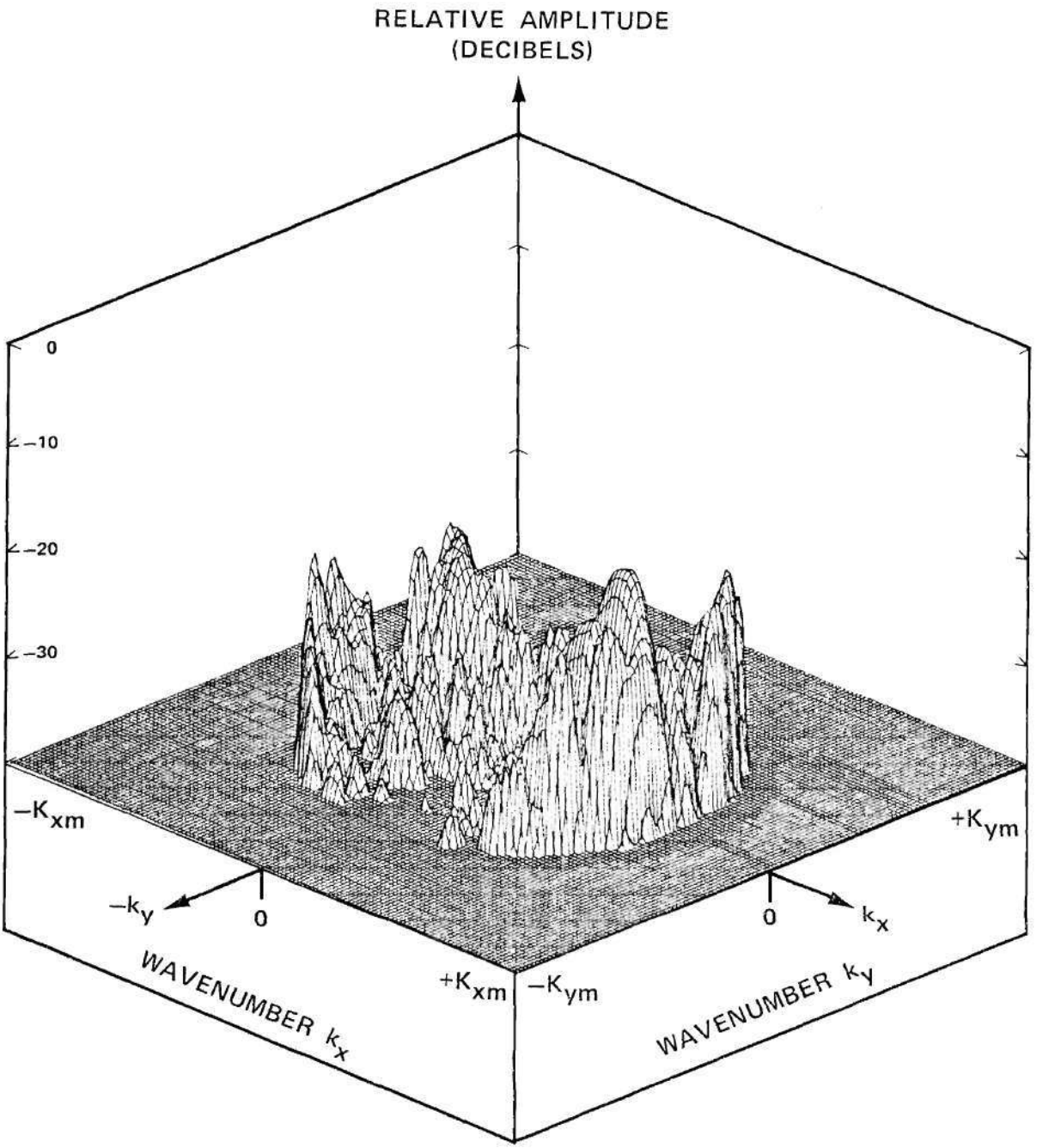

Figure E-4. Amplitude of Measured Spectrum for Open-End Waveguide Probe in Orientation #2.

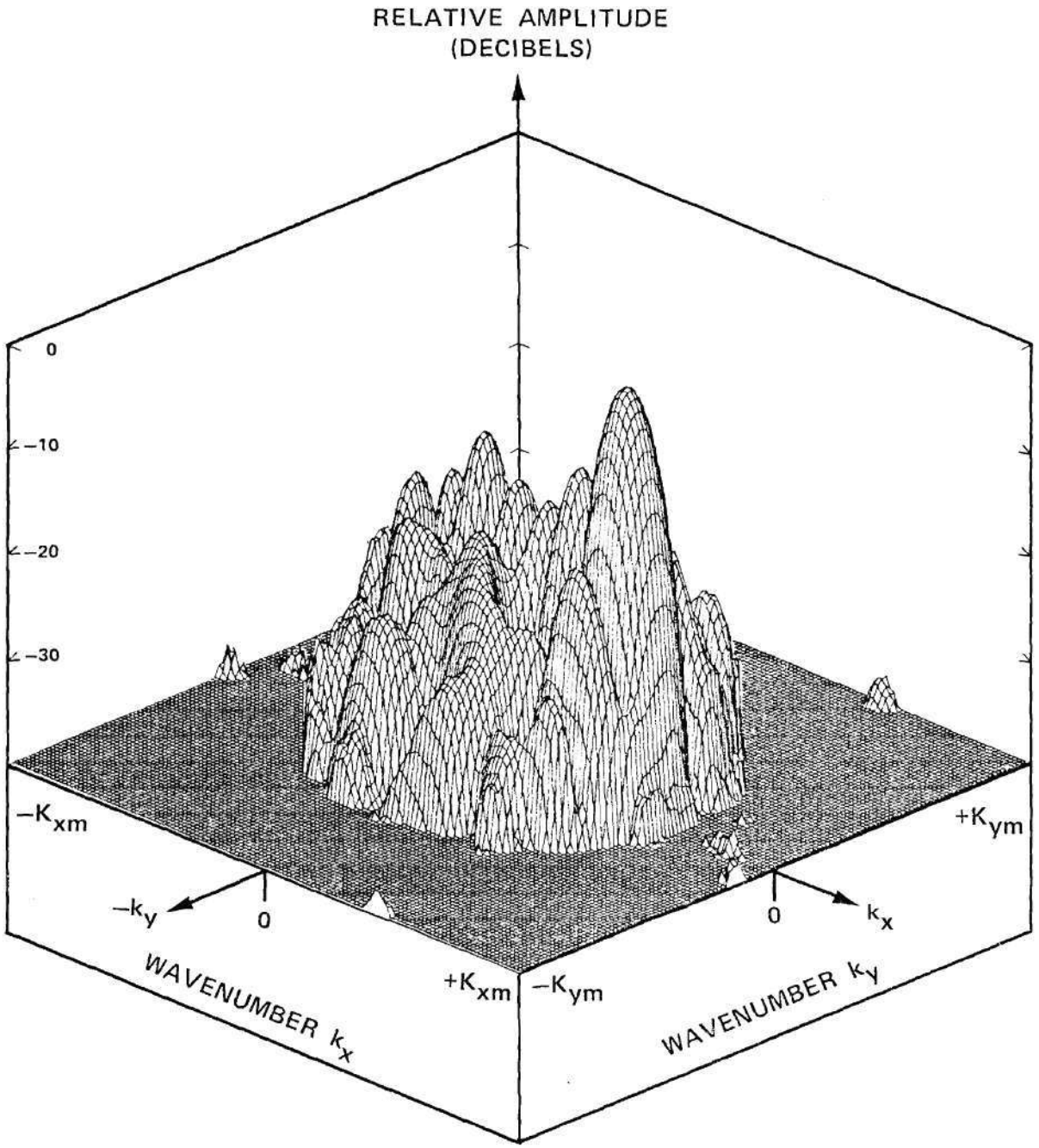

Figure E-5. Amplitude of Measured Spectrum for E-Plane Horn Probe in Orientation #1.

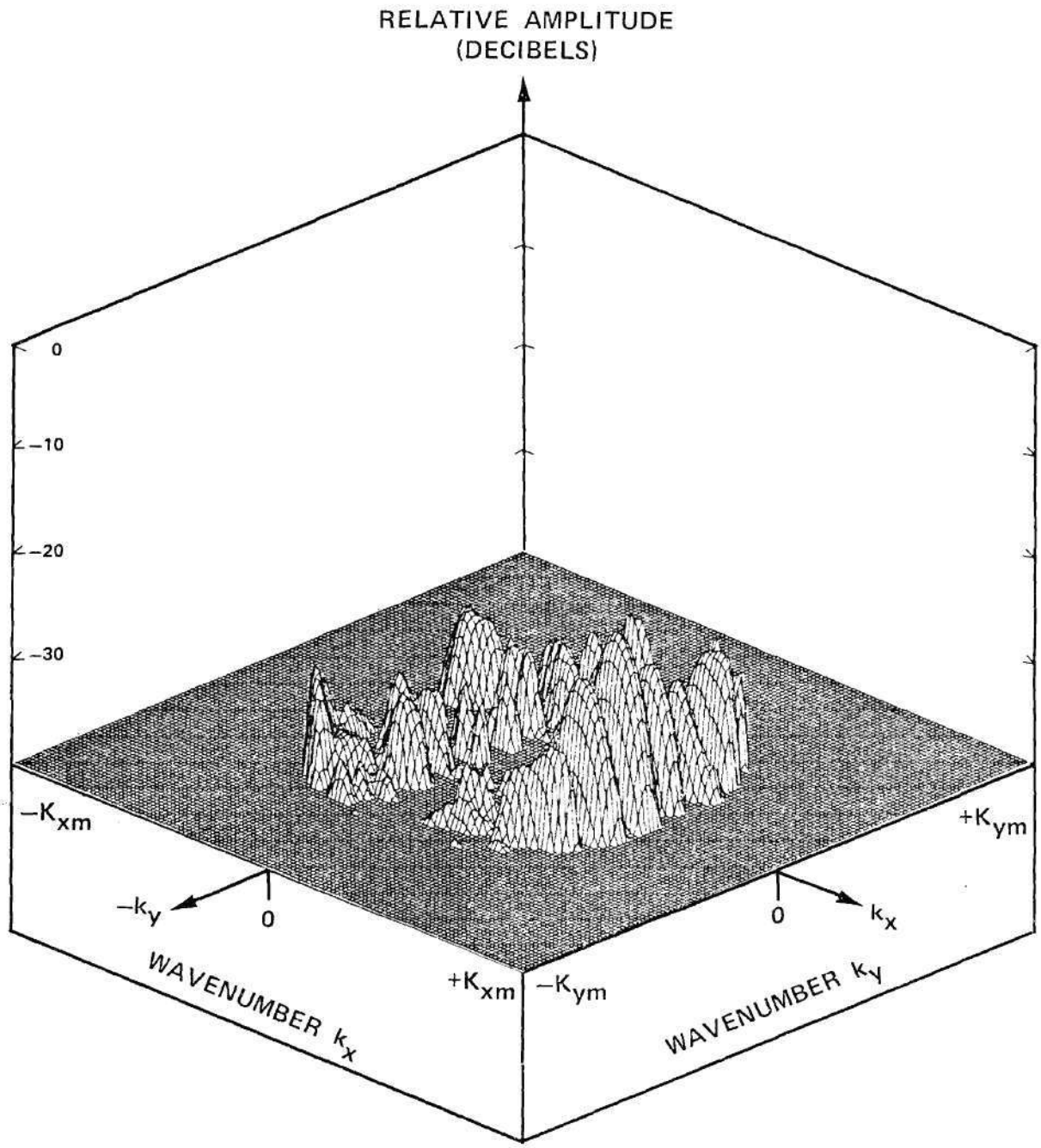

Figure E-6. Amplitude of Measured Spectrum for E-Plane Horn Probe in Orientation #2.

APPENDIX F

ADDITIONAL POWER PATTERNS OF TEST ANTENNA

This appendix presents predicted power patterns (elevation and azimuth components) of the phased array test antenna as predicted from the near-field responses of the three probe antennas used in the investigation. Both H-plane (k_{yn}=0) patterns and conical cut (k_{xn}=.707) patterns are presented for angles corresponding to ±90 degrees. The true patterns were predicted by using all the data in the appropriate 128 x 128 measured data arrays and are shown as solid lines in the graphs. The patterns predicted from the 32 x 32 arrays are shown as dotted lines. The vertical scale in each graph ranges from zero to -40 dB. All patterns are shown relative to the peak of the main beam of the pattern shown in Figures 5-23 through 5-25 for the respective probes.

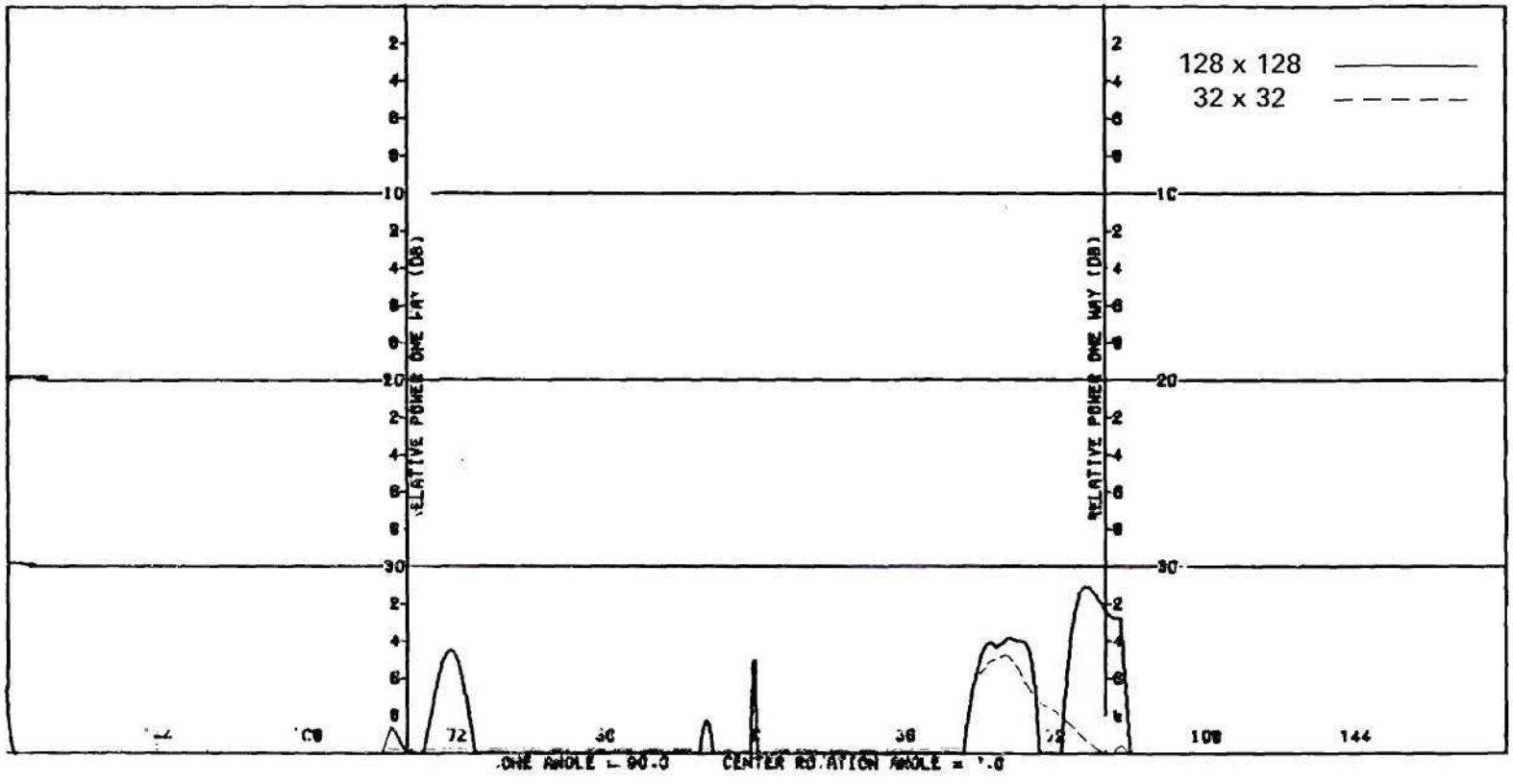

Figure F-1. H-Plane Power Patterns Predicted From Near-Field Measurements Using Undersize Waveguide Probe (Azimuth Component).

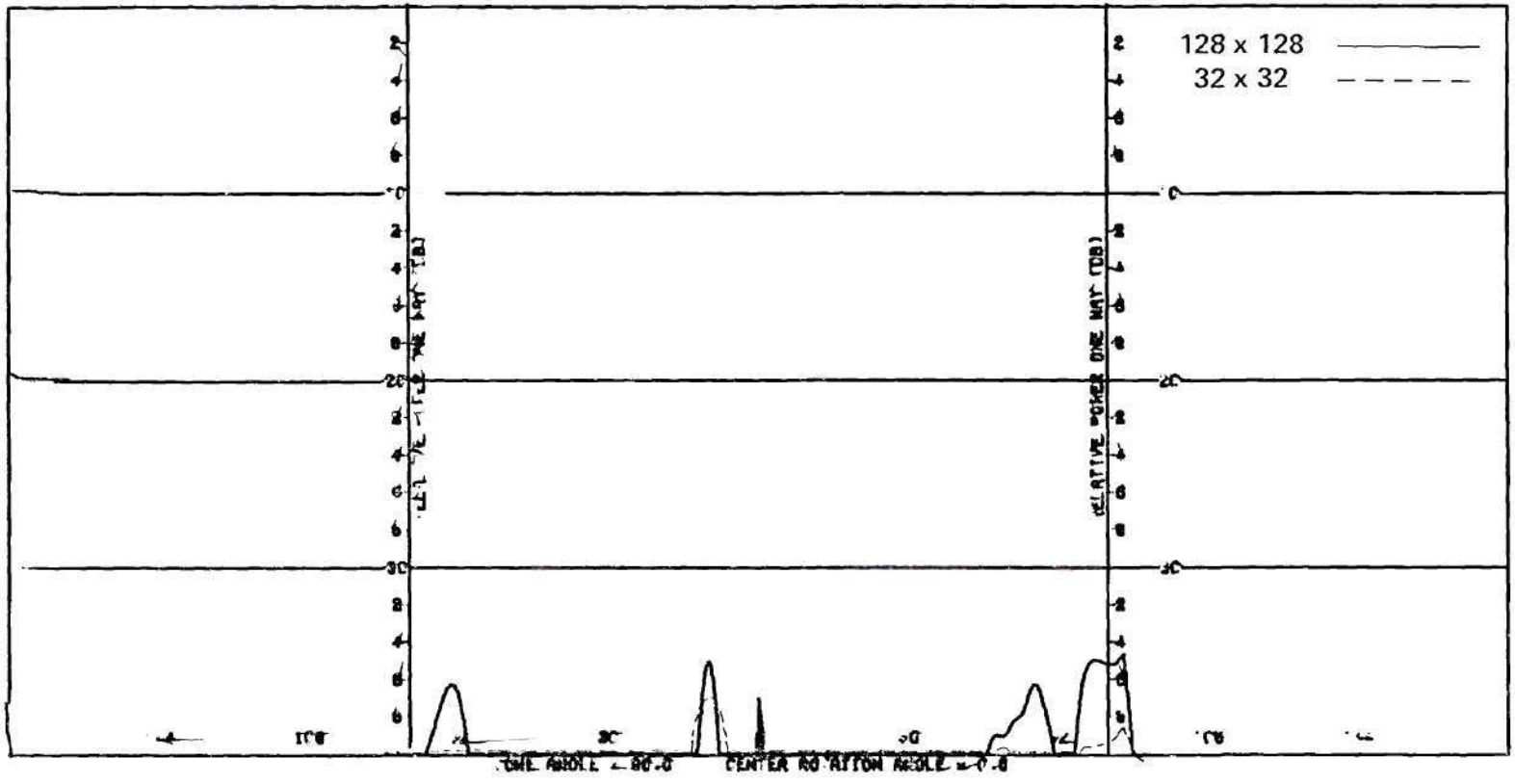

Figure F-2. H-Plane Power Patterns Predicted From Near-Field Measurements Using Open-End Waveguide Probe (Azimuth Component).

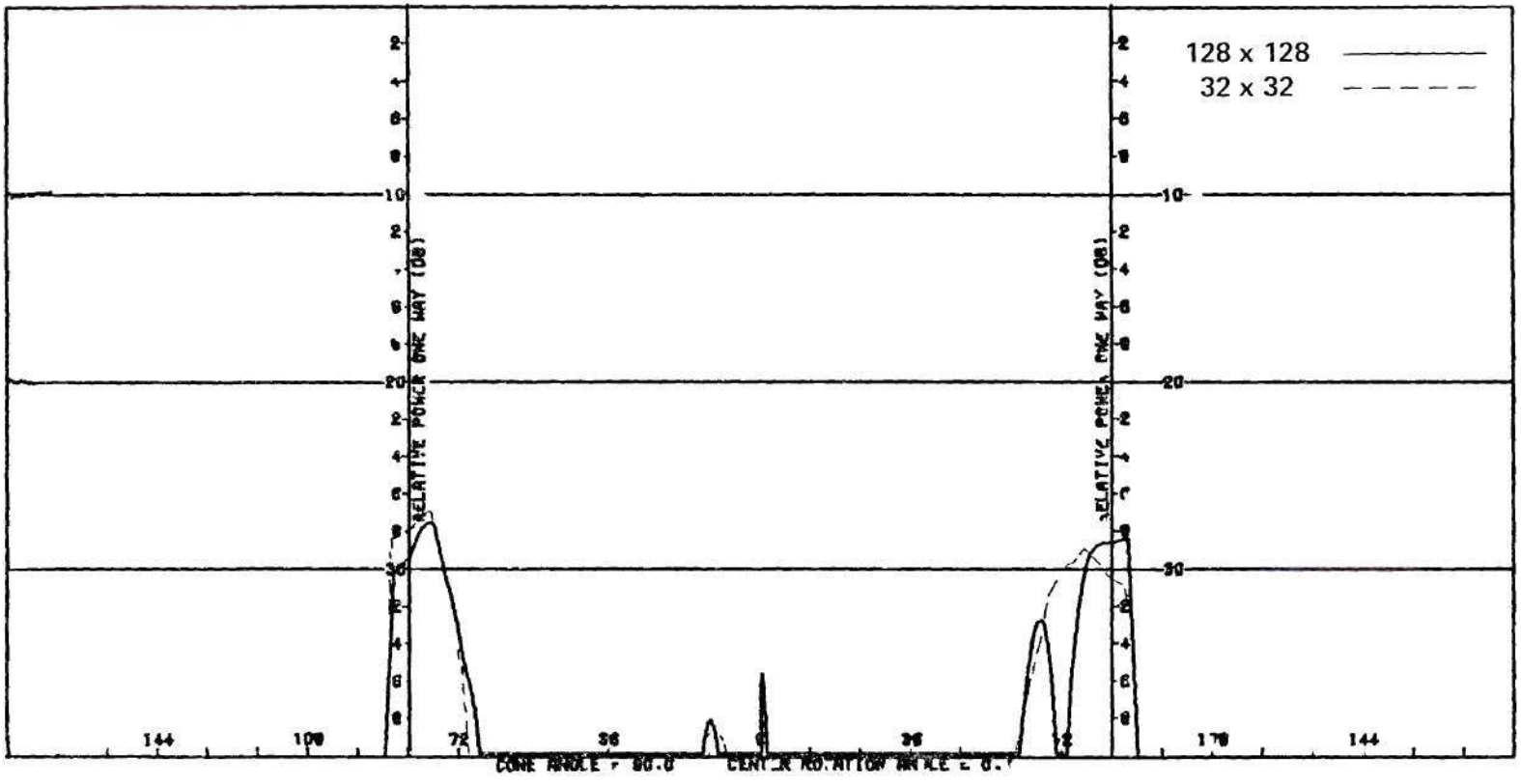

Figure F-3. H-Plane Power Patterns Predicted From Near-Field Measurements Using E-Plane Horn Probe (Azimuth Component).

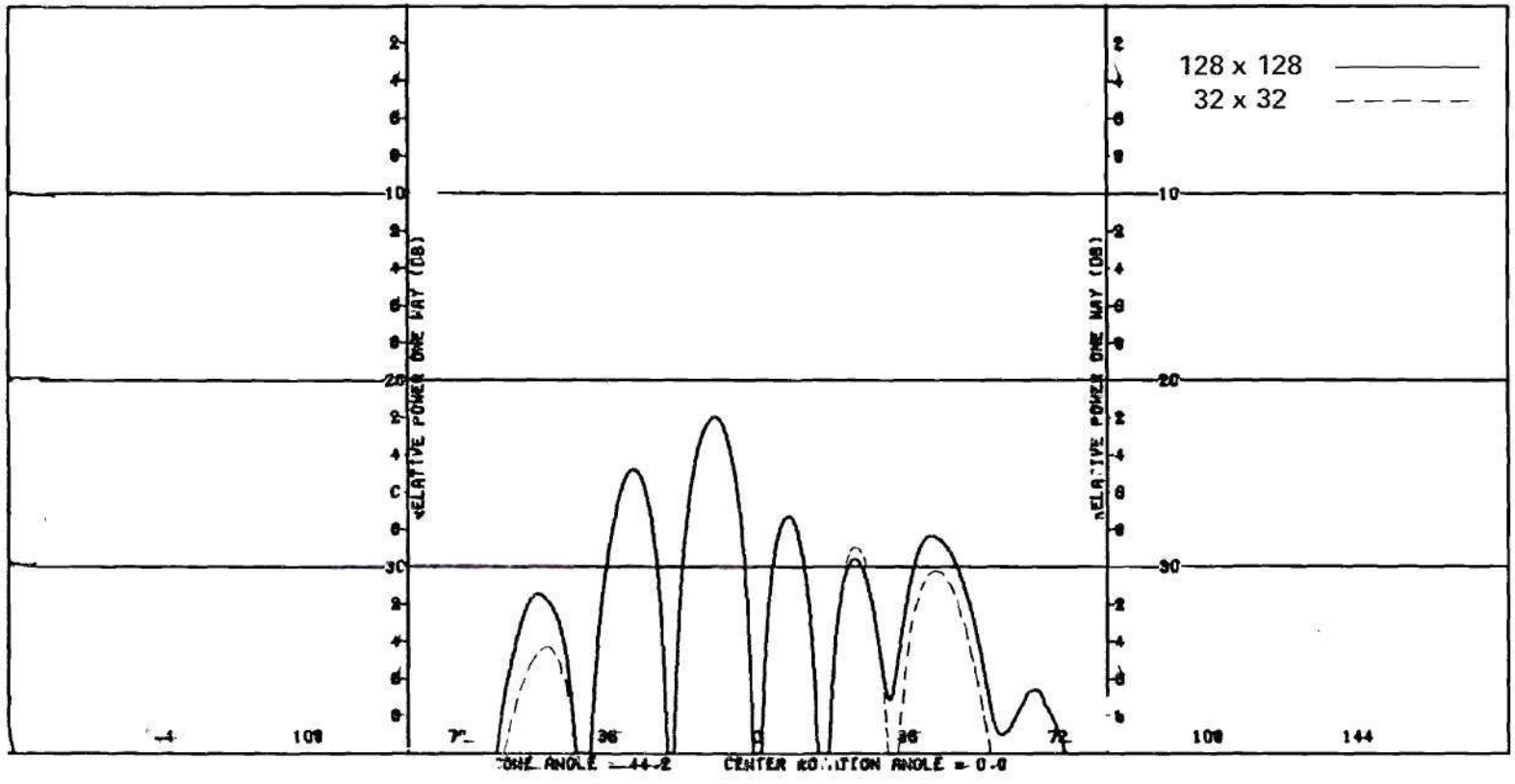

Figure F-4. Conical Cut Power Patterns Predicted From Near-Field Measurements Using Undersize Waveguide Probe (Azimuth Component).

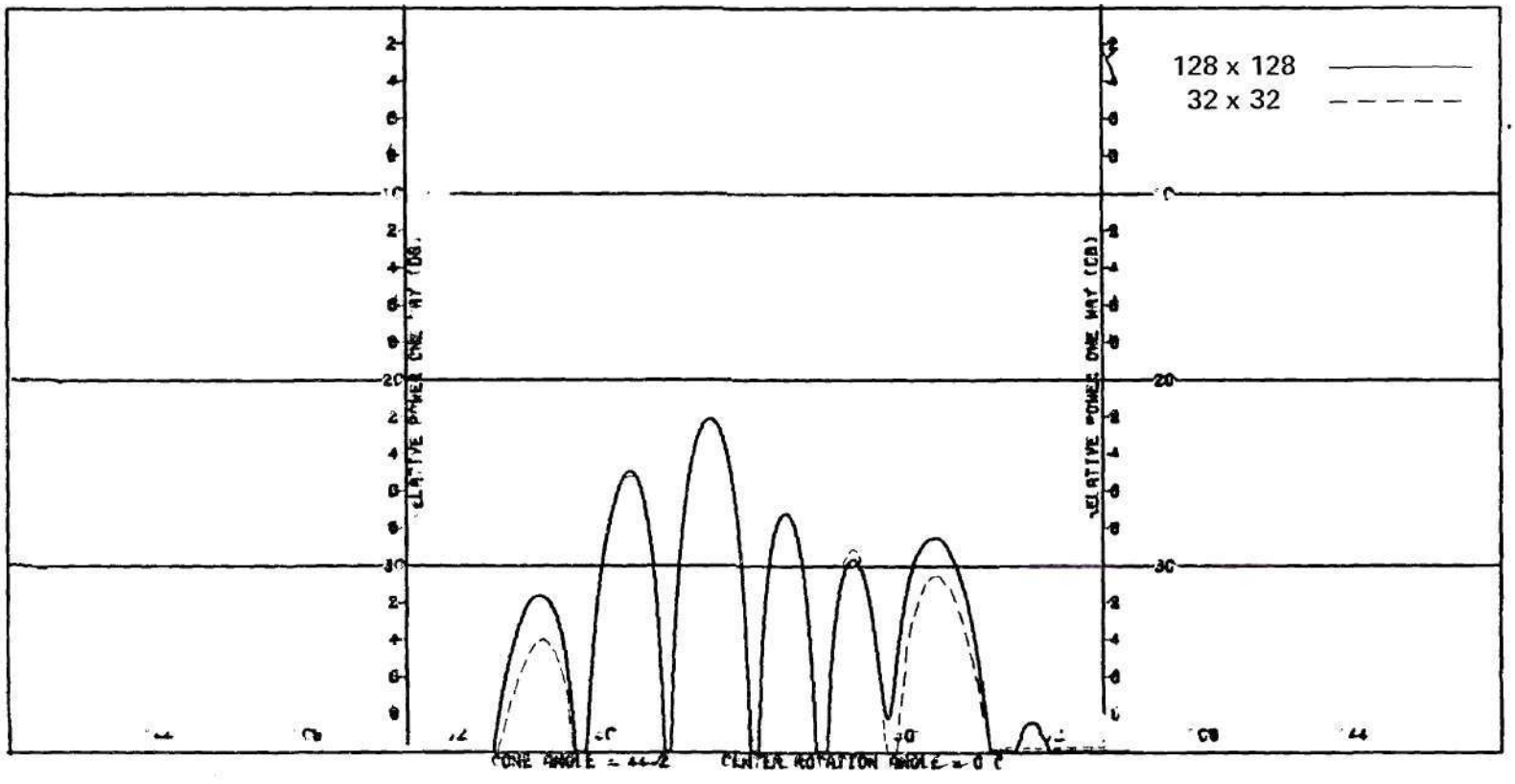

Figure F-5. Conical Cut Power Patterns Predicted From Near-Field Measurements Using Open-End Waveguide Probe (Azimuth Component).

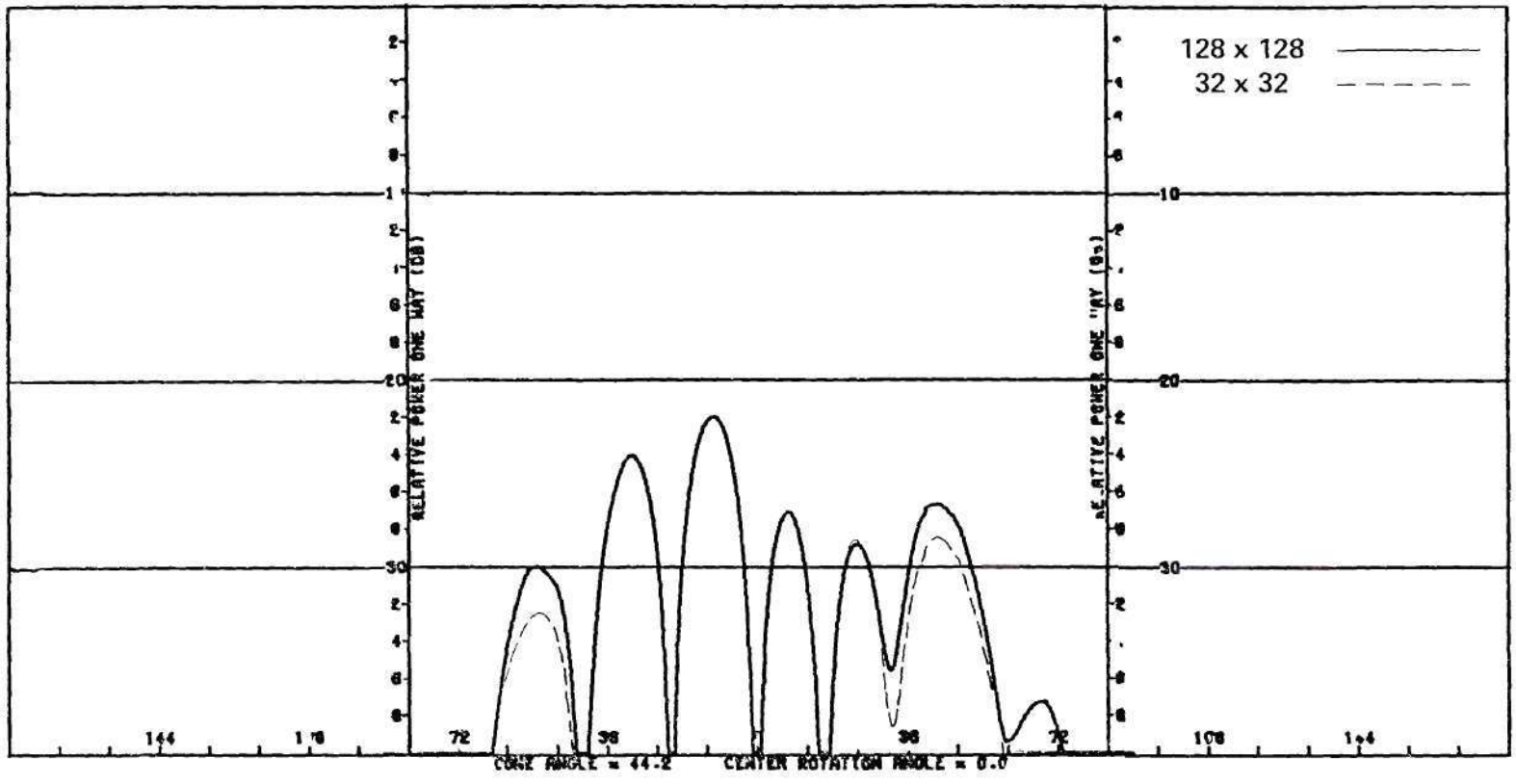

Figure F-6. Conical Cut Power Patterns Predicted From Near-Field Measurements Using E-Plane Horn Probe (Azimuth Component).

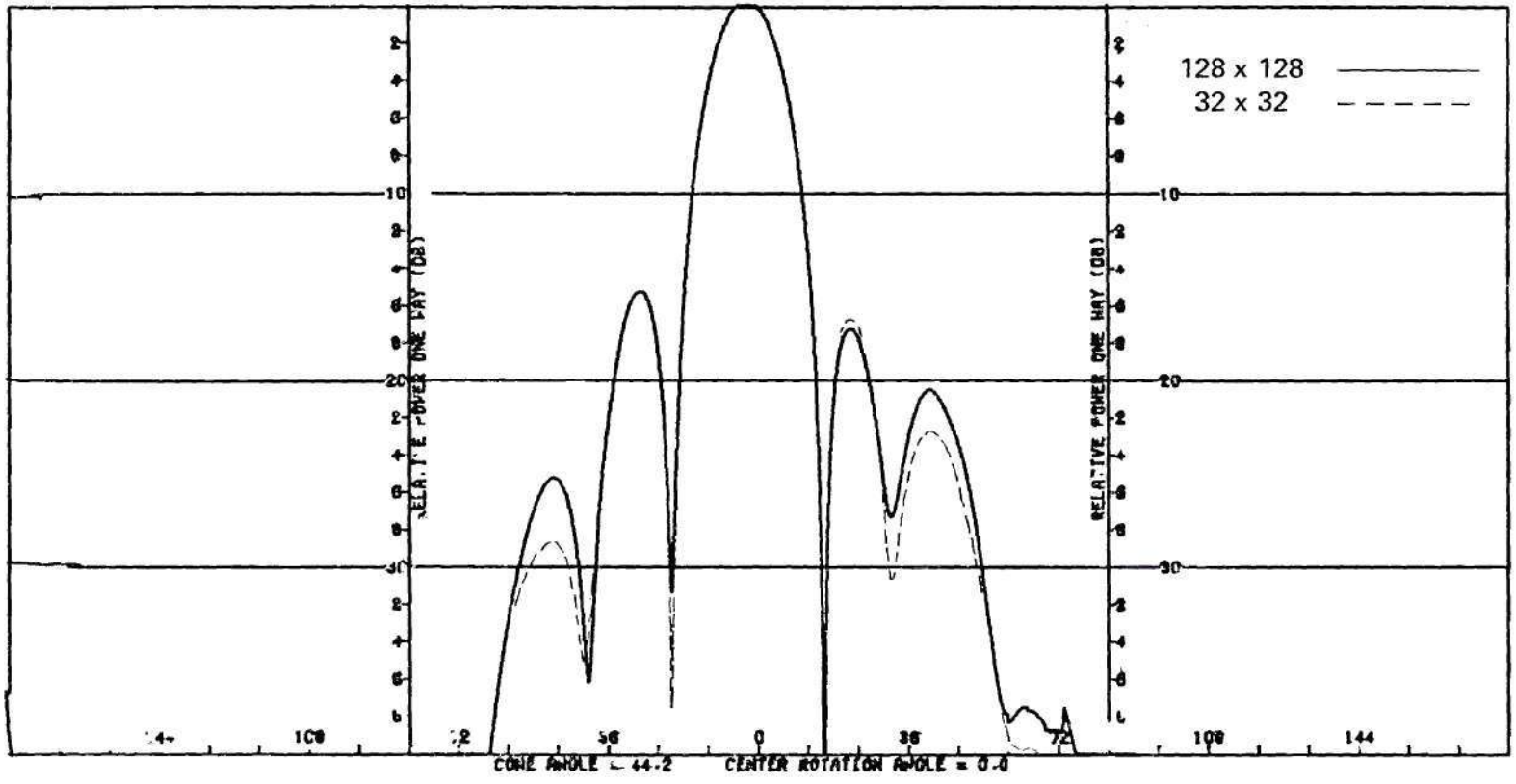

Figure F-7. Conical Cut Power Pattern Predicted From Near-Field Measurements Using Undersize Waveguide Probe (Elevation Component).

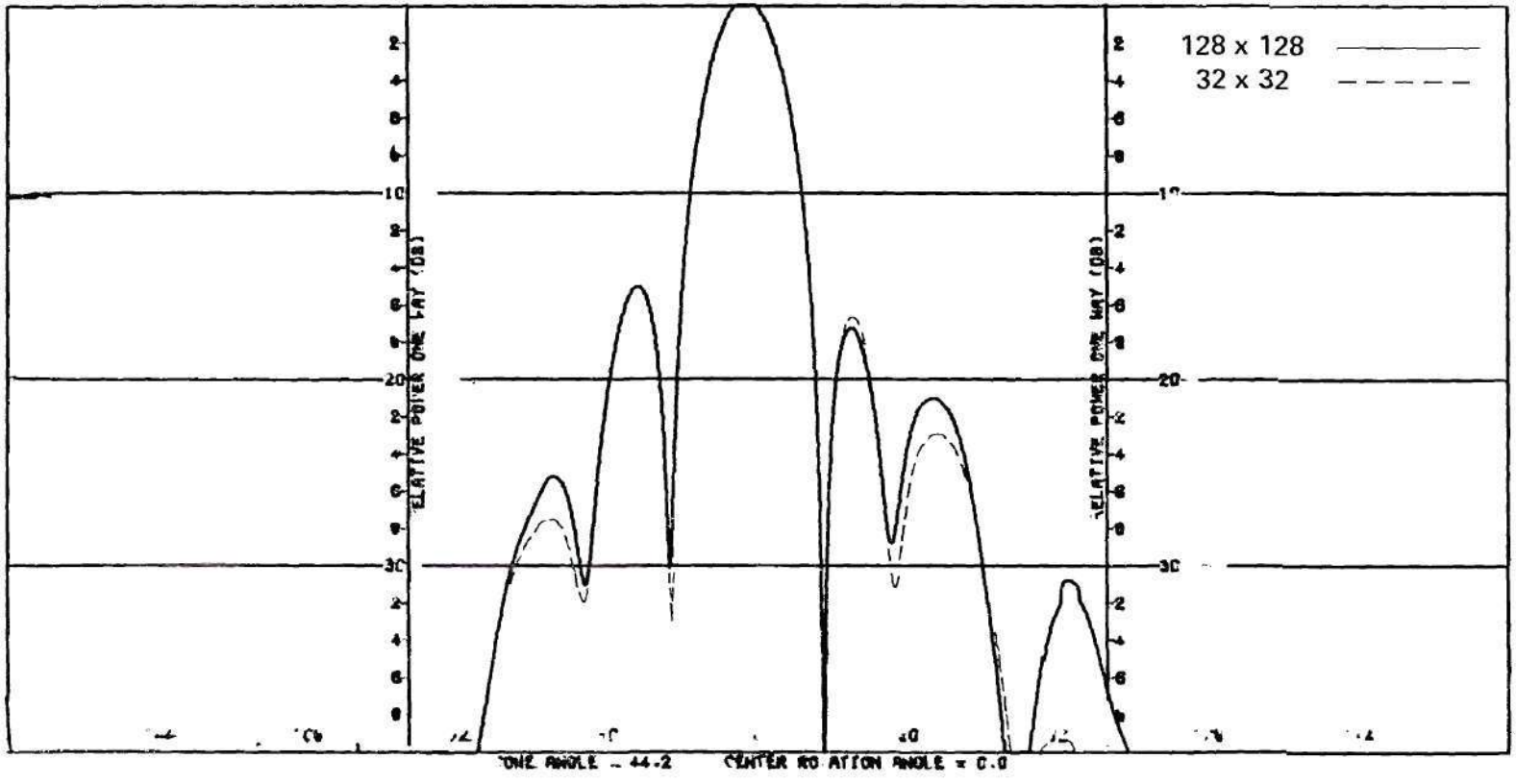
128 x 128
32 x 32
RELATIVE POWER ONE WAY (DB)
RELATIVE POWER ONE WAY (DB)
CONE ANGLE = 44.2
CENTER ROTATION ANGLE = 0.0

Figure F-8. Conical Cut Power Patterns Predicted From Near-Field Measurements Using Open-End Waveguide Probe (Elevation Components).

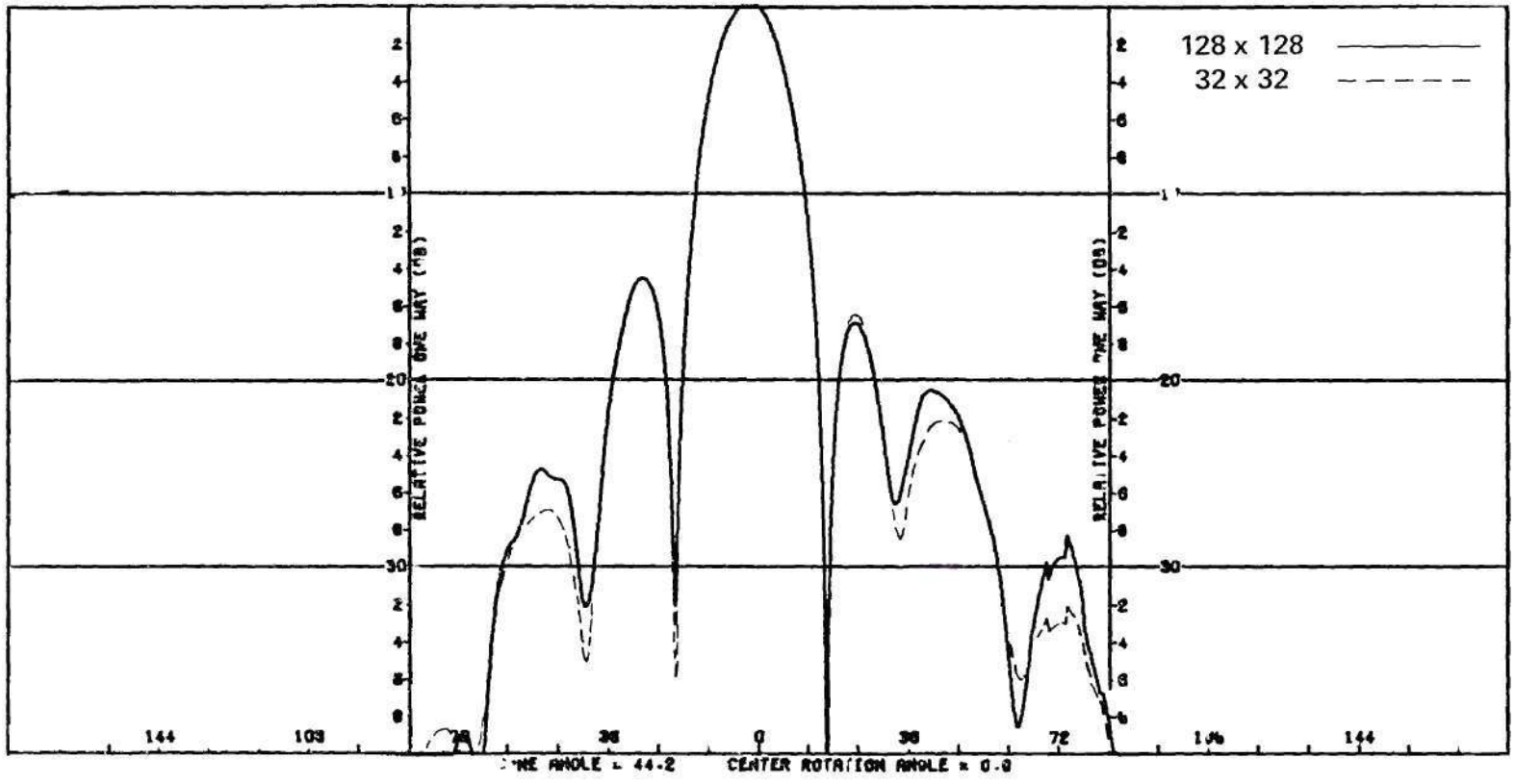

Figure F-9. Conical Cut Power Patterns Predicted From Near-Field Measurements Using E-Plane Horn Probe (Elevation Component).

REFERENCES

1. D. M. Kerns, "Correction of Near-Field Antenna Measurements Made with an Arbitrary But Known Measuring Antenna," Electronics Letters, vol. 6, no. 11, pp. 346-347, May 1970.

2. Principles of Microwave Circuits, edited by C. G. Montgomery, R. H. Dicke, and E. M. Purcell, Radiation Laboratory Series, McGraw-Hill, Ch. 5, New York, 1948.

3. P. C. Clemmow, The Plane Wave Spectrum Representation of Electromagnetic Fields, Pergamon Press, Oxford, 1966.

4. Edward B. Joy, "Spatial Sampling and Filtering in Near-Field Measurements," Doctoral Thesis, Georgia Institute of Technology, Atlanta, GA, November 1970.

5. C. E. Shannon, "Communication in the Presence of Noise," Proceedings IRE, pp. 10-21, January 1949.

6. W. M. Leach, "Probe Compensated Near-Field Measurements on a Cylinder," Doctoral Thesis, Georgia Institute of Technology, Atlanta, GA, August 1972.

7. D. T. Paris and F. K. Hurd, Basic Electromagnetic Theory, McGraw-Hill, pp. 502-505, New York, 1969.

8. J. A. Stratton, Electromagnetic Theory, McGraw-Hill, Ch. 7, New York, 1941.

9. M. A. K. Hamid, "The Radiation Pattern of an Antenna From Near-Field Correlation Measurements," IEEE Trans., AP-16, pp. 351-353, May 1968.

10. John Brown and E. V. Jull, "The Prediction of Aerial Radiation Patterns from Near-Field Measurements," Proceedings IEE, vol. 108B, pp. 635-644, November 1961.

11. Frank Jensen, "Electromagnetic Near-Field - Far-Field Correlations," Doctoral Thesis, The Technical University of Denmark, Lyngby, July 1970.

12. Paul F. Wacker, "Non-planar Near-Field Measurements: Spherical Scanning," Technical Report AFAL-TR-75-38, by National Bureau of Standards for Air Force Avionics Laboratory, Contract No. F33615-74-M-6001, April 1975.

13. G. P. Rodrigue, E. B. Joy, and C. P. Burns, "An Investigation of the Accuracy of Far-Field Radiation Patterns Determined From Near-Field Measurements," Technical Report for U.S. Army Missile Command by Georgia Institute of Technology, Contract No. DAAH01-72-C-0950, August 1973.

14. G. P. Rodrigue, E. B. Joy, G. K. Huddleston, C. P. Burns, E. C. Burdette, and J. Hanfling, "A Study of Phased Array Antenna Patterns Determined by Measurements on a Near-Field Range," Technical Report for U.S. Army Missile Command by Georgia Institute of Technology, Contract No. DAAH01-72-C-0950, March 1975.

15. G. K. Huddleston, E. B. Joy, G. P. Rodrigue, C. P. Burns, and W. J. Storey, "A Study of Near-Field Data Handling and Probe Design Techniques," Technical Report for U.S. Army Missile Command by Georgia Institute of Technology, Contract No. DAAH01-75-C-0953, April 1976.

16. Arthur D. Yaghjian, "Planar Near-Field Measurement Techniques on High Performance Arrays - Part I: Error Analysis for Non-Scanning Beam Patterns," Technical Report AFAL-TR-75-67 for Air Force Avionics Laboratory by National Bureau of Standards, July 1975.

17. A. C. Newell and M. L. Crawford, "Planar Near-Field Measurements on High Performance Array Antennas," NBSIR-74-380, National Bureau of Standards, Boulder, Colorado, July 1974.

18. J. Arsac, Fourier Transforms and the Theory of Distributions, Ch. 5, Prentice-Hall, Inc., Englewood Cliffs, NJ, 1966.

19. A. Papoulis, The Fourier Integral and Its Application, McGraw-Hill, New York, Ch. 2, 1962.

20. D. Gabor, "Theory of Communication," Journal IEE (London), vol. 93, Part 3, no. 26, pp. 429-441, 1946.

21. J. H. H. Chalk, "The Optimum Pulse Shape for Pulse Communications," Journal IEE (London), vol. 87, pp. 88-92, 1950.

22. D. Slepian and H. O. Pollak, "Prolate Spheroidal Wave Functions, Fourier Analysis and Uncertainty-I," BSTJ, 40, pp. 43-64, January 1961.

23. H. J. Landau and H. O. Pollak, "Prolate Spheroidal Wave Functions, Fourier Analysis and Uncertainty-II," BSTJ, 40, pp. 65-84, January 1961.

24. H. J. Landau and H. O. Pollak, "Prolate Spheroidal Wave Functions, Fourier Analysis and Uncertainty-III," BSTJ, 41, pp. 1295-1336, July 1962.

25. J. A. Stratton, P. M. Morse, L. J. Chu, J. D. C. Little, and F. J. Corbato, Spheroidal Wave Functions, The Technology Press of MIT, Cambridge, MA, and John Wiley & Sons, New York, 1956.

26. C. Flammer, Spheroidal Wave Functions, Stanford University Press, Stanford, CA, 1957.

27. David Slepian, "Prolate Spheroidal Wave Functions, Fourier Analysis and Uncertainty-IV: Extensions to Many Dimensions; Generalized Prolate Spheroidal Functions," BSTJ, 43, pp. 3009-3057, November 1964.

28. David Slepian, "Some Asymptotic Expansions for Prolate Spheroidal Wave Functions," J. Math. and Physics, 44, no. 2, pp. 99-140, June 1965.

29. David Slepian and Estelle Sonneblick, "Eigenvalues Associated With Prolate Spheroidal Wave Functions of Zero Order," BSTJ, 44, pp. 1745-1759, October 1965.

30. Thomas S. Fong, "On the Problem of Optimum Antenna Aperture Distribution," Journal of the Franklin Institute, vol. 283, no. 3, pp. 235-249, 1967.

31. D. R. Rhodes, Synthesis of Planar Antenna Sources, Oxford University Press, London, 1974.

32. Julius S. Bendat and Allan G. Piersol, Random Data: Analysis and Measurement Procedures, John Wiley and Sons, Inc., Ch. 7, New York, 1971.

33. B. R. Hunt and J. R. Breedlove, "Scan and Display Considerations in Processing Images by Digital Computer," IEEE Trans. on Computers, pp. 848-853, August 1975.

34. R. Legault, "Aliasing Problems in Two-Dimensional Sampled Imagery," in Perception of Displayed Information, L. Biberman, Ed., Plenum Press, Ch. 7, New York, 1973.

35. D. P. Peterson and D. Middleton, "Sampling and Reconstruction of Wave-Number Limited Functions in N-Dimensional Euclidean Spaces," Information and Control, 5, pp. 279-323, 1962.

36. B. R. Friedman, "Image Enhancement and Restoration," in Digital Picture Processing, T. S. Huang, Ed., Ch. 5, Springer-Verlag, New York, 1975.

37. John D. Dyson, "Measurement of Near-Fields of Antennas and Scatters," IEEE Trans., AP-21, no. 4, pp. 446-460, July 1973.

38. J. H. Richmond and T. E. Tice, "Probes for Near-Field Measurements," IRE Trans., MTT-3, pp. 32-34, April 1955.

39. R. Justice and V. H. Rumsey, "Measurement of Electric Field Distribution," IRE Trans., AP-3, pp. 177-180, October 1955.

40. D. T. Paris, W. M. Leach, Jr., and E. B. Joy, "Basic Theory of Probe-Compensated Near-Field Measurements," to be published.

41. David Middleton, An Introduction to Statistical Communication Theory, McGraw-Hill, pp. 206-210, New York, 1960.

42. W. W. Bell, Special Functions for Scientists and Engineers, Von Nostrand, Ch. 8, London, 1968.

43. Robert E. Collin and Francis J. Zucker, Antenna Theory, Part I, McGraw-Hill, Ch. 4, New York, 1969.

44. Samuel Silver, Microwave Antenna Theory and Design, Dover Publications, Ch. 5, New York, 1965.

45. Collin and Zucker, Ch. 15.

46. J. Boersma, "Computation of Fresnel Integrals," Mathematics of Computation, 14, p. 380, 1960.

47. Collin and Zucker, Ch. 5.

48. Silver, Sec. 10.2.

49. E. B. Joy and D. T. Paris, "A Practical Method for Measuring the Complex Polarization Ratio of Arbitrary Antennas," IEEE Transactions, vol. AP-21, no. 4, pp. 432-435, July 1973.

50. Paris and Hurd, p. 9.

51. D. M. Kerns, "Plane-Wave Scattering Matrix Theory of Antennas and Antenna-Antenna Interaction: Formulation and Applications," Journal of Research of the National Bureau of Standards, Vol. 80B, No. 1, January-March 1976.

VITA

Gene Keith Huddleston was born in Gainesville, Florida, on February 13, 1941. He is the son of James Daniel Huddleston, Jr. and Louise Davis Huddleston. He was married to Victoria McAllister Etzel of Brooklyn and Westhampton Beach, New York, in July 1967.

He attended elementary and secondary schools in Boston, Georgia, and graduated from Boston High School in June 1959. In September 1959, he entered Georgia Institute of Technology under the cooperative work-study plan. He was awarded the Bachelor of Electrical Engineering, with Highest Honor, in June 1964, and was commissioned a Second Lieutenant in the United States Marine Corps.

Upon completion of the basic officers' course at Quantico, Virginia, and ranger and airborne training at Fort Benning, Georgia, he served as a reconnaissance platoon commander with the Third Marine Division in the Republic of Vietnam. Returning from overseas in June 1965, he served at Marine Barracks, Washington, D.C., and at the Marine Corps Institute until August 1968.

In September 1968, he entered the Graduate Division of the Georgia Institute of Technology. He served as a graduate research assistant at the Georgia Tech Engineering Experiment Station from September 1968 to March 1970, when he was awarded the Master of Science in Electrical Engineering and became a Research Engineer. In September 1972, he joined the faculty of the School of Electrical Engineering, serving in the rank of Instructor until July 1977. He has worked as a Lecturer in the School of Electrical Engineering from July 1977 to August 1978.